The Strength of Massive Lac du Bonnet Granite Around Underground Openings

By

Charles Derek Martin

A THESIS

SUBMITTED TO THE FACULTY OF GRADUATE STUDIES

IN PARTIAL FULFILLMENT OF THE REQUIREMENTS

FOR THE DEGREE OF

DOCTOR OF PHILOSOPHY

Department of Civil & Geological Engineering

University of Manitoba

Winnipeg, Manitoba

June 1993

Name_____

Dissertation Abstracts International is arranged by broad, general subject categories. Please select the one subject which most nearly describes the content of your dissertation. Enter the corresponding four-digit code in the spaces provided.

Geotechnology
SUBJECT TERM

0 4 2 8   U·M·I

SUBJECT CODE

Subject Categories

THE HUMANITIES AND SOCIAL SCIENCES

COMMUNICATIONS AND THE ARTS
Architecture 0729
Art History 0377
Cinema 0900
Dance 0378
Fine Arts 0357
Information Science 0723
Journalism 0391
Library Science 0399
Mass Communications 0708
Music 0413
Speech Communication 0459
Theater 0465

EDUCATION
General 0515
Administration 0514
Adult and Continuing 0516
Agricultural 0517
Art 0273
Bilingual and Multicultural 0282
Business 0688
Community College 0275
Curriculum and Instruction 0727
Early Childhood 0518
Elementary 0524
Finance 0277
Guidance and Counseling 0519
Health 0680
Higher 0745
History of 0520
Home Economics 0278
Industrial 0521
Language and Literature 0279
Mathematics 0280
Music 0522
Philosophy of 0998
Physical 0523

Psychology 0525
Reading 0535
Religious 0527
Sciences 0714
Secondary 0533
Social Sciences 0534
Sociology of 0340
Special 0529
Teacher Training 0530
Technology 0710
Tests and Measurements 0288
Vocational 0747

LANGUAGE, LITERATURE AND LINGUISTICS
Language
    General 0679
    Ancient 0289
    Linguistics 0290
    Modern 0291
Literature
    General 0401
    Classical 0294
    Comparative 0295
    Medieval 0297
    Modern 0298
    African 0316
    American 0591
    Asian 0305
    Canadian (English) 0352
    Canadian (French) 0355
    English 0593
    Germanic 0311
    Latin American 0312
    Middle Eastern 0315
    Romance 0313
    Slavic and East European 0314

PHILOSOPHY, RELIGION AND THEOLOGY
Philosophy 0422
Religion
    General 0318
    Biblical Studies 0321
    Clergy 0319
    History of 0320
    Philosophy of 0322
Theology 0469

SOCIAL SCIENCES
American Studies 0323
Anthropology
    Archaeology 0324
    Cultural 0326
    Physical 0327
Business Administration
    General 0310
    Accounting 0272
    Banking 0770
    Management 0454
    Marketing 0338
Canadian Studies 0385
Economics
    General 0501
    Agricultural 0503
    Commerce-Business 0505
    Finance 0508
    History 0509
    Labor 0510
    Theory 0511
Folklore 0358
Geography 0366
Gerontology 0351
History
    General 0578

Ancient 0579
Medieval 0581
Modern 0582
Black 0328
African 0331
Asia, Australia and Oceania 0332
Canadian 0334
European 0335
Latin American 0336
Middle Eastern 0333
United States 0337
History of Science 0585
Law 0398
Political Science
    General 0615
    International Law and
        Relations 0616
    Public Administration 0617
Recreation 0814
Social Work 0452
Sociology
    General 0626
    Criminology and Penology ... 0627
    Demography 0938
    Ethnic and Racial Studies 0631
    Individual and Family
        Studies 0628
    Industrial and Labor
        Relations 0629
    Public and Social Welfare 0630
    Social Structure and
        Development 0700
    Theory and Methods 0344
Transportation 0709
Urban and Regional Planning 0999
Women's Studies 0453

THE SCIENCES AND ENGINEERING

BIOLOGICAL SCIENCES
Agriculture
    General 0473
    Agronomy 0285
    Animal Culture and
        Nutrition 0475
    Animal Pathology 0476
    Food Science and
        Technology 0359
    Forestry and Wildlife 0478
    Plant Culture 0479
    Plant Pathology 0480
    Plant Physiology 0817
    Range Management 0777
    Wood Technology 0746
Biology
    General 0306
    Anatomy 0287
    Biostatistics 0308
    Botany 0309
    Cell 0379
    Ecology 0329
    Entomology 0353
    Genetics 0369
    Limnology 0793
    Microbiology 0410
    Molecular 0307
    Neuroscience 0317
    Oceanography 0416
    Physiology 0433
    Radiation 0821
    Veterinary Science 0778
    Zoology 0472
Biophysics
    General 0786
    Medical 0760

EARTH SCIENCES
Biogeochemistry 0425
Geochemistry 0996

Geodesy 0370
Geology 0372
Geophysics 0373
Hydrology 0388
Mineralogy 0411
Paleobotany 0345
Paleoecology 0426
Paleontology 0418
Paleozoology 0985
Palynology 0427
Physical Geography 0368
Physical Oceanography 0415

HEALTH AND ENVIRONMENTAL SCIENCES
Environmental Sciences 0768
Health Sciences
    General 0566
    Audiology 0300
    Chemotherapy 0992
    Dentistry 0567
    Education 0350
    Hospital Management 0769
    Human Development 0758
    Immunology 0982
    Medicine and Surgery 0564
    Mental Health 0347
    Nursing 0569
    Nutrition 0570
    Obstetrics and Gynecology .. 0380
    Occupational Health and
        Therapy 0354
    Ophthalmology 0381
    Pathology 0571
    Pharmacology 0419
    Pharmacy 0572
    Physical Therapy 0382
    Public Health 0573
    Radiology 0574
    Recreation 0575

Speech Pathology 0460
Toxicology 0383
Home Economics 0386

PHYSICAL SCIENCES
Pure Sciences
Chemistry
    General 0485
    Agricultural 0749
    Analytical 0486
    Biochemistry 0487
    Inorganic 0488
    Nuclear 0738
    Organic 0490
    Pharmaceutical 0491
    Physical 0494
    Polymer 0495
    Radiation 0754
Mathematics 0405
Physics
    General 0605
    Acoustics 0986
    Astronomy and
        Astrophysics 0606
    Atmospheric Science 0608
    Atomic 0748
    Electronics and Electricity 0607
    Elementary Particles and
        High Energy 0798
    Fluid and Plasma 0759
    Molecular 0609
    Nuclear 0610
    Optics 0752
    Radiation 0756
    Solid State 0611
Statistics 0463

Applied Sciences
Applied Mechanics 0346
Computer Science 0984

Engineering
    General 0537
    Aerospace 0538
    Agricultural 0539
    Automotive 0540
    Biomedical 0541
    Chemical 0542
    Civil 0543
    Electronics and Electrical 0544
    Heat and Thermodynamics ... 0348
    Hydraulic 0545
    Industrial 0546
    Marine 0547
    Materials Science 0794
    Mechanical 0548
    Metallurgy 0743
    Mining 0551
    Nuclear 0552
    Packaging 0549
    Petroleum 0765
    Sanitary and Municipal 0554
    System Science 0790
Geotechnology 0428
Operations Research 0796
Plastics Technology 0795
Textile Technology 0994

PSYCHOLOGY
General 0621
Behavioral 0384
Clinical 0622
Developmental 0620
Experimental 0623
Industrial 0624
Personality 0625
Physiological 0989
Psychobiology 0349
Psychometrics 0632
Social 0451

Nom _____

Dissertation Abstracts International est organisé en catégories de sujets. Veuillez s.v.p. choisir le sujet qui décrit le mieux votre thèse et inscrivez le code numérique approprié dans l'espace réservé ci-dessous.

SUJET

☐☐☐☐☐ U·M·I
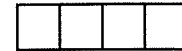
CODE DE SUJET

Catégories par sujets

HUMANITÉS ET SCIENCES SOCIALES

COMMUNICATIONS ET LES ARTS
Architecture 0729
Beaux-arts 0357
Bibliothéconomie 0399
Cinéma 0900
Communication verbale 0459
Communications 0708
Danse 0378
Histoire de l'art 0377
Journalisme 0391
Musique 0413
Sciences de l'information 0723
Théâtre 0465

ÉDUCATION
Généralités 515
Administration 0514
Art 0273
Collèges communautaires 0275
Commerce 0688
Économie domestique 0278
Éducation permanente 0516
Éducation préscolaire 0518
Éducation sanitaire 0680
Enseignement agricole 0517
Enseignement bilingue et
    multiculturel 0282
Enseignement industriel 0521
Enseignement primaire. 0524
Enseignement professionnel 0747
Enseignement religieux 0527
Enseignement secondaire 0533
Enseignement spécial 0529
Enseignement supérieur 0745
Évaluation 0288
Finances 0277
Formation des enseignants 0530
Histoire de l'éducation 0520
Langues et littérature 0279

Lecture 0535
Mathématiques 0280
Musique 0522
Orientation et consultation 0519
Philosophie de l'éducation 0998
Physique 0523
Programmes d'études et
    enseignement 0727
Psychologie 0525
Sciences 0714
Sciences sociales 0534
Sociologie de l'éducation 0340
Technologie 0710

LANGUE, LITTÉRATURE ET LINGUISTIQUE
Langues
    Généralités 0679
    Anciennes 0289
    Linguistique 0290
    Modernes 0291
Littérature
    Généralités 0401
    Anciennes 0294
    Comparée 0295
    Médiévale 0297
    Moderne 0298
    Africaine 0316
    Américaine 0591
    Anglaise 0593
    Asiatique 0305
    Canadienne (Anglaise) 0352
    Canadienne (Française) 0355
    Germanique 0311
    Latino-américaine 0312
    Moyen-orientale 0315
    Romane 0313
    Slave et est-européenne 0314

PHILOSOPHIE, RELIGION ET THÉOLOGIE
Philosophie 0422
Religion
    Généralités 0318
    Clergé 0319
    Études bibliques 0321
    Histoire des religions 0320
    Philosophie de la religion 0322
Théologie 0469

SCIENCES SOCIALES
Anthropologie
    Archéologie 0324
    Culturelle 0326
    Physique 0327
Droit 0398
Économie
    Généralités 0501
    Commerce-Affaires 0505
    Économie agricole 0503
    Économie du travail 0510
    Finances 0508
    Histoire 0509
    Théorie 0511
Études américaines 0323
Études canadiennes 0385
Études féministes 0453
Folklore 0358
Géographie 0366
Gérontologie 0351
Gestion des affaires
    Généralités 0310
    Administration 0454
    Banques 0770
    Comptabilité 0272
    Marketing 0338
Histoire
    Histoire générale 0578

Ancienne 0579
Médiévale 0581
Moderne 0582
Histoire des noirs 0328
Africaine 0331
Canadienne 0334
États-Unis 0337
Européenne 0335
Moyen-orientale 0333
Latino-américaine 0336
Asie, Australie et Océanie 0332
Histoire des sciences 0585
Loisirs 0814
Planification urbaine et
    régionale 0999
Science politique
    Généralités 0615
    Administration publique 0617
    Droit et relations
        internationales 0616
Sociologie
    Généralités 0626
    Aide et bien-àtre social 0630
    Criminologie et
        établissements
        pénitentiaires 0627
    Démographie 0938
    Études de l' individu et
        de la famille 0628
    Études des relations
        interethniques et
        des relations raciales 0631
    Structure et développement
        social 0700
    Théorie et méthodes. 0344
    Travail et relations
        industrielles 0629
Transports 0709
Travail social 0452

SCIENCES ET INGÉNIERIE

SCIENCES BIOLOGIQUES
Agriculture
    Généralités 0473
    Agronomie. 0285
    Alimentation et technologie
        alimentaire 0359
    Culture 0479
    Élevage et alimentation 0475
    Exploitation des péturages 0777
    Pathologie animale 0476
    Pathologie végétale 0480
    Physiologie végétale 0817
    Sylviculture et faune 0478
    Technologie du bois 0746
Biologie
    Généralités 0306
    Anatomie 0287
    Biologie (Statistiques) 0308
    Biologie moléculaire 0307
    Botanique 0309
    Cellule 0379
    Écologie 0329
    Entomologie 0353
    Génétique 0369
    Limnologie 0793
    Microbiologie 0410
    Neurologie 0317
    Océanographie 0416
    Physiologie 0433
    Radiation 0821
    Science vétérinaire 0778
    Zoologie 0472
Biophysique
    Généralités 0786
    Medicale 0760

SCIENCES DE LA TERRE
Biogéochimie 0425
Géochimie 0996
Géodésie 0370
Géographie physique 0368

Géologie 0372
Géophysique 0373
Hydrologie 0388
Minéralogie 0411
Océanographie physique 0415
Paléobotanique 0345
Paléoécologie 0426
Paléontologie 0418
Paléozoologie 0985
Palynologie 0427

SCIENCES DE LA SANTÉ ET DE L'ENVIRONNEMENT
Économie domestique 0386
Sciences de l'environnement 0768
Sciences de la santé
    Généralités 0566
    Administration des hipitaux .. 0769
    Alimentation et nutrition 0570
    Audiologie 0300
    Chimiothérapie 0992
    Dentisterie 0567
    Développement humain 0758
    Enseignement 0350
    Immunologie 0982
    Loisirs 0575
    Médecine du travail et
        thérapie 0354
    Médecine et chirurgie 0564
    Obstétrique et gynécologie ... 0380
    Ophtalmologie 0381
    Orthophonie 0460
    Pathologie 0571
    Pharmacie 0572
    Pharmacologie 0419
    Physiothérapie 0382
    Radiologie 0574
    Santé mentale 0347
    Santé publique 0573
    Soins infirmiers 0569
    Toxicologie 0383

SCIENCES PHYSIQUES

Sciences Pures
Chimie
    Généralités 0485
    Biochimie 487
    Chimie agricole 0749
    Chimie analytique 0486
    Chimie minérale 0488
    Chimie nucléaire 0738
    Chimie organique 0490
    Chimie pharmaceutique 0491
    Physique 0494
    PolymCres 0495
    Radiation 0754
Mathématiques 0405
Physique
    Généralités 0605
    Acoustique 0986
    Astronomie et
        astrophysique 0606
    Electronique et électricité 0607
    Fluides et plasma 0759
    Météorologie 0608
    Optique 0752
    Particules (Physique
        nucléaire) 0798
    Physique atomique 0748
    Physique de l'état solide 0611
    Physique moléculaire 0609
    Physique nucléaire 0610
    Radiation 0756
Statistiques 0463

Sciences Appliqués Et Technologie
Informatique 0984
Ingénierie
    Généralités 0537
    Agricole 0539
    Automobile 0540

Biomédicale 0541
Chaleur et ther
    modynamique 0348
Conditionnement
    (Emballage) 0549
Génie aérospatial 0538
Génie chimique 0542
Génie civil 0543
Génie électronique et
    électrique 0544
Génie industriel 0546
Génie mécanique 0548
Génie nucléaire 0552
Ingénierie des systàmes 0790
Mécanique navale 0547
Métallurgie 0743
Science des matériaux 0794
Technique du pétrole 0765
Technique minière 0551
Techniques sanitaires et
    municipales 0554
Technologie hydraulique 0545
Mécanique appliquée 0346
Géotechnologie 0428
Matières plastiques
    (Technologie) 0795
Recherche opérationnelle 0796
Textiles et tissus (Technologie) 0794

PSYCHOLOGIE
Généralités 0621
Personnalité 0625
Psychobiologie 0349
Psychologie clinique 0622
Psychologie du comportement 0384
Psychologie du développement .. 0620
Psychologie expérimentale 0623
Psychologie industrielle 0624
Psychologie physiologique 0989
Psychologie sociale 0451
Psychométrie 0632

🌐

THE STRENGTH OF MASSIVE LAC DU BONNET GRANITE

AROUND UNDERGROUND OPENINGS

BY

CHARLES DEREK MARTIN

A Thesis submitted to the Faculty of Graduate Studies of the University of Manitoba in partial
fulfillment of the requirements for the degree of

DOCTOR OF PHILOSOPHY

© 1993

Abstract

Tunnels excavated in massive unfractured Lac du Bonnet granite at the 420 Level of the Underground Research Laboratory showed typical signs of instability, i.e., spalling, slabbing, notch development. Two-dimensional elastic stress analyses of the failed tunnels indicated that failure was occurring at stress levels of about 100 MPa. A laboratory testing program was carried out using conventional unconfined-compression tests and triaxial-compression tests. In addition, uniaxial and biaxial tests of physical models containing circular holes were also conducted. All the laboratory tests indicated that the laboratory strength of Lac du Bonnet granite was twice the calculated stress level at which failure occurred. This result led to a study of massive rock strength using laboratory data and field observations.

In classical geotechnics, the shear strength of a rock is regarded as made up of two components, intrinsic strength or cohesion, and frictional strength. Laboratory tests were carried out which showed that initially, when rock deformations are essentially elastic, there is a maximum cohesive strength which is about 0.7-0.8 of the standard laboratory unconfined compressive strength. As the loads increase above this maximum cohesive strength, friction is increasingly mobilized and the associated nonelastic displacements damage the cohesion. Consequently at displacements near the peak strength, i.e., when friction is fully mobilized, approximately 70% of the initial cohesion has been lost. The laboratory tests showed that most of the cohesion loss results from very small displacements. The loss in cohesion was modelled using the Griffith locus based on a sliding crack model.

Microseismic monitoring of a circular test tunnel excavated on the 420 Level of the Underground Research Laboratory revealed that considerable damage, i.e., cracking, was

occurring near the face of the advancing tunnel. Three dimensional numerical stress analyses were carried out to investigate the loading path near the face of the test tunnel. The analyses showed that the loading path exceeded the crack initiation stress measured in the laboratory tests but that the loading path did not exceed the initial cohesion values measured in the laboratory tests. Thus the loading path stress magnitudes were not sufficient to mobilize friction.

The effect of stress rotation, near the advancing tunnel face, was also investigated since it has been demonstrated, for tensile loading, that cracks can be made to grow at a constant load by rotating the direction of the applied load. Three-dimensional numerical stress analyses showed that the principal stress directions near the face of the tunnel rotate as the tunnel advances. It is proposed that the rotation of the stresses near the face amplifies the damage *in situ* and that this damage is equivalent to the damage in the laboratory tests in which the cohesion was reduced after only small displacements by 70%. Thus, when the maximum principal stress magnitude is above the crack initiation stress, the maximum cohesion *in situ*, that can be relied on, is only 50% or more of that measured in the laboratory.

Two-dimensional modelling of the failure process was carried out using a phenomenological approach and a discrete fracture approach. The phenomenological approach uses a degraded strength to simulate the damage that has occurred near the advancing tunnel face. This approach, although practical, has several limitations, the most significant of which is the assumption that the entire rock mass strength around the tunnel has been degraded. The discrete fracture approach was carried out using a preliminary version of the finite element code InSight[2D] designed to model fracture growth in compression. A major advantage of the discrete fracture method is that it does not require the rock mass strength to be degraded. This approach holds much promise and captures one of the key physical processes, i.e. slabbing, observed around failing underground openings in brittle rocks.

The major contributions to our understanding of strength and failure that have resulted

from the investigations and analyses carried out during the course of this thesis are noted below:

- Samples obtained from a pre-stressed medium were damaged by the sampling process when the far field stress exceeded about $0.1\sigma_c$.

- The effects of scale, loading-rate and moisture on intact rock strength is minimal and do not explain the observed strength reduction investigated in this thesis.

- Maximum friction and maximum cohesion are not mobilized at the same displacements. By the time friction is fully mobilized a significant portion of the maximum cohesion in the sample has been lost. The Griffith locus was successfully used to model the mobilization of friction and the loss of cohesion.

- Cracking around underground openings initiates at about the same stress level as crack initiation in the laboratory tests. The zone of crack initiation, with $\phi = 0$, appears to define the limit of progressive failure around the openings at the 420 Level of the Underground Research Laboratory.

- The loading path of rock near the tunnel face suggests that stress rotation in the areas of maximum tangential stress concentration is a significant contributor to the localized degradation of the rock mass cohesive strength. Failure initiates in these locally damaged areas when the maximum tangential stress reaches about 100 MPa.

- Failure around the underground openings at the 420 Level of the Underground Research Laboratory initiates at a point, called the process zone, and is progressive. Failure occurs as a slabbing mechanism and stops when the geometry of the notch becomes convex and the process zone becomes contained.

- Modelling of the extent of failure cannot be captured by plane-strain modelling unless some effort is made to account for the initiation of failure at a point near the tunnel face before plane strain conditions are reached.

Acknowledgments

This thesis could not have happened without the support of my wife, Peggy and our daughter Nancy. Thank you both, from the bottom of my heart.

I would like to thank my supervisor, Dr. Brian Stimpson, for creating the opportunity for me to carry out this research. He helped to keep the thesis focused and was always there to listen to the reasons why things didn't quite work out the way I thought they should.

I would also like to thank Dr. Emery Lajtai, for hours of fruitful discussions and access to volumes of his test results. His knowledge in experimental testing made the laboratory work a success.

I also wish to express my appreciation to the following people:

Dr. M. L. Ayari for introducing me to fracture mechanics and his program SIMEX.

Mr. W. Grajewski for his technical assistance with the physical model studies.

Dr. Bruce Carter for the many interesting discussions on modelling the compressive fracture.

Mr. R. Jackson and Mr. B. Gorski of CANMET, and Mr. J. Lau of AECL for developing some of the unique testing methods used in this study.

Dr. Peter Kaiser and Dr. Dougal McCreath of Laurentian University for many stimulating discussions on progressive failure.

Dr. Paul Young and his colleagues at Queen's University for introducing me to the world of microseismics.

I would like to acknowledge and thank my colleagues at the Underground Research Laboratory. In particular, Dr. Neil Chandler, for patiently answering all my questions on energy concepts, Mr. Ed Dzik for developing the program InSight^{2D}, and Mr. Rod Read for making the Mine-by test tunnel a success.

Finally, I would like to thank AECL Research. In particular, Mr. Gary Simmons for providing me the opportunity to return to school and for tolerating my absence from work.

Contents

List of Figures

xiii

xiv

List of Tables

Symbols And Notation

a	Hole radius
r	Radial distance from centre of hole
α	Fracture surface energy for Mode II fracture
γ	Fracture surface energy for Mode I fracture
$\mathcal{G}$	Strain energy release rate
c	Crack half-length
n	Number of cracks per unit volume
bl	Width and length of volume containing one crack
K_{Ic}	Mode I fracture toughness
E	Young's modulus
ν	Poisson's ratio
G	Modulus of Rigidity
m, s	Hoek-Brown failure parameters
S_o	Cohesion
ϕ	Angle of friction
ϕ_b	Basic or residual angle of friction
ϕ_i	Angle of friction caused by roughness or interlocking
μ	Coefficient of friction
σ_1	Maximum principal stress
σ_2	Intermediate principal stress
σ_3	Minimum principal stress
ϵ_1	Maximum principal strain
ϵ_2	Intermediate principal strain
ϵ_3	Minimum principal strain
τ	Shear Stress
σ_n	Normal stress

σ_{rr}	Radial stress in cylindrical coordinate system
$\sigma_{\theta\theta}$	Tangential stress in cylindrical coordinate system
$\sigma_{r\theta}$	Shear stress in cylindrical coordinate system
σ_c	Short-term unconfined compressive strength
$\sigma_{c_{lt}}$	Long-term unconfined compressive strength
σ_t	Tensile strength
B_t, σ_{B_t}	Brazilian tensile strength
σ_{cd}	Crack damage stress or axial stress at volumetric strain reversal
σ_{ci}	Crack initiation stress
$\frac{\Delta V}{V}$	Volumetric strain
ω_a	Axial damage
ω	Volumetric damage
R	Curve fitting parameter in the Rocker function
USR	Factor of safety for Rocker function
θ	Angle between maximum applied stress and failure surface

Chapter 1

Introduction

In their efforts to extract resources from the earth and to find solutions for the disposal of waste, engineers are forced to create openings at ever increasing depths in the earth's crust. In Canada, mineral extraction is taking place at depths of 2000 m with plans to extend the mining operations to depths of 3000 m. In South Africa, the deepest working levels are 3800 m below surface and shaft systems to mine at depth in excess of 4000 m are being developed. In the nuclear industry in France, Sweden, Canada, Germany, the United Kingdom and the United States, plans are being made for the disposal of spent fuel from nuclear power plants at depths between 300 to 1000 m. In the petroleum industry, boreholes at depths greater than 1000 m are drilled on a routine basis. The design of these openings requires an estimate of the *in situ* stress and the strength of the rock mass. Both of these topics have been the focus of much research for the past 40 years. Yet, in his general report on Underground Openings in Overstressed Rock to the 6th Congress of the International Society of Rock Mechanics held in Montreal in 1987 H. Wagner [151] from South Africa stated:

> "It is fair to say that more research has been devoted to the clarification of the strength properties than any other aspect of the rock behaviour. Nevertheless, it is still doubtful whether reliable predictions can be made with regard to the failure of rock surrounding underground excavations."
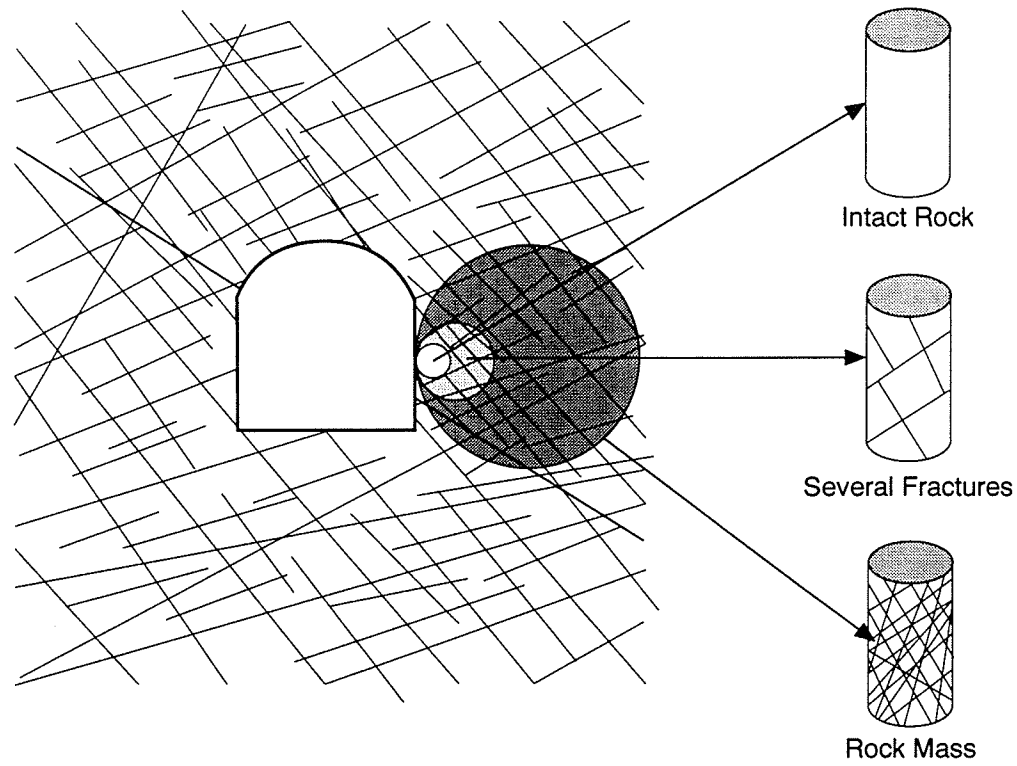
Figure 1.1: Illustration of the difficulty in determining the rock mass strength around an underground opening. The intact strength can be determined in the laboratory but the rock mass strength must be determined by other means.

Wagner [151] also commented that one of the reasons for this difficulty is that strength is usually obtained from small samples of intact pieces of rock tested under artificial loading conditions. This strength must then be extrapolated to account for the presence of joints, fractures and other planes of weakness in the rock mass (Figure 1.1).

The most significant attempt at quantifying the rock mass strength in recent years is the empirical failure criterion developed by Hoek and Brown [75]. This failure criterion starts with the intact rock strength and reduces that strength depending on the rock mass quality as determined from the rock mass classification systems of Bieniawski [9] and Barton [4].

It is not surprising that the main focus of research on rock mass strength has been on the reduction of the intact strength due to the presence of fractures as most civil and mining

engineering projects take place at shallow depth in moderate to highly fractured rock masses with low *in situ* stresses (Figure 1.2). In these situations, the rock mass strength is largely attributed to frictional resistance along fractures. However, at depth, large volumes of massive rock are sometimes encountered and frequently in these situations the *in situ* stress is high, relative to the intact strength. Under these conditions the strength of the rock mass can be attributed to the intact strength (Figure 1.2). For excavations in massive rock it is generally assumed that the strength of an intact sample would be similar to that of the rock mass. For example in the Hoek-Brown guide to their failure criterion, the parameters for the failure envelope for massive rock are the same for laboratory and the *in situ* conditions. This implicit assumption that the laboratory strength and *in situ* strength would be similar if the rock mass was unfractured has not been questioned. Excavations in massive granite in south-eastern Manitoba, for evaluating nuclear waste disposal concepts have provided an excellent opportunity to test this assumption.

1.1 Problem Statement and Research Activities

The nuclear industry is faced with assessing the concept of deep geological disposal of nuclear waste. One of the preferred characteristics for a suitable disposal site is low permeability. Hence, unlike the mining industry, which usually creates excavations in highly fractured rock masses with major faults and geologic boundaries, the nuclear industry is looking for uniform, stable conditions in rock masses with minimum faulting and fracturing. Thus, the shafts and tunnels for a waste repository may be excavated in nearly intact rock. AECL Research, which is charged with the responsibility for assessing the geologic disposal concept in plutonic rocks in Canada, has constructed the Underground Research Laboratory (URL) near Lac du Bonnet in south-eastern Manitoba. Portions of this facility are constructed in massive unfractured granite.

The tunnels excavated at the URL at a depth of 420 m in massive unfractured granite, displayed extensive spalling and slabbing during construction. Preliminary stress analyses
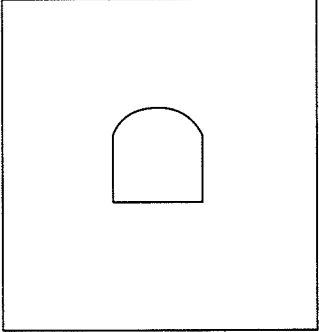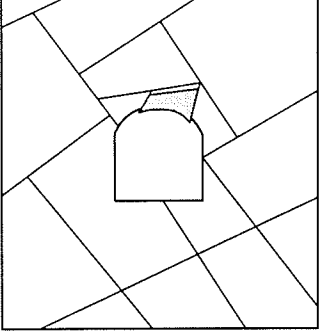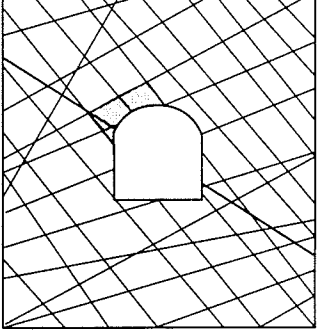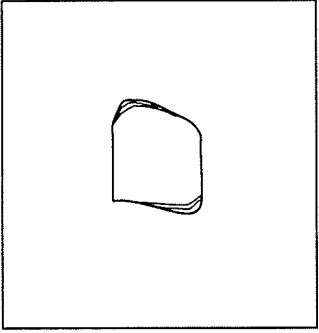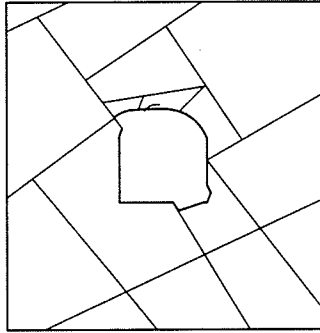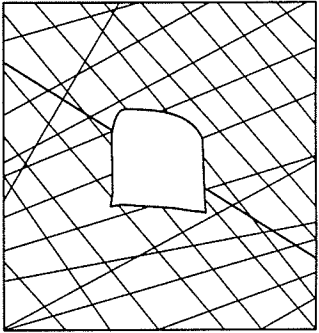
	Massive	Moderately Fractured	Highly Fractured
Low In Situ Stress	Linear elastic response with little or no rock failure. Excavation shape can be chosen on the basis of an elastic analysis	Failure involves falling or sliding of blocks and wedges defined by intersecting discontinuities. Stability analysis can be performed using limiting equilibrium or distinct element models.	Failure controlled by unravelling of small blocks and wedges from the excavation surface. Distinct element models can be used to explore mechanisms of failure with various joint set configurations.
High In Situ Stress	Crack initiation and fracture propagation occurs in rock adjacent to the excavation boundary. Linear elastic analysis gives information on fracture initiation points and possible failure directions.	Failure of both intact rock and discontinuities occurs. Elastic analysis gives some indication of possible points of failure initiation but analysis of progressive failure is very difficult.	Rock mass tends to behave as elastic/plastic continuum. Analysis of progressive deformation and failure can be carried out by means of continuum models which include post-peak plastic behaviour.

Figure 1.2: Various classes of failures as a function of *in situ* stress and fracturing (after Hoek, pers. comm.).

of these tunnels indicated that the spalling and slabbing occurred where the maximum tangential stress on the boundary of the tunnels exceeded approximately 80–100 MPa. Thus the *in situ* strength around the perimeter of the tunnels is about 100 MPa or approximately 1/2 the unconfined compressive strength of intact rock samples tested in the laboratory. Similar findings have been reported elsewhere [125, 128, 117, 69]. However, in those cases explanations related to scale effects, heterogeneous materials and incipient fractures, were offered as reasons for the observed strength reduction. At the URL, however, the rock mass is relatively homogeneous and isotropic, elastic and fracture free. Thus the usual reasons put forth for the observed strength reduction, including scale effects, can not be supported at the URL. The inability of the classic stress-strength approach to predict tunnel performance at the 420 Level of the URL prompted the research described in this thesis.

1.1.1 Finding A Solution

When comparing measured laboratory strength to calculated stresses around tunnels, two important steps have to be carried out: 1) establish the far-field *in situ* stresses required to calculate the stresses around the tunnel, and 2) establish how the laboratory strength can be translated to a field strength. One additional step which is considered in this thesis is to establish if the loading path around the tunnel is similar to the loading path in the laboratory tests which were used to establish the in situ strength. In addition to these steps, one must also consider the assumptions employed in the numerical analyses. The rock mass at the URL is relatively homogeneous, isotropic, and fracture free, consequently, the analyses which appear most appropriate are ones which represent a continuous, homogeneous, isotropic, linear, elastic (CHILE) material. Thus, as a starting point, the calculated stresses around the URL tunnels are based on linear elastic analysis.

The first step in determining the stresses at the boundary of the tunnels at the URL was to establish the far field *in situ* stresses. It is well known that the measurement of *in situ* stress is fraught with difficulties. Accordingly, it becomes essential to establish the *in*

situ stress magnitudes and direction with some reasonable degree of confidence. Although overcoring and hydraulic fracturing are traditional methods for determining the *in situ* stress state at a point, the convergence method provides the stress state at the tunnel scale. Martin et al [109] demonstrated that this type of stress measurement was considerably more reliable than the information obtained from overcore measurements at the URL.

The second step in the process was to establish the laboratory strength for the rock mass in which the tunnels will be excavated. In massive granite, this first appears as a routine task. Testing of Lac du Bonnet granite has been on-going since about 1980 by the University of Manitoba and AECL. Samples have been collected from two sources, Cold Spring Quarry and the URL. Preliminary compilation of the tests results from these two sources indicated that the strength of the granite varied spatially and also decreased considerably with depth at the URL. This latter finding was rather surprising because *in situ*, the quality of the rock mass improves with depth, i.e., the rock mass changes from a jointed rock mass near surface to a massive rock mass at depth. Thus in order to establish the likely *in situ* strength at the 420 Level of the URL, the possibility of sample disturbance needed to be explored.

Another important issue is translating the laboratory strength to the field strength. In the initial stress-strength analysis the laboratory unconfined compressive strength was compared to the calculated maximum tangential stress on the perimeter of the tunnel. However, it is well known that the short-term unconfined compressive strength is somewhat higher than the long-term strength of intact rock. The long-term strength of Lac du Bonnet granite has been determined by Schmidtke and Lajtai [140] to be about 130 MPa. However, this still does not explain failure occurring at stresses around 100 MPa. Interestingly, the 130 MPa long-term strength is projected from tests conducted over one month's duration and represents the predicted strength for times greater than 1000 years. The long-term strength from the one month tests was 155 MPa. Because failure was occurring as soon as the excavations were created it does not appear that the long-term strength plays a significant role in the observed strength reduction around the tunnels. In addition to the

long-term strength, there is also the issue of scale (volume) effects, loading-rate effects, moisture effects and loading path effects. All of these effects are explored in this thesis.

As part of the study of the strength of Lac du Bonnet granite, physical model studies were also carried out. The initial stress-strength analysis compared the laboratory uniaxial compressive strength to the tangential stress around a tunnel. However, the stress at the boundary of a tunnel is not truly uniaxial because of the tunnel curvature and the load parallel to the axis of the tunnel. Thus in order to assess the strength around a tunnel granite blocks containing a circular opening were loaded in uniaxial or biaxial compression and cracking carefully monitored.

The next step in this research was to consider the role the loading path around the tunnel might play in determining the strength of the rock. Talebi and Young [149] established, by microseismic monitoring, that cracking, i.e., damage, was occurring ahead of the shaft excavated from the 240 Level to the 420 Level at the URL, although failure around the shaft was not observed in the areas where cracking had occurred. Observations of the failure process on the 420 Level indicated that it was progressive, i.e., initiating at a point and progressing into a typical well-bore breakout geometry. Thus, in order to understand the role of progressive failure a series of damage-controlled laboratory tests were conducted which enabled the cohesion and frictional strength components to be isolated and tracked as crack damage accumulated in the test specimen. This unique testing method indicated that as crack damage accumulates, at stress levels below the peak strength, cohesion is lost at a very rapid rate. Thus in a damaged sample, the cohesion can be as low as about half the cohesion measured in an undamaged sample. The strength at the boundary of an underground opening is essentially due to rock cohesion, thus these laboratory tests demonstrated that if damage is occurring around an advancing tunnel face the rock strength will be reduced to less than half the unconfined compressive strength.

The final stage of this research was to examine in detail how the loading path around an advancing tunnel face, causes damage and to attempt to model the process. Two and three

dimensional numerical analyses were carried out. Finally numerical analyses were used to simulate the failure process around a tunnel at the 420 level of the URL. Two approaches to modelling the failure process were used, a phenomenological approach and a discrete fracture approach. Both methods, demonstrate that progressive failure around the tunnel can be modelled reasonably well once the mechanism of failure is thoroughly understood.

In summary, the primary objective of this thesis is to determine why the strength of massive granite from back analysis of tunnels excavated at the 420 Level of the Underground Research Laboratory was about 100 MPa when the the reported laboratory unconfined compressive strength of the granite was around 200 MPa. This objective is met by investigating the effects of scale, loading rate, moisture, damage and loading path on the rock strength.

1.2 Organization Of Thesis

This thesis examines the strength of openings in massive Lac du Bonnet granite at the Underground Research Laboratory at depths between 240 and 420 m. Chapter 2 provides the geotechnical setting for the URL. The *in situ* stress state at the 420 Level of the URL is established and the effects of this stress state on the properties of samples tested in the laboratory is described.

Extensive testing of Lac du Bonnet granite has been carried out over the past ten years. Chapter 3 provides a summary of those test results. It is commonly implied that scale (volume) effects is the major reason for the reduction in strength from the laboratory measured value to the *in situ* strength. Scale effects, loading rate effects, moisture, and long-term strength are all investigated and reviewed in arriving at an estimate of the likely *in situ* strength.

Interpretation of laboratory test results requires an understanding of the failure process. Chapter 4 provides a review of laboratory testing in compression and establishes the key fracture parameters in compression testing. Chapter 4 then examines the progressive failure of brittle rock. The classical strength envelope for a brittle rock assumes that full

cohesion and full friction are mobilized simultaneously. Results from damage-controlled laboratory tests are used to investigate this assumption. A model, based on energy concepts, is developed for progressive failure and compared to the laboratory results.

In Chapter 5 it is demonstrated that the back calculated strength around the excavations at the 420 Level of the Underground Research Laboratory is about half the laboratory unconfined compressive strength. Microseismic monitoring of a test tunnel shows that damage is occurring to the rock immediately around the face of the advancing tunnel. Mechanisms which could cause this damage are investigated, using numerical simulations, and compared to the laboratory test results.

Chapter 6 describes two approaches, the phenomenological approach and the discrete fracture approach, to modelling progressive failure around the openings at the URL. The phenomenological approach requires no understanding of the failure process whereas the discrete fracture method requires a thorough understanding of the failure process.

A discussion and summary of the thesis is provided in Chapter 7.

Chapter 2

Geotechnical Setting

The Underground Research Laboratory (URL) was constructed in southeastern Manitoba for the purposes of conducting large scale *in situ* experiments related to the disposal of nuclear fuel waste from nuclear power plants (Figure 2.1). The access shaft for the URL began with the shaft collar construction in 1982 and was excavated in two stages. Stage 1 (upper shaft) was excavated from the surface to a depth of 255 m between 1983 March and 1985 April. This stage was excavated as a nominal 2.8 m by 4.9 m rectangular shaft by the traditional drill and blast benching method. Stage 2 (lower shaft) was excavated from the 255-m depth to the 443-m depth between 1987 July and 1988 August. This stage was excavated as a 4.6-m-diameter circular shaft using a full-face drill and blast technique. Between 1985 and 1987, the 240 Level access tunnels were developed and the ventilation raise was excavated between the 240 Level and the surface. The final activity of the construction phase, development of the access tunnels on the 420 Level and the ventilation shaft from the 420 Level to the 240 Level, was completed in 1990. The URL at the end of the construction phase is shown in Figure 2.2. The URL's operating phase, which began in 1989, will continue until 2000 and will include a series of nine major experiments designed to address some of the technical issues associated with the disposal of nuclear fuel waste [146].
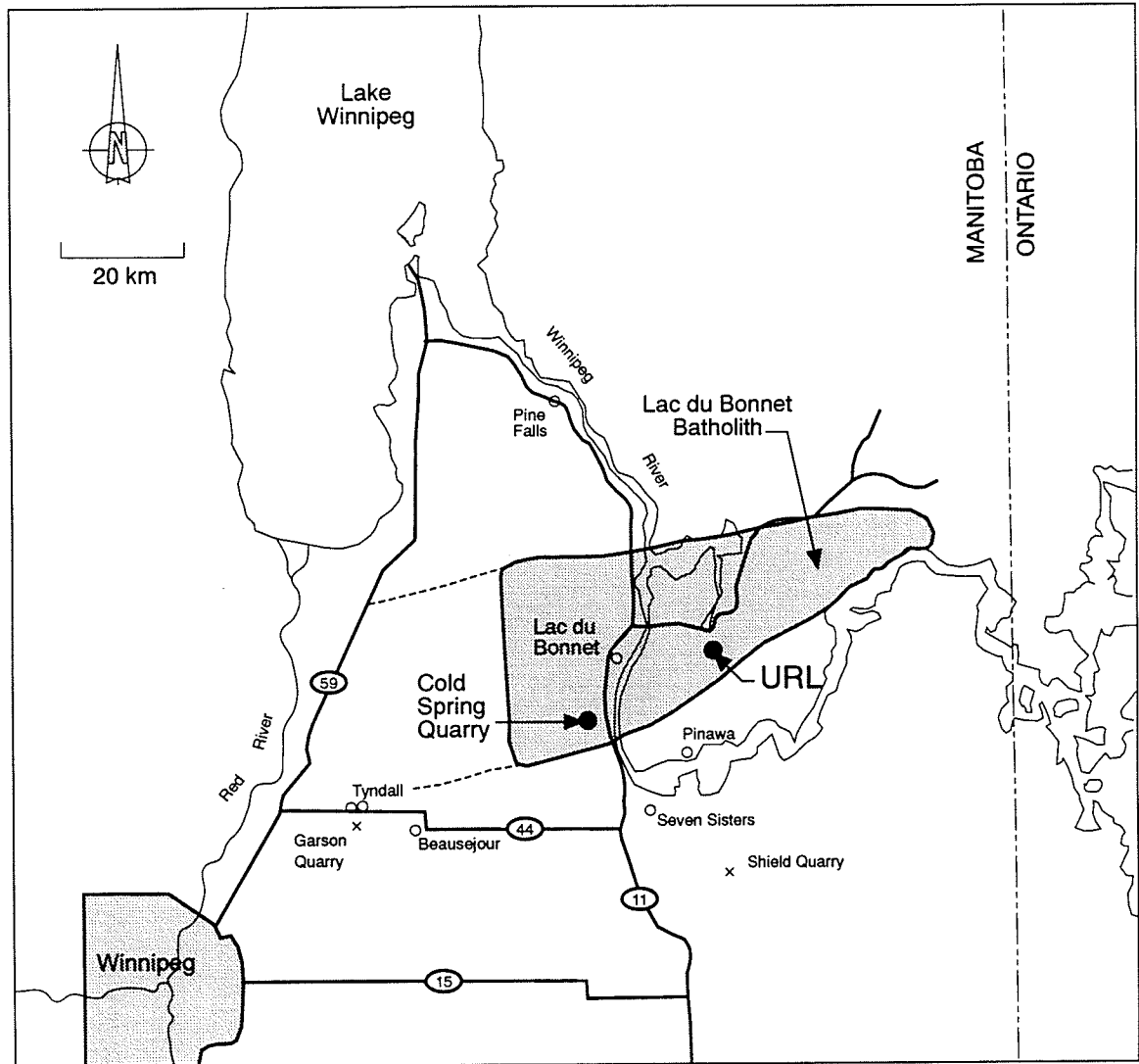
Figure 2.1: Location map of the Lac du Bonnet batholith and the Underground Research Laboratory.
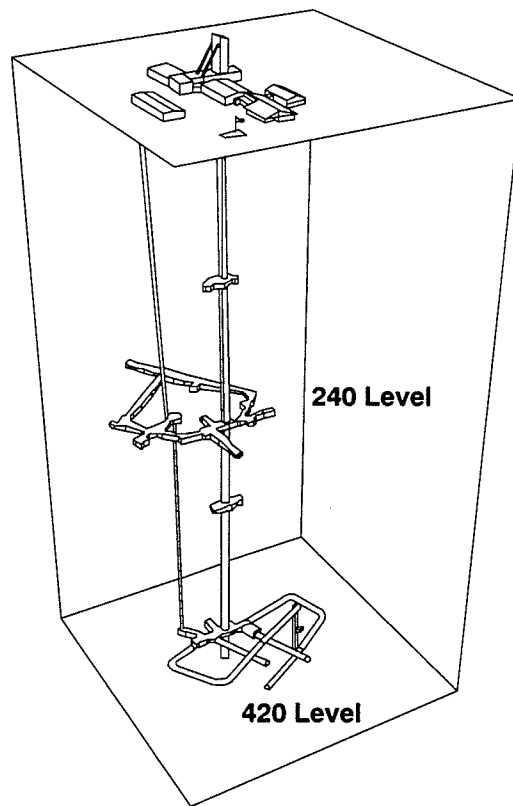
Figure 2.2: Isometric of the Underground Research Laboratory. The 420 Level is excavated in massive, unfractured granite

2.1 Geology

2.1.1 Regional Setting

Brown et al. [17] and Everitt et al. [46]. have described the geological setting of the URL. In summary, the URL is located within the Lac du Bonnet granite batholith (LDBB), which is considered to be representative of many granitic intrusions of the Precambrian Canadian Shield. The batholith trends east-northeast and its elongated body is about 75 by 25 km at surface (Figure 2.1) and extends to a depth of about 10 km. The batholith, dated as Late Kenoran age (2680±81 Ma), lies in the Winnipeg River plutonic complex of the English River gneiss belt of the western Superior Province. The batholith is a relatively undifferentiated pink and grey massive porphyritic granite-granodiorite. The massive, medium- to coarse-grained porphyritic granite is relatively uniform in texture and composition over the batholith, although locally it displays subhorizontal gneissic banding.

Low-dipping thrust faults and associated systems of predominantly north-northeast striking subvertical joints occur throughout the LDBB. The style of fracturing within the central portion of the LDBB near the URL is dominated by large, low-dipping thrust faults and splays. The blocks between the thrust faults are crosscut by one or more sets of subvertical joints, the pattern and frequency of which varies from one block (fracture domain) to the next. The factors influencing the pattern of intra-block jointing include the overall distance from the surface, the proximity to the bounding faults, and the local rock type. The subvertical joints become less frequent, less continuous, and simpler in pattern with increasing depth.

2.1.2 Local Setting

The local geological setting was first determined by site investigations carried out from the surface. The location of the URL shaft was selected to provide a range of lithological and structural domains. Excavation of the URL shaft intersected two major thrust faults that dip about 25 to 30° southeast. These faults are referred to as Fracture Zone 3 and Fracture

Zone 2 and the splays as Fracture Zones 2.5 and 1.9 (Figure 2.3). The fracture zones are composed of chloritic slip surfaces, which grade into cataclastic zones where displacements in the order of metres to tens of metres have occurred. Where the URL shaft intersects Fracture Zone 2 there is an estimated 7.3 m of reverse displacement [46]. The cataclastic zones range in thickness from 20 mm to 1 m and contain breccia and clay-gouge. These fracture zones are considered to be the main pathways for groundwater flow in the Lac du Bonnet batholith [37].

Between the surface and Fracture Zone 2.5, the rock is pink granite and contains a prominent subvertical joint set striking about 020° near surface, to 040° at the 240 Level. A less prominent subvertical joint set strikes between 150 and 180°. The pink colour is due to alteration by groundwater flow. The general rock type below Fracture Zone 2.5 is a massive unjointed grey granite. Excavation of the shaft from the 240 Level to the 420 Level and the excavation of the several hundreds of metres of tunnel on the 420 Level were completed in this granite. In the immediate area of Fracture Zones 2 and 1.9, the grey granite shows pink alteration.

2.2   *In Situ* Stress

In situ stress is one of the key parameters needed for the design of an underground opening. Yet it is one of the most difficult and most costly parameters to obtain. Stress is defined at a point and hence if one needs to know the stress in a large volume of rock then a large number of measurements are required. In reality, only a few stress measurements are made at any one site, e.g., only about 133 triaxial stress measurements have been made for all of the Canadian Shield [70]. An exception to this paucity of data is the Underground Research Laboratory, where about 350 triaxial stress measurements have been made in a volume of rock about 100 m × 100 m × 500 m deep. In addition to the triaxial measurements, 2D overcoring, hydraulic fracturing, convergence measurements, microseismic monitoring, well-bore breakouts and excavation back-analysis have also been used to help determine the
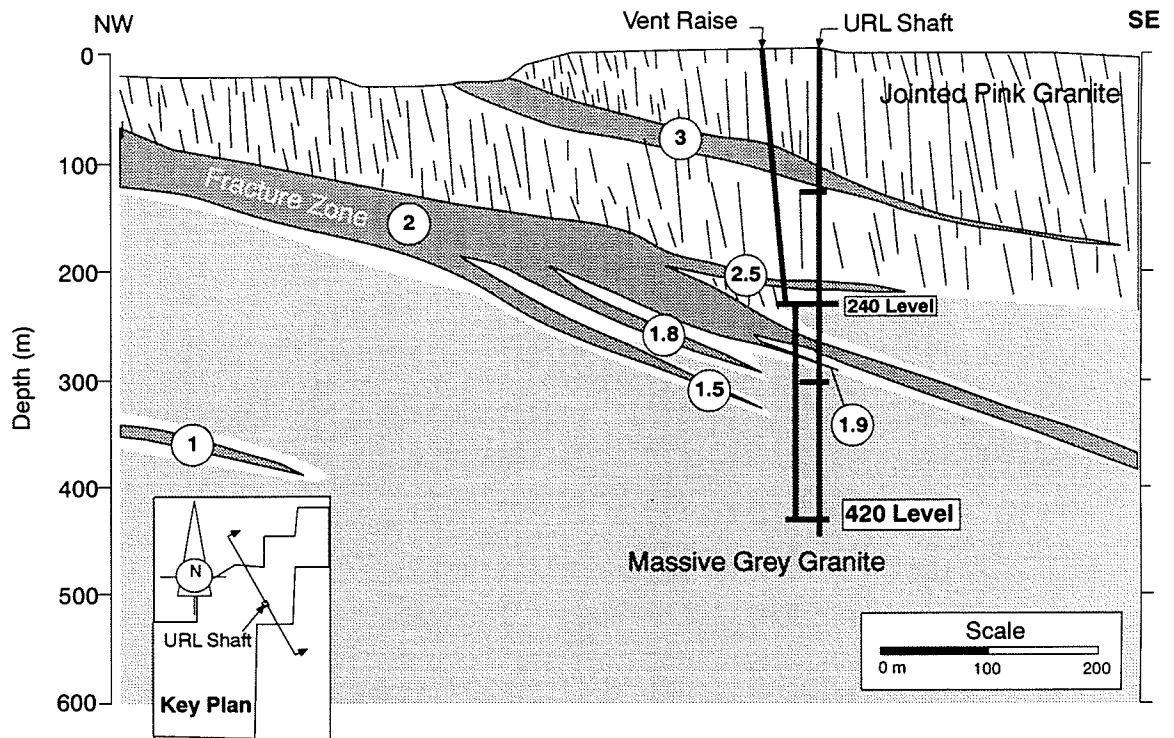
Figure 2.3: Geological section through the URL showing the major fracture zones and the extent of subvertical fracturing. The number in the small circle refers to the fracture zone designation. Below Fracture Zone 2 the rock is massive unfractured gneissic grey granite

stress state. Within the Canadian Shield and the Underground Research Laboratory σ_1 tends to be horizontal and σ_3 tends to be vertical. Hence, these data can be conveniently divided into horizontal stress and vertical stress measurements. These will be discussed in turn following a brief review of the limitations of stress measurement techniques.

2.2.1 Limitations of Stress Determination Techniques

Before discussing the horizontal and vertical stresses at the URL, it is important to be aware of the limitations of techniques for determining in situ stress. The two traditional techniques are the overcoring method and the hydraulic fracturing method. With the overcoring method, the overcored samples must behave elastically in order to interpret the stress magnitudes and orientations from the measured strains. At the URL, Martin and Christiansson [107] demonstrated that on the 240 Level the rock exhibited non-linear behaviour. They demonstrated that the *in situ* stress from the overcore samples with this non-linear behaviour could be approximated using a transverse isotropic model. However, below the 240 Level the non-linear behaviour was so severe that the overcoring technique provided no information on the orientations of the *in situ* stresses but did provide approximate magnitudes [106].

In order to interpret hydraulic fracturing results the hydraulically produced fracture must be coaxial with the axis of the borehole. Thus a hydraulic fracture test in vertical borehole producing a coaxial fracture will provide the maximum and minimum horizontal stress magnitudes and orientations, assuming σ_3 is vertical. However, at the URL below Fracture Zone 2, hydraulic fracturing in near vertical boreholes produced only subhorizontal fractures. A solution for the interpretation of data from such tests is provided by Ljunggren and Amadei [103]. However as pointed out by Martin [105] the magnitudes for the maximum horizontal stress and the ratio of maximum horizontal stress to minimum horizontal stress, given by this solution, are unrealistically high. Hefny and Lo [67] provided a new method to interpret horizontal hydrofracs. As with the solution given by Ljunggren and Amadei [103]

it would appear that the new method also gives unrealistically high magnitudes and stress ratios. Thus at the 420 Level of the URL *in situ* stress cannot be determined by the traditional methods.

Several methods were developed and tested to determine the *in situ* stress state at the 420 Level. Of these methods, the convergence method was simplest to implement and evaluate.

2.2.2 Convergence Method

The solution for radial displacements (u_r) around a circular hole subjected to a biaxial stress state is given by the well known Kirsch equations [75, 15]. Using these equations the radial displacements are calculated given the far-field *in situ* stress. However, when attempting to determine the *in situ* stress from the measured radial displacements the Kirsch equations, such as those given in [75, 15], are not adequate. Using the theory of elasticity [53] a general solution was developed for radial displacements which does not require prior knowledge of the *in situ* stress state (a complete derivation of the relationships between stress and radial displacements is given in Appendix A).

The total convergence U between two diametrically opposite points on the boundary of a circular opening or $2u_r$ can be expressed as follows, assuming the conditions of plane strain, as

$$U = \frac{a}{2G}\left\{(1 + (3-4\nu)\cos 2\theta)\sigma_x + (1 - (3-4\nu)\cos 2\theta)\sigma_y + 2(3-4\nu)\sin 2\theta\tau_{xy}\right\} \quad (2.1)$$

where G = the shear modulus, ν = Poisson's ratio, $\sigma_x, \sigma_y, \tau_{xy}$ = biaxial stress state and θ = orientation of the convergence diameter relative to the maximum stress (see Figure 2.4). Thus U varies with position θ around the opening. Note that for a given value of θ equation 2.1 is of the general form

$$U = C_1\sigma_x + C_2\sigma_y + C_3\tau_{xy} \quad (2.2)$$
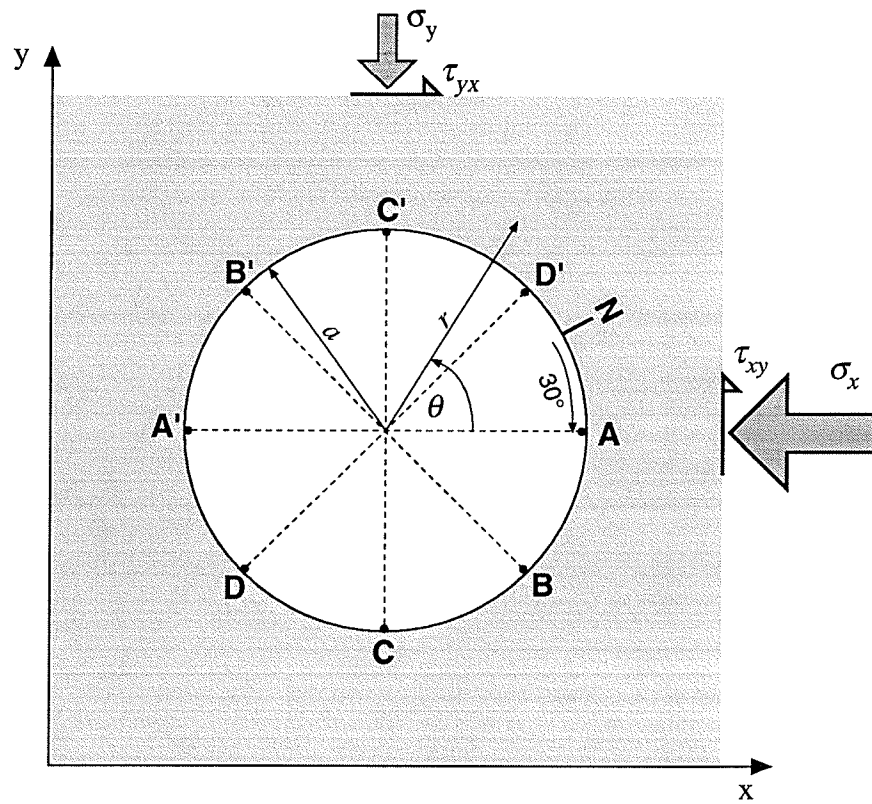
Figure 2.4: Horizontal section through shaft and location of convergence measurements.
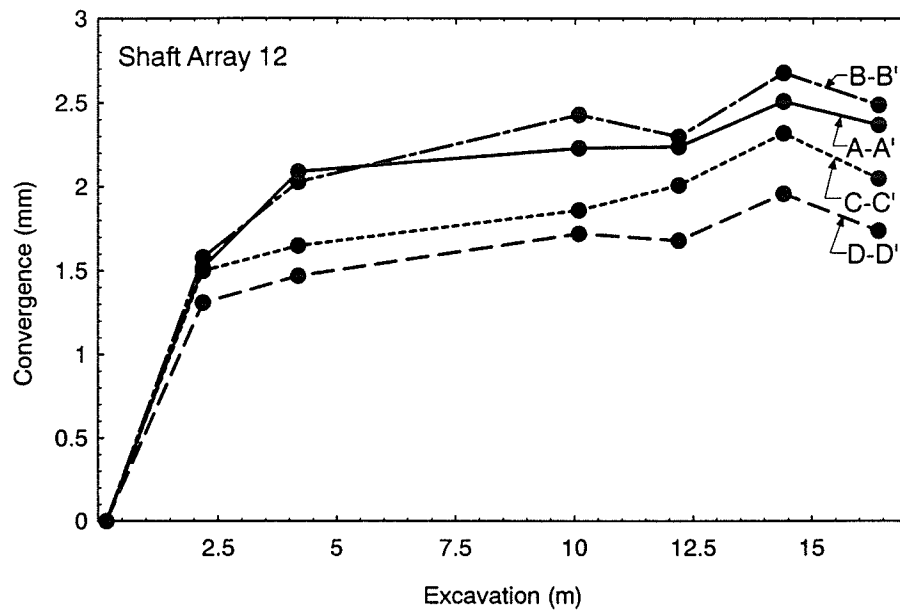
Figure 2.5: An example of measured convergence (Array 12) obtained during shaft construction. The excavation distance on the x-axis in the figure refers to the distance of the shaft bottom below the plane of measurement.

Hence equation 2.1 can be solved for the stress state provided at least three convergence diameters are measured.

During the construction of the shaft at the URL from the 240 Level to the 420 Level convergence of the shaft walls was recorded using a Kerns Distometer. The convergence was recorded along four diametrical lines $(A - A',\ B - B',\ C - C',\ D - D')$ as illustrated in Figure 2.4. An example of a typical convergence plot obtained during construction is given in Figure 2.5. Using the measured convergence, it is possible to back calculate the *in situ* stress state assuming the amount of radial displacements that have occurred before the instruments were installed is known. Martin et al [110] established that approximately 60% of the total convergence had already occurred prior to installation of the instrumentation used in the shaft convergence arrays.

In a typical array there were four convergence measurements, yet only three are required to define the biaxial stress state. Using the additional data, a least squares solution was

obtained to equation 2.1 to determine the best fit far-field *in situ* stresses. The results from all the shaft data are given in Table 2.1. A typical shaft convergence array, with the best fit solution compared to the actual measurements, is given in Figure 2.6. The two convergence arrays in Figure 2.6 illustrate the rotation of the maximum horizontal stress with depth (see Table 2.1 for the locations of the arrays).

Convergence was also measured in a circular horizontal tunnel on the 420 Level using six diametrical measurements. Figure 2.7 shows a typical result from that tunnel. Note the dramatic change in stress ratio obtained from the Mine-by tunnel compared to the results from the shaft convergence measurements (see Figure 2.6). This reflects the difference in the horizontal stresses measured by the shaft convergence and the horizontal to vertical stress ratio measured by the Mine-by convergence. A discussion of the results from the convergence data follows in the next section.

2.2.3   Horizontal Stress

The relationship between the orientation of the maximum horizontal stress (σ_{max}) and depth indicated two distinct stress domains at the URL [106]: one from the surface to Fracture Zone 2, where the maximum horizontal stress is oriented parallel to the major subvertical joint set, striking about 040° (Figure 2.8); and the second extending below Fracture Zone 2, where the maximum horizontal stress has rotated about 90° and is aligned with the dip direction ($\approx 130°$) of Fracture Zone 2 (Figure 2.8). The maximum horizontal stress direction in the second domain is coincident with the direction of major compression noted by Herget [68] for this area of the Canadian Shield.

The rotation of the maximum horizontal stress across the domain boundary may be explained using a simple mechanical model. Fracture Zone 2 tends to follow the weaker xenolithic layers within the Lac du Bonnet batholith. Considerable reverse slip in the direction 130° has occurred along Fracture Zone 2 (about 7 m where the shaft intersects the fracture zone), and this movement may have led to stress relief in the direction of thrusting.

Table 2.1: Summary of horizontal stress magnitudes and orientations determined from convergence measurements taken during shaft construction.

Depth (m)	Array No.	σ_{max} (MPa)	σ_{min} (MPa)	Azimuth σ_{max} (°)	Ratio $\frac{\sigma_{max}}{\sigma_{min}}$
Beginning of Fracture Zone 2					
267.6	2	40.3	25.2	143	1.60
269.7	3	38.1	22.1	129	1.72
271.9	4	39.9	34.0	050	1.17
273.2	5	43.1	39.4	80	1.09
274.2	6	70.8	51.8	100	1.37
276.2	7	59.1	40.5	061	1.46
283.2	8	56.7	46.4	089	1.22
287.6	9	53.7	48.5	033	1.11
288.8	10	54.7	46.3	056	1.18
Fracture Zone 1.9					
290.0	11	59.5	45.3	072	1.31
293.3	12	54.1	42.3	062	1.28
303.3	13	53.6	41.4	067	1.29
End of Fracture Zone 2					
334.0	16	43.5	40.0	153	1.09
346.4	17	43.2	38.4	163	1.12
364.0	19	57.0	49.5	142	1.15
374.2	20	61.5	55.9	161	1.10
393.7	23	56.4	39.6	129	1.42
400.8	24	55.9	49.4	140	1.13
410.8	25	55.1	50.9	169	1.08
429.2	26	73.6	62.3	131	1.18
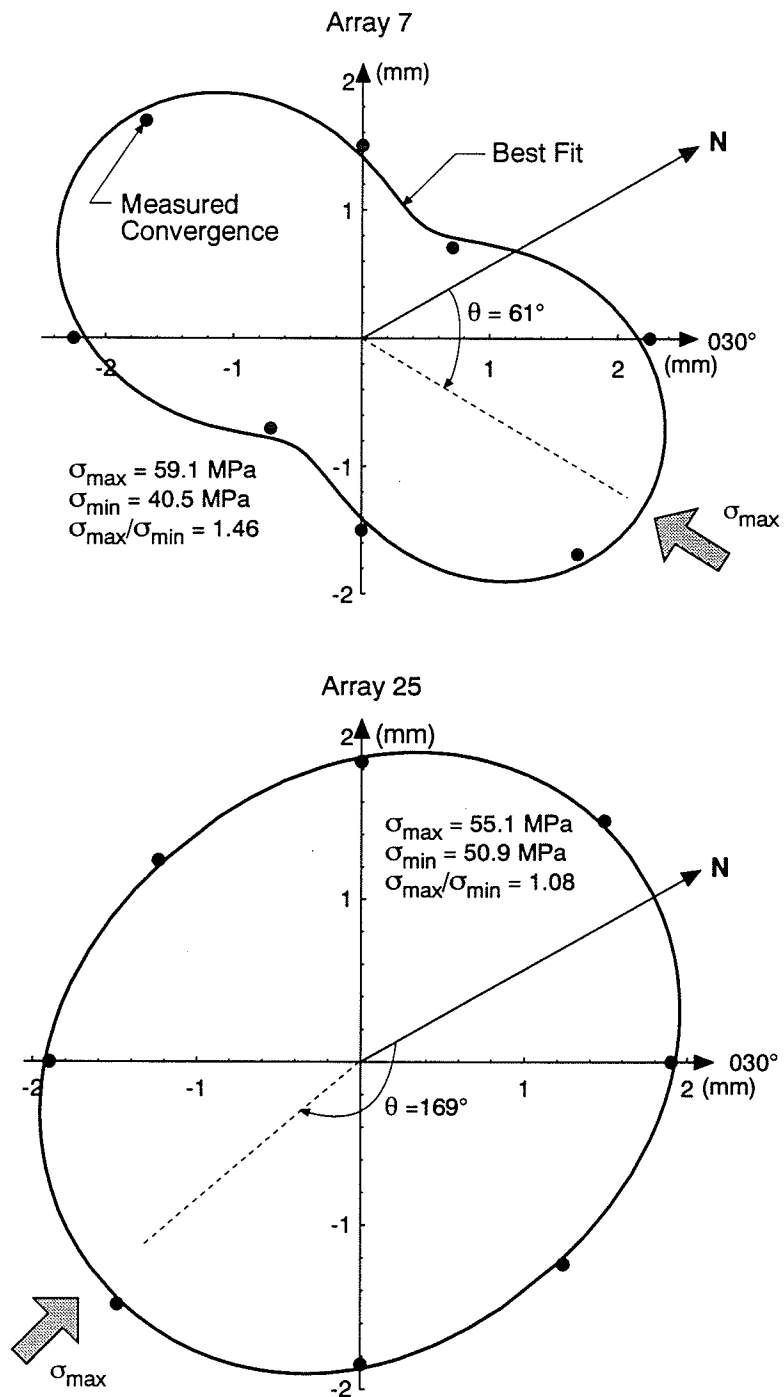
Figure 2.6: Comparison of the measured convergence from the shaft and the best fit solution using equation 2.1.
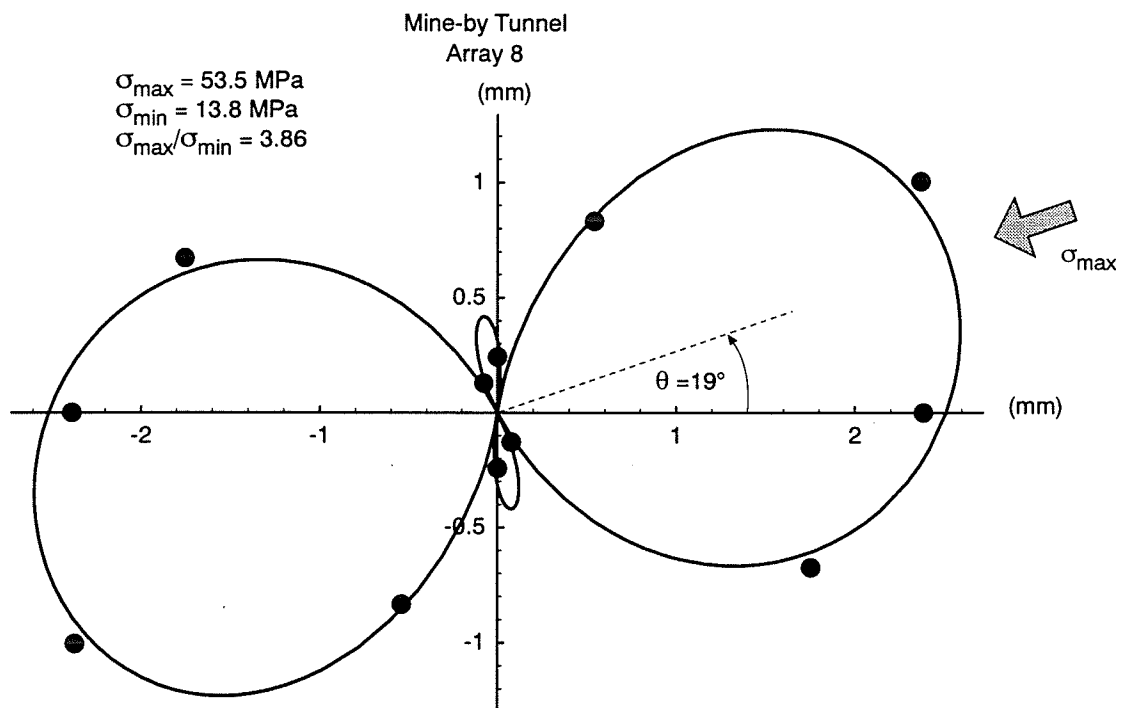
Figure 2.7: Comparison of the measured convergence from the Mine-by test tunnel on the 420 Level and the best fit solution using equation 2.1.
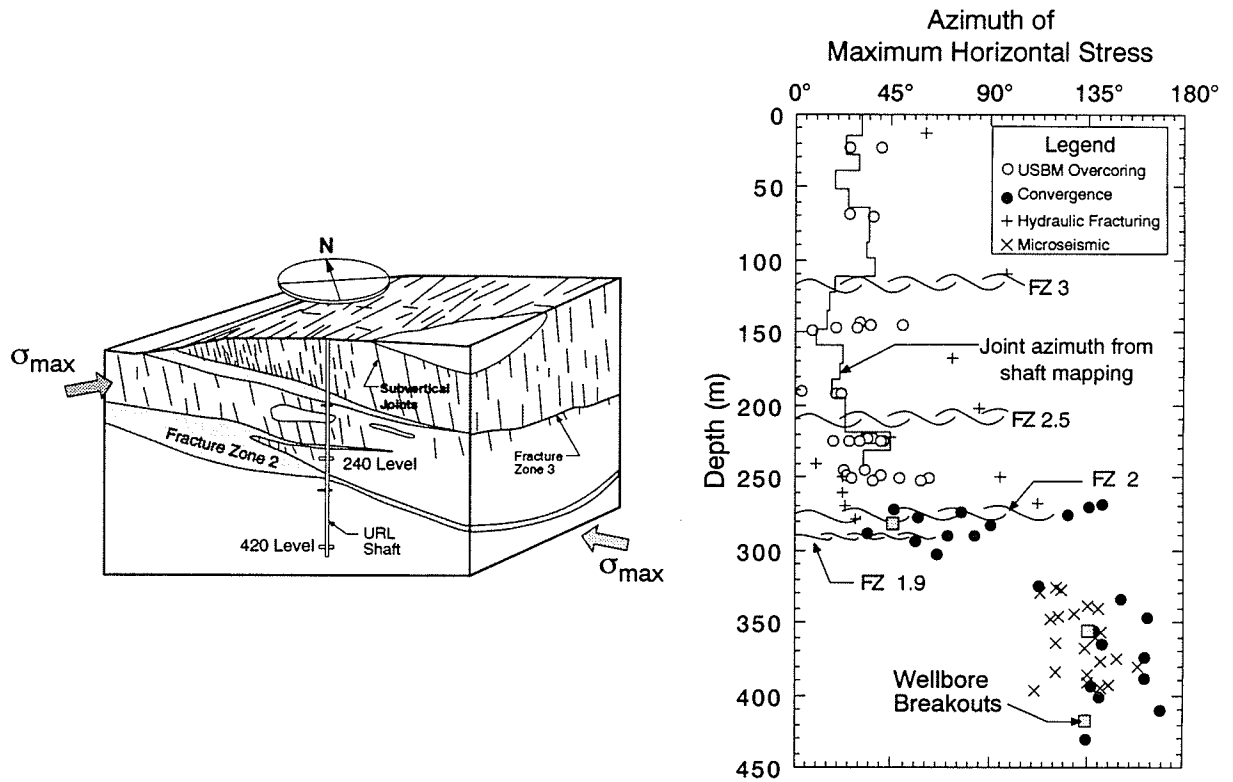
Figure 2.8: Plot of the azimuth of maximum horizontal stress versus depth. Note the rotation of the stress below Fracture Zone 2 (FZ2). The isometric figure illustrates the maximum horizontal stress orientation relative to the strike and dip of Fracture Zone 2.

Below Fracture Zone 2 no such stress relief occurred because faulting is absent.

A numerical model was used to simulate the mechanism of stress rotation across the fracture zone. At the URL, the maximum horizontal stress at depth is in the dip direction of Fracture Zone 2 (see Figure 2.8) and the ratio between the maximum and minimum horizontal stresses is about 1.2. These assumptions were employed in a UDEC [80] 2-dimensional numerical model, as shown in Figure 2.9, where a vertical section of the URL site was taken in the dip direction of Fracture Zone 2. The model was compressed in the horizontal direction and Fracture Zones 2, 2.5 and 3 allowed to slip. The resulting horizontal stresses versus depth are shown in Figure 2.9. As is the case at the URL (see Figure 2.8), the maximum horizontal stress direction rotates from the dip direction of Fracture zone 2 below the fracture zone to the strike direction of Fracture Zone 2 above the fracture zone. This type of stress release and associated stress rotation is commonly observed in modelling with constant-displacement boundary conditions, where the block of rock above the fault has lost its original load because of displacements along the fault. Two other points are also worth noting from the results of this simple model. First, the magnitudes of the maximum stress above Fracture Zone 2 are considerably less than the stress magnitudes below Fracture Zone 2. In the UDEC model no allowance is made for vertical fracturing in the proximity of Fracture Zones 2.5 and 3, which would tend to reduce the horizontal stresses even more and bring the predicted stresses closer to those measured (Figure 2.9). Second, the stress magnitudes below Fracture Zone 2 are fairly constant with depth (the model had a depth of 1.5 km). This is in keeping with the stress measurements and construction observations at the URL which suggest that the maximum horizontal stress from Fracture Zone 2 to 512 m is fairly constant at about 55 MPa (Figure 2.9).

2.2.4 Vertical Stress

The vertical stress magnitudes from and around the shaft at the URL were obtained from triaxial overcore results, from hydraulic fracturing conducted in horizontal boreholes and
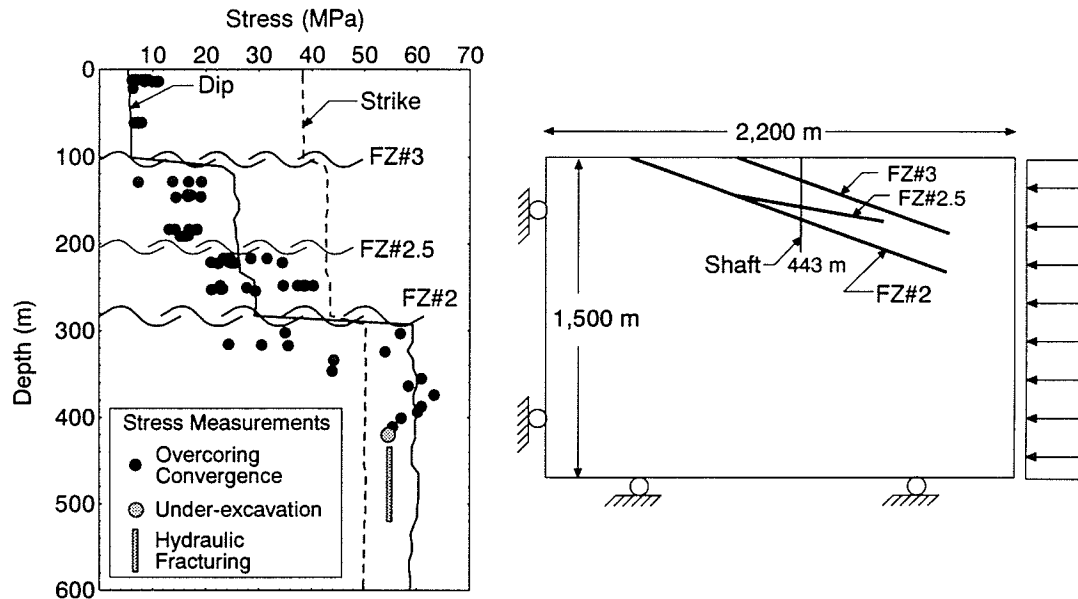
Figure 2.9: Stress magnitudes from UDEC model, parallel to the dip direction and strike of Fracture Zone 2, compared with measured values of maximum horizontal stress. Model parameters were $\phi = 20°$, $K_n = 100$ MPa/mm, $K_s = 0.01 K_n$, $\nu = 0.2$ and $E = 60$ GPa.

from subhorizontal hydraulic fractures in near-vertical boreholes. A summary of the ratio of σ_3 to the calculated lithostatic stress using a vertical stress gradient of 0.0265 MPa/m, based on the density of the rock, is shown in Figure 2.10. Clearly, the measured σ_3 values in the proximity of Fracture Zone 2 exceed the calculated lithostatic stress. Since σ_3 approaches the calculated value both above and below Fracture Zone 2, it would appear that σ_3 values are significantly affected by the presence of Fracture Zone 2. A possible explanation for this phenomenon relates to the spatial variation in the thickness and normal stiffness of Fracture Zone 2 [108]. A cross section through Fracture Zone 2 (Figure 2.11) reveals the variation in the thickness of the fracture zone as well as the variation in normal stress measured on both sides of the fracture. Martin et al. [108] found that the thickest parts of the fracture zone correlated to the areas of high permeability, low normal stiffness and low normal stress, whereas the portions of the fracture zone 10 m thick or less correlated to areas of low permeability, high normal stiffness and high normal stress. Areas of high normal stiffness,
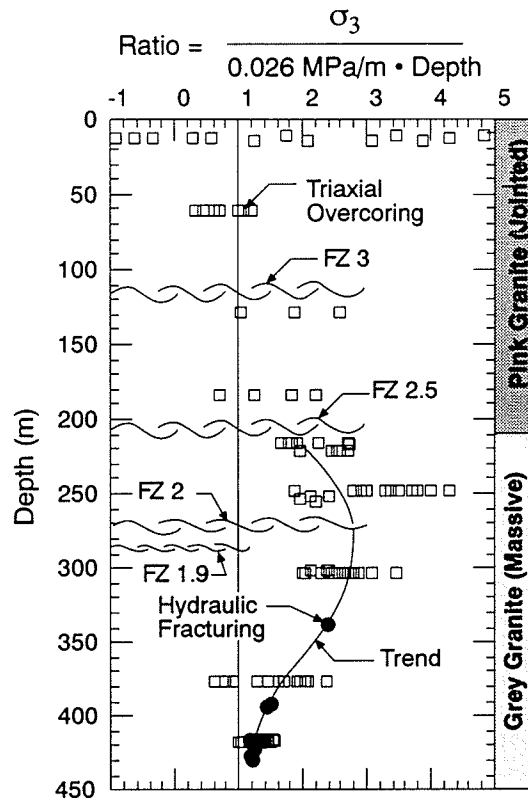
Figure 2.10: Measured σ_3 normalized to the calculated lithostatic stress. Note the increase in σ_3 around Fracture Zone 2 and how σ_3 approaches the calculated lithostatic stress above and below the fracture zone.

where the fracture zone is less than 10 m thick would be expected to transmit a high normal stress than the thicker and less stiff portions of the fracture zone. Figure 2.11 shows that the areas around the shaft, i.e., where the fracture zone is thin, is transmitting high normal stress.

Using the correlation between thickness and stress, an elastic solution was explored to explain the variation in σ_3 with depth in Figure 2.10 as follows. Examination of Figure 2.10 reveals a similarity between the distribution of vertical stresses below the fracture zone and the Boussinesq stress distribution found below a loaded plate or footing on an elastic half space. The stresses measured above and below Fracture Zone 2 ranged from 6 to 43 MPa and
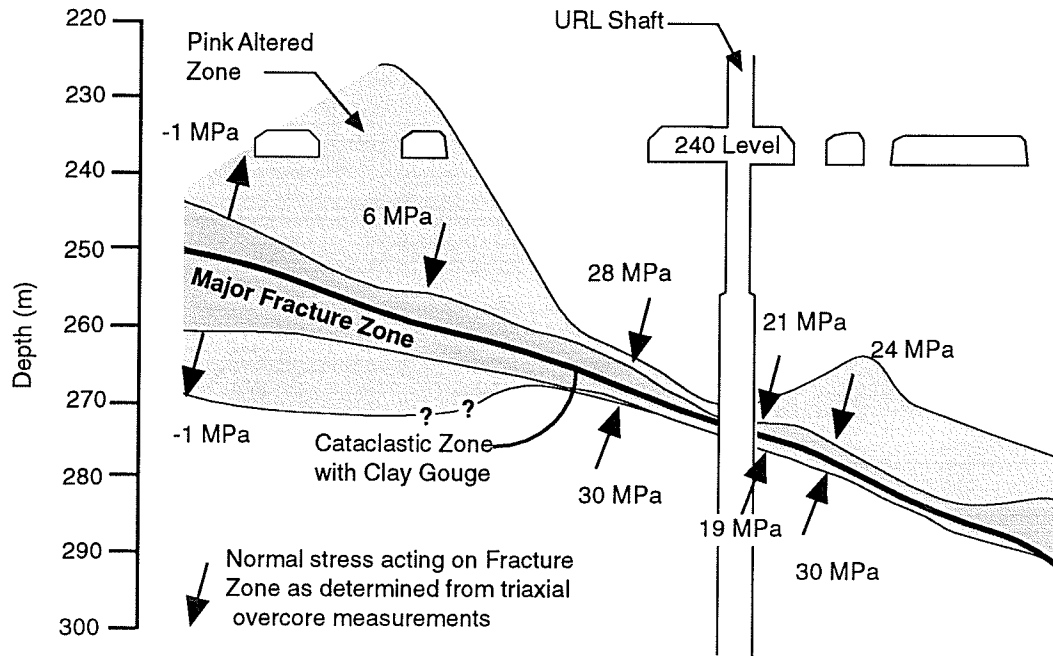
Figure 2.11: Measured stresses normal to Fracture Zone 2. Note the increase in normal stress as the fracture zone thins to about 10 m thick.

are shown in Figure 2.12. Using the thickness contours for the fracture zone to estimate a "footing" size, two trial footings were analyzed (Figure 2.12). The smallest footing followed the 10-m-thickness contour and the largest footing followed the 30-m-thickness contour. The normal stress acting on the footing was chosen as 30 MPa for the small footing, and 25 MPa and 20 MPa for the large footing. The stress was reduced for the large footing based on the assumption that the bigger the area, the lower the average stress. These values were also in keeping with the measured stress values shown in Figures 2.11 and 2.12. Using the solution developed by Li [101], the vertical stresses below the fracture zone were calculated to a depth of about 400 m. The results from this simple analysis are shown in Figure 2.13 and illustrate that the high normal stress transmitted across the thinner section of the fracture zone (Figure 2.11) affects the vertical stress for a distance of about 130 m below the fracture zone. The UDEC modelling described earlier also indicated that the vertical stress around Fracture Zone 2 was slightly above that due to the weight of the overburden. It is therefore
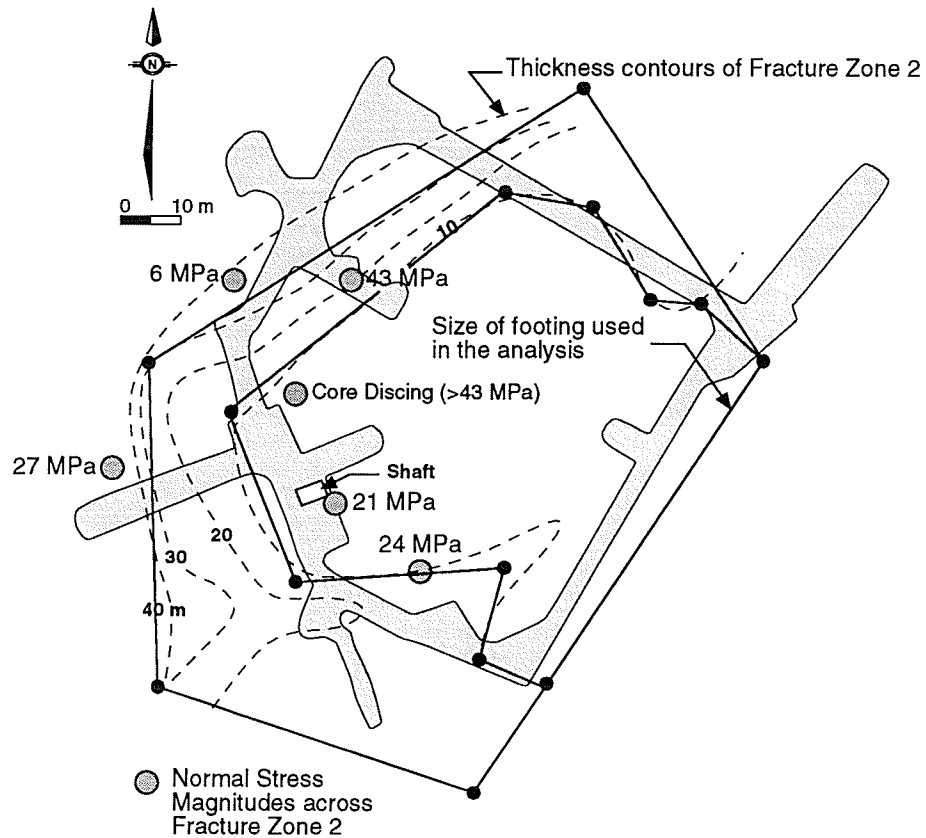
Figure 2.12: Plan of the 240 Level with the thickness contours of Fracture Zone 2. The figure shows the small and large footing used in the Boussinesq analysis and the measured normal stress acting on Fracture Zone 2.

postulated that the combination of variations in thickness and normal stiffness, and the reverse displacements are responsible for the vertical stress distribution in Figure 2.10.

2.2.5   *In Situ* Stresses at the 420 Level

The *in situ* stress measurements at the Underground Research Laboratory serve to show that even in a large, relatively homogeneous pluton such as the Lac du Bonnet batholith, *in situ* stress magnitude and orientation are highly variable. This is particularly true near fault zones where our findings show that stress magnitudes can increase and/or decrease significantly and stress orientations can rotate as much as 90° when these faults are crossed.
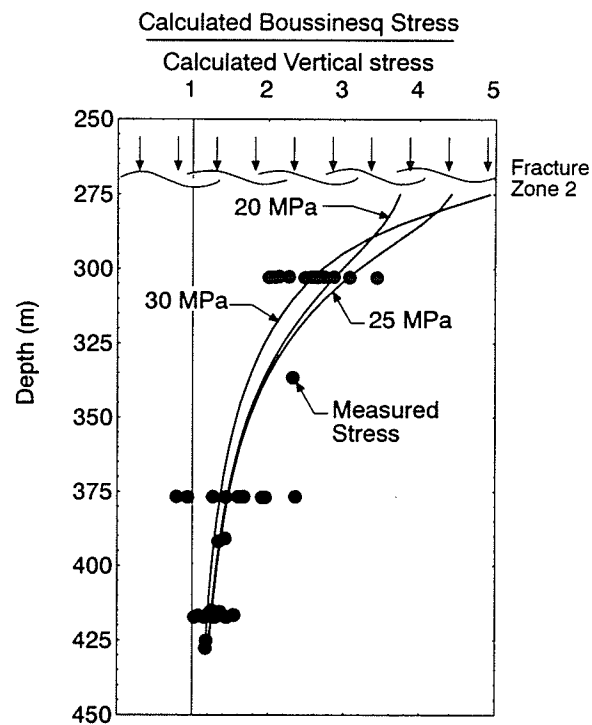
Figure 2.13: Predicted vertical stress distribution beneath the small and large footings compared with the measured vertical stress. The applied "footing" stress used for each analysis is indicated.

However, away from these faults the *in situ* stress state is relatively uniform.

The extensive *in situ* stress data base at the URL has revealed three distinctive stress domains (Figure 2.14). Stress Domain I which extends from the surface to Fracture Zone 2.5 contains the stress magnitudes which are considered normal for the Canadian Shield for depths up to 200 m [70]. In this domain, the *in situ* deformation modulus is about 30 GPa and the maximum horizontal stress ($\approx\sigma_1$) increases with depth to about 20 MPa above Fracture 2.5.

Stress Domain II serves as the transition from Stress Domain I to Stress Domain III. In this domain the rock mass contains very few joints and σ_1 is about 25 MPa.

Within Stress Domain III, the rock mass contains no joints and the *in situ* deformation modulus is about 60 GPa. Stress measurements within this domain have been carried out to a depth of 550 m and show that there is little variation of the maximum horizontal stress magnitude with depth (Figure 2.14). Drilling of boreholes to a depth of 1200 m also suggest that there is no significant increase in horizontal stress with depth because the extent and amount of core discing and well bore breakouts does not increase below 550 m. Hence the magnitude of σ_1 shown in Figure 2.14 for Stress Domain III is $\approx$55 MPa and there is no evidence, at present, to suggest that it increases significantly below 550 m.

In summary, despite the fact that the traditional methods of overcoring and hydraulic fracturing in vertical boreholes did not provide meaningful information on the stress magnitudes and orientations in Stress Domain III, other non-traditional methods did provide sufficient information to develop a stress tensor including:

- the mean σ_{Hmax} from the shaft convergence measurements was 55 MPa.

- $\sigma_{Hmax}/\sigma_{Hmin} \approx 1.15$ from the shaft convergence measurements.

- $\sigma_{Horizontal}/\sigma_{vertical} \gg 3$ for horizontal excavations on the 420 Level since the measured radial displacements diverged (This can only occur if the stress ratio $\gg$ 3).
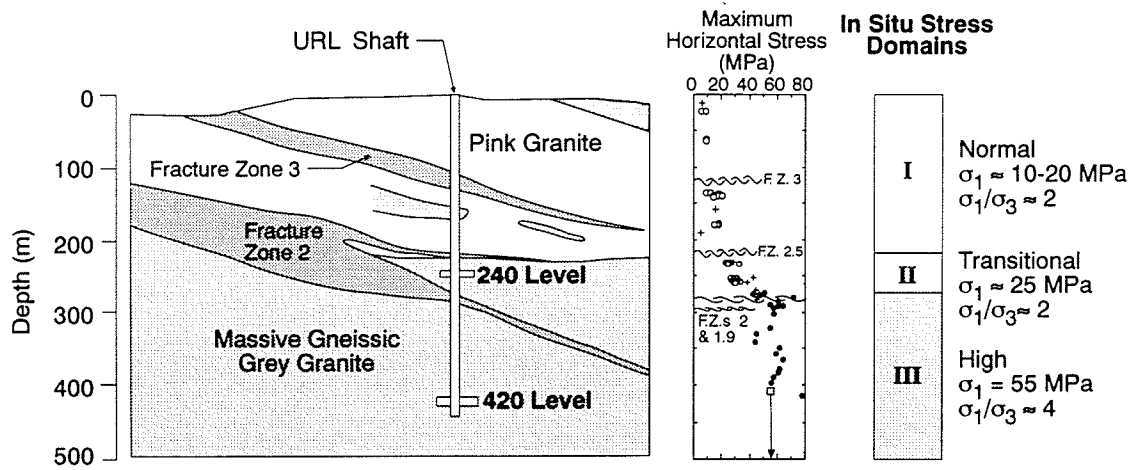
Figure 2.14: Geological section through the URL showing three stress domains.

- $\sigma_{vertical} \approx 14$ MPa at the 420 Level. This was determined from hydraulic fracture testing in horizontal boreholes. The value of 14 MPa is very close to the value of 11.1 MPa calculated from density of the overburden using a stress gradient of 0.0265 MPa/m.

- The under-excavation method [163] gave $\sigma_1 = 55$ MPa.

The in situ stresses shown in Table 2.2 have been determined for the 420 Level based on the information above and on construction observations [105] and will be used in Chapters 5 and 6.

2.3   Sample Disturbance in Brittle Rocks

The design of an underground opening requires an estimate of the rock mass strength. The first step in this process is to collect representative samples of the rock type and conduct laboratory tests to determine the strength properties. These samples are generally obtained from the location at which the opening will be constructed. It is generally recognized that softer rocks, i.e., shales and porous sandstones, are susceptible to sample disturbance when the samples are obtained at great depths and that this process affects their laboratory

Table 2.2: Summary of *in situ* stress magnitudes and orientations at the 420 Level of the Underground Research Laboratory.

	Magnitude (MPa)	Trend (°)	Plunge (°)
σ_1	55 ±3	135	14
σ_2	48 ±3	47	8
σ_3	14 ±2	73	74
Stress ratios			
σ_1/σ_2	1.15		
σ_1/σ_3	3.9		

properties. In the previous section it was shown that the *in situ* stress magnitudes at the URL vary considerably with depth and reach about 55 MPa at the 420 Level. Thus it becomes important to quantify possible sample disturbance effects on the properties of samples taken from the 420 Level of the URL.

The process of drilling a core sample from a stressed medium induces a stress concentration at the sampling point. When this stress concentration is sufficient, core discing [121, 43], an extreme form of sample disturbance, is observed. *In situ* stress magnitudes generally increase with depth, consequently, one would suspect that samples of the same rock obtained at increasing depths should contain a higher density of microcracks. Thus the process of stress-induced microcracking is progressive and a function of the stress environment, i.e., the sampling depth (Figure 2.15). Geotechnical properties of laboratory specimens are affected by crack density. In this section we will examine the evidence and effects of stress-induced microcracks, caused by sample disturbance, on the laboratory properties of Lac du Bonnet granite samples obtained at depths ranging from near surface to 1000 m. This sampling depth provided samples from the three stress domains established for the URL (see Figure 2.14).
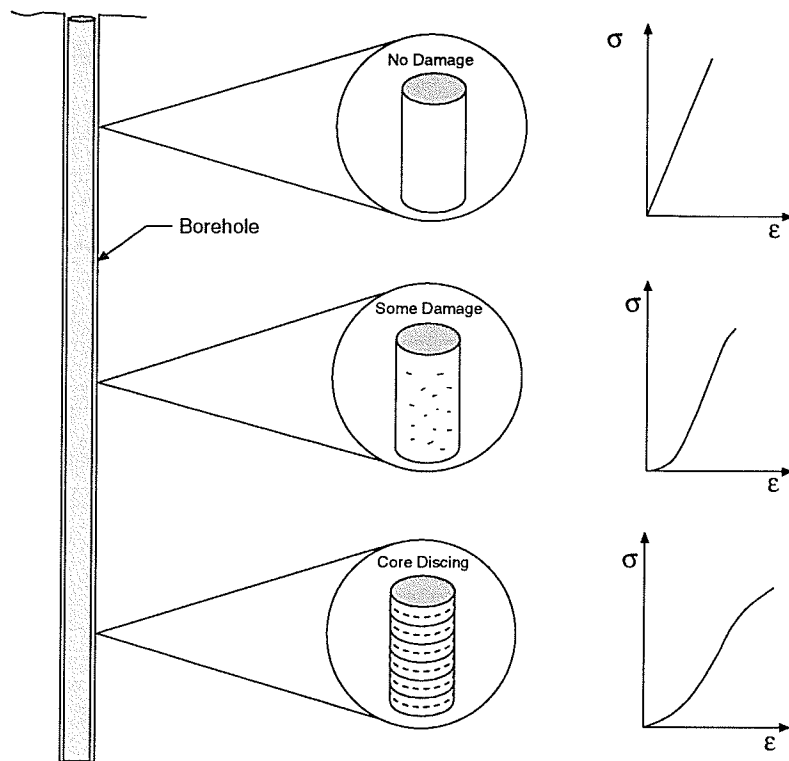
Figure 2.15: Illustration of sample disturbance and depth. The stress-strain plots in the right part of the figure illustrate the type of response as damage increases.
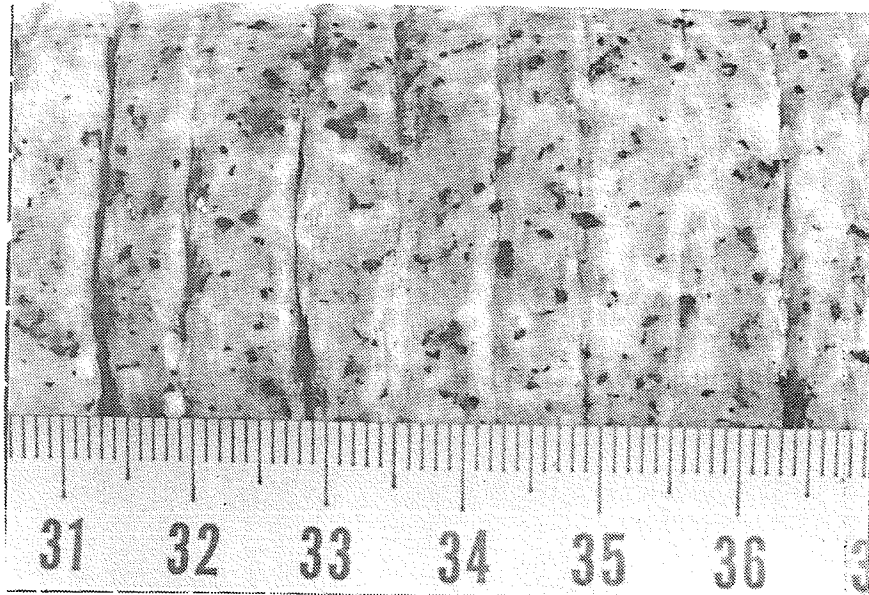
Figure 2.16: Core discing. The core is 45 mm in diameter.

2.3.1   Visual Evidence for Sample Disturbance

The most significant form of visual evidence for sample disturbance is core discing (Figure 2.16). Core discing has been observed at the URL with core samples ranging in diameter from 18 mm to 1.25 m. The thickness of the discs varies from a few mm to several cm with stress magnitude, e.g., a borehole drilled from an underground opening on the 420 Level displayed the thinnest discs near the opening. As the borehole advanced away from the stress concentration near the opening the thickness of the disc increased. It should be noted that core discing is only observed in Stress Domain III and near fracture zones at the URL.

Other visual evidence for sample disturbance is the microcracks observed in samples. Natural and stress-induced microcracks are differentiated by their physical characteristics. Natural microcracks in crystalline rocks have rough or irregular walls and/or small infillings. Stress-induced microcracks are identified by their smooth, parallel walls, which would mate perfectly under normal stress (suggesting an extensional origin), sharp terminations and a lack of infilling or bridging material [14, 29]. Stress-induced microcracks in samples from Stress Domain III are up to 15 μm in width in drill core samples and can be seen with the

naked eye (see Figure 2.17). Within the samples from Stress Domain I the percentage of microcracks is about 16% of that found in the Stress Domain III samples and there is no significant increase in the percentage of microcrack porosity in the Stress Domain I samples with depth. In Stress Domain III samples however, the percentage of microcrack porosity increases with depth to about 20% of the total porosity (0.5%) of the samples at depths of about 400 m [29]. An example of a stress-induced microcrack is provided in Figure 2.18.

An attempt was made using the imaging facilities and software at the University of Manitoba Department of Geological Sciences to quantify crack length and density in various samples. Techniques using reflected lighting were tried. Unfortunately, the technique did not produce convincing evidence that the imaging software could separate "real" cracks from contrasting mineral grains. These techniques, if made successful, could provide a significant improvement to quantifying crack densities in rock samples.

2.3.2 Properties versus Depth

Samples were collected from various near-vertical boreholes drilled in the Lac du Bonnet batholith near the Underground Research Laboratory, and were tested to establish the unconfined compressive strength, tangent Young's modulus, Poisson's ratio and P-wave velocity (Figure 2.19). All samples were tested at ambient room temperature and humidity with a standard loading rate of 0.75 MPa/s [83]. It is evident from Figure 2.19 that either the *in situ* rock is changing with depth or that the microcrack density in the samples is simply increasing with depth. Based on the P-wave velocities measured *in situ*, and discussed later, the latter is true.

P-wave velocity is sensitive to crack density and hence a good indicator of sample disturbance. In order to establish if the P-wave velocity trends observed in the laboratory samples in Figure 2.19 are present *in situ*, P-wave velocities from several borehole velocity surveys carried out at the URL were compiled (Figure 2.20). The velocity surveys were
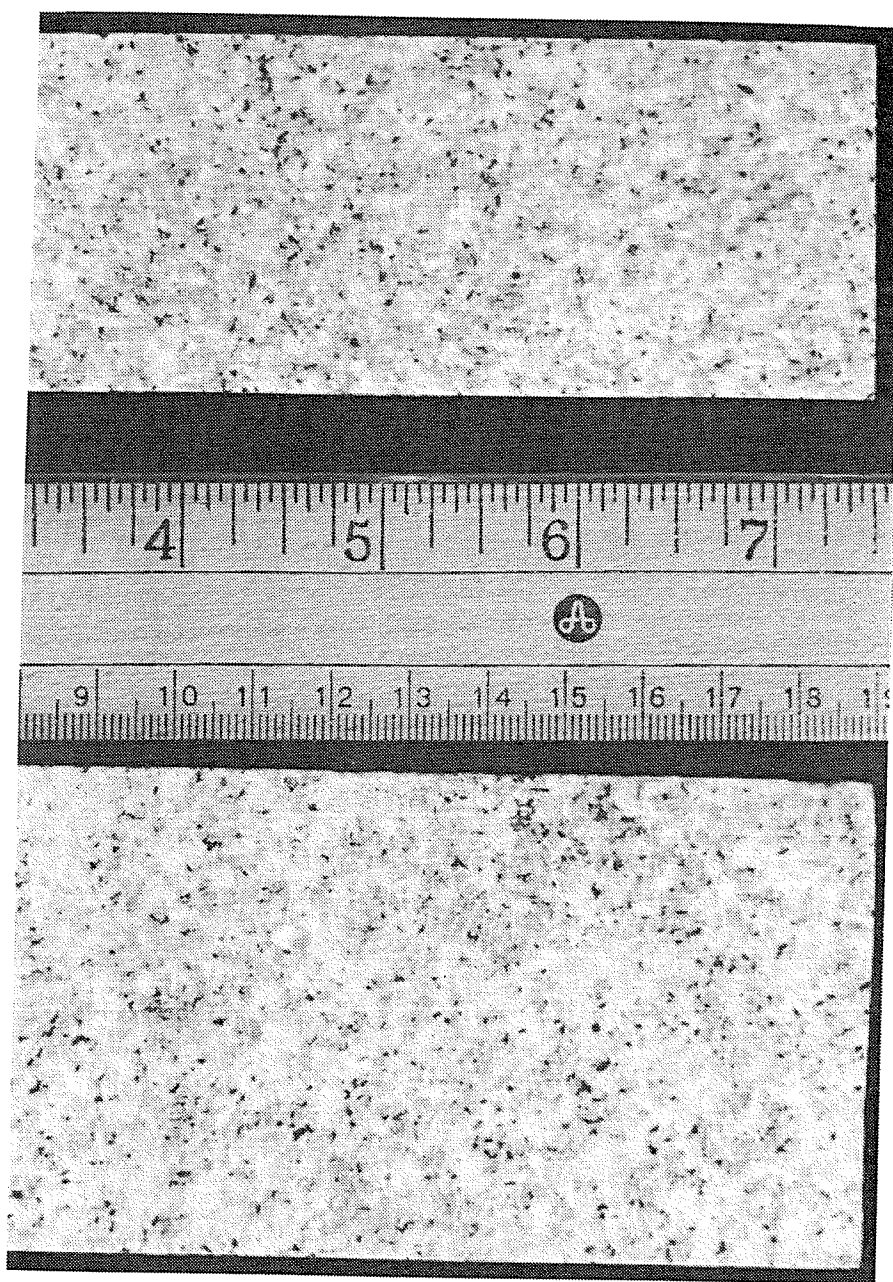
Figure 2.17: Photograph of core from Stress Domains I (top sample in photo) and III (bottom sample in photo). Most of the cracking in the core from Stress Domain III occurs along grain boundaries.
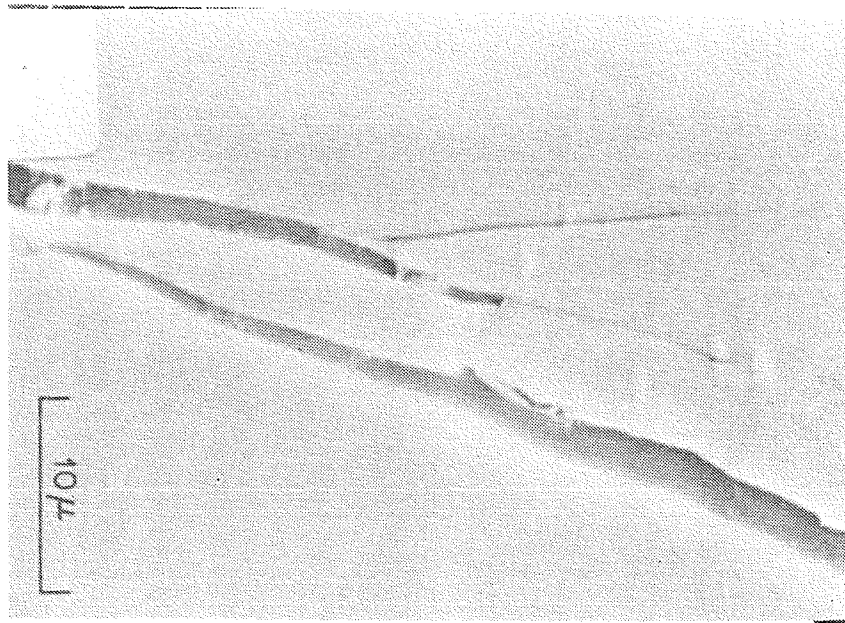
Figure 2.18: Stress-induced microcrack with characteristic well-matched parallel walls and sharp tips in a sample of Lac du Bonnet granite from URL (after [29]).

carried out using a variety of techniques: standard borehole logging tool, cross-hole geophysics and microseismic survey. The cross hole geophysics survey at a depth of 420 m was carried out from tunnels and boreholes which gave access to a 40 m × 40 m vertical panel (Figure 2.21). The results from the survey indicate that there is essentially no difference in P-wave and S-wave velocities in the vertical and horizontal directions *in situ*, indicating isotropic conditions. Also note that the P-wave velocities are very similar to those measured at the 240 Level. Figures 2.20 and 2.21 give no evidence to suggest that the microcrack density *in situ* increases with depth and consequently it can be concluded that the core samples taken at depth are disturbed.

2.3.3 Permeability

Katsube [86] carried out a series of permeability tests on samples taken from several near vertical boreholes drilled in the Lac du Bonnet granite to depths of about 1000 m. The
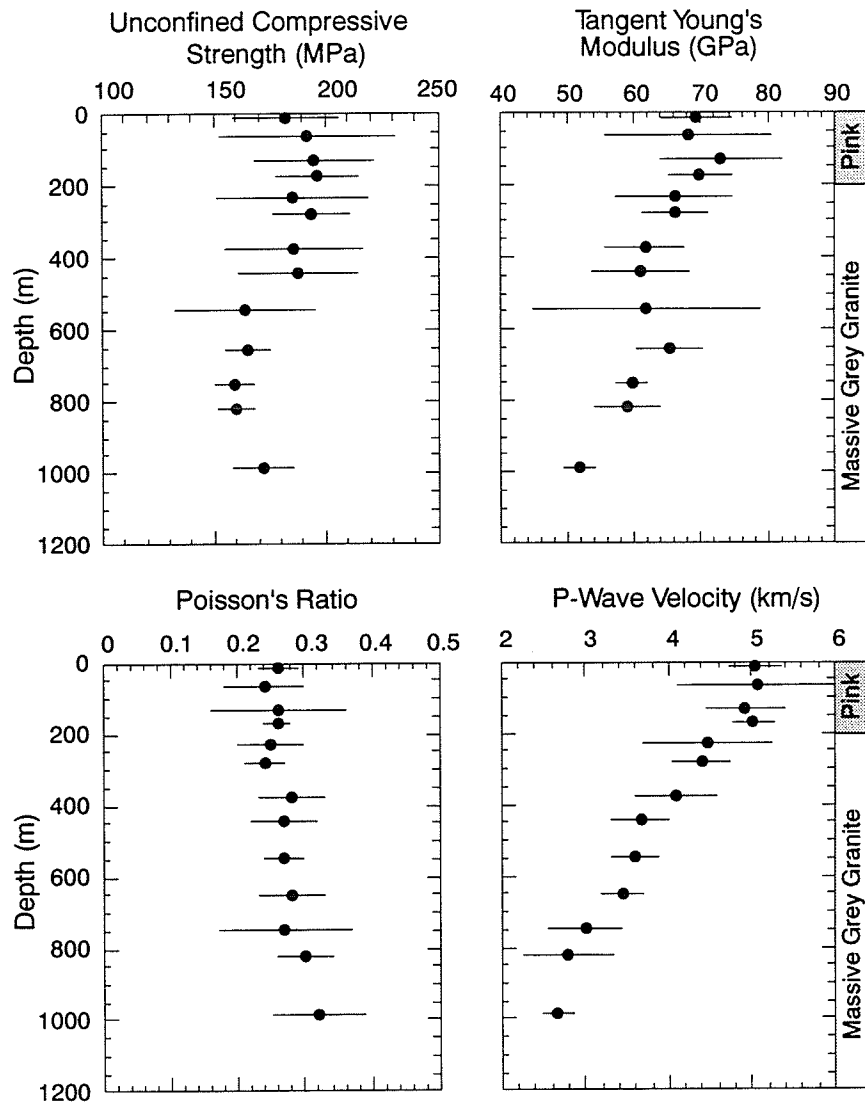
Figure 2.19: Laboratory properties versus depth. Note the significant decrease in P-wave velocity with depth.
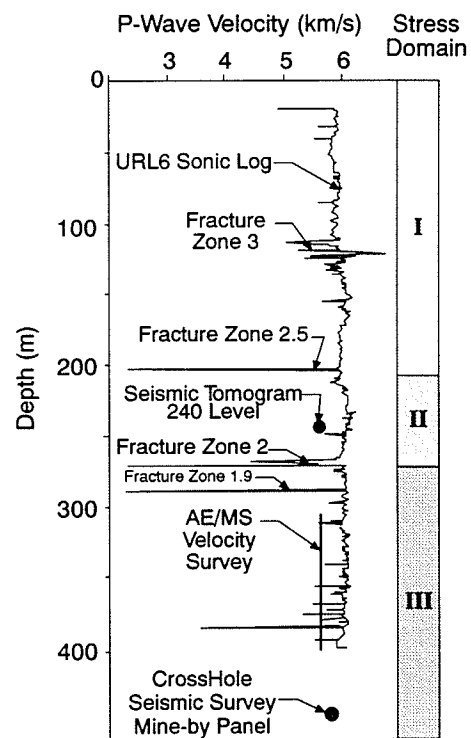
Figure 2.20: P-wave velocities *in situ*. The sonic log for borehole URL6 show a constant P-wave velocity with depth except where the fracture zones are encountered.
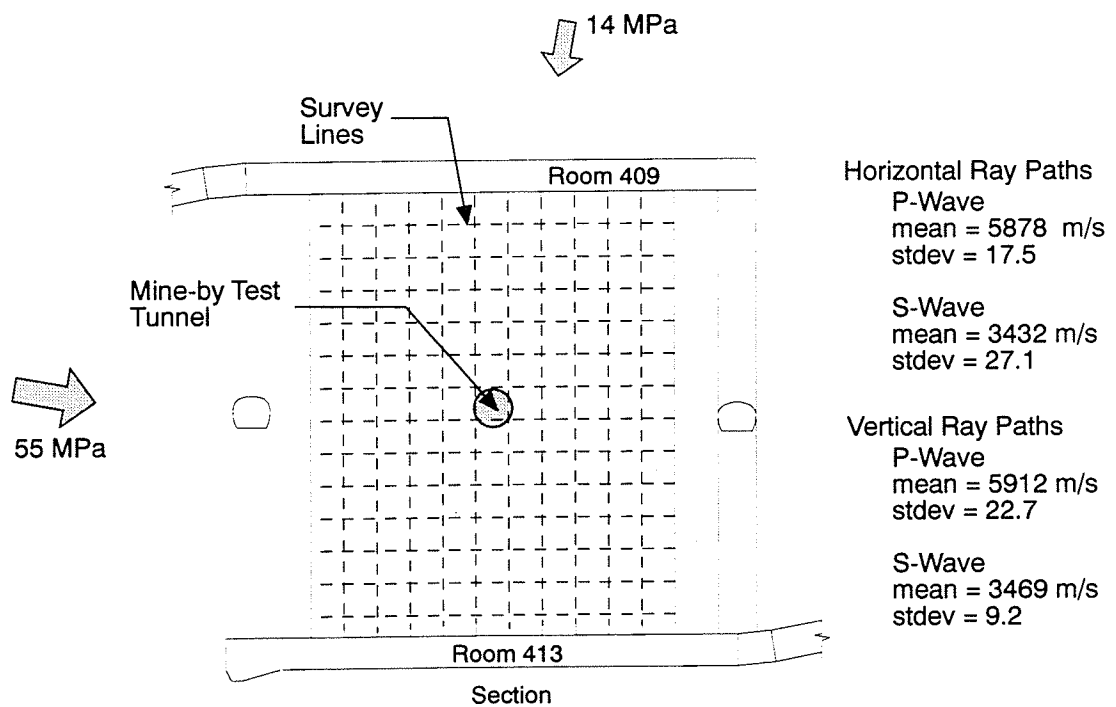
Figure 2.21: P-wave velocities from vertical and horizontal ray paths. The spatial coverage is 40 m × 40 m. (after Hayles, pers. comm.)
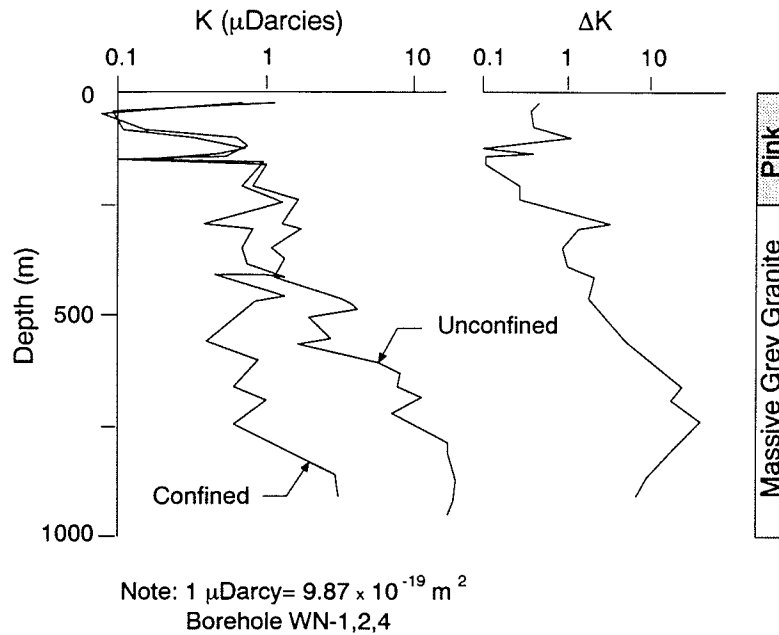
Figure 2.22: Permeability versus depth. Note that the permeability starts to increase below a depth of about 300 m, i.e., the beginning of Stress Domain III (after [86]).

tests were conducted on samples 45 mm in diameter and 20 to 30 mm in length using a transient method that measured the decay of a small step change of pressure imposed at one end of the sample. Tests were conducted for confined and unconfined samples where the confining pressure was set to 22.6 KPa per metre depth. Katsube's results are shown in Figure 2.22 and show an increase in permeability with depth. The ΔK in Figure 2.22, which is the difference between the confined and unconfined permeability, shows that significant increases in permeability occur below a depth of about 300 m. This suggests that the increases in K are found in core samples taken from Stress Domain III.

2.3.4 Modulus

Young's modulus is very sensitive to crack density. The tangent moduli of samples from Stress Domain I and Stress Domain III were determined at confining stresses ranging from 0 to 60 MPa (Figure 2.23). The modului were measured when the samples were loaded to about 50% of their ultimate load. Figure 2.23 shows that the samples from Stress Domain I
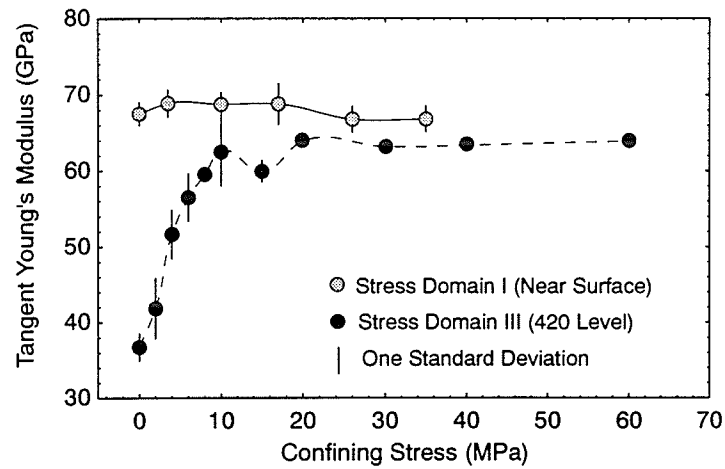
Figure 2.23: Tangent Young's modulus versus confining stress. Note that the modulus from Stress Domain I shows no dependence on confining stress.

showed no dependence on confining stress, whereas the samples from Stress Domain III show a strong pressure-dependent modulus as described by Santarelli and Brown [139]. However, the granite from Stress Domain I through III is all part of the same batholith and shows no significant variation in mineralogy or grain size. In addition the samples were selected from the main mass of homogenous granite and hence it is concluded that the stress-dependent modulus for the samples from Stress Domain III is an expression of the increased crack density in the sample.

The modulus of the samples from Stress Domain III in Figure 2.23 remain somewhat lower then the results from Stress Domain I, even at confining pressures above 20 MPa. This would imply that the moduli of the damaged samples cannot be regained by simply applying confining stress.

2.3.5 Compressive Strength

In order to estimate the rock strength based on laboratory testing, it becomes important to establish whether or not sample disturbance affects the strength envelope. The samples were first divided into three groups corresponding to the three *in situ* stress domains

established at the URL: Stress Domain I (0-200 m depth), Stress Domain II (240 Level) and Stress Domain III (420 Level). The σ_1 stress magnitudes increased from $\approx$10–20 MPa in Stress Domain I to $\approx$55 MPa in Stress Domain III, suggesting that the stress-induced microcracking in the samples should increase with depth. The samples from Stress Domain I were further subdivided into two groups (pink and grey) to determine if the colour would indicate different properties. The samples from all domains were also screened for lithological uniformity to ensure that only samples of the medium-grained homogenous granite typical of the main mass of granite at the URL were analyzed.

Triaxial test results for the four sample groups were analyzed using the Hoek-Brown failure criterion. The Hoek-Brown failure criterion is expressed in terms of σ_1 and σ_3 by

$$\sigma_1 = \sigma_3 + \sqrt{m\sigma_3\sigma_c + s\sigma_c^2} \qquad (2.3)$$

where σ_1 = stress at failure, σ_3 = confining stress, σ_c = uniaxial compressive strength of intact rock and m, s = empirical constants.

The Hoek-Brown parameters for the four groups are summarized in Table 2.3 and presented in Figure 2.24. As shown in Figure 2.24, there is essentially no difference between the two groups from Stress Domain I, indicating that the colour of the samples has no bearing on the strength. Note in Figure 2.24 that the samples from the 240 Level show a slight reduction in strength at low confining stresses, but that the entire strength envelope is reduced for samples from Stress Domain III regardless of the confining stress. Based on the relative shapes of these failure envelopes, it appears that the sample disturbance process is one that reduces the cohesion of the highly disturbed samples to about 70% of that of the undisturbed samples, but the frictional component of the failure envelopes is not affected. This phenomenon was also explored by Rosengren and Jaeger [132] and later by Gerogiannopolous [56]. By heating samples of coarse grained marble, the bonds between the grain boundaries were fractured by the differential thermal expansion of the grains. The material produced is a very low porosity tightly interlocking assemblage of grains. The
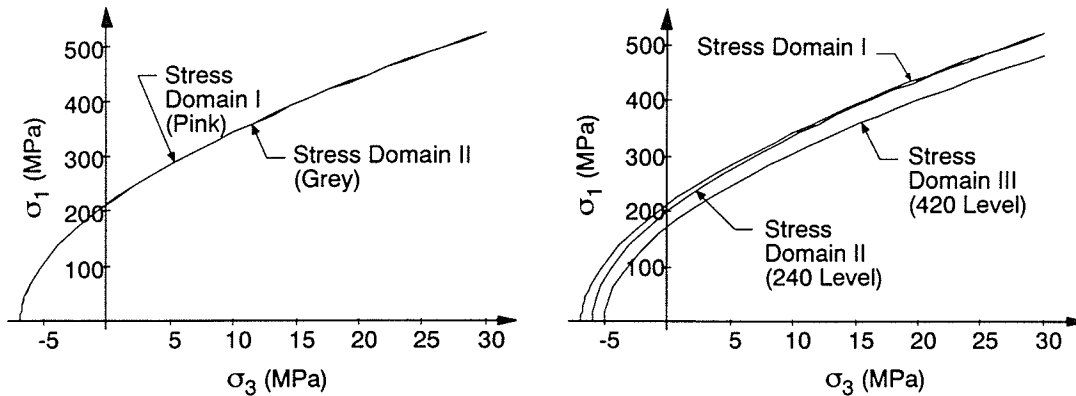
Figure 2.24: Hoek-Brown failure envelopes for the data provided in Table I. Note the loss in cohesion for samples from Stress Domain III.

Table 2.3: Comparison of Hoek-Brown failure criteria for medium grained granite samples taken from different stress domains at the URL

Stress Domain	m	s	σ_c	r^2	n
I (0-200 m)	30.80	1	213.2	0.96	147
I (0-200 m)	31.96	1	209.9	0.98	63
II (240 Level m)	34.83	1	193.5	0.97	73
III (420 Level)	40.36	1	149.6	0.95	113

results obtained by Gerogiannopolous [56] are given in (Figure 2.25). Note the similarity between Figure 2.25 and Figure 2.24. It would appear that in both cases, granite and marble, the cracking reduces only the cohesion component of the strength envelope by grain boundary cracking.

This hypothesis of reduced cohesion is in keeping with the strength predicted from the sliding crack model of Cook [32]. For example if a crack length of 1 mm is used for the average grain size and the crack length is increased to 3 mm, approximately a 40% reduction in strength (cohesion) is realized (Figure 2.26). It is also worth noting that a further 3-fold increase in crack length to 9 mm only results in a decrease in cohesion of about 25%. Thus initial crack extension is significant, even as little as 1 or 2 mm.
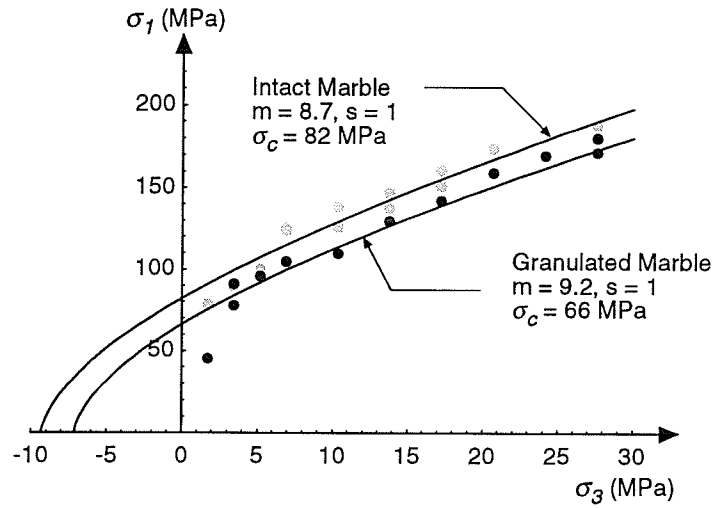
Figure 2.25: Hoek–Brown failure envelopes for intact marble and perfectly interlocked marble. Note the loss in strength affects the cohesion rather than the friction. (after [73]).
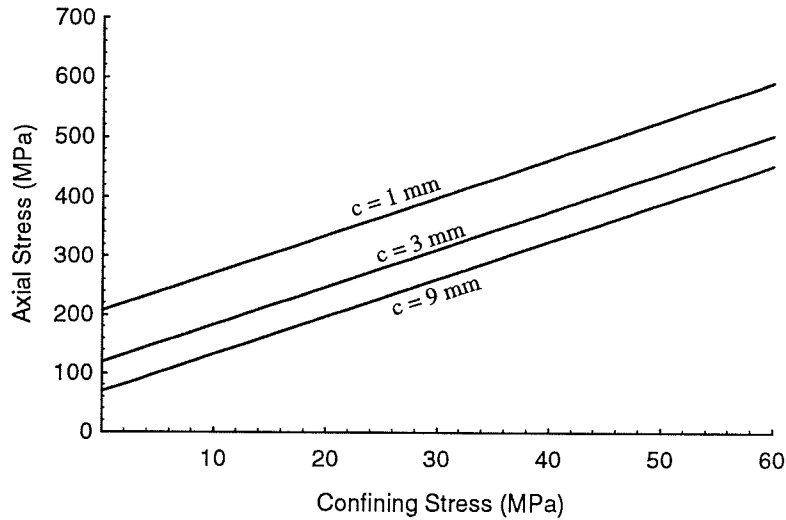
Figure 2.26: Predicted failure envelopes for Lac du Bonnet granite with different crack length. Note the increase in crack length only affects the cohesion and not the friction.

2.3.6 Tensile Strength

The tensile strength of a material may be considerabley more sensitive to crack density then the compressive strength, particularly in direct tension. Direct tension tests were carried out on samples of Lac du Bonnet granite taken from Cold Spring Quarry, the 240 Level of the URL and the 420 Level of the URL. The direct tensile strength for each of the groups tested was 4.9 ± 1.5 MPa, 3.5 ± 0.3 MPa and 1.5 ± 0.7 MPa, respectively. The tensile strength of the samples from the 420 Level was only 30% of the tensile strength of the samples from the Cold Spring Quarry and 42% of the tensile strength of the samples from the 240 Level. Clearly the density of microcracks in the core samples plays a major role in determining the tensile strength.

2.3.7 Damage Classification

The various stress domains at the URL have provided an opportunity to correlate sample disturbance, e.g., crack damage, to far field stress conditions. A classification system, based on this experience, has been developed for the Lac du Bonnet granite which relates crack damage to the ratio of maximum stress to the undamaged unconfined compressive strength (D_i) (see Figure 2.27). D_i varies from 0 to 0.5. A D_i ranging from 0 to 0.1 indicates the samples are linear elastic, i.e., undamaged, and a D_i ranging from 0.4 to 0.5 indicates the samples will be totally damaged as core discing will be severe. Note that damage starts to occur when the $D_i > 0.1$. A similar classification was first developed in South Africa to indicate sidewall failure in square tunnels in massive quartzite [75].

2.4 Summary

The data presented in this chapter has demonstrated two important points: 1) the *in situ* stress at the 420 Level of the URL is reasonably uniform and that the stress magnitudes are well defined, and 2) the laboratory properties of Lac du Bonnet granite are dependent on the damage (crack volume) contained in the sample prior to testing. The latter is an important
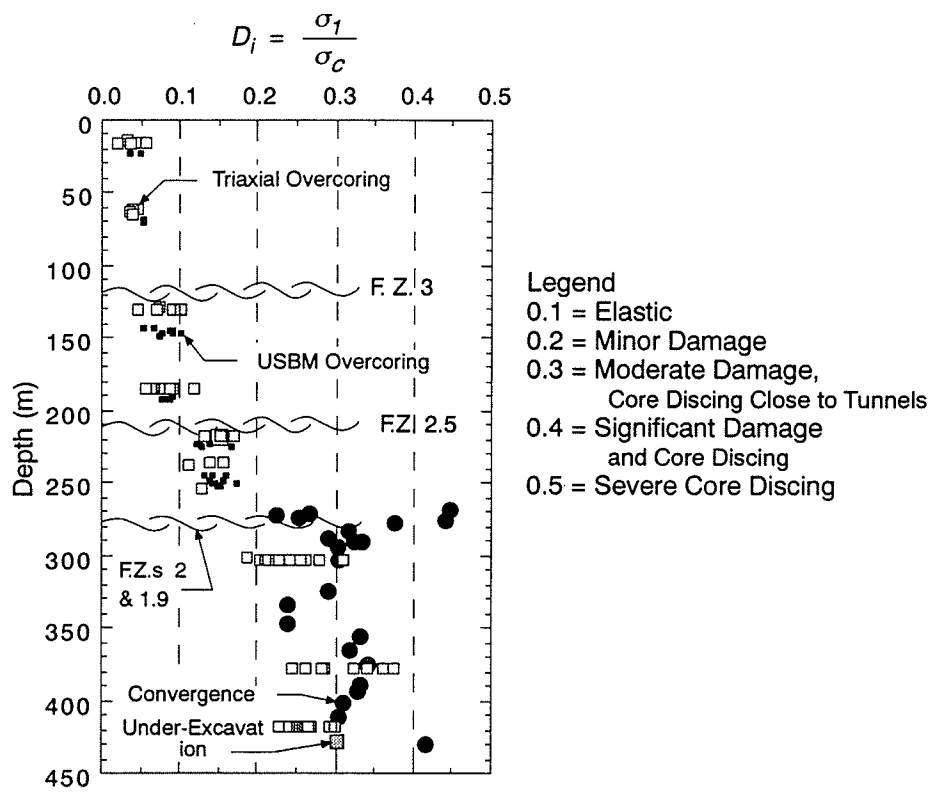
Figure 2.27: Crack damage versus depth.

issue because sample disturbance, in the form of stress-induced microcracking in a brittle rock, is a significant problem when trying to establish *in situ* rock properties at depth. The results from the testing program show that the strength, deformability, and P-wave velocity decrease as the samples are taken from higher and higher *in situ* stresses, i.e., increasing depth. What is most important is that the cohesion of the damaged samples cannot be regained by applying a modest confining stress, and if the damage is severe, such as with the samples from the 420 Level, no reasonable amount of confining stress can compensate for the cohesion loss. Hence, strength envelopes of damaged samples, i.e., samples from the 420 Level, do not reflect the *in situ* strength. Thus in order to estimate the *in situ* strength of the Lac du Bonnet granite at the 420 Level of the URL, samples with a minimum amount of crack volume should be tested. Base on the data base of testing done to date, this would suggest that the properties of the samples of Lac du Bonnet granite from the Cold Spring Quarry best represent the *in situ* strength at the 420 level of the URL.

Also the stress-dependent moduli observed in the samples of Lac du Bonnet granite from stress domain III may be only an expression of sample disturbance rather then an intrinsic property.

Chapter 3

Laboratory Properties of Lac du Bonnet Granite

Laboratory testing of Lac du Bonnet granite has been carried out by the University of Manitoba, AECL Research and CANMET since 1980. The two primary sources for the testing samples are the Cold Spring Quarry and the Underground Research Laboratory (see Figure 2.1). This chapter is a compilation of the results from the various testing programs carried out by these organizations over the past ten years. Before considering the laboratory results, it is worth noting that by Deere's classification system for uniaxial compressive strength and Young's modulus [38], the Lac du Bonnet granite is a standard granite when compared to other granites from around the world (Figure 3.1).

In addition to the summary of standard laboratory properties, which is given in the first section of this chapter, considerable testing has also been carried out under the author's direction, at CANMET's testing facilities in Ottawa and Elliot Lake, to determine the effect of scale and loading rate on the strength of Lac du Bonnet granite. The results from those studies are also summarized in this chapter.

Laboratory tests were also carried out at the University of Manitoba, as part of this thesis, to investigate the strength of Lac du Bonnet granite around small circular openings relative to the laboratory unconfined compressive strength. The results from this study are presented in the last section of this chapter.
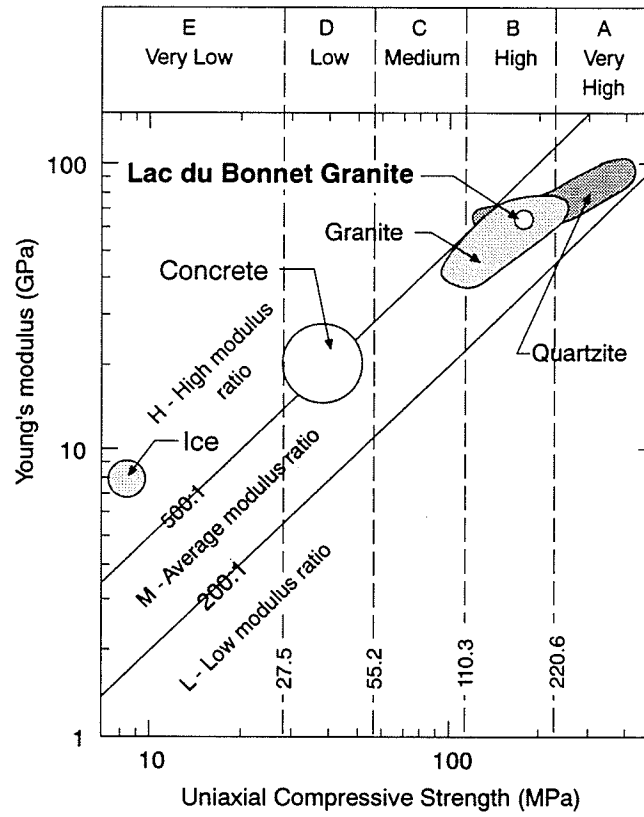
Figure 3.1: Comparison of Lac du Bonnet granite with other granites using Deere's classification system.

3.1 Standard Laboratory Properties

The strength of intact rock is generally measured by standard, short duration compression and tension tests. However, because of the long times required for nuclear waste storage, the strength of Lac du Bonnet granite has also been studied using static fatigue testing methods to determine the long-term strength. The long-term problem also brings up the issue of slow, time-dependent cracking and consequently, considerable work has also been done to establish the fracture toughness (K_{Ic}) of Lac du Bonnet granite under various environmental conditions. This section summarizes the standard properties of Lac du Bonnet granite, including the static-fatigue strength and fracture toughness.

3.1.1 Compressive Strength

Data on the compressive dry strength of Lac du Bonnet granite are summarized in Figures 3.2 and 3.3. The average unconfined compressive strength of Lac du Bonnet granite generally ranges from 200 MPa for samples collected from near surface (0-200 m) at the Underground Research Laboratory to about 220 MPa for samples from the Cold Spring Quarry (see Table 3.2). The Hoek-Brown failure criterion is fitted to the data from triaxial testing in Figure 3.3. The m value of 28.9 is in keeping with Hoek and Brown's classification for coarse grained igneous rocks [75].

The compressive strength of Lac du Bonnet granite was also determined in a wet environment. For these tests the samples were saturated over a seven day period and tested using normal loading rates. For the both the samples from the Cold Spring Quarry and from the URL the compressive strength wet was only slightly reduced ($\approx 1\%$) from the compressive strength found for the dry samples of Lac du Bonnet granite (see Table 3.2).

3.1.2 Tensile Strength

The tensile strength of Lac du Bonnet granite has been determined using the indirect Brazilian tensile test. The results are summarized in Table 3.2. Lajtai [95] also investigated the
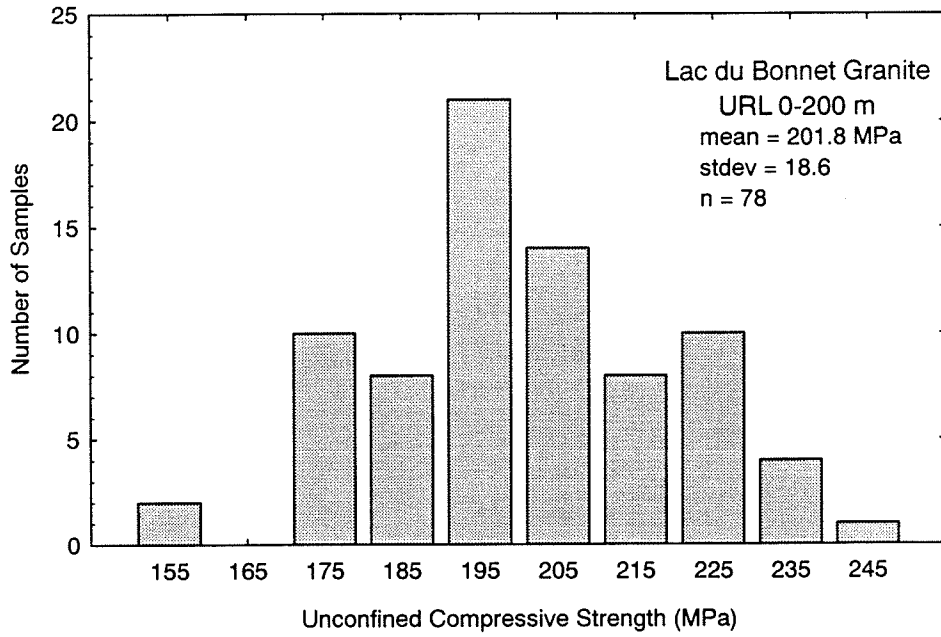
Figure 3.2: Histogram of the unconfined compressive strength of Lac du Bonnet granite from the URL (0-200 m).
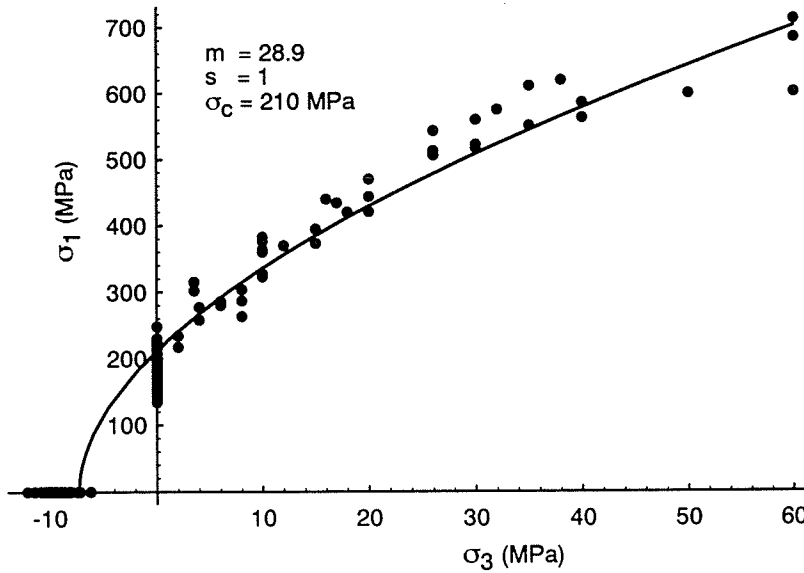
Figure 3.3: Failure envelope from triaxial testing of samples of Lac du Bonnet granite from 0-200 m at the URL. Also shown is the best fit to the Hoek-Brown failure criterion given by equation 2.3
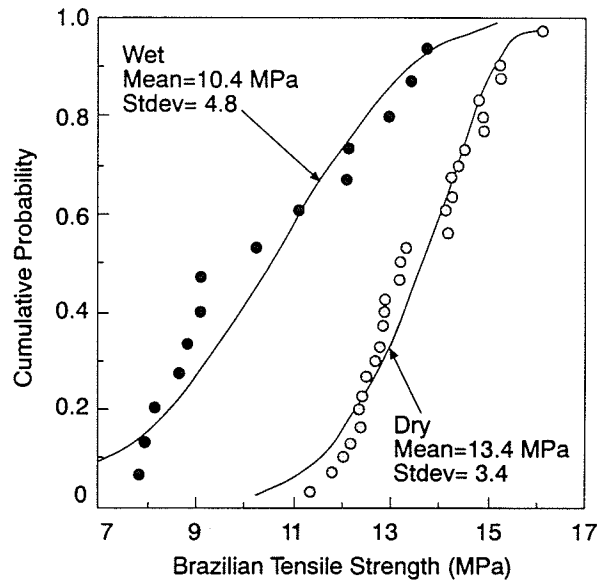
Figure 3.4: Comparison of the wet and dry Brazilian tensile strength for Lac du Bonnet granite from Cold Spring Quarry. The curves are best fit to the Weibull equation [95]

influence of moisture on the Brazilian strength of Cold Spring Quarry samples (Figure 3.4). Here, the results clearly show a reduction in the dry tensile strength of 13.4 MPa to the wet tensile strength of 10.4 MPa, a reduction of about 22%.

3.1.3 Static Fatigue Strength

Schmidtke and Lajtai [140] carried out a series of static fatigue tests on samples of Lac du Bonnet granite from Cold Spring Quarry. For this set of tests a suite of samples is subjected to a constant load and timed to failure. They concluded that the static fatigue limit for Lac du Bonnet granite decayed as the log of time and that the mean 226 MPa short term unconfined compressive strength would drop to 161 MPa in 1 yr, to 150 MPa in 10 yr, to 140 MPa in 100 yr and to 130 MPa in 1000 yr (Figure 3.5).

3.1.4 Fracture Toughness

Three independent methods were used to establish the fracture toughness of Lac du Bonnet granite taken from the 240 Level of the URL: the three-point Chevron beam test; the short
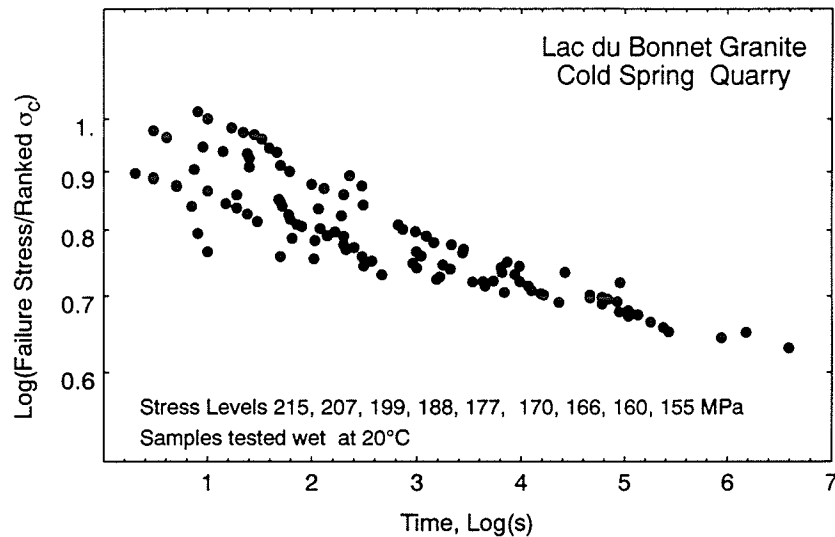
Figure 3.5: Summary of static fatigue tests on Lac du Bonnet granite (after [140]).

rod test; and the burst test [65]. The burst test is similar to sleeve fracturing [26]. In all cases the ISRM suggested methods were followed [124]. The fracture toughness was determined parallel and perpendicular to the core axis. The results from the various test methods are summarized in Table 3.1 and indicate the fracture toughness varies from 1.49 to 2.02 with a mean of 1.72 MPa$\sqrt{m}$. The results suggest the fracture toughness is directionally dependent but the number of tests is small.

Wilkins [158] carried out a series of 3-point bending tests on samples of Lac du Bonnet granite from Cold Spring Quarry in various moisture and temperature environments (Figure 3.6). The results in Figure 3.6 show that the K_{Ic} is reduced by about 13% by immersing in water at temperatures of 20°C. An additional 10% reduction occurs when the water temperature is elevated to 80°C. Wilkins results for the dry environment at 20° are somewhat lower than the fracture toughness of 2.5 MPa$\sqrt{m}$ reported by Svab and Lajtai [148] for Cold Spring Quarry samples.

Table 3.1: Summary of fracture toughness test results for Lac du Bonnet granite from the 240 Level of the URL (after [65]).

	Chevron Beam Method	Short Rod Method	Burst Method
Mean (MPa$\sqrt{m}$)	1.82		
Stdev (MPa$\sqrt{m}$)	0.08		
n	5		
Perpendicular to Core Axis			
Mean (MPa$\sqrt{m}$)		2.02	1.64
Stdev (MPa$\sqrt{m}$)		0.08	0.15
n		4	3
Parallel to Core Axis			
Mean (MPa$\sqrt{m}$)		1.64	1.49
Stdev (MPa$\sqrt{m}$)		0.08	0.15
n		4	3
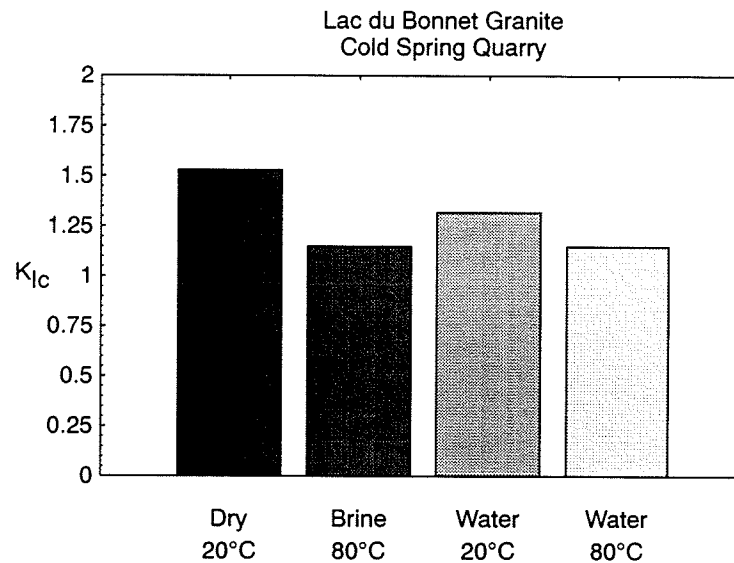
Figure 3.6: Comparison of the Mode I fracture toughness (K_{Ic}) tested in various environments (after [158]).

3.1.5 Summary of Standard Laboratory Properties

A summary of the standard laboratories properties of Lac du Bonnet granite obtained from testing samples from the Cold Spring Quarry and samples from near surface (0-200 m) from the Underground Research Laboratory is given in Table 3.2. It would appear that the samples from the Cold Spring Quarry are stronger in all respects to the samples taken from the Underground Research Laboratory. As discussed in Chapter 2 this is likely due to a higher crack volume in the samples from the URL.

3.2 The Effect of Scale on Strength

One of the most common reasons put forth for the difference between the laboratory strength of rock and the rock strength found *in situ* is the effect of specimen scale. This is not surprising given that the rock mechanics community has spent the last 25 years trying to understand the role of joints/fractures on the reduction of fractured rock mass strength, and

Table 3.2: Comparison and summary of the laboratory properties for Lac du Bonnet granite samples obtained from Cold Spring Quarry and near surface (0-200 m) at the Underground Research Laboratory. (Note: All samples were tested at room temperature. Also the fracture toughness samples from the URL were obtained from the 240 Level.)

	Cold Spring Quarry	URL	Ratio Cold Spring/URL
Tangent Young's modulus at 50% uniaxial compression			
Mean (GPa)	71	69	1.03
Stdev	±4.7	±5.8	
n	15	81	
Poisson's ratio			
Mean	0.25	0.26	0.96
Stdev	±0.04	±0.04	
n	15	81	
Uniaxial Compressive Strength (dry)			
Mean (MPa)	228	200	1.14
Stdev	±15	±22	
n	62	81	
Uniaxial Compressive Strength (wet)			
Mean (MPa)	222	198	1.12
Stdev	±12	±18	
n	14	10	
Brazilian Tensile Strength (dry)			
Mean (MPa)	13.5	9.3	1.45
Stdev	±1.2	±1.3	
n	43	39	
Brazilian Tensile Strength (wet)			
Mean (MPa)	10.4		
Stdev	±2.1		
n	14		
Fracture Toughness K_{Ic} (dry)			
Mean (MPa$\sqrt{m}$)	2.57	1.82	1.41
Stdev	±0.15	±0.08	
n	15	5	

has developed a wealth of empirical rules for determining the strength reduction. However, it is not obvious that the scale effects apply to the strength of massive unfractured rocks.

Brown [18] reviewed published data on rock strength and found that the strength was influenced by such factors as specimen geometry, end restraint, stress gradients, surface conditions and the initial degree of microcracking present. He suggested that intact rock that contained few natural microcracks would not show a size effect under uniform stress conditions. Fairhurst [49] also reported that bending tests on granite beams ranging from 304 mm long × 25 mm thick to 9,144 mm long × 304 mm thick indicated virtually identical strengths. Fairhurst [49] also reported that cylinders of limestone and marble ranging from 12 mm to 150 mm in diameter gave size-independent strength in uniaxial compression tests.

3.2.1 Unconfined Compressive Strength

Testing of scale effects was carried out on granite samples taken from the 240 Level of the URL [82]. A total of 53 cylindrical samples, with diameters ranging from 33 to 300 mm, were tested in uniaxial compression. The length to diameter ratio was kept constant at 2.5 for all samples and the loading rate of 0.75 MPa/s was also constant for each test. The results are summarized in Figure 3.7 and suggest a modest scale effect for the peak strength. Beyond ≈ 140 mm diameter the uniaxial strength is relatively constant and trends towards about 0.8 of the uniaxial strength obtained from 63 mm diameter samples, which is considered the standard core diameter for the URL.

Hoek and Brown [75] reported an empirical strength/scale relationship for various rock types (Figure 3.8). Their relationship is given by

$$\frac{\sigma_c}{\sigma_{c50}} = \left(\frac{50}{d}\right)^{0.18} \tag{3.1}$$

where σ_{c50} is the uniaxial compressive strength of a specimen of 50 mm diameter, and d is the diameter of the specimen in mm. Inspection of the individual data points used to derive Eq. 3.1 suggests that, for samples greater than 150 mm in diameter the strength
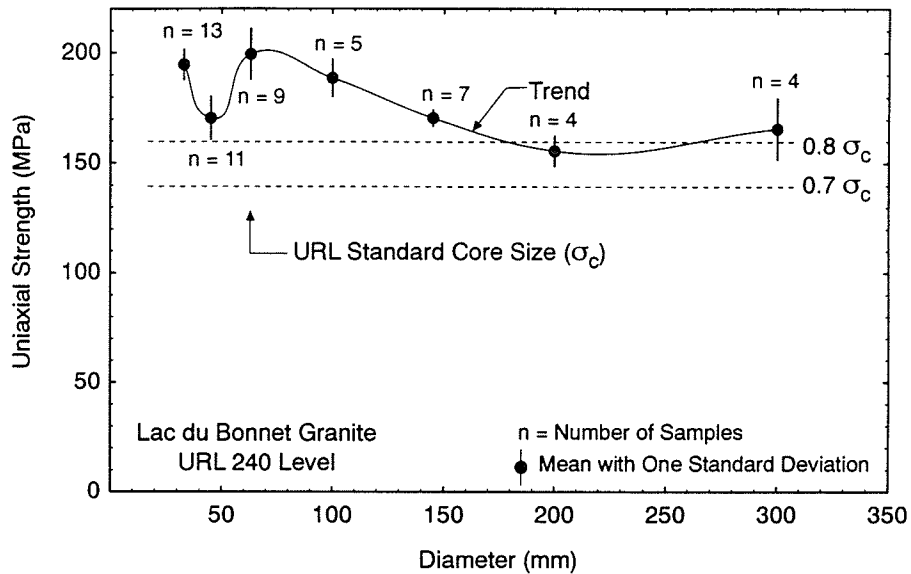
Figure 3.7: Summary of the unconfined compressive strength as a function of scale. The samples were taken from the 240 Level of the URL. Note how the peak strength is trending towards a plateau value in the larger diameter samples and that this plateau value is about 0.8 of the peak strength obtained from the smaller standard core size.

may be asymptotically approaching 0.8 of the failure strength of 50 mm diameter samples (Figure 3.8).

Fairhurst [49] has shown, based on elastic energy principles, that strength and sample size can be expressed in the general form $LS^2 = $ constant, where L is the length of the critical flaw, e.g., an existing crack, and S is the strength of the test specimen. Thus, if the size of the critical flaw increases with the specimen size, the strength should decrease as $L^{-0.5}$. Millard et al. [113], Holland [76] and Salamon and Munro [136] demonstrated that the strength of coal pillars could also be approximated by this relationship. It is well known that coal contains numerous large flaws in the form of cleat planes or joints. If the critical flaw is a grain boundary in a brittle rock like granite, then it would be expected that provided the specimen is large enough to accommodate a representative sampling of the full range of grain sizes, the strength will be independent of size. The grain size of Lac du Bonnet granite ranges from 3 to 7 mm with an average of 5 mm. Thus from Figure 3.7
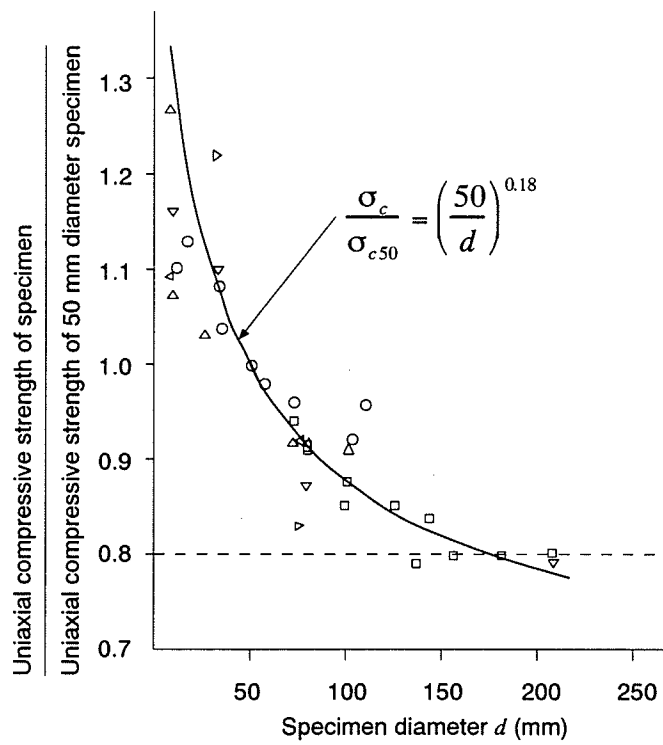
Figure 3.8: The unconfined compressive strength versus sample diameter (after [75]).

it would appear that for samples taken from the 240 Level of the URL, a specimen diameter of about 140 mm is required to contain a representative sampling of the grain sizes at that location. Nonetheless, the effect of scale on the compressive strength of Lac du Bonnet granite is not very significant.

3.2.2 Brazilian Tensile Strength

It is now well established that the tensile strength of rocks is stress gradient dependent. Hodgson and Cook [71] showed that under uniform stresses, strength will be independent of size but that with high stress gradients strength will be a function of sample size. They concluded that the higher the stress gradient the higher the apparent strength. In laboratory samples, stress gradients usually vary inversely with sample size, thus the size effect should be more apparent in small samples than in large samples.

The Brazilian tensile test is usually employed to determine the tensile strength of rock. However, the stress distribution within the sample is not uniform except over the central portion. Thus the tensile strength, determined from Brazilian tests, should show a strength increase at the smaller sizes.

Brazilian tests [159, 120] were carried out on 182 samples of Lac du Bonnet granite, from Cold Spring Quarry, ranging in diameter from 25 to 102 mm. These test data were analyzed by the author and the results are summarized in Figure 3.9. It would appear that the above discussion is correct and that once the diameter of the sample is greater then about 50 mm the tensile strength is constant at about 10 MPa. The same tensile strength data in Figure 3.9 is replotted versus sample volume in Figure 3.10. Using sample volume as a guide it would appear that the sample volume must approach 100 cm^3 before the 10 MPa tensile strength is achieved.

The data presented in Figure 3.9 is in good agreement with the findings of Wijk et al. [156]. Wijk et al. concluded that for Bohus granite, the tensile strength is independent of sample size over a very large range. Hence it would appear that for samples with a diameter
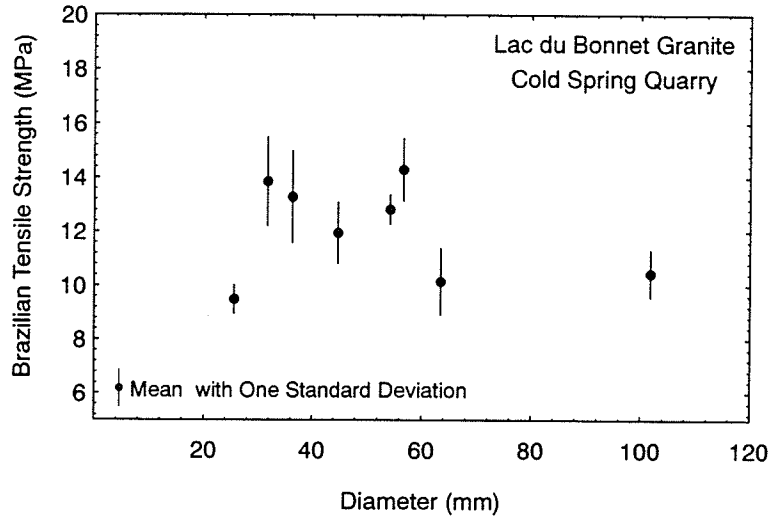
Figure 3.9: Summary of the tensile strength of the Lac du Bonnet granite from Cold Spring Quarry using the Brazilian test method.
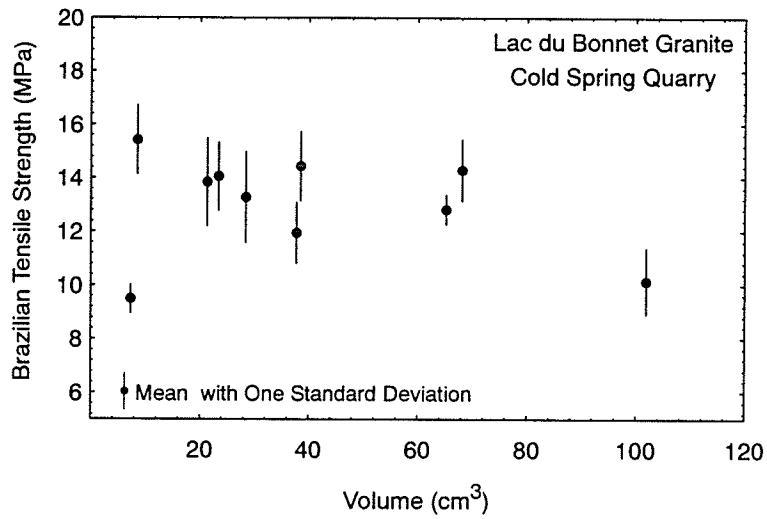
Figure 3.10: Summary of the tensile strength of the Lac du Bonnet granite from Cold Spring Quarry using the Brazilian test method.
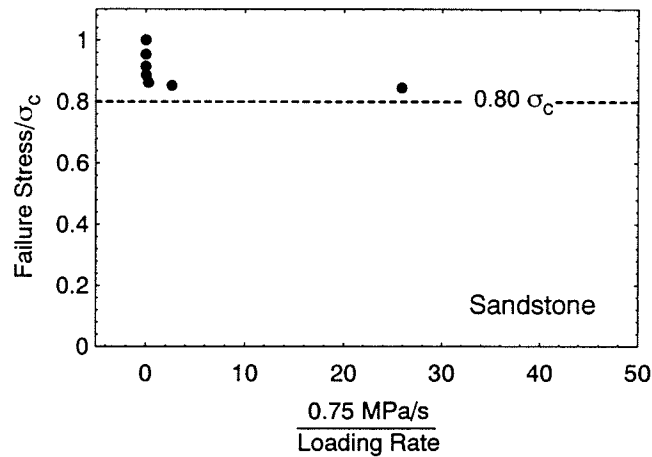
Figure 3.11: Summary of loading rate tests carried out on sandstone, after [138]. Note that the loading rate has been normalized to the standard loading rate of 0.75 MPa/s and that the failure stress has been normalized to the unconfined compressive strength (σ_c) at the fastest loading rate.

of 60 mm or greater, the effect of scale on the Brazilian tensile strength is insignificant.

3.3 Effects of Loading Rate on Compressive Strength

The effect of loading rate on uniaxial compressive strength has been investigated by many researchers. Sangha and Dhir [138] tested a sandstone over loading rates which varied from 29 to 2.9×10^{-5} MPa/s. Their results are summarized in Figure 3.11 and indicate that slow loading rates ($<$ 1MPa/s) tend to reduce the strength to a level approaching about 0.8 of the maximum strength achieved. Sangha and Dhir also noted that the modes of rupture changed as the loading rate changed. At fast loading rates the failure occurred by the development of shear planes. However, as loading rates decreased no consistent failure pattern was discernible. They attributed this to the influence of stress gradients within the sample. From these early studies the ISRM Commission on testing recommended a standard loading rate between 0.5 and 1 MPa/s [19].

Loading-rate tests were also conducted on the grey granite from the 240 Level of the URL [81]. Seven samples were initially tested at the recommended ISRM loading-rate
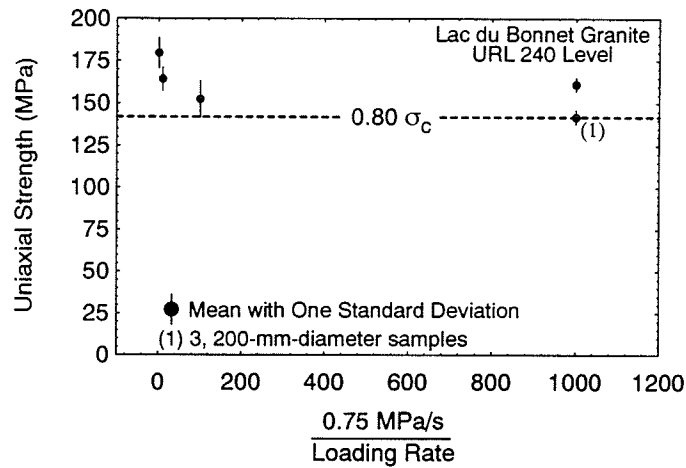
Figure 3.12: Summary of the peak strength obtained from a series of loading rate tests on Lac du Bonnet granite samples obtained from the 240 Level of the URL.

of 0.75 MPa/s. Subsequently, seven samples were tested at each of the loading rates of 0.075 and 0.0075 MPa/s, and six samples were tested at 0.00075 MPa/s. These results are summarized in Figure 3.12. Three additional samples, 200-mm diameter, were tested at the loading rate of 0.00075 MPa/s. In Figure 3.12 we again see the peak strength decreasing towards about 0.8 of the strength obtained from the samples tested at the standard loading rate.
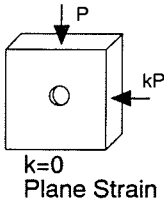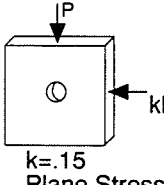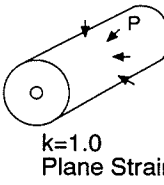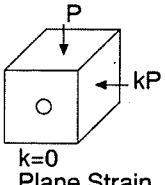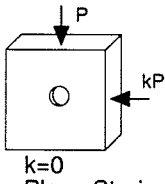
3.4 Strength Around Circular Openings: Physical Model Studies

The effect of size and stress gradients on the failure strength around underground openings has been examined by many researchers, e.g., Carter [23], Ewy and Cook [47], Hamison and Herrick [63], Mastin [112], Hoek [72], using various physical models. A summary of the loading conditions used for some of these tests is provided in Figure 3.13. One of the commonly reported outcomes of such tests is that the tangential stress at the boundary of the borehole required to cause sidewall failure is about twice the unconfined compressive strength of the material. Carter [23], and Haimson and Herrick [63] conducted an extensive set of tests on limestone using circular openings which ranged in diameter from 6.4 to 110

mm. The tests consisted of loading in uniaxial compression and monitoring, using strain gauges, when sidewall failure occurred. Figure 3.15 is a summary of the results of their study and indicates that as the borehole size increases the tangential stress approaches the unconfined compressive strength of the material.

A similar set of tests was carried out at the University of Manitoba on samples of Lac du Bonnet granite from Cold Spring Quarry to investigate the effect of opening size on the sidewall stress required to initiate failure. Eleven unconfined tests were carried out with circular openings ranging in diameter from 20 to 103 mm. An example of the test setup and a typical strain gauge configuration used to monitor the deformations is given in Figure 3.14. The placement of strain gauges on each sample was modified depending on sample size. The results from the eleven tests are given in Table 3.3 and are also plotted in Figure 3.15. The results for the Lac du Bonnet granite generally agree with the results of Carter [23], and Haimson and Herrick [63], and indicate that with boreholes greater than about 75 mm the sidewall stress required to initiate spalling is about equal to the unconfined compressive strength of the granite.

What is most obvious in Figure 3.15 is the increase in the tangential stress required to cause sidewall failure for boreholes less then about 100 mm in diameter. Because most laboratory studies are carried out with 25-mm diameter boreholes or less (see Figure 3.13) a scale effect of 2 should be anticipated when comparing the ratio of tangential stress to sidewall strength (Figure 3.15). However, it would appear that when the borehole is at least 100-mm in diameter, the strength is close to the unconfined compressive strength and the apparent scale-effects disappears. This result is also supported by field evidence at the URL where a 3.5-m-diameter circular tunnel contained a central 100-mm-diameter borehole. Both the borehole and the tunnel showed sidewall spalling indicating the absence of scale effects *in situ*.

Test Set Up	Rock Properties	Sample and Hole Dimensions (mm)	(1) Failure Stress in terms of σ_c	Reference
k=0 Plane Strain	Tyndall Limestone $\sigma_c = 41$ MPa $E = 4.2$ GPa $\nu = 0.31$	305 x 305 x 89 5 to 61 mm ϕ	For 5 mm ϕ 2.4 σ_c For 61 mm ϕ 1.5 σ_c	Carter, 1991
k=.15 Plane Stress	Chert $\sigma_c = 579$ MPa $E = 82$ GPa $\nu = 0.2$	127 x 127 x 3 19 mm ϕ	1.19 σ_c	Hoek, 1966
k=1.0 Plane Strain	Sandstone $\sigma_c = 44 - 74$ MPa $E = 20$ GPa $\nu = 0.26$	O.D. = 89 I.D. =25.4	2-3 σ_c	Ewy and Cook, 1990
k=0 Plane Strain	Alabama Limestone $\sigma_c = 43$ MPa $E = ?$ GPa $\nu = ?$	180 x 130 x 130 25 to 110 mm ϕ	For 25 mm ϕ 2.6 σ_c For 110 mm ϕ 0.81 σ_c	Haimson and Herrick, 1989
k=0 Plane Strain	Sandstone $\sigma_c = 44 - 74$ MPa $E = 20$ GPa $\nu = 0.26$	203 x 203 x 89 45 mm ϕ	For 45 mm ϕ 1.84-1.9 σ_c	Mastin, 1984

(1)Failure is defined as the first indication of hole sidewall instability.

Figure 3.13: Summary of the various boundary conditions used to investigate the failure process around circular openings.
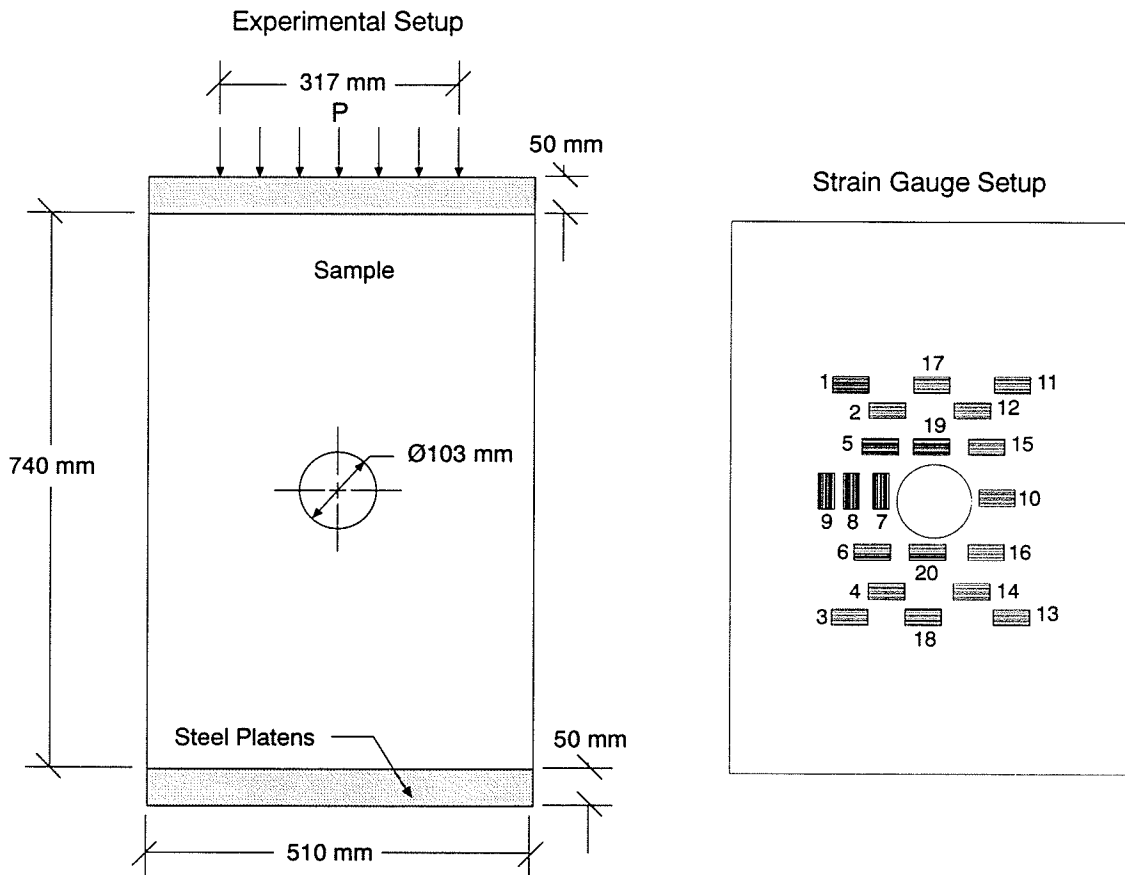
Figure 3.14: Summary of the test set up and strain gauge configuration used to investigate the effect of opening size on the sidewall strength around circular openings of Lac du Bonnet granite from Cold Spring Quarry. This figure illustrates the largest experimental setup.

Table 3.3: Summary of test results for blocks of Lac du Bonnet granite from Cold Spring Quarry containing a circular opening and subjected to uniaxial loading.

Block Label	Nominal Block Dimensions H W D (mm)	Hole Diameter (mm)	Sidewall Spalling Stress (σ_s) (MPa)	Primary Crack Stress (σ_t) (MPa)	Ratio $3\sigma_s/\sigma_c$	Ratio $3\sigma_s/\sigma_t$
F4-1	152 x 110 x 102	20	105	42	1.43	7.5
F4-2	152 x 110 x 102	20	120	48	1.64	7.4
F4-3	152 x 110 x 102	25	116	47	1.58	7.4
F4-4	152 x 110 x 102	20	110	40	1.50	8.3
F5-1	198 x 126 x 109	25	95	33	1.29	8.7
F10-1	378 x 255 x 103	52	92	36	1.26	7.8
F15-1	587 x 382 x 105	75	75	27	1.02	8.5
F15-2	587 x 382 x 105	75	92	24	1.25	11.6
F15-3	726 x 382 x 105	75	78	14	1.06	16.4
F20-1	739 x 508 x 105	103	86	27	1.18	9.5
F20-2	739 x 508 x 105	103	73	22	0.99	9.7

Note: The sidewall spalling stress (σ_s) is the applied stress required to initiate spalling. The actual tangential stress at the sidewall of the opening is $3\sigma_s$. σ_c refers to the unconfined compressive strength of 220 MPa.
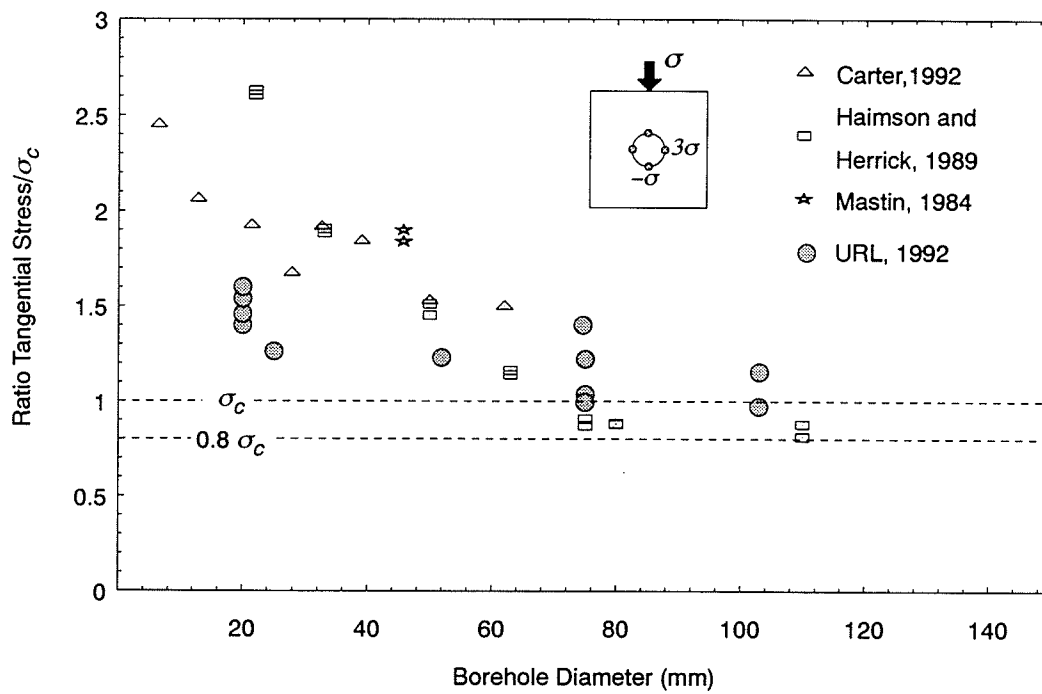
Figure 3.15: Summary of the uniaxial testing of blocks containing a circular opening. Note that the spalling stress, i.e., strength, around the opening shows a rapid increase as the opening diameter decreases below about 75 mm but that the strength for the openings greater than 75 mm is close to the uniaxial compressive strength.

3.5 Long-Term Strength

Static fatigue or long-term strength has been investigated most extensively by the concrete industry. As early as 1959 Rusch [133] summarized extensive studies where concrete samples from the same batch mix were subjected to sustained loads as well as short term compression tests. Rusch concluded that the long-term strength of concrete was defined by the stress level associated with volumetric strain reversal[1] and that this occurred at approximately 0.7 to 0.85 of the short term strength. Since 1959 other techniques have been used to determine the long term strength of concrete including: Log Stress-Log Strain [39], Incremental Poisson's ratio [40] and Limiting Strain Concept [116]. However, it appears that Rusch's general conclusion that the long-term strength is defined by volumetric strain reversal is still valid today.

One of the earliest set of tests to determine the long-term strength of rock was carried out by Wiid [155]. Wiid, in presenting his results, normalized the stress level at failure to the unconfined compressive strength of the material. His tests conducted on both wet and dry samples of dolerite are summarized in Figure 3.16. Note that Wiid's tests show two distinct behaviours: if the sample is dry and the applied axial stress is greater than about $0.8\sigma_c$, failure occurs within several hours. However, if the applied axial stress is less than the $0.8\sigma_c$, failure did not occur even after 360 hours of constant loading. If the sample is wet, failure is seen to occur at stress levels below $0.8\sigma_c$, suggesting that the presence of water aids the failure process. Note that even for the wet samples the lowest stress which actually caused failure was about 0.65 of the short-term unconfined compressive strength. This is similar to the findings of Schmidtke and Lajtai [140] reported earlier.

It is clear from the above that moisture plays a significant role in the time-dependent aspects of the long-term strength. Wiid [154] and Colback and Wiid [30] suggested that moisture lowers the surface free energy in the path of the growing cracks which results in a

---

[1]Volumetric strain reversal is defined and described in Chapter 4
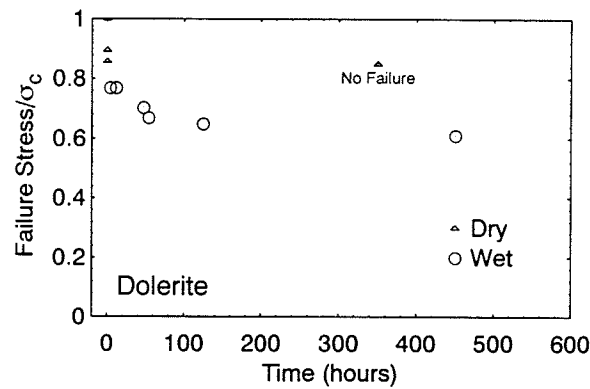
Figure 3.16: Results from long-term tests carried out on dolerite (after [155]).

reduction in ultimate strength. If the loading rate is too fast, moisture will not have time to migrate to the crack tips and the moisture will, therefore, have no effect on the strength. Wiid also noted from his studies that the angle of internal friction of the rock was not sensitive to moisture content, because the failure envelopes for different moisture contents were offset but parallel. Wiid suggested that the reduction in strength with increasing moisture content was due primarily to a reduction in the molecular cohesive strength of the material.

Atkinson and Meredith [3] noted that the phenomenon of stress corrosion, can result in significant subcritical crack growth, i.e., crack growth below the critical stress intensity factor (K_{Ic}) in quartz in a water environment. Stress corrosion is produced when a wet sample is subjected to a load which causes stress concentrations at the crack tip. Under such conditions a time-dependent response such as recorded by Schmidtke and Lajtai [140] should be expected (see Figure 3.5). However, Labuz and Berger [93] carried out tests on granite core subjected to zero load. They used a bar of aluminum as a reference and simply sprayed a small amount of water on both the aluminum bar and the granite core. The granite expanded by 15 microstrains within about 10 minutes, whereas the aluminum bar remained unstrained. Labuz and Berger postulated that a 15% difference in Young's modulus in compression and tension caused local stresses in the sample, presumably when

the sample was taken from the rock mass, and the water provided a means to equilibrate these stresses through subcritical crack growth.

Though long-term strength reduction is influenced by moisture the primary process is not moisture related. For any rock, the reduction from peak strength to about 75% of peak strength occurs almost immediately (see Figure 3.16), whereas the additional decrease to 65% of peak strength (the lowest reduction seen due to moisture in long-term strength tests) is only an additional 10% of peak. The primary role of moisture is that it provides a mechanism for time-dependent behaviour in brittle rock.

3.6 Summary

In Chapter 2 it was pointed out that the laboratory properties of Lac du Bonnet granite were dependent on the density of microcracks in the samples and that the crack density in the samples increased with the location depth of the sample, i.e., sample disturbance. In this chapter standard properties of Lac du Bonnet granite were compiled from laboratory tests conducted on samples obtained from either the Cold Spring Quarry or from the near surface (0-200 m) at the URL. It was reasoned that by taking most of the samples from these two locations the bias introduced by sample disturbance on the laboratory properties would be minimized. However, as shown in Table 3.2 the samples from Cold Spring Quarry are stronger in all respects to the samples taken from the URL, although the reduced compressive strength for the URL samples is only about 10%. Because some of the samples from the URL were taken from near fracture zones where stress concentrations exist, it seems likely that sample disturbance did introduce a small bias into the test results.

In Chapter 2 it was shown that the *in situ* seismic velocities at the 420 Level of the URL were nearly identical with the velocities measured near the surface of the URL. Thus, one can conclude that the density of microcracks at the 420 Level must be similar to density of microcracks near the surface and that the laboratory properties of the 420 Level must be similar to the laboratory properties of the URL near surface samples. Because the 420

Level consists of massive unfractured granite it is likely that the properties at this depth may actually be better then those properties for the URL near surface samples and the samples from Cold Spring Quarry. Nonetheless, before any disturbance the following properties are considered representative of the Lac du Bonnet granite at the 420 Level: the unconfined compressive strength (σ_c)=200 MPa; the Brazilian tensile strength (B_t)=10 MPa; and the fracture toughness (K_{Ic})=2 MPa$\sqrt{\text{m}}$.

In addition to the measurement of standard laboratory properties, extensive testing was carried out to investigate the effect of scale and loading rates on the unconfined compressive strength. It was shown that by either increasing the sample volume (diameter), or lowering the loading rate by several orders of magnitude the compressive strength only decreased by about 20%. Figure 3.12 showed that this reduction also held true if the sample diameter was increased and the loading rate decreased. Thus the compressive strength around the perimeter of the underground openings at the URL should be reduced by 20% to about 160 MPa based on scale and loading rate effects. This value of 160 MPa is very close to the same value (161 MPa) predicted by Schmidtke and Lajtai [140] from their static fatigue tests.

In an effort to determine if the strength around circular openings was different from the unconfined compressive strength, a series of physical model tests was carried out. These tests supported the notion that the strength of the rock surrounding a circular opening was similar to that measured in unconfined compression tests, provided that the diameter of the circular opening was greater than about 75 mm. At smaller diameters a noticeable scale effect was present, i.e., the strength of the rock around the opening was greater then the unconfined compressive strength. The lack of any scale effect with opening diameters > 75 mm is also supported by observations at the 420 Level of the URL, where failure was observed in both a 100-mm diameter borehole and a 3.5-m diameter tunnel.

In summary, there does not appear to be any evidence from the laboratory properties, to suggest why the strength around tunnels excavated at the 420 Level should be reduced to

half that measured in a standard unconfined compression test, particularly when the failure process is observed immediately upon excavation.

Chapter 4

Compressive Failure In Brittle Rock

Testing procedures for determining the compressive deformational behaviour of rock samples are given by ISRM [19]. These include recording the axial (ϵ_{axial}) and lateral ($\epsilon_{lateral}$) strains in a sample as it is loaded with or without a fixed confining stress. Richart et al. [131], in 1928, first noted that volumetric strain, in addition to the axial and lateral strains, was also an important measurement in compression testing, and Cook [33] proved that the volumetric strain of a sample measured by surface strain gauges was a pervasive volumetric property of the rock and not a superficial phenomenon. For a cylindrical sample subjected to axial loading, with or without a confining stress, and under small strains, the volumetric strain ($\frac{\Delta V}{V}$) is given by:

$$\frac{\Delta V}{V} \simeq \epsilon_{axial} + 2\epsilon_{lateral}. \tag{4.1}$$

Hence by plotting the axial, lateral and the calculated volumetric strains versus the applied axial stress the path of a rock sample to failure can be followed. An example of axial, lateral and volumetric strain versus axial stress curves for Lac du Bonnet granite in uniaxial compression is given in Figure 4.1.

4.1 Stages in the Compressive Failure Process

The failure of brittle rocks has been investigated by many researchers [74, 13, 8, 12, 141, 153, 152, 126, 66, 150]. These researchers clearly showed that the stress-strain curves for

76
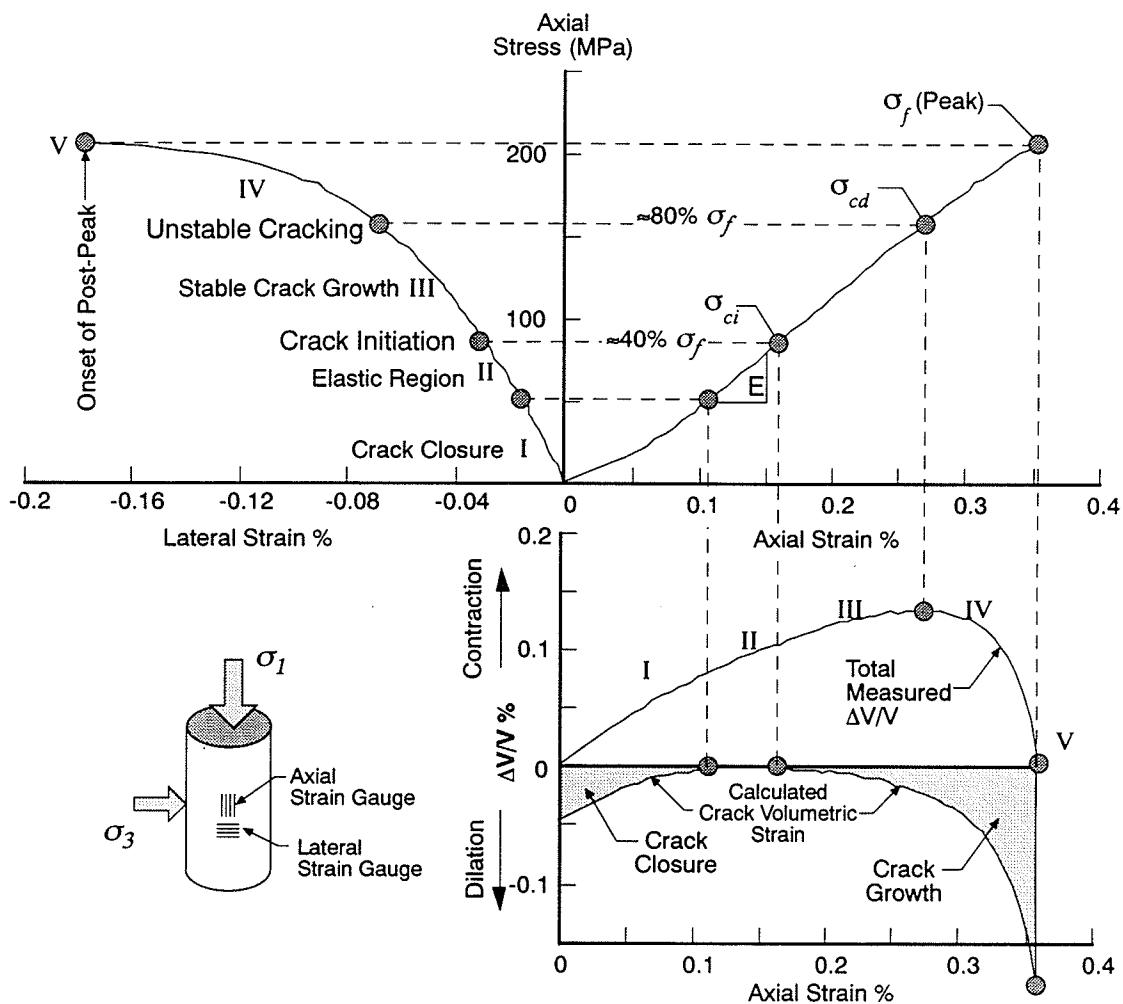
Figure 4.1: A stress-strain diagram obtained from a single uniaxial compression test of Lac du Bonnet granite. Note only the axial and lateral strains are measured. The volumetric strain and crack volumetric strain are calculated.

a brittle material can be divided into five regions (Figure 4.1). The initial region of the stress-strain curves in Figure 4.1 represents the closure of existing microcracks in the sample and may or may not be present depending on the initial crack density and crack geometry. Once the existing cracks are closed, then the rock is presumed to be a linear, homogeneous, elastic, material (Region II). The elastic properties of a rock sample can be determined from this portion of the stress-strain curves. The Regions III to V represent the progressive cracking of the rock and will be discussed in the following sections.

4.1.1 Region III: Stable Crack Growth

In 1921, Griffith [59] presented a theory which stated that tensile fracture of a brittle material initiates at microscopic flaws or cracks. Using the Inglis [79] solution for the stress on the boundary of an ellipse, Griffith suggested the material cracks as a result of intense tensile stress concentrations near the tips of sub-microscopic elliptical flaws. If the material is subjected to a tensile stress then, according to Griffith [59] the tensile strength (σ_t) is given by

$$\sigma_t = \sqrt{\frac{2E\gamma}{\pi c}} \qquad (4.2)$$

where E is the Young's modulus, γ is the fracture surface energy and c is the crack half-length.

Griffith [60] expanded his theory in 1924 to deal with compression and showed that the uniaxial compressive strength, σ_c, is 8 times the tensile strength or

$$\sigma_c = 8\sqrt{\frac{2E\gamma}{\pi c}} \qquad (4.3)$$

The tensile strength for Lac du Bonnet granite is $\approx$10 MPa, hence the unconfined compression strength should, according to Griffith, be $\approx$80 MPa. The measured unconfined compressive strength of Lac du Bonnet granite is $\approx$200 MPa. Griffith assumed that once the stress level around the microscopic flaw was sufficient to overcome the fracture surface energy then failure or rupture would occur. Since 1924, several researchers, most noticeably

Brace [11], Hoek[72], and Bieniawski [8] have demonstrated that cracks do start to form at axial stresses of about $8\sigma_t$ under uniaxial compression and at low confining pressures in biaxial loading, but that this form of crack growth is stable, i.e., failure will not occur at this stress level. In the unconfined compression test stress has to be increased to nearly 3 times this level before failure occurs. Hence, Region III marks stable crack growth, which implies that additional load is required in order for cracks to extend.

Using the Inglis [79] solution for stresses around an ellipse it is easy to see why these axial cracks are stable. Assume an inclined ellipse to represent an existing crack in a sample loaded in uniaxial compression (Figure 4.2). When the sample is subjected to a small load tension develops on the boundary near the tips of the ellipse. When the tensile strength is exceeded, a tensile crack will grow at this location, and extend in the direction of the applied load. However, at a small distance away from the boundary of the ellipse the tension disappears and hence the crack growth would be arrested until the load is increased.

The onset of crack growth marks the beginning of Region III and for Lac du Bonnet granite in uniaxial compression begins at an axial stress (σ_{ci}) of about 40% of the peak strength (Figure 4.1). The most important feature of stable crack growth is that the cracks propagate parallel to the direction of the applied compressive load, because it is observed that only the lateral strain gauge registers the cracking. σ_{ci} is difficult to identify from the laboratory stress-strain curves, particularly if the sample already contains a high density of microcracks. σ_{ci} is best determined using a plot of crack volumetric strain versus axial strain. Crack volumetric strain is calculated as follows. First the elastic volumetric strains are calculated using the elastic constants (E, ν) determined from the linear portion of stress-strain curves in Region II by

$$\Delta V/V_{elastic} = \frac{1 - 2\nu}{E} (\sigma_1 - \sigma_3) \tag{4.4}$$

The elastic volumetric strains are subtracted from the total measured volumetric strains to determine the volumetric strains caused by axial cracking (Figure 4.1). σ_{ci} is the stress at
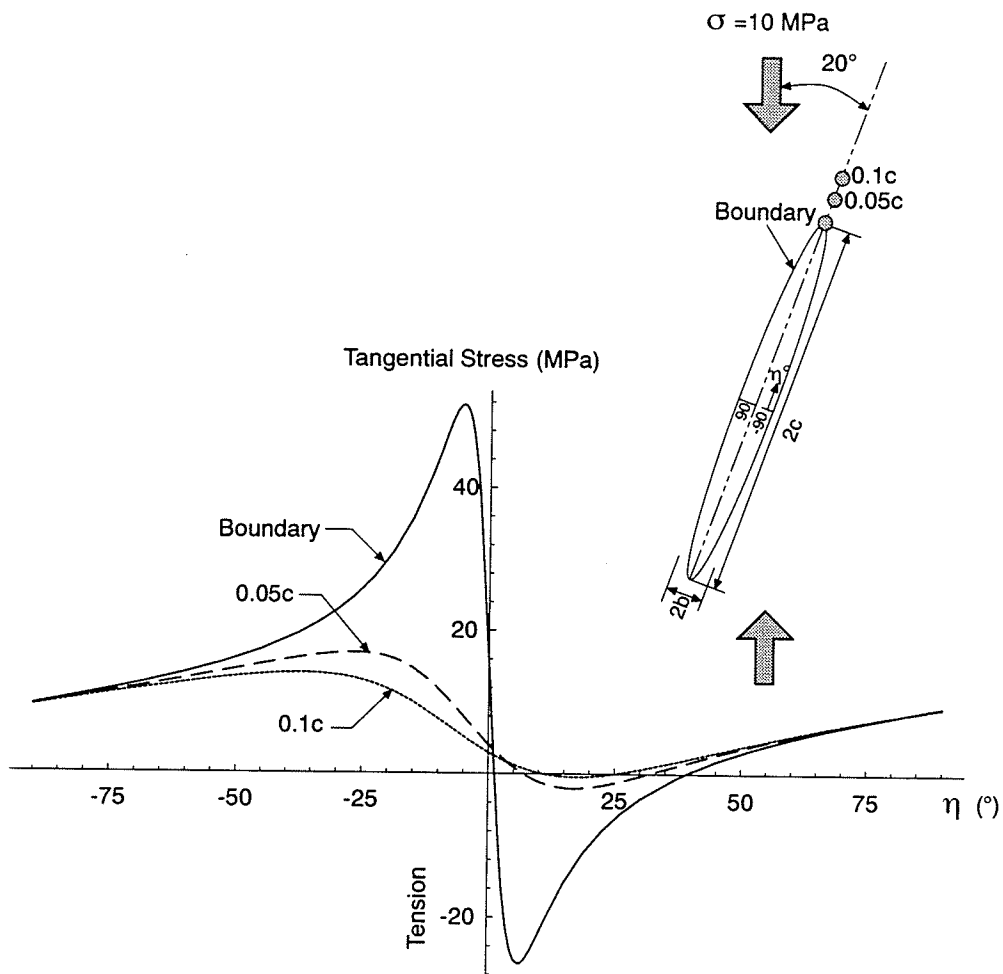
Figure 4.2: The tangential stress around an elliptical crack under uniaxial compression.

which dilation just begins on the crack volume plot as shown in Figure 4.1. Researchers [74, 8, 64] have found that the cracking associated with stresses slightly above σ_{ci} do not result in reducing the rock strength. Therefore these random stable axial cracks are not considered damaging to the rock strength in laboratory tests.

Brace and Byerlee [12] investigated the onset of cracking and found that it varied between 30 to 60% of the peak strength (σ_f) for various low porosity rock such as aplite, basalt, diabase, granite, marble, quartzite, quartz monzonite and soapstone. They noted that this range was also found in concretes.

A sample of Lac du Bonnet granite was loaded in uniaxial compression and monitored for cracking using acoustic emission techniques [50]. The results are given in Figure 4.3 and illustrate a monotonic increase in acoustic emission (crack growth) during Region III of the stress–strain curves. Note also the relatively flat portion of the acoustic emission curve in the elastic Region II. These findings are similar to those of Scholz [142] and Mogi [114], who noted that in Region III the noise associated with microcracking occurs randomly throughout the sample as independent events.

4.1.1.1   Types of Cracking

One of the issues which has received considerable study is the type of cracking which occurs during this stage of stable crack growth. Unlike unstable crack growth, discussed in the next section, cracks associated with stable crack growth are very difficult to detect visually. The difficulty arises from the fact that brittle solids such as rock contain numerous flaws. These flaws include grain boundaries, holes along the grain boundaries, stiff grains such as quartz adjacent to softer grains such as biotite, cleavage planes within the grains and partially healed tectonically-formed microcracks. The various types of cracks reported are summarized in Figure 4.4 [150, 90, 91, 52]. The so called "Griffith crack" is an inclined flat ellipse with wing cracks developing near the ends of the ellipse in the areas of high tangential tensile stress (Figure 4.4). Unfortunately the "Griffith" crack is seldom observed
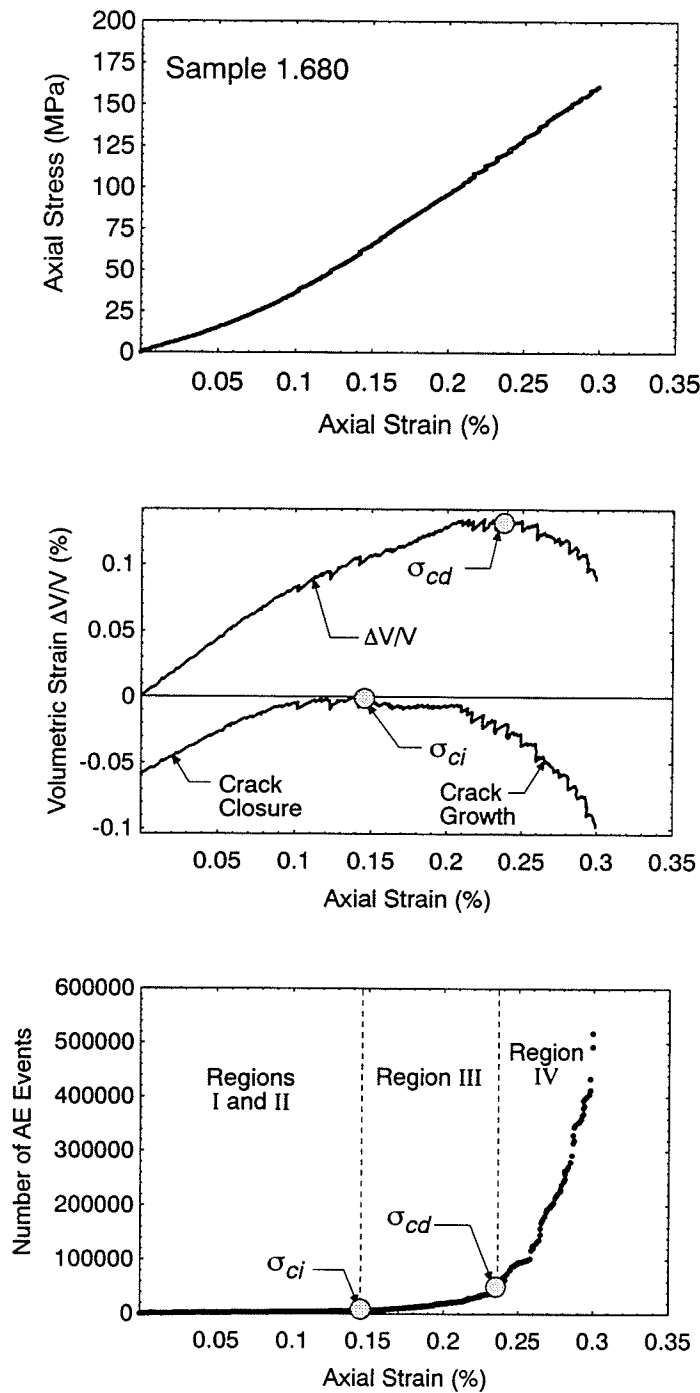
Figure 4.3: The number of microseismic events recorded during the uniaxial compression testing of a sample of Lac du Bonnet granite from the 240 Level of the URL compared to the volumetric strain and crack volume. Note the increase in the number of events at the crack initiation stress (see Figure 4.1 for definitions).
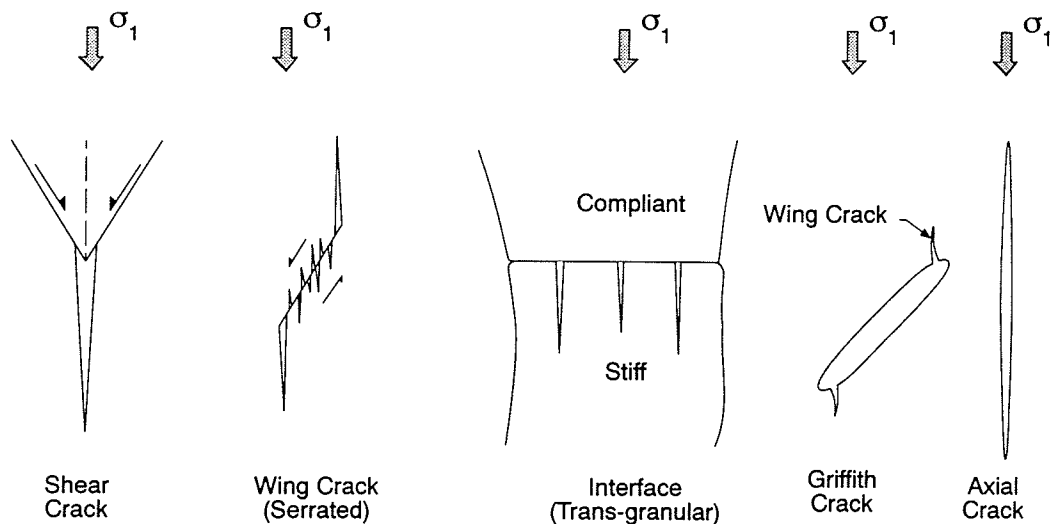
Figure 4.4: Illustration of the types of cracks observed, during compression tests, by various researchers [150, 90, 91, 52].

in rock samples.

Tapponnier and Brace [150] used a scanning electron microscope (SEM) with a resolution of about 0.1 μm to investigate cracks in thin sections obtained from samples of Westerly granite subjected to various loads. Tapponnier and Brace were unable to report, with any confidence, any difference in crack population between three samples taken at 37, 56 and 84% of the failure load. Foneska et al. [52], using SEM and acoustic emission measurements on granodiorite, dolerite and marble, concluded that above 50% of the failure stress small grain boundary and serrated cracks begin to appear, having dimensions of a few μm in length and widths of $\approx$ 0.1 μm. Bombolakis [10] loaded a prismatic sample of a very coarse pegmatite. He noted that crack growth began at between 50 and 66% of the peak strength and that the first cracks to grow were the existing axially-oriented cleavage cracks in feldspar. This observation is also in keeping with the findings of Lajtai [97], who noted that the feldspars in the Lac du Bonnet granite were the first to register cracking. It is also important to note that during stable crack growth, the axial cracks are contained within individual grains, i.e., there are no trans-granular axial cracks (see Figure 4.4).

4.1.2   Region IV: Crack Damage/Unstable Crack Growth

The axial stress level where the total volumetric strain reversal occurs marks the beginning of Region IV and represents the onset of unstable crack growth as defined by Bieniawski [8]. This onset generally occurs at axial stress levels between 70 to 85% of the peak strength. It is at this stress level that the axial strain versus axial stress relationship becomes non-linear and hence sliding must be initiating along flaws and grain boundaries (see Figure 4.1). This stress level has particular significance in the concrete industry as it is used to establish the long-term strength of concrete [133, 134, 45, 116]. Lajtai et al [97] found that the unstable crack stress for the Lac du Bonnet granite from the Cold Spring Quarry occurred at 0.71 of the peak strength. Schmidtke and Lajtai [140] also did extensive long-term compression testing of Lac du Bonnet granite from Cold Spring Quarry (see Chapter 3). Their results were reanalyzed by the author and have been replotted in Figure 4.5. Figure 4.5 clearly shows that for "long-term" loads above ≈ 0.70 of the short-term peak strength failure occurs almost immediately. Thus, the increase in load above the unstable crack stress is only a temporary strain hardening effect which cannot be relied on for even short-term strength. Hence, we will refer to this stress level as the crack damage stress (σ_{cd}) because loads above this stress level result in damage to the material which cannot be tolerated even under a constant load.

Hallbauer et al. [66] pointed out that this phase is characterized by the most significant structural changes to the sample, with the density of microcracks increasing by about sevenfold. Figure 4.3 supports these observations as the the amount of acoustic emission increases dramatically beyond σ_{cd}.

Bombalakis [10] notes that when the stress level reaches σ_{cd} there is an "abrupt development of finite frictional slip along inclined flaws and grain boundaries, beginning with the displacements of the order of the dimensions of grain-boundary asperities. Crack growth still occurs at various locations throughout the specimen at this stage but there is also a
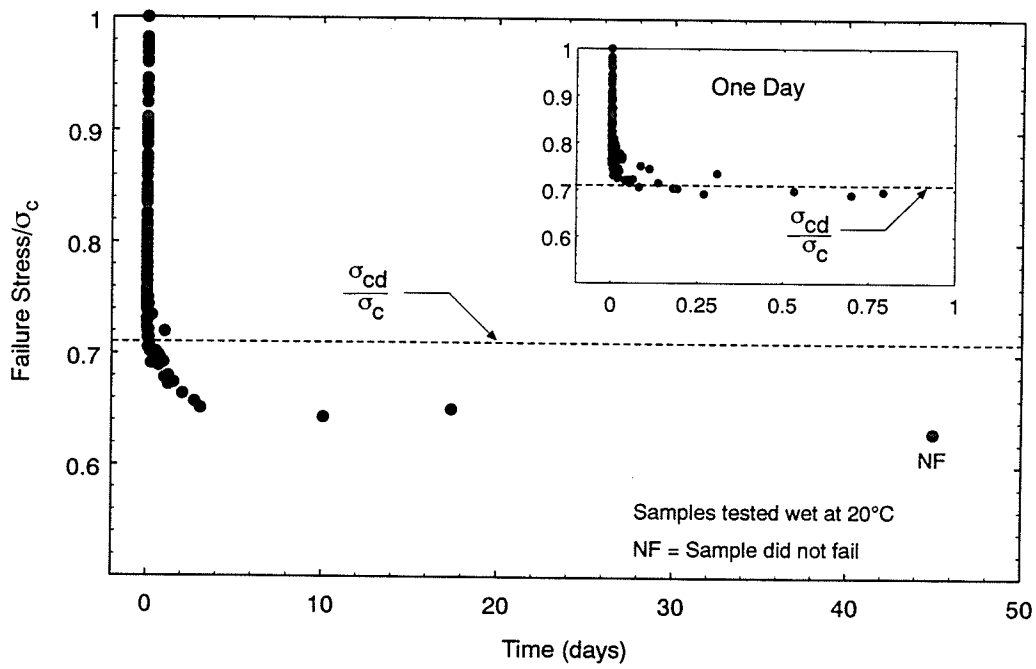
Figure 4.5: The compressive strength of Lac du Bonnet granite from Cold Spring Quarry subjected to different uniaxial loads. The failure stress has been normalized to the short-term unconfined compressive strength σ_c.
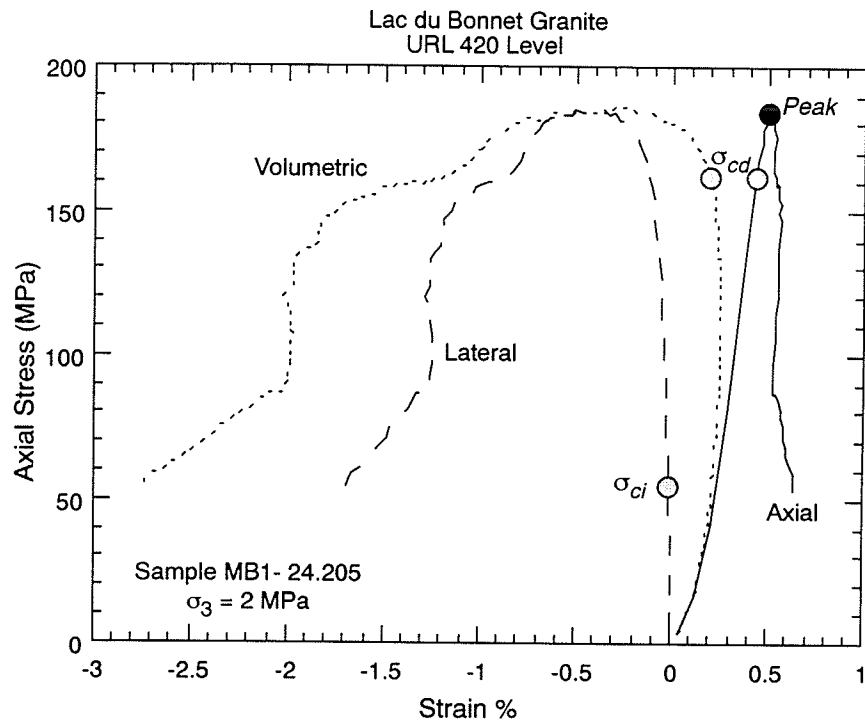
Figure 4.6: Typical post-peak stress-strain response of Lac du Bonnet granite.

detectable concentration of growth along potential shear zones."

4.1.3 Region V: Peak and Post-Peak Behaviour

The peak strength of the material (σ_f) marks the beginning of post-peak behaviour, Region V, and is almost universally used to establish the failure strength envelope. An example of the complete stress-strain curves for Lac du Bonnet granite is shown in Figure 4.6. Beyond the peak, the lateral and axial strain curves indicate continuing dilation. The axial stress versus axial strain that was only slightly affected by the initial microcracking process, shows a rapid decrease which is interrupted by one or more short strengthening interludes, marked by steps in the descending axial stress curve. Lockner et al [104] reported that during the first portion of the post-peak axial stress versus axial strain descent, the loci of the seismic events indicated the development of a major inclined shear fracture.

Table 4.1: Summary of step-loading experiments on ice (after [20]).

Loading Step	Stress (MPa)	% Max. Stress.	Comments
1	2.35	35	First inclined crack forms
2	3.92	59	Larger inclined cracks form
3	5.17	78	Small sail cracks form
4	5.48	83	Sails elongate while new inclined cracks are formed
5	5.8	88	
6	6.19	94	Two large sails interact retarding each other
7	6.35	97	Sails become wings
8	6.58	100	Wings reach ends and specimen splits

4.1.4 Fracture in Ice

Ice is a polycrystalline material which when loaded rapidly in compression, behaves in a brittle manner similar to rock. Shulson et al. [145], Cannon et al. [20] and Shulson [144], using high speed photography techniques, filmed the compressive failure process of ice. Their results showed that sliding occurs along grain boundaries at loads above 50% of the peak strength. Sliding along these grain boundaries eventually leads to the formation of axial cracks in the form of wing-cracks at loads above $\approx$ 80% of the peak strength. Shulson et al. [145] concluded that the frictional crack sliding-wing crack mechanism plays an important role in the brittle compressive failure of ice. Cannon et al. [20] carried out a step-loading experiment on $150 \times 150 \times 40$ mm samples of columnar ice with grains 6 to 12 mm long. Eight loading steps were applied to the sample causing initiation and propagation of cracks. The tests were terminated when the propagating cracks reached the sample ends. The results are summarized in Table 4.1 and indicate the initial step in the failure process is sliding along grain boundaries, with the wing or axial cracks developing much later in the failure process.

4.1.5 Summary of Observations in Compressive Failure

The failure process in rock subjected to compression loading commences with the growth of stable axial cracks (Region III). These axial cracks grow in numbers until the loads are high enough that sliding can initiate. Sliding begins at the crack damage stress and marks the end of Region III and the beginning of Region IV. As the loads are increased above the crack damage stress through-going axial cracks are generally formed (Figure 4.7). Beyond the peak strength of the sample the material can no longer carry the peak loads and so the axial stress decreases rapidly. It is in this Region (V) that the sliding which initiated at the crack damage stress manifests into a through-going shear zone. A summary of the various Regions during the compressive failure process of laboratory samples is given in Table 4.2. In the remainder of this chapter we will explore more evidence to support these observations and look in detail at the failure process when sliding commences.

4.2 Fracture Parameters in Compression

In the previous section three characteristic stress levels were identified in the laboratory stress/strain curves (see Figure 4.1): the crack initiation stress (σ_{ci}) caused by stable tensile cracking, the crack damage stress (σ_{cd}) caused by crack sliding, and the peak strength (σ_f). In order to understand material behaviour it is important to establish which of these stress levels are true material parameters and which are a function of the particular loading conditions used in the uniaxial test. Hudson et al. [78] concluded that the peak strength of a sample was a function of the boundary conditions of the test and hence not an inherent material property.

Glucklich and Cohen [57, 58] used stored strain energy to explain peak strength scale effects, which are commonly observed. They point out that during the stage of stable crack growth there is equilibrium between the external load and the crack length. This was also confirmed by Hoek and Bieniawski [74]. Both the loads and the stable crack lengths increase up to the critical moment at which the strain-energy release rate equals
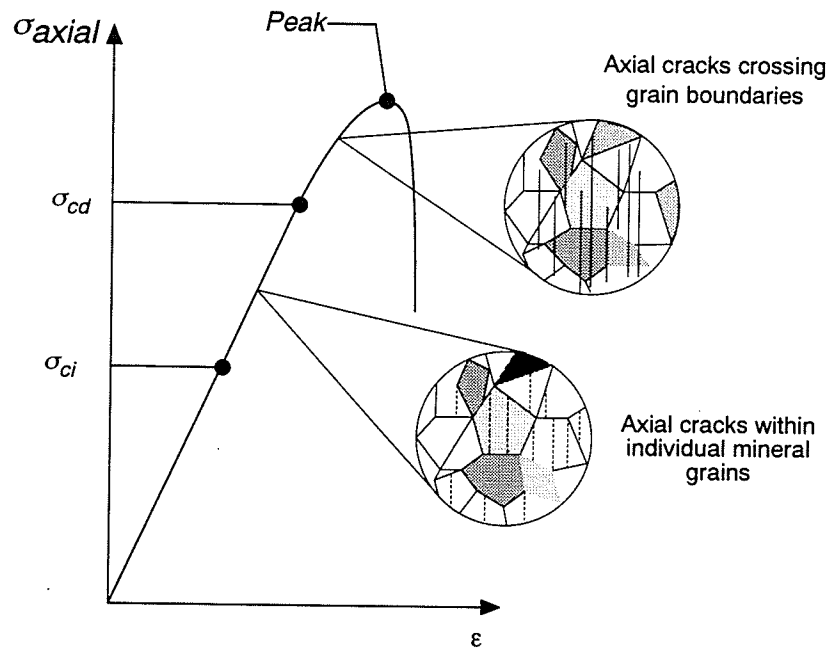
Figure 4.7: Illustration of when various stages of axial cracks are noted during compressive loading. Note that the axial cracks that cross grain boundaries are not observed until the load is very near the failure load.

Table 4.2: General relations between crack growth observations and measured strains during loading of laboratory samples in compression.

Region	ϵ_{axial}	$\epsilon_{lateral}$	$\epsilon_{volumetric}$	Comments
Crack Closure				
I	Nonlinear	Linear	Compression	Closure of microcracks in the sample.
Linear Elastic (No crack growth)				
II	Linear	Linear	Compression	Linear elastic range.
Stable Crack Growth $\approx 40\% \sigma_f$				
III	Linear	Nonlinear	Compression	Crack initiation occurs. Cracking occurs mainly along cleavage planes in individual minerals and from voids in the grains and along grain boundaries. All crack growth during this region is occuring parallel to the applied load because only the lateral strain shows nonlinear behaviour. SEM studies at this loading stress have not found axial crack growth greater than the grain size. Random acoustic emission events occur throughout the sample.
Unstable Crack Growth $\approx 80\% \sigma_f$				
IV	Nonlinear	Nonlinear	Dilation	This region marks the beginning of permanent crack damage and sample dilatancy. The dilatancy occurs with the development of cracks parallel to the applied load and the growth of inclined cracks (grain boundaries) because both axial and lateral strains are nonlinear. A rapid increase in acoustic emission events occurs.
Post Failure				
V	Nonlinear	Nonlinear	Dilation	Development of macrocracks which leads to collapse of the sample.

or exceeds that of energy absorption. At this moment crack propagation becomes unstable and the material reaches its peak strength. For heterogeneous materials such as rock the propagating failure crack will most likely encounter material which is stronger or weaker (an area of pre-existing stable cracks) than the mean strength. In either case, after the propagating crack advances through the softened or hardened material there is an excess of energy released which is converted to kinetic energy and is available to do work against the remaining uncracked material. It is here that the volume of the sample and the stiffness of the testing machine play a critical role because the stored energy in the total system dictates the energy release rate. In essence, Glucklich and Cohen are pointing out that a properly conducted compressive strength test would balance the stored strain energy in the sample and loading frame with the fracture surface energy required for fracture growth, i.e., there would be no kinetic energy available to propagate the crack. In reality this is very difficult to do because in compression testing two modes of cracking are developing simultaneously, the axial crack and the sliding crack. One approach to this problem is to reduce the loading rate such that the fracture surface has time to grow and increase the sample volume to minimize the effect of heterogeneity on the fracture process. A similar approach is used to reduce strain hardening effects in more ductile materials [92].

The long-term test data of Schmidtke and Lajtai [140] (see Figure 4.5) also suggest that the peak load above the crack damage stress is only sustained by the rock for a short duration and cannot be relied on for the long term. This leaves only σ_{ci} and σ_{cd} as possible fracture parameters which should therefore be independent of sample volume.

To determine the effect of scale on σ_{cd} and σ_{ci}, the stress-strain curves for 53 samples with diameters ranging from 33 to 300 mm diameter, were analyzed by the author. The results are summarized in Figure 4.8 and the peak strength is shown for comparison. Both σ_{ci} and σ_{cd} appear to be unaffected by sample volume. Note that except for the largest sample diameter tested, the data suggest that the peak strength is trending towards the σ_{cd} strength, i.e., ≈ 0.7 of the peak strength. This result is in keeping with that of Hoek
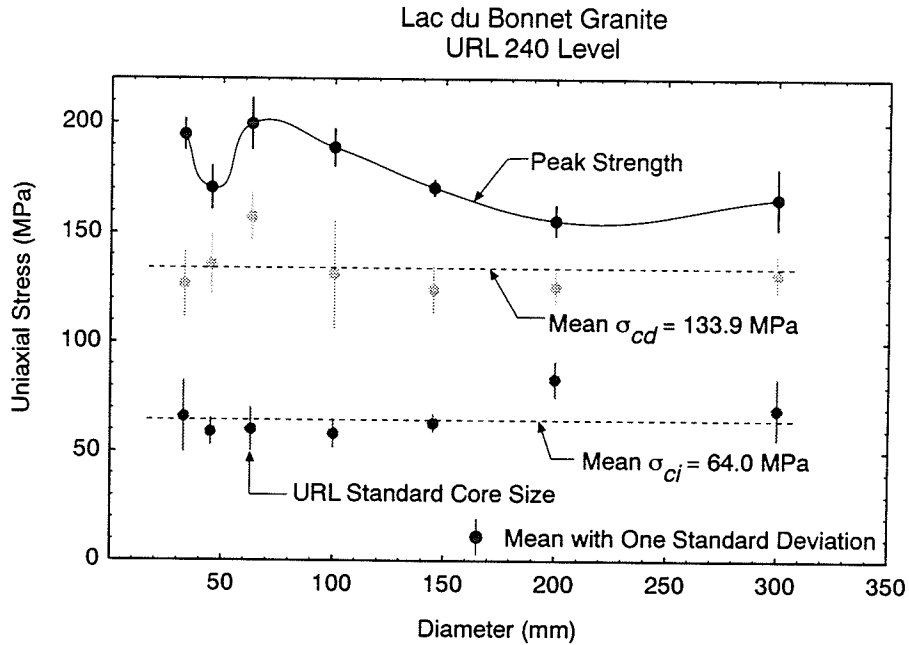
Figure 4.8: The effect of sample diameter on peak strength, crack damage stress and crack initiation stress.

and Brown [75] who showed the unconfined compressive strength reducing to ≈ 0.8 of the peak strength of a small sample, as the sample diameter increased from 10 to 200 mm (see Figure 3.8).

In an effort to minimize the potential influence of uncontrolled strain energy on the test results one final series of tests was carried out which attempted to combine the effects of scale and a slow loading rate. Four 200-mm diameter samples of Lac du Bonnet granite from the 240 Level of the URL were tested at the loading rate of 0.00075 MPa/s, which is 1000 times slower then the normal loading rate. In two samples failure occurred at the stress level generally associated with σ_{cd} and those samples did not display the normal volumetric strain reversal (Figure 4.9). Interestingly, the samples which were subjected to slow loading rates all developed characteristic shear planes rather than the axial splitting planes generally associated with standard unconfined testing (Figure 4.10). This also concurs with the previously mentioned notion that the failure mechanism for σ_{cd} is one of sliding. It would

appear that with the appropriate boundary conditions, i.e., loading rate, loading frame stiffness, and sample volume, the peak strength of a sample of Lac du Bonnet granite would be reduced to about 0.7-0.8 of the standard uniaxial strength (σ_c), similar to the failure loads of Schmidtke and Lajtai [140] from their static fatigue tests.

Having established that σ_{cd} is the true peak strength of the rock in a monotonically-loaded uniaxial compression test and that σ_{cd} and σ_{ci} are scale-independent parameters with completely different modes of origin, the next step was to determine the effect of the amount of crack damage in a specimen on these two parameters.

4.3 Damage–Controlled Testing

The growth of cracks during a single-stage monotonic loading test was described earlier. Much less is known about the cracking process in multiple-loading-unloading tests and practically nothing of crack growth in the post-peak region. The laboratory testing program described below was designed to fill this need. The tests were carried out by incrementing the amount of crack damage in the sample and then re-testing the sample to evaluate the effect of the increased damage on the stress level σ_{ci} and σ_{cd}. The incremented damage was accomplished by a series of load-unload cycles, with each load-unload cycle referred to as a damage increment.

The Lac du Bonnet granite used in this testing program is medium to coarse grained and composed of approximately 30% K-feldspar, 30% plagioclase, 30% quartz and 10% mafic minerals, mainly biotite. The average grain size of the medium grained granite is about 3 mm. The samples were obtained from the 420 Level of AECL's Underground Research Laboratory. Six post-peak uniaxial compression tests and thirty-one post-peak triaxial compression tests were conducted on the 63-mm-diameter grey samples.

The testing was carried out by CANMET, the Canada Centre for Mineral and Energy Technology [100]. Specimens were prepared in accordance with the methods suggested by the International Society for Rock Mechanics [19]. The end surfaces of each specimen were
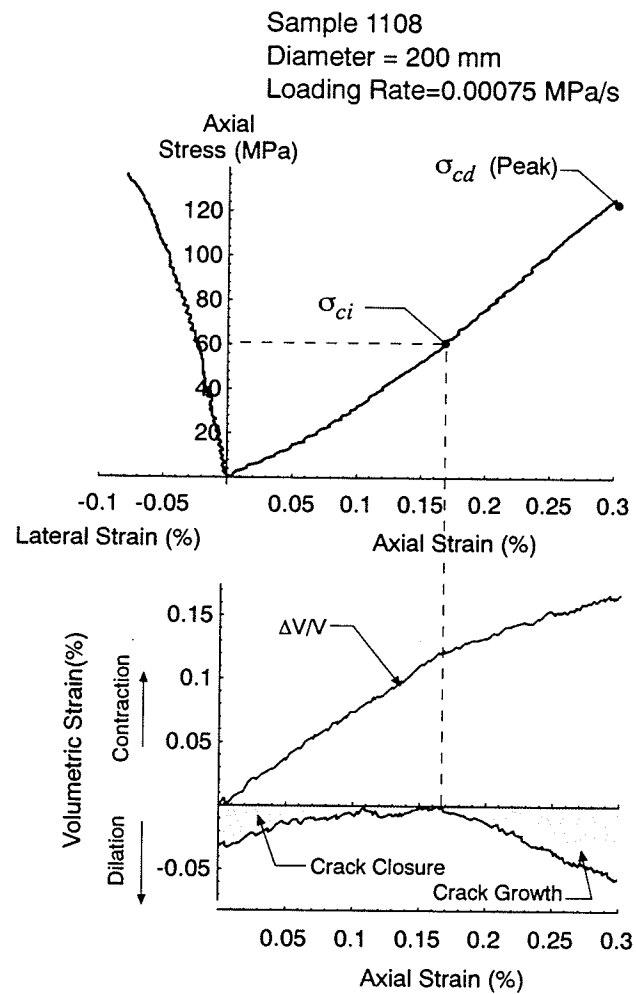
Figure 4.9: The combined effect of sample diameter and slow loading on peak strength, crack damage stress and crack initiation stress on a sample of Lac du Bonnet granite from the 240 Level of the URL. In this sample the crack damage stress is coincident with the peak strength.
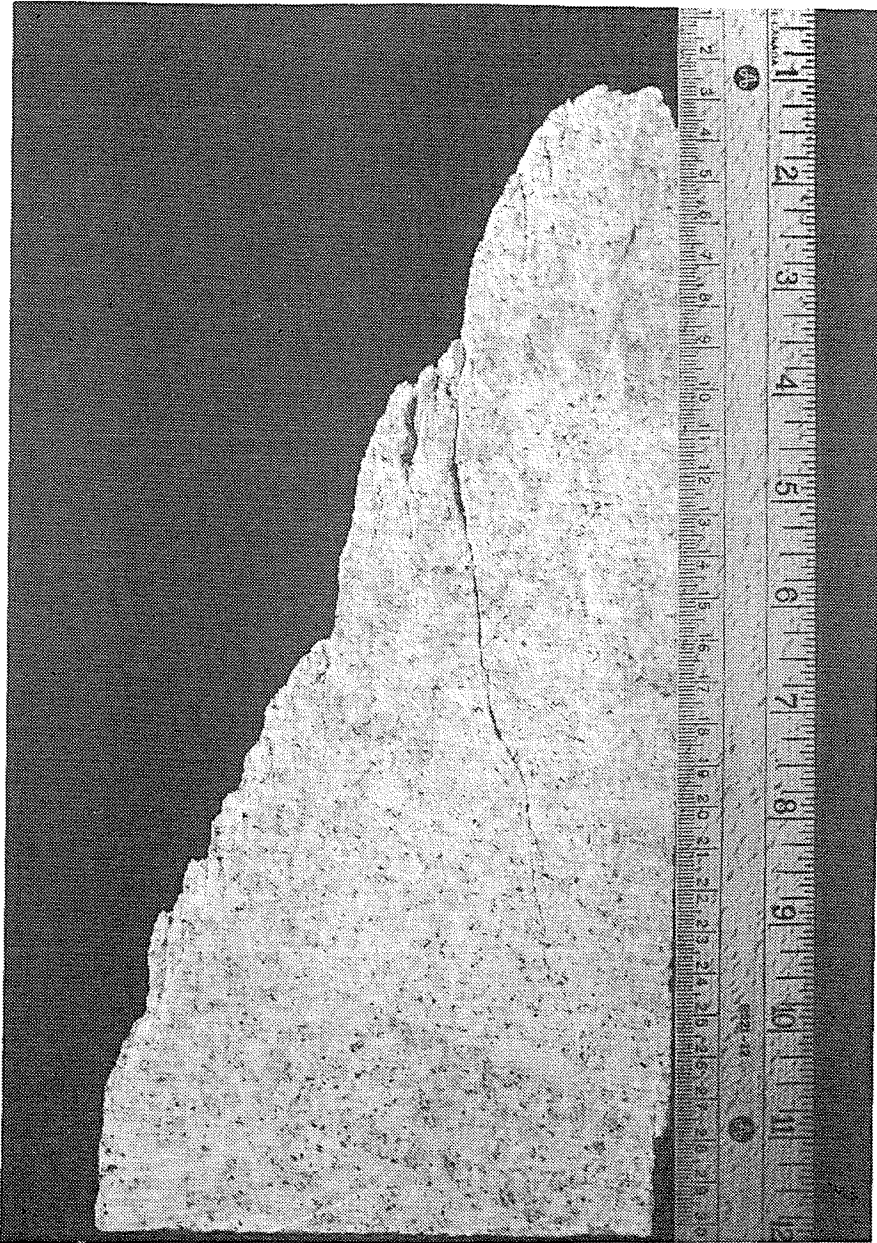
Figure 4.10: Photo of the failure surface developed in a sample of Lac du Bonnet from the 240 Level of the URL, subjected to 0.00075 MPa/s loading rate. The failure surface is inclined 23° with respect to the direction of loading. Note the short axial cracks that form adjacent to the failure surface.

ground flat to 0.025 mm to ensure that they were parallel to each other and perpendicular to the axis of the specimen. The post-failure tests were conducted using an MTS 815 Rock Test System, a computer-controlled, servo-hydraulic compression machine, consisting of a 2.22 MN rated load cell, load frame, hydraulic power supply, triaxial cell, confining pressure subsystem, test controller, test processor and DEC micro PDP 11/73 computer. The triaxial cell is equipped with three linear variable differential transducers (LVDT) for the measurement of axial strain and a circumferential extensometer to measure the lateral strain.

The confining pressure and the axial stress were initially increased simultaneously from zero to the required confining stress at the rate of 0.75 MPa/s. The axial stress was then increased using axial strain-rate control at a rate approximating a loading rate of 0.75 MPa/s. The instrumentation was scanned every 3 seconds. Load-unload cycles were carried out at 40 MPa increments up to approximately 75% of the peak strength. As the peak strength of the sample was approached special care was taken to prevent rapid failure in order to continue the test into the post-peak region. After reaching $\approx 75\%$ of the peak strength the load-unload cycles were performed at 0.063 mm increments of circumferential deformation using axial-strain control. A test took about eight hours to complete with a typical result shown in Figure 4.11. It should be noted that for the unconfined samples the load could not be completely removed during the unloading cycle. In the unconfined case the load was reduced to about 5 MPa or $\approx 2\%$ of the peak strength. For the confined samples this was not a problem as the samples were unloaded to the confining pressure.

An initial concern was whether the load-unload cycles influenced the overall stress-strain curve. Figure 4.12 compares the results from an unconfined damage-controlled test to a traditional uncycled unconfined post-peak test. Figure 4.12 illustrates that the general shape of the stress/strain plot is unaffected by the loading method. This was also found true for the confined tests. An important corollary of Figure 4.12 is that the same amount of damage accumulates if the axial stress is taken directly to a certain axial stress, σ_a,
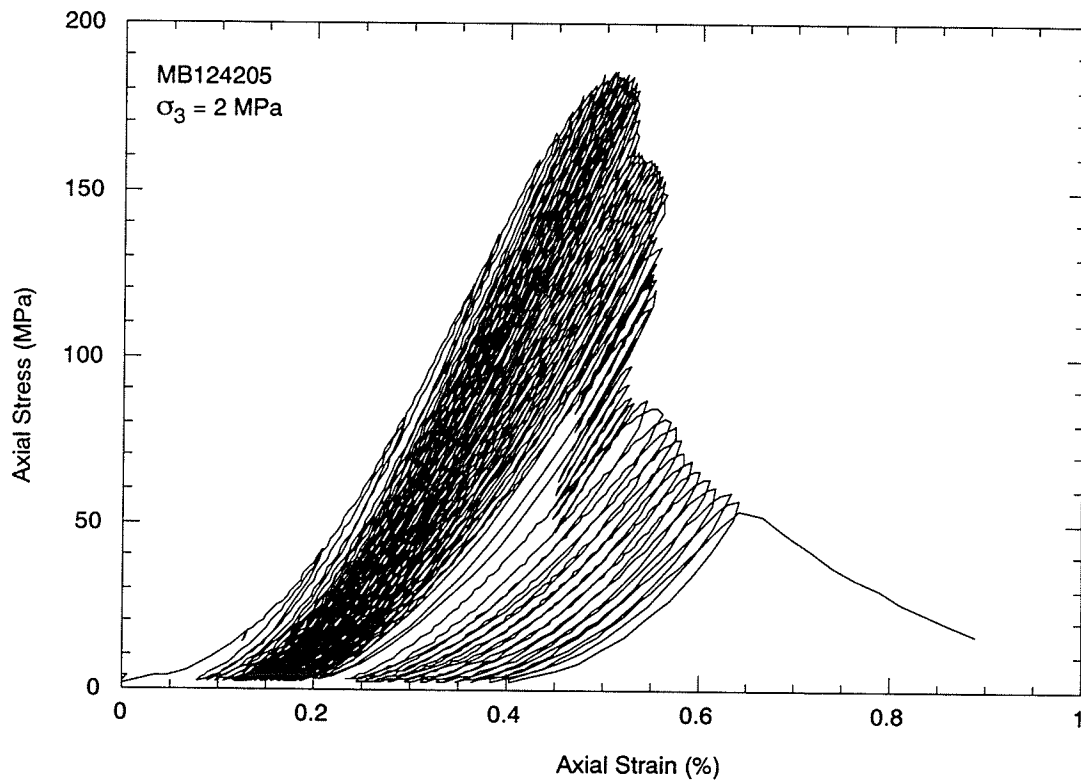
Figure 4.11: Example of the repeated loading and unloading used in a damage-controlled test
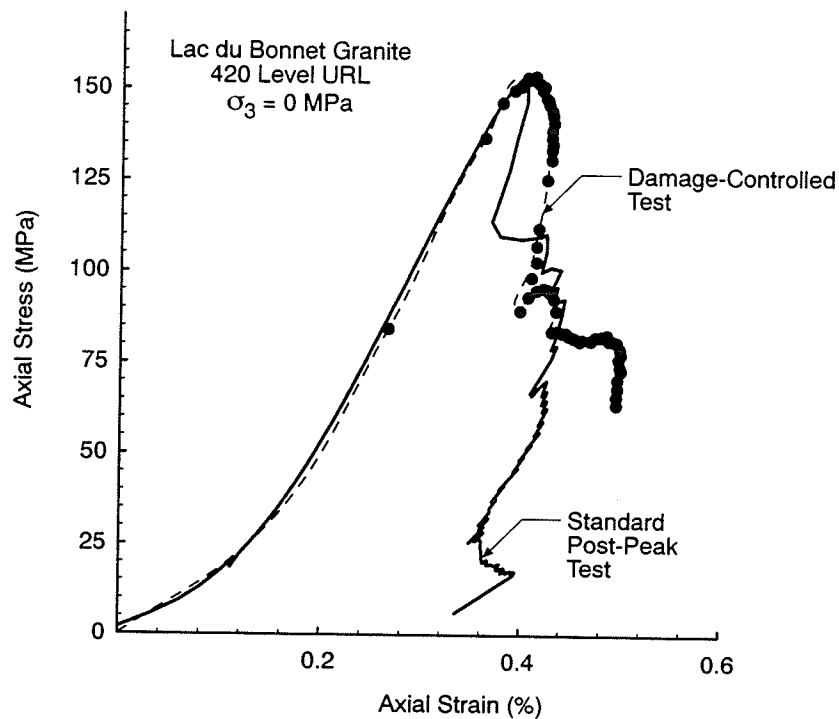
Figure 4.12: Comparison of the axial stress-axial strain curves of an unconfined damage-controlled test and a standard unconfined post-peak test. (Note: The load-unload cycles of the damage-controlled tests have been deleted.)

$(\sigma_a \geq \sigma_{cd})$ or by increasing the number of load-unload cycles. This is important in that the rock around the tunnel does not experience the multiple load-unload cycles used in the damage-controlled tests.

4.4 Test Results

The purpose of the testing was to determine the effect of damage on the stress levels associated with crack initiation and crack damage with each load-unload cycle. Damage can be measured by the permanent axial strain (ϵ_a^p) in a given load-unload cycle and a damage parameter (ω_a) can be defined as the cumulated permanent axial strain in any one test.

$$\omega_a = \sum_{i=1}^{n} (\epsilon_a^p)_i \%$$

(4.5)
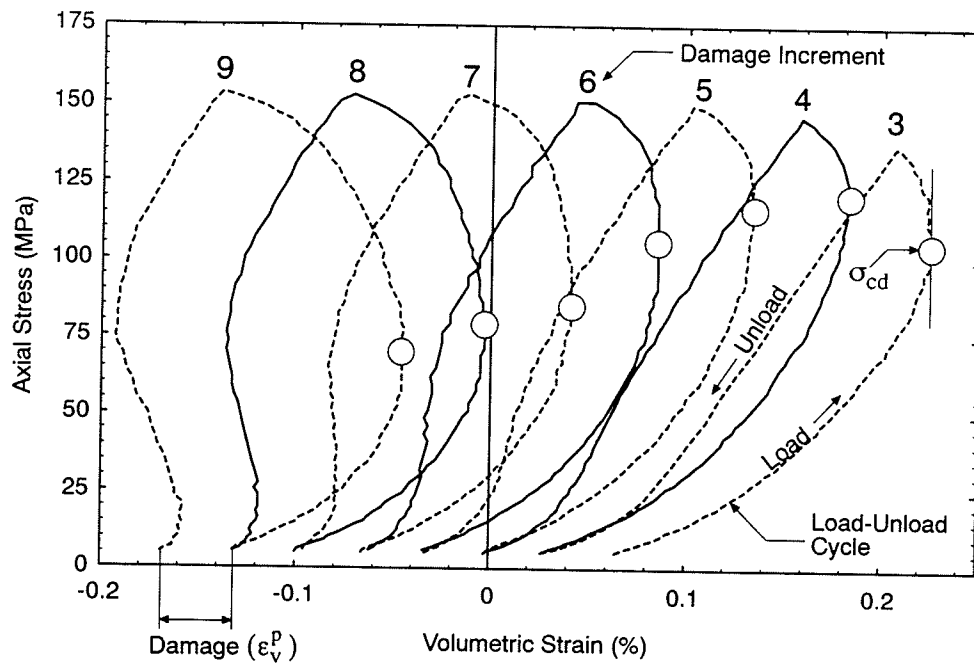
Figure 4.13: Damage is defined as the permanent volumetric strain resulting from a single damage increment.

The volumetric strain encompasses both the damage in the lateral and axial direction and can be related to crack initiation and crack damage stress (see Figure 4.1). In a given test, a damage increment (i), i.e., a load-unload cycle, will produce permanent volumetric damage (ϵ_v^p). A damage parameter (ω) is therefore also defined as the accumulated permanent volumetric strain in any one test (Figure 4.13)

$$\omega = \sum_{i=1}^{n} \left(\epsilon_v^p \right)_i \%$$ (4.6)

The volumetric damage definition is preferred to the axial damage definition because it is a volumetric rather than a one-dimensional measure and therefore records the total damage in the sample.

It is useful to plot the peak stress, σ_{cd} and σ_{ci} versus the damage parameter ω. The collection of these values of peak stress, σ_{cd} and σ_{ci} for any one test will be referred to as the peak(ω) locus, the σ_{cd} locus and the σ_{ci} locus.

4.4.1 Crack Initiation and Crack Damage

The crack initiation stress occurs when the load first exceeds about 0.2 to 0.4 of the peak strength. Initially, in the early stages of the test, the crack initiation stress appears to increase slightly, however, as damage accumulates the slope of the crack initiation locus appears to level off. One could speculate that the initial increase in the σ_{ci} locus is related to less critical cracks requiring more load to reach crack initiation. Given the difficulty in determining the σ_{ci} stress in the early stages of the test, it may be that the initial σ_{ci} slope is within the error of the analysis. Also, this phenomenon was not observed in all the test results. Thus it is reasonable to conclude that the crack initiation locus remains fairly constant with each damage increment and is therefore independent of the damage accumulated in the sample (Figure 4.15).

Figure 4.14 shows the crack initiation stress as a function of confining stress. It would appear that the crack initiation stress is only slightly dependent on the confining stress, as indicated by the linear best fit line shown in the figure. This is not too surprising if, as stated previously, the crack forming process is tensile.

The crack damage stress first occurs at about 0.8 of the peak strength during the first damage increment. However, unlike the crack initiation stress, the crack damage stress reduces significantly in the early stages of the test and reaches a threshold value as the damage accumulates in the sample (Figure 4.15). Plotting the test results against axial damage (ω_a) presents essentially the same picture (Figure 4.16). This phenomena is seen at all confining stress levels and is quite consistent from test to test (Figure 4.17). Similar observations [135, 143, 62] have been made during the cyclic testing of brittle rocks. It should be noted that the threshold value of σ_{cd} corresponds approximately to σ_{ci} when the sample is unconfined. As the confining stress is increased the threshold value of σ_{cd} becomes greater than σ_{ci} (Figure 4.18). Figures 4.19 and 4.20 are examples of the test results obtained for each of the confining stresses used in the damage-controlled tests.
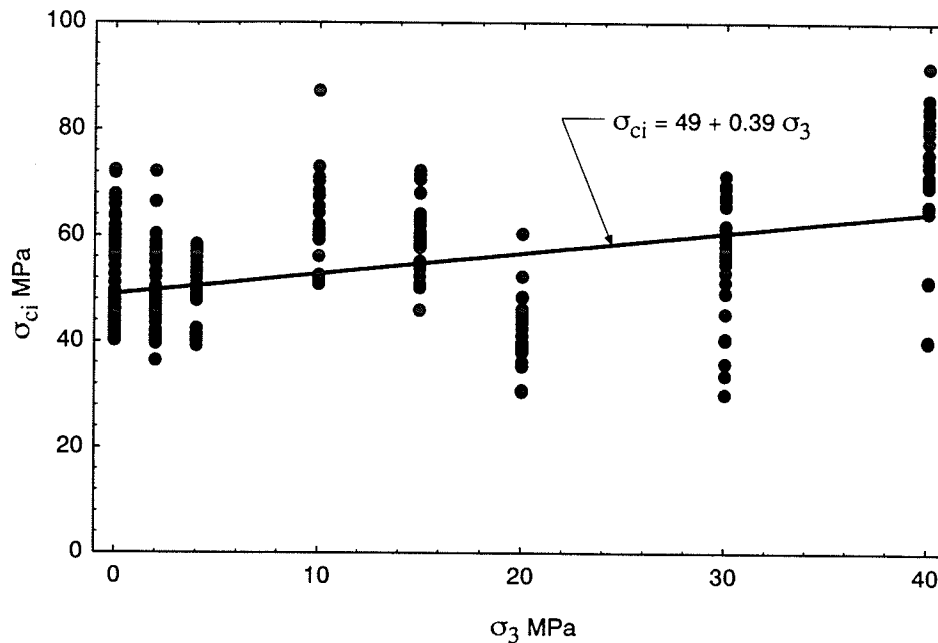
Figure 4.14: Crack initiation stress, σ_{ci}, as a function of confining stress, σ_3. The line through the data points is a linear best fit.

4.4.2 Deformation Constants

Young's modulus and Poisson's ratio can be determined for each damage increment. Each increment is treated as a separate test and the modulus and Poisson's ratio are computed for the part of the stress-strain curve that lies between the crack closure stress and the crack initiation stress. A plot of Young's modulus and Poisson's ratio versus damage is compared to the crack damage locus in Figure 4.21. As the sample is subjected to increasing damage, a gradual reduction in stiffness is indicated (Figure 4.21). In the post-peak region of the test in which the peak(ω) stress dropped from about 150 MPa to 56 MPa ($\approx$ 35% of maximum value), the modulus decreased from 50 to 24 GPa ($\approx$ 50% of maximum value). At a confining pressure greater than 20 MPa, the reduction in the modulus in the post-peak regime was considerably less. In all cases, the strength reduced faster than the modulus.

In the early portion of testing, i.e., before σ_{cd} is reached, Poisson's ratio is about 0.14 and increases to about 0.2 at the maximum σ_{cd} (Figure 4.21). As the peak(ω) stress level
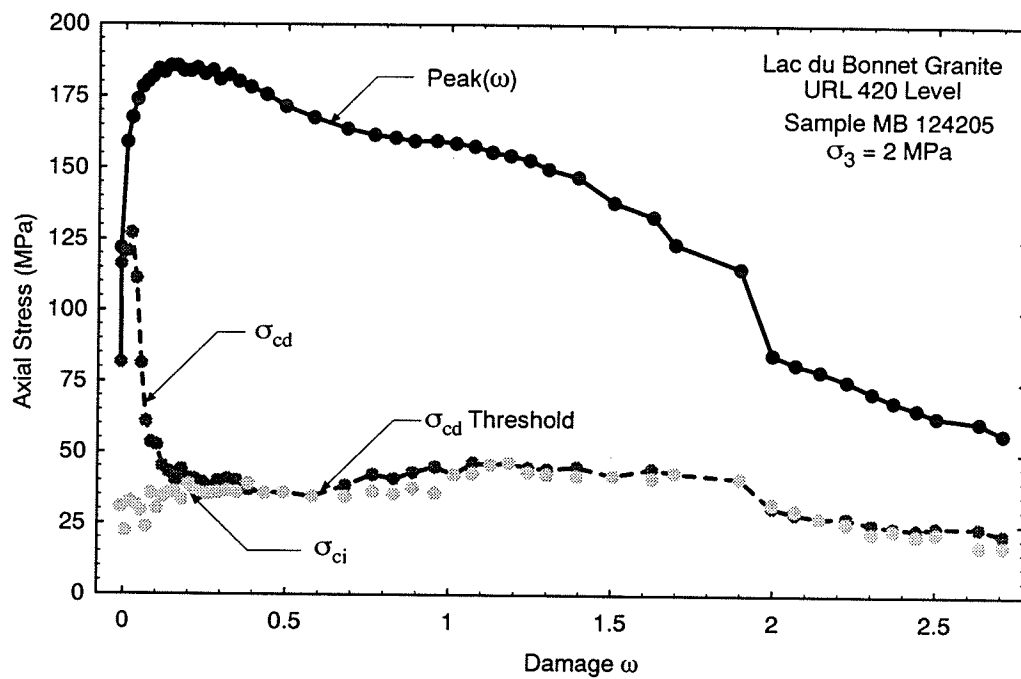
Figure 4.15: Example of the crack initiation stress and the crack damage stress as a function of damage. Note that at low confining stresses the crack damage stress is essentially the same magnitude as the crack initiation stress.
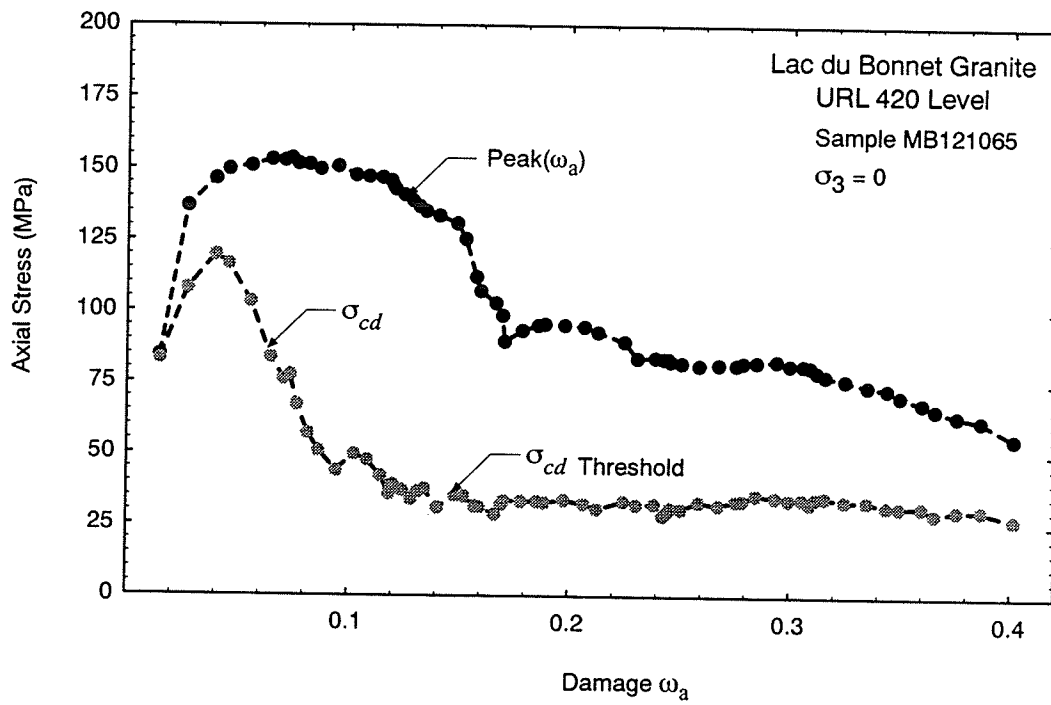
Figure 4.16: Crack damage stress as a function of axial damage. Note the same general trends as in Figure 4.15.
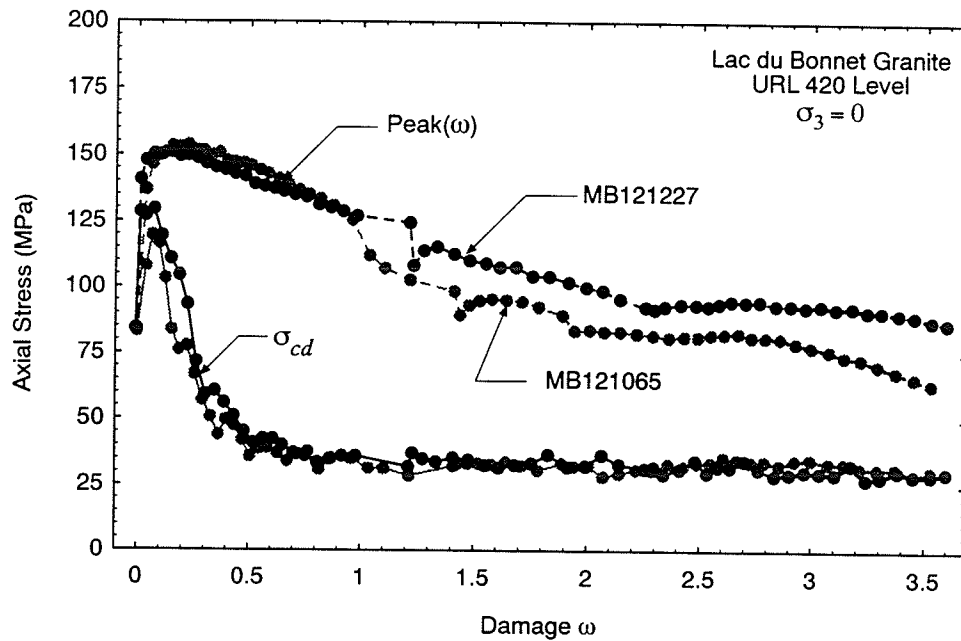
Figure 4.17: Crack damage stress and the peak stress as a function of damage for two unconfined samples. Note the repeatability between tests.

exceeds the initial σ_{cd} and starts its descent to the post-peak strength, Poisson's ratio increases quite sharply to ≈ 0.9. It is obvious that above 0.5 this ratio is only relating lateral strains to axial strains and is not an elastic constant. As the σ_{cd} threshold is reached and after the initial large drop in the post-peak strength the ratio remains relatively high ranging from 0.6 to 0.9. The locus of Poisson's ratio clearly reveals two phases of crack growth. The first phase occurs in the pre-peak strength portion of the test when Poisson's ratio increases quite rapidly indicating significant axial crack growth. The second phase occurs in the post-peak strength region where the first significant strength drop occurs. This phase is more indicative of sliding than axial cracking. The second phase occurs at the same stage as shear fracture development as identified by Lockner et al [104].
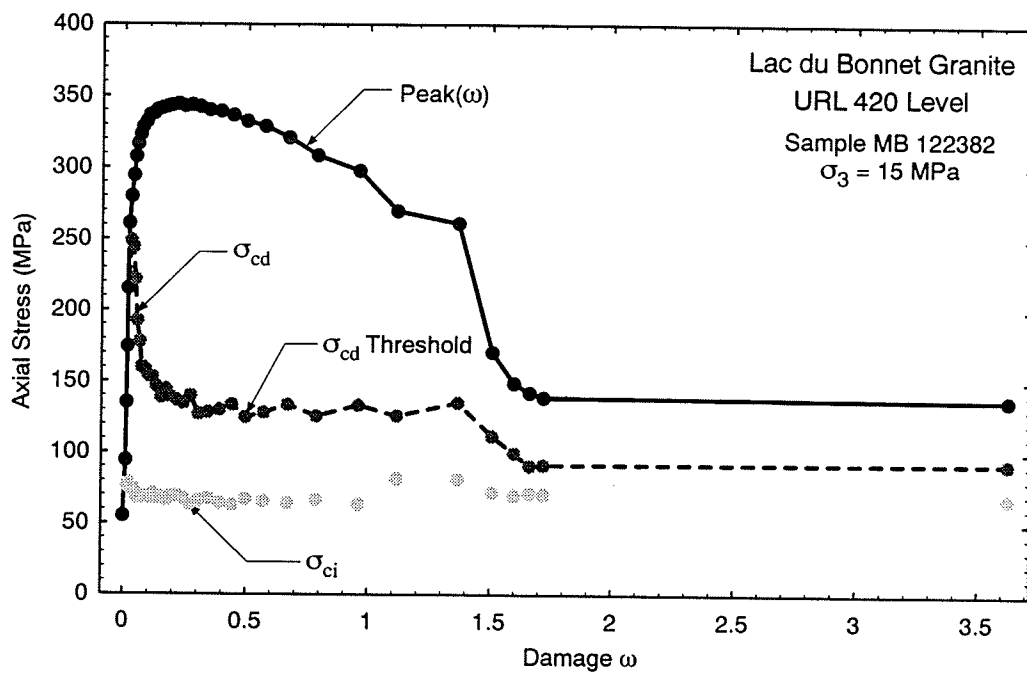
Figure 4.18: Crack initiation stress and the crack damage stress as a function of damage for a confined sample. Note that at higher confining stresses the crack damage stress is considerably higher than the crack initiation stress. The large damage increment towards the end of the test indicates the difficulty in controlling the test at this stage of failure.
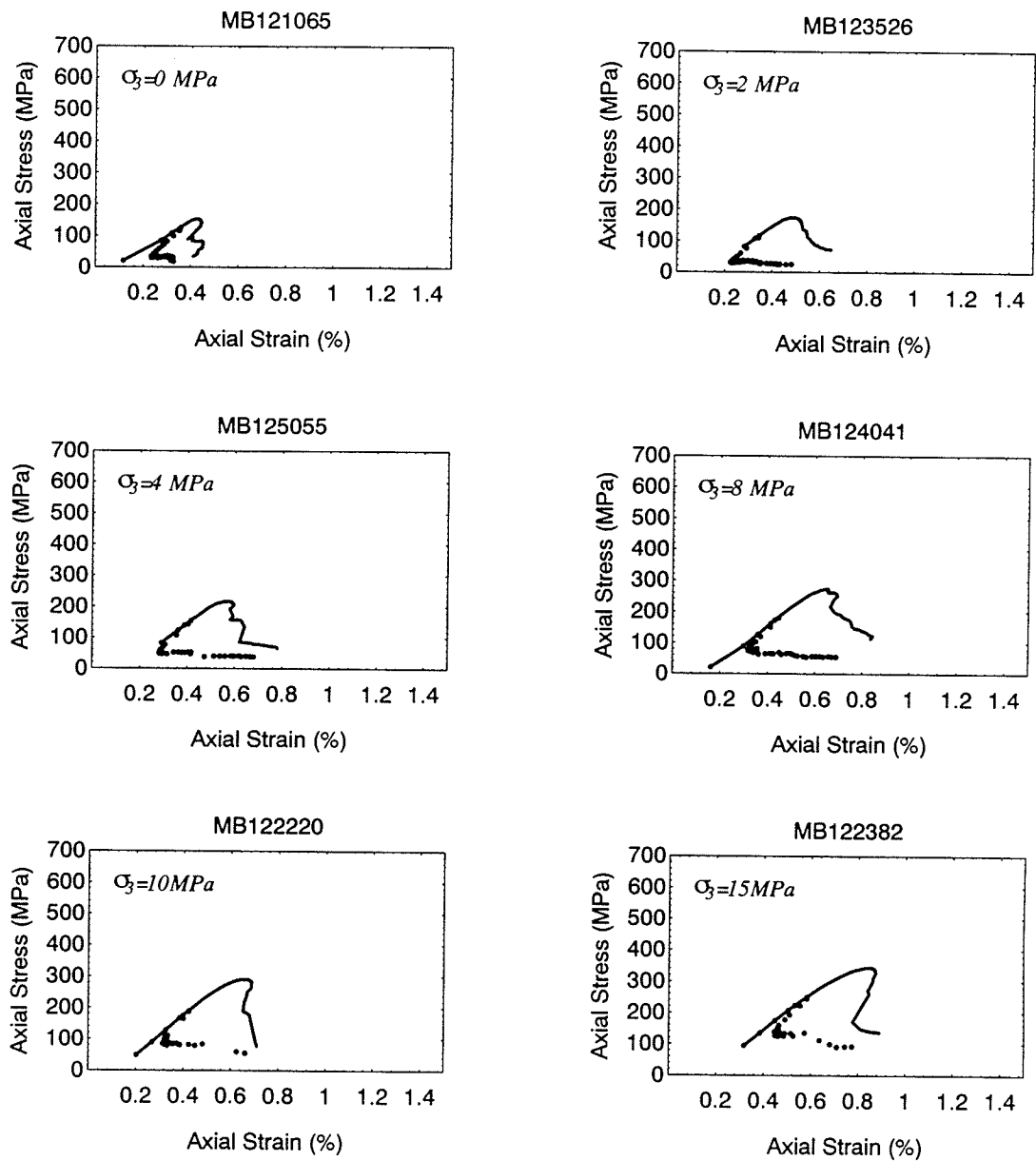
Figure 4.19: Summary of peak strength and crack damage loci for samples of Lac du Bonnet granite from the 420 level of the URL tested at confining stresses ranging from 0 to 15 MPa.
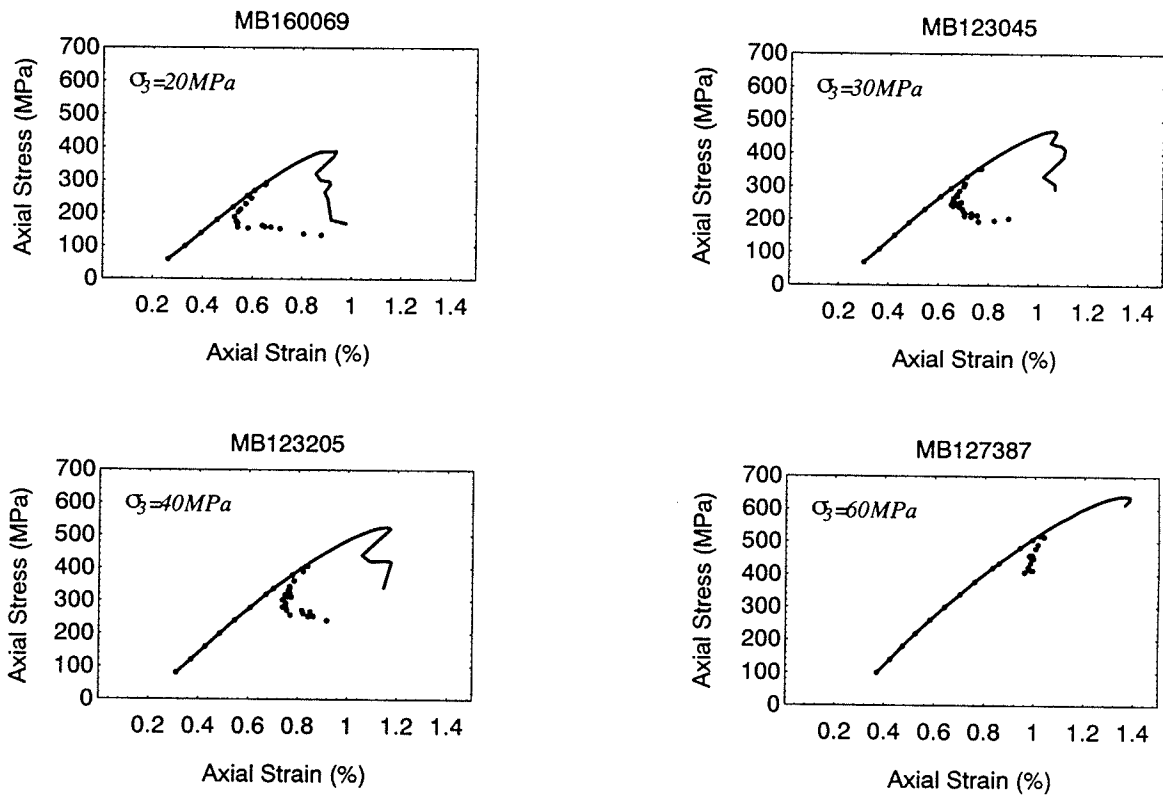
Figure 4.20: Summary of peak strength and crack damage loci for samples of Lac du Bonnet granite from the 420 level of the URL tested at confining stresses ranging from 20 to 60 MPa.
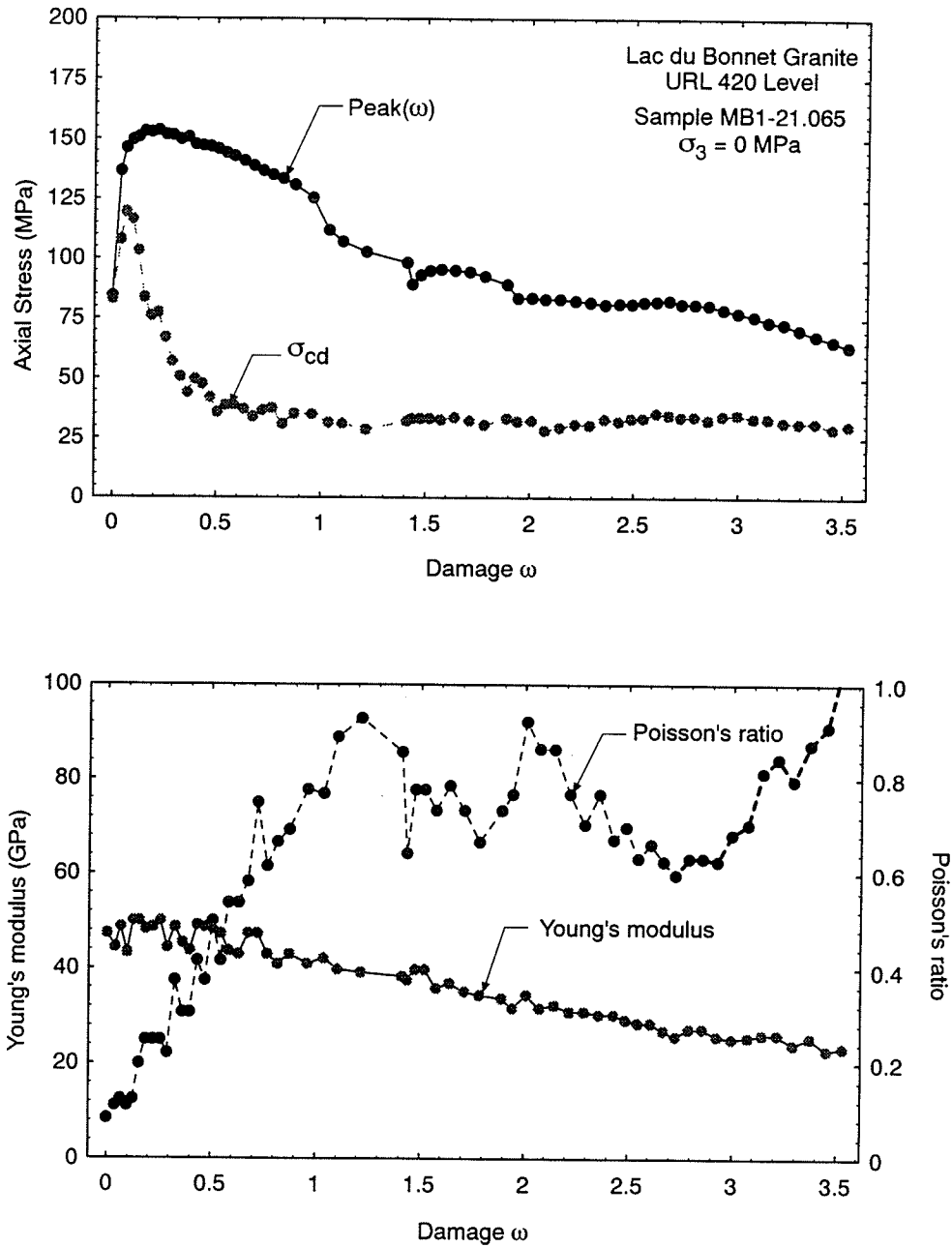
Figure 4.21: Young's modulus and Poisson's ratio as a function of damage for an unconfined test (lower figure). The upper figure shows loci for σ_{cd} and Peak(ω) strength for the same sample.

4.5 Crack Damage Locus

The theoretical locus of crack growth for brittle materials has been evaluated by Berry [6, 7], for tensile crack extension, and by Cook [32] for crack sliding. Cook [32] refers to this limit for crack growth as the Griffith locus and it follows the general form ABCD given in Figure 4.22. According to Berry, the Griffith locus can be interpreted in the following way. The portion AB, during the early stages of crack extension, indicates a rapid loss in strength with no increase in axial strain. Unless the strain energy released from the elastically strained regions around the propagating crack is removed from the system, the excess energy will be converted to kinetic energy. It is generally not possible to follow the unloading path AB because most systems, e.g., an underground opening, have a finite unloading stiffness, represented by AC in Figure 4.22. Thus a crack starting at σ_A will propagate dynamically[1]. Berry [6] noted that the excess strain energy represented by the shaded area ABC will cause the crack growth to accelerate. Hence it will continue to extend even as the stress drops below σ_C corresponding to point C on the failure locus. Below σ_C the crack will finally stabilize when the excess strain energy ABC is equal to the strain energy CDE. The area ABC=CDE and hence the energy CDE is the surface energy required to create longer cracks. The material containing the longer crack is now represented by OD with a reduced modulus E_{c+dc}. These cracks are now loaded to a subcritical stress level σ_E and hence will not propagate until the stress level is increased to σ_D. Thus the Griffith locus has two key elements; the stiffness of the initial material which controls the position of OA, and the crack properties which controls the shape and position of BCD (see Figure 4.22).

Thus far the crack damage locus has been plotted versus the damage parameter ω which is defined by the volumetric strain. Although σ_{cd} is defined by the volumetric strain reversal it also corresponds to the onset of non-linearity in the axial stress versus axial strain plot,

---

[1]In a servo-controlled laboratory test the energy which causes the dynamic propagation is controlled. Hence it is possible to follow this stage of crack growth.
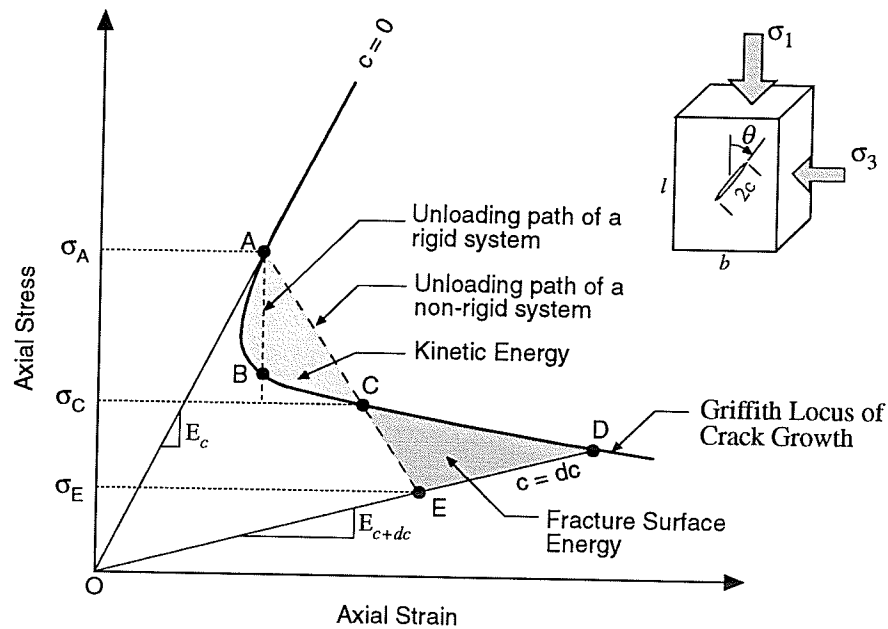
Figure 4.22: Illustration of the Griffith locus.

as shown in Figure 4.1. Earlier it was suggested that this nonlinear response is a direct result of sliding along crack surfaces angled with respect to the direction of the maximum load. Thus it is instructive to replot the test results to see the relationship between the crack damage locus and the peak(ω) stress versus axial strain. Figure 4.23 shows a typical plot of the crack damage locus and peak(ω) stress locus versus axial strain. The volumetric strain versus axial strain is also shown to illustrate how the plot is generated. Note that the reduction of σ_{cd} to its threshold level occurs by damage increment 10, i.e., before the peak strength of the sample is reached. This was not evident in the previous plots. The shape of the damage locus on an axial stress versus axial strain plot is similar for all confining stresses.

It has been suggested that the crack damage stress is defined by sliding because the axial strain registers permanent damage. This would imply that the crack damage locus is the locus of axial stress required to initiate crack sliding or simply the Griffith locus as defined by Cook [32]. The underlying assumption used in the Griffith locus of Cook,
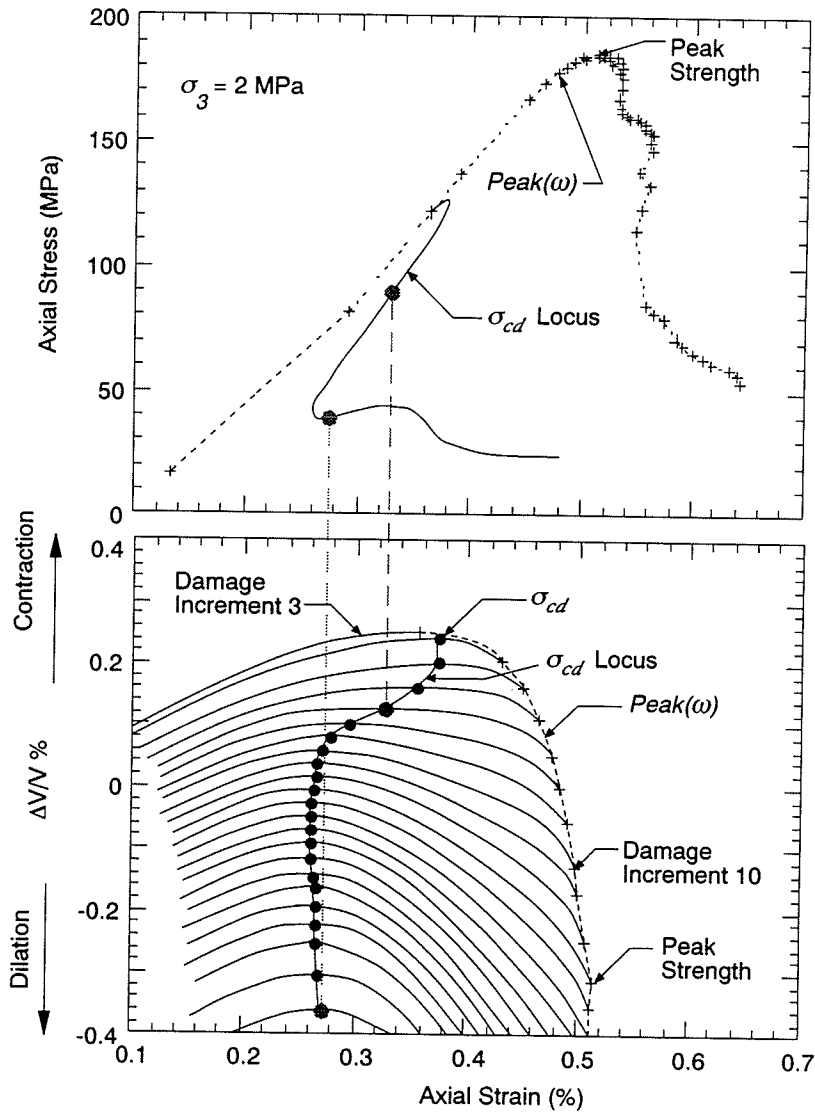
Figure 4.23: Crack damage locus and peak strength versus axial strain. The volumetric strain for each damage increment is also shown. Note that the major drop in the crack damage locus occurs before the peak strength is reached.

was first proposed by Starr [147] in 1928. Starr showed that sliding of a frictionless crack, subjected to a shear displacement, occurred when

$$\tau_o = \sqrt{\frac{8\alpha G}{\pi(1 - \nu)c}} \tag{4.7}$$

where ν is the Poisson's Ratio, G is the modulus of rigidity, τ_o is the shear stress in the direction of crack slip, c is the crack half length, and α is the fracture surface energy. Cook [32] modified equation 4.7 to take account of friction along the crack in compressive shearing, replacing τ_o by $\tau - \mu\sigma_n$, where τ is the shear stress in the direction of the crack slip, μ is the friction across crack faces, and σ_n is the normal stress acting on the surface of the crack. Only a brief summary of Cook's original work follows and the interested reader is referred to Cook's paper for the derivation of the formulas (a complete derivation of the Griffith locus is given in Appendix B). For the confined case consider a single elliptical crack of length $2c$, inclined at some angle θ to the direction of the applied load σ_1, in a specimen where n represents the number of cracks per unit volume (see Figure 4.22). Using the approach of Cook the critical axial strain, ϵ_{cr}, at which sliding occurs, is given by

$$\epsilon_{cr} = \frac{\sigma_1 - 2\nu\sigma_3}{2G(1 + \nu)} + \frac{2}{bl(\sigma_1 - \sigma_3)}\left(W_s + \frac{W_f}{2}\right)n \tag{4.8}$$

where

$$
\begin{aligned}
W_s &= \frac{\pi}{4}(1 - \nu)\frac{(\tau^2 - \mu^2\sigma_n^2)}{G}c^2 \\
W_f &= \frac{\pi}{2}(1 - \nu)\mu\sigma_n\frac{(\tau - \mu\sigma_n)}{G}c^2 \\
c &= \frac{8\alpha G}{\pi(1 - \nu)(\tau - \mu\sigma_n)^2}
\end{aligned}
$$

For the conditions of triaxial compression and assuming the plane of the crack is parallel to the direction of the intermediate compressive stress:

$$
\begin{aligned}
\sigma_n &= \frac{\sigma_1 + \sigma_3}{2} - \frac{\sigma_1 - \sigma_3}{2}\cos 2\theta \\
\tau &= \frac{\sigma_1 - \sigma_3}{2}\sin 2\theta
\end{aligned}
\tag{4.9}
$$

where θ is the angle of the critical crack and the direction of the maximum applied load, σ_1.

Hence ϵ_{cr} in equation 4.8 can be obtained provided the crack density n and the fracture surface energy α are known. The other parameters are available from standard laboratory tests and the fracture surface energy can be equated to the strain energy release rate $\mathcal{G}$ by $\mathcal{G} = 2\alpha$. The strain energy release rate is one of the most important parameters with regard to fracture and is defined as the the amount of energy release per unit increase in crack surface area. Rice [130] proposed a method for determining $\mathcal{G}_c$, the strain energy release rate at failure, for shear faulting. Using Rice's approach Kemeny and Cook [88] calculated a $\mathcal{G}_c$ value of 1.05 J/m^2 for the creation of a single shear fault for Westerly granite. An alternative approach is to calculate the fracture surface energy [16] by

$$\alpha = (1 - \nu)\frac{K_{Ic}^2}{4G} \qquad (4.10)$$

where K_{Ic} is the fracture toughness for Mode I crack failure, i.e., tensile splitting. An alternative approach for calculating the fracture surface energy is described in Appendix C.

Although K_{Ic} is the fracture toughness for Mode I crack failure and the model describes Mode II crack slip, K_{Ic} has been measured for the Lac du Bonnet granite and provides a reasonable starting point in evaluating the model. To calibrate the model against the σ_{cd} locus for the crack density n, the σ_{cd} locus from an unconfined test was fitted to equation 4.8 to determine n. The other input parameters, for equation 4.8, were taken from laboratory test results. Those parameters were then used to predict the critical strain, ϵ_{cr} at confining stresses of 2, 15 and 30 MPa from equation 4.8, and the predicted values were compared to the measured crack damage locus at those confining stresses (Figure 4.24). It should be noted that the nonlinear strains which were measured in the initial "seating phase" of each test were simply taken as a constant value which was added to all the calculated results in order to compare the predictions with the measured strains. The parameters used in equation 4.8 are shown in Figure 4.24. It should be noted that in Figure 4.24 the
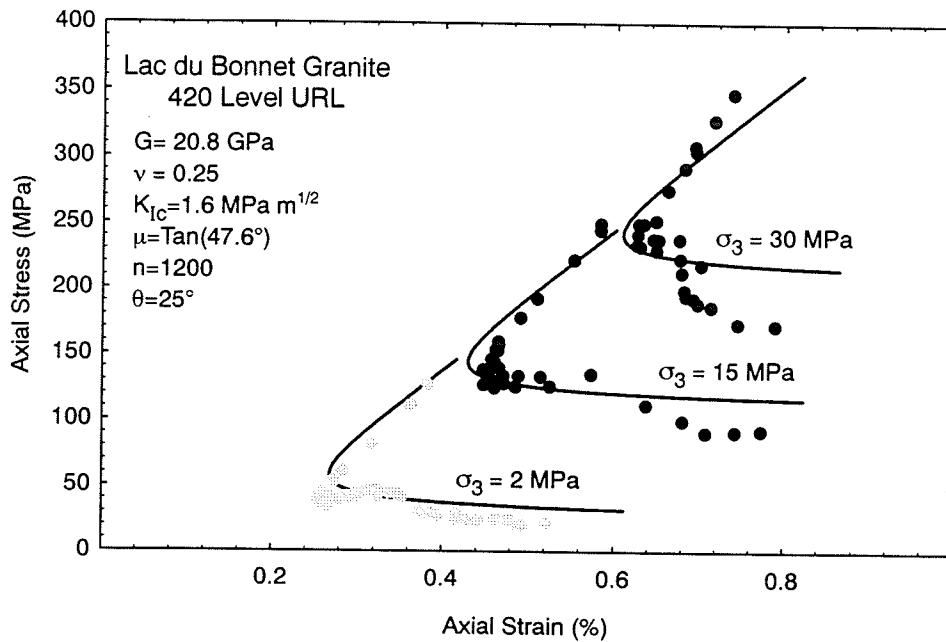
Figure 4.24: Comparison of the measured crack damage locus and the predicted Griffith locus at various confining stresses.

initial positive slope of the locus is somewhat less than that of the measured values at the higher confining stresses and the discrepancy increases with confining pressure. This occurs because no correction for the increasing stiffness (E) of the samples with confining stress was made. Because of the high density of microcracks in the samples, Young's modulus increases from about 50 GPa for the unconfined samples to about 60 GPa for the 30 MPa confining stress. Even without this correction the agreement between the measured and the predicted loci is quite good.

According to Cook, the critical condition for the initiation of crack slip occurs when stresses acting on the crack exceed the fracture surface energy (4α) which is given by

$$\frac{\pi}{2}(1-\nu)\frac{(\tau-\mu\sigma_n)^2}{G}c \geq 4\alpha \qquad (4.11)$$

Substituting equation 4.9 into equation 4.11 provides the strength of the specimen in a

general Mohr-Coulomb form:

$$\sigma_{1f} \geq \frac{\sqrt{\frac{8\alpha G}{c\pi(1-\nu)}}}{\sin\theta\cos\theta(1 - \mu\tan\theta)} + \sigma_3 \frac{(1 + \frac{\mu}{\tan\theta})}{1 - \mu\tan\theta} \quad (4.12)$$

Note that the critical angle of θ will be related to μ in order that $(\tau - \mu\sigma_n)$ in equation 4.11 is a maximum when

$$\theta_{cr} = \frac{1}{2}\tan^{-1}\frac{1}{\mu}. \quad (4.13)$$

Thus, equation 4.12 can be rewritten by substituting θ_{cr} from equation 4.13

$$\sigma_1 = \frac{\sqrt{\frac{8\alpha G}{c\pi(1-\nu)}}}{\sqrt{1 + \mu^2} - \mu} + \sigma_3 \left(\frac{\sqrt{1 + \mu^2} + \mu}{\sqrt{1 + \mu^2} - \mu}\right) \quad (4.14)$$

It was stated previously that the crack damage loci were similar in shape regardless of confining stress. Figure 4.25 shows typical examples of the crack damage locus for some of the tests at different confining stresses. Not all of the results are shown for reasons of clarity. Figure 4.26 shows the σ_{cd} threshold values as measured in all the tests plotted in σ_1–σ_3 space. The reason for plotting the σ_{cd} threshold value in Figure 4.26 is related to the theoretical basis of the Griffith locus. Earlier, it was noted that the initial rapid decrease in Griffith locus was essentially one of unstable crack propagation. The crack only became quasi-stable once it reaches the plateau or threshold portion of the Griffith locus. In the damage-controlled testing, the servo-control mechanism on the testing machine allowed us to follow the σ_{cd} locus even in the initial unstable portion. However, around an underground opening once the crack starts sliding, it is likely that it will propagate until the σ_{cd} threshold is reached. Also shown in Figure 4.26 is the initial crack damage stress for each test and a Hoek-Brown envelope is fitted to the data. Interestingly, at high confining stresses the initial crack damage stress approaches the crack damage threshold.

The condition for sliding, according to equation 4.12 is a linear relationship in σ_1–σ_3 space. The crack damage threshold values also follows a linear relationship in σ_1–σ_3 space (Figure 4.26) which gives a friction angle of 47.6°. This friction value is similar to residual friction angle of 45° reported by Gyenge et al. [61] and 42–43° reported by Lajtai and
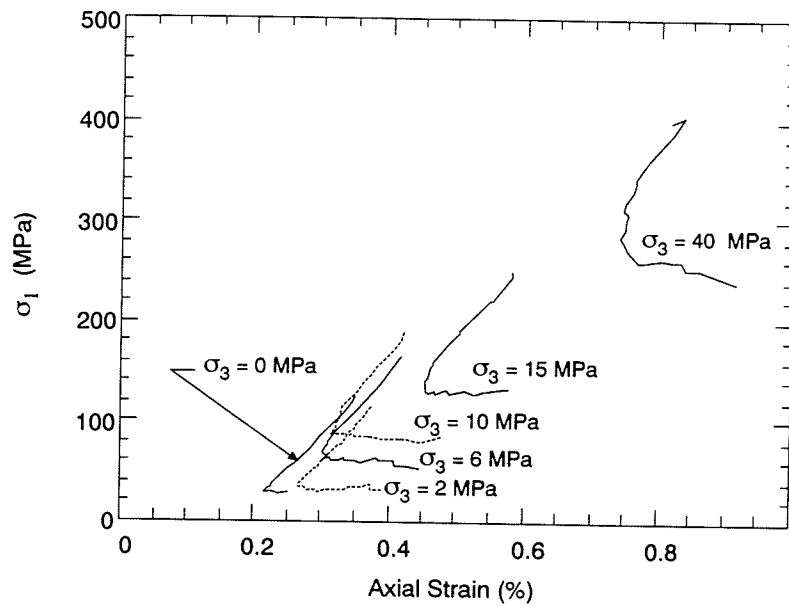
Figure 4.25: Crack damage locus at various confining stresses.

Gadi [98] for Lac du Bonnet granite (Figure 4.27). The peak strength, for each test, is also shown in Figure 4.26 and a Hoek-Brown failure envelope is fitted to the data.

4.5.1 Interpretation of Test Results and Griffith Locus

Coulomb (1796) [15] postulated that the shear strength of rock and of soil is made up of two components,– a constant cohesion and a normal stress-dependent frictional component. It is generally assumed that these components are mobilized at the same displacements such that both components can be relied on simultaneously in rock engineering design. The strength of intact rock is determined in the laboratory using triaxial tests and the cohesion and friction components are combined in the strength value obtained from any one test. The Griffith locus can be used to determine the relationship between cohesion and friction during the failure process.

The shear criterion given in equation 4.14 can be reduced to

$$\sigma_{1f} = 2\sqrt{\frac{2\alpha G}{c\pi(1-\nu)}} \tan\left(45 + \frac{\phi}{2}\right) + \sigma_3 \tan^2\left(45 + \frac{\phi}{2}\right) \tag{4.15}$$
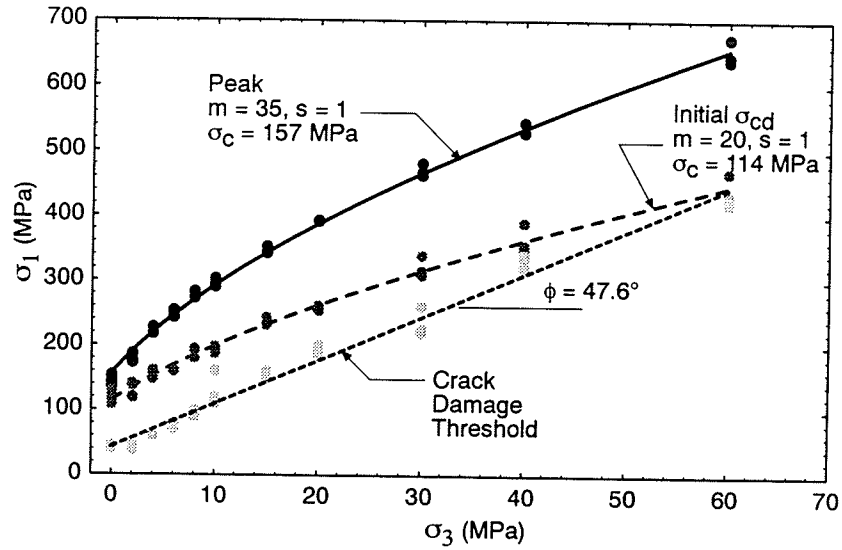
Figure 4.26: The peak strength, initial crack damage and crack damage threshold envelopes.
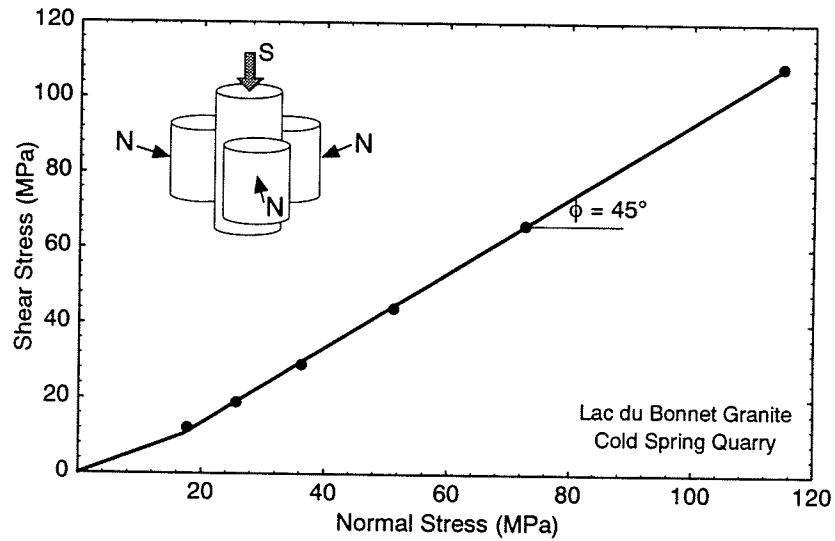
Figure 4.27: Basic friction angle for Lac du Bonnet granite (after [61]).

by substituting $\mu = \tan\phi$, where ϕ is the friction angle.

The shear strength of a material with friction and cohesion is also given by the well known Mohr-Coulomb criterion

$$\sigma_{1f} = 2S_o \tan\left(45 + \frac{\phi}{2}\right) + \sigma_3 \tan^2\left(45 + \frac{\phi}{2}\right) \tag{4.16}$$

where S_o is the empirical cohesion intercept and ϕ is the friction angle. It is interesting to note that the shear criterion in equation 4.15 differs from equation 4.16 only by a constant. In equation 4.15 this constant is expressed in terms of fracture surface energy and crack length, whereas in equation 4.16 the constant is the empirical shear strength. More importantly, examination of equations 4.15 and 4.16 reveals that fracture surface energy and crack length only apply to the cohesion of the material and that the frictional strength is not dependent on these parameters.

The interpretation of a standard set of uniaxial test results, using equation 4.16 would imply that

$$\sigma_{1f} = 2S_o \tan\left(45 + \frac{\phi}{2}\right) \tag{4.17}$$

Thus the cohesion can be equated to the strength just as sliding starts, which for our tests results is given by the crack damage stress. For an unconfined test, at the instant sliding starts, the cohesion becomes

$$2S_o = \sigma_{cd} \tag{4.18}$$

Once sliding initiates the strength of the sample starts to increase above the crack damage stress. However, we have seen from our test results that as the sample is subjected to increasing damage, only a small amount of damage to the sample is necessary to bring the crack damage stress to a threshold value, suggesting that cohesion must also decrease. The total strength of the sample has not changed therefore the frictional component of equation 4.17 must be increasing as the cohesion is decreasing. In equation 4.15 the drop in cohesion is related to an increase in crack length. Figure 4.28 is an example of this progressive fracturing, illustrating the loss in cohesion and the mobilization of friction.
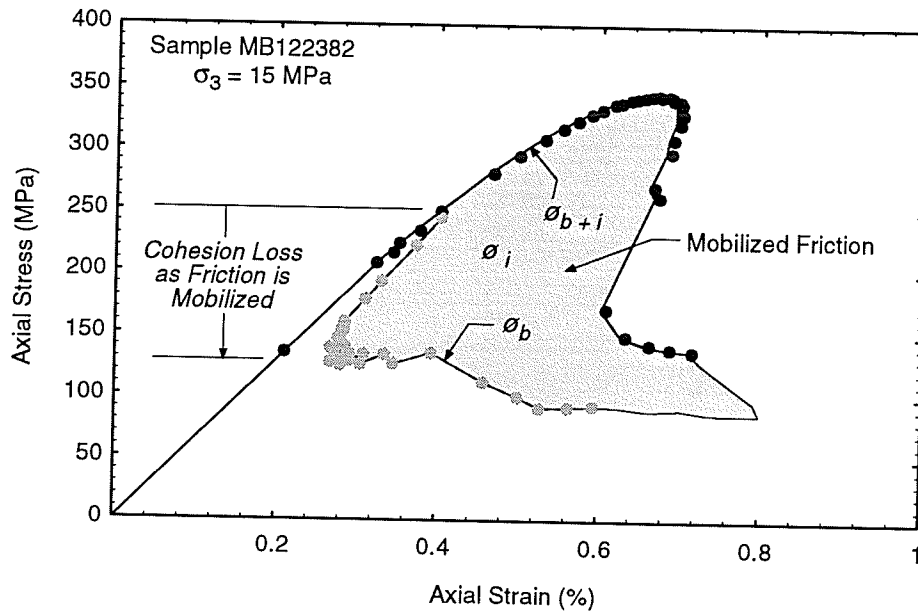
Figure 4.28: Mobilization of friction and loss of cohesion as a function of axial strain.

Ultimately at large displacements the peak stress and the crack damage stress should be equal as illustrated in Figure 4.28.

The cohesion loss described above can only occur if nonelastic deformations are required to mobilize friction and the frictional component is made up of a residual component (ϕ_b) and a roughness or interlocking component (ϕ_i), such that the total frictional resistance can be expressed as ϕ_{b+i}. As friction is mobilized, the interlocking is at a maximum and as the damage accumulates the residual friction and the minimum cohesion must be approached (see Figure 4.29). In Figure 4.29 the value of ϕ was calculated using

$$\phi = 2\tan^{-1}\left(\frac{\sigma_1}{\sigma_{cd}}\right) - \frac{\pi}{2} \qquad (4.19)$$

Also in Figure 4.29 the damage has been normalized with respect to the value of ω at the end of the test, the strength has been normalized to the peak strength and the cohesion has been normalized to the maximum cohesion. Figure 4.29 illustrates that the peak friction angle ($\phi = 63°$) occurs as the rapid drop in cohesion declines. With increasing damage the friction angle gradually decreases to about 42°. This friction value is similar to the residual

friction angle of 45° and 42° for Lac du Bonnet granite reported by [61, 98]. Thus for the test in Figure 4.29 it appears that the residual friction is nearly reached. The peak friction angle of 63°, although high, is not unrealistic, e.g., Dusseault and Morgenstern [42] reported that natural slopes of uncemented locked sands have inclinations greater then 54°. Thus 63° does not seem unreasonable for perfectly interlocked mineral grains subjected to small displacements.

According to Figure 4.29 the friction angle of the material changes as damage accumulates in the sample. Hence the angle the sliding plane makes with the applied load must also be changing. The critical angle of failure for equation 4.17, relative to the applied load, can be found from a Mohr's circle and is given by

$$\theta = 45 - \frac{\phi}{2} \tag{4.20}$$

Using equation 4.20, the angle θ between the applied load and the sliding surface was calculated as the friction angle changed (Figure 4.31). In the initial stages of the test when there is essentially no damage, $\phi = 0$ and $\theta = 45°$. As damage accumulates and the crack damage stress starts to decrease θ also decreases and reaches a minimum of about 15° when the crack damage stress reaches its threshold value. By the end of the test the failure plane is oriented at $\approx 25°$ which is in agreement with the orientation of the failure plane in Figure 4.10. It is obvious that the nucleation and growth of a shear fracture is complex. In this simple analysis no allowance is made for the role of the axial crack in the failure process. Du and Aydin [41] have shown that the axial cracks tend to form echelon arrays. These arrays probably provide the nucleation of the shear crack. Hence, the orientation of the shear crack from the onset of damage through to when the friction is at its maximum in Figure 4.31 is an oversimplification, because it is assumed that the shear crack is a through going crack, not one that is interrupted by small axial cracks. An illustration of the concept of cohesion loss and the role played by the axial cracks is illustrated in Figure 4.30.

A damage-controlled test of Lac du Bonnet granite was carried out and the test stopped
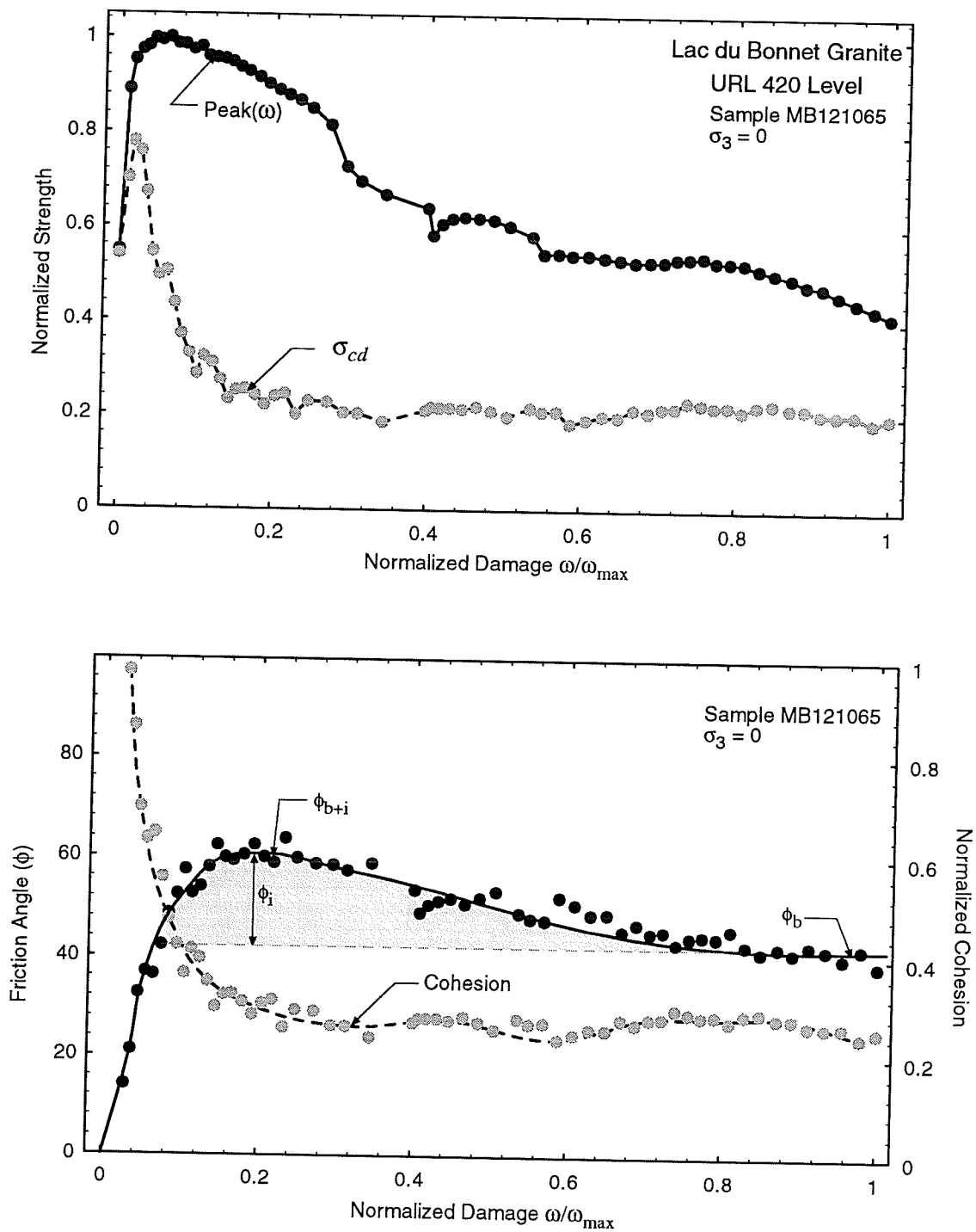
Figure 4.29: Mobilization of friction and cohesion as a function of damage.
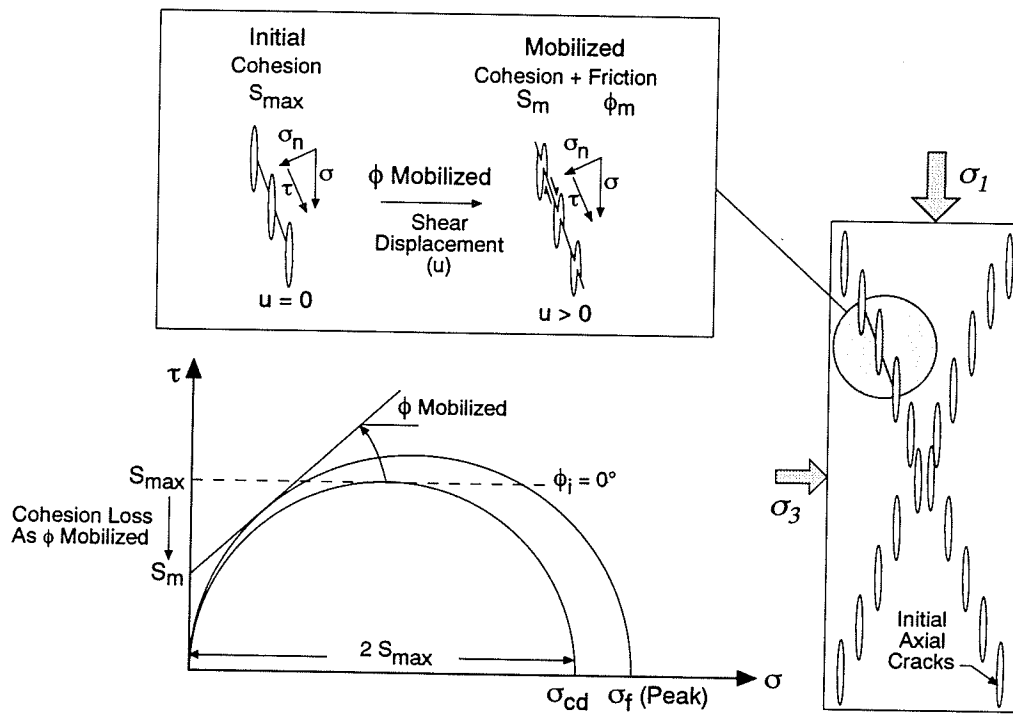
Figure 4.30: Illustration of cohesion loss and mobilization of friction in terms of Mohr stress diagram. A possible role for axial cracks is illustrated on the right and top portion of the figure.
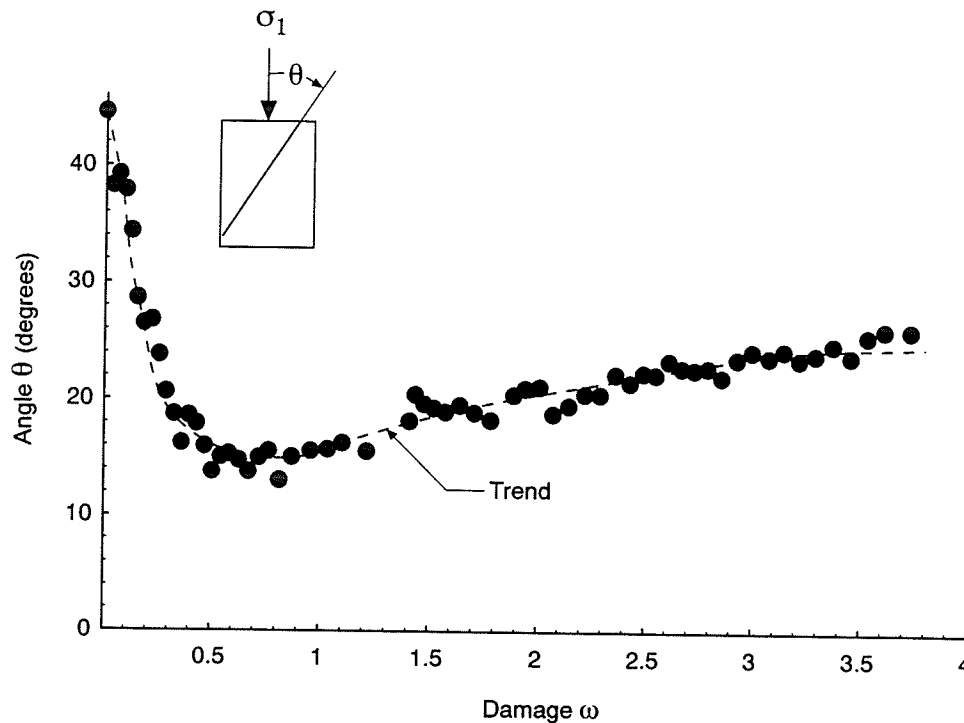
Figure 4.31: The angle, between the failure surface and the applied stress (σ_1), as a function of damage.

shortly after the crack damage stress decreased to near its threshold value. The peak stress at this point in the test was 190 MPa. The sample at this point appeared very much intact although there was some evidence of cracking visible on the surface of the sample. The sample was then cut parallel to the direction of loading and visually inspected for cracks. Figure 4.32 shows the cracks observed in this sample and clearly shows a major crack located near the centre of the sample, $\approx$ 20 mm long, and inclined 11° with respect to the direction of loading. This 11° inclination is very close to the predicted 15° inclination in Figure 4.31 for when the cohesion reaches its threshold value and ϕ is at its maximum. It should also be noted that small axial cracks are present in the sample and essentially form two echelon arrays, as suggested by [41].

Figure 4.32: Photo of the cracks developed in a damage controlled test as the crack damage stress reaches its threshold value. The major crack ($\approx$ 20 mm long) in the center of the sample is inclined 11° with respect to the direction of loading. The test sample was 63 mm in diameter.

4.5.2 Crack Damage Locus in Other Rock Types

It has already been stated that the Lac du Bonnet granite from the Cold Spring Quarry is stronger in all respects to the Lac du Bonnet granite from the URL. Hence the samples from Cold Spring Quarry should be more brittle then the samples from the URL. Damage-controlled testing was attempted on two 63-mm diameter samples from the Cold Spring Quarry. These tests were carried out when we were getting the "bugs" out of the system. As a result, the data quality is not comparable to that presented in the previous test results. Nonetheless the data in Figure 4.33 can be used to examine the differences between the samples of Lac du Bonnet granite from the 420 Level of the URL and the Cold Spring Quarry. The results in Figure 4.33 show the characteristic decrease in crack damage stress with increasing axial strain. However, note how little axial strain is required to cause the crack damage decrease. For the Lac du Bonnet granite from the Cold Spring Quarry the slope of the crack damage curve is nearly the same as the initial loading curve.

It was suggested previously that the crack damage locus represented the locus of sliding and that the crack damage threshold indicated when friction was fully mobilized. It has also been shown that the peak stress and initial crack damage stress in a sample is a function of crack damage. Figure 4.34 is comparison of the peak stress and crack damage stress as a function of normalized damage for two samples of Lac du Bonnet granite tested with a confining stress of 2 MPa. The sample with the highest peak stress is from the Cold Spring Quarry and represents the undamaged sample. The second sample in Figure 4.34 is from the 420 Level of the URL and represents the damaged sample. Note that the peak stress and initial crack damage stress is strongly dependent on the initial amount of damage in the sample yet the crack damage stress threshold for both samples is nearly identical. This supports the notion that the initial crack damage stress and the peak stress are a function of the initial cohesion of the sample but that the crack damage threshold, which represents when friction is fully mobilized, is independent of the initial amount of damage
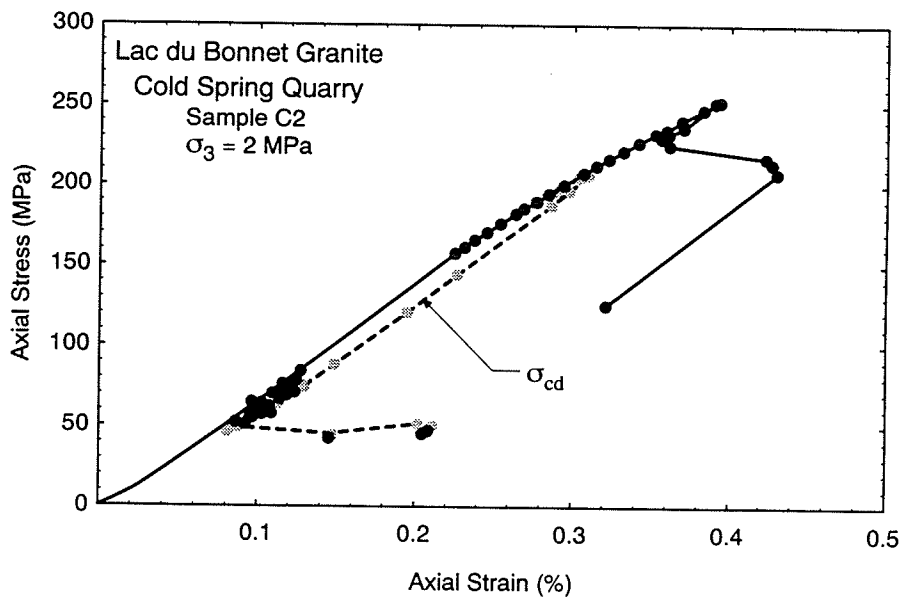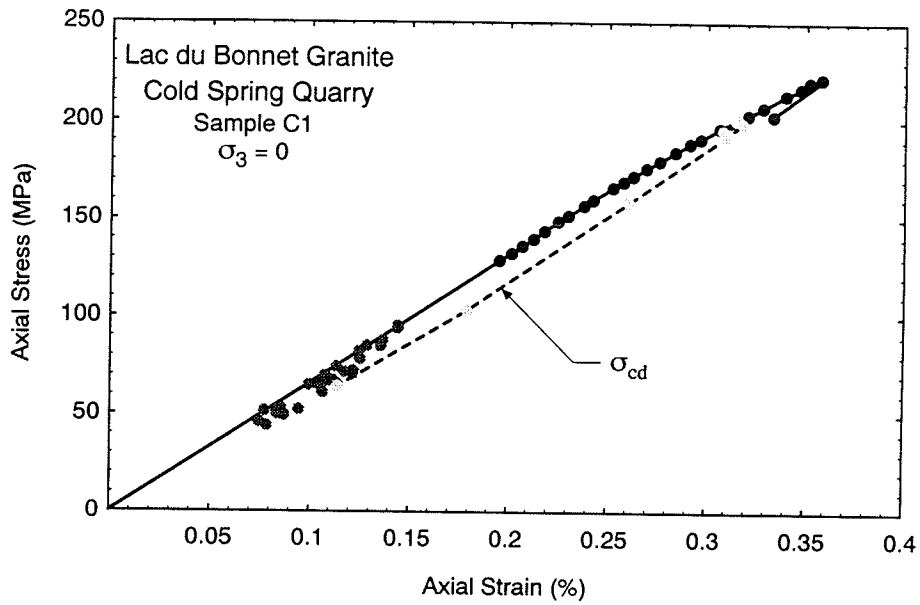
Figure 4.33: Damage-controlled test results for two samples of Lac du Bonnet granite from Cold Spring Quarry. Note the small amount of axial stain required to cause the crack damage locus to decrease to the crack damage threshold.
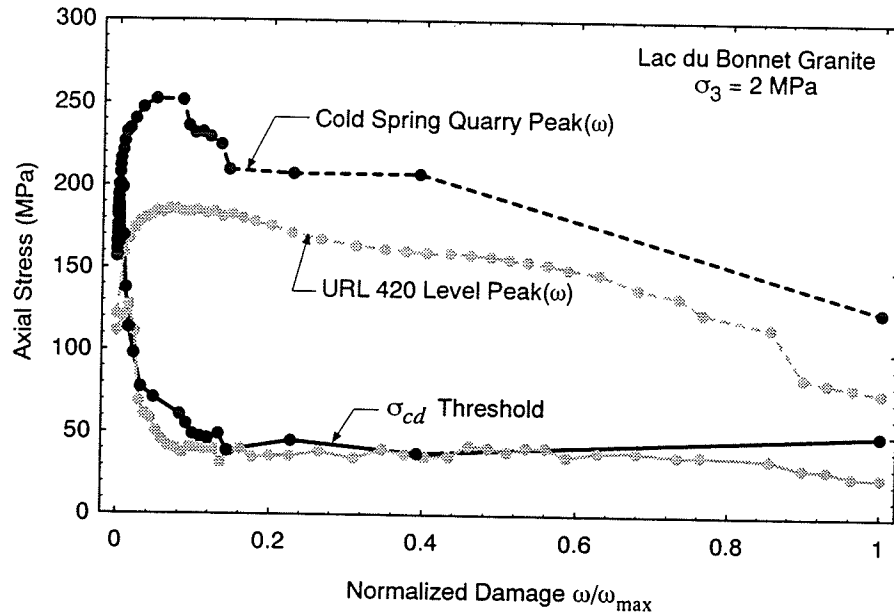
Figure 4.34: Damage-controlled test results for two samples of Lac du Bonnet granite tested with a confining stress of 2 MPa. One sample is from Cold Spring Quarry and the other sample is from the URL 420 Level. Note the large difference in peak stress betwen the two samples but almost no difference in the crack damage stress threshold.

in the sample.

For comparison purposes three samples of Indiana limestone were also tested using the damage-controlled procedure. It should be noted that the testing procedure for the Indiana limestone was also not as well controlled as for the 420 Level granite samples. Hence, load-unload cycles near the maximum loads are missing. The tests were carried out unconfined and with confining stresses of 4 and 10 MPa. This rock has a Young's modulus of about 25 GPa which is nearly half the modulus of Lac du Bonnet granite but it still shows the characteristic crack damage decrease, although now it takes considerable more axial strain to achieve the crack damage threshold (Figure 4.35). At low confining stresses the crack damage threshold is essentially the same as the crack initiation stress. However, as the confining stress increases, the crack damage threshold greater than the crack initiation stress (Figure 4.36). This feature also occurred in the samples of Lac du Bonnet granite.
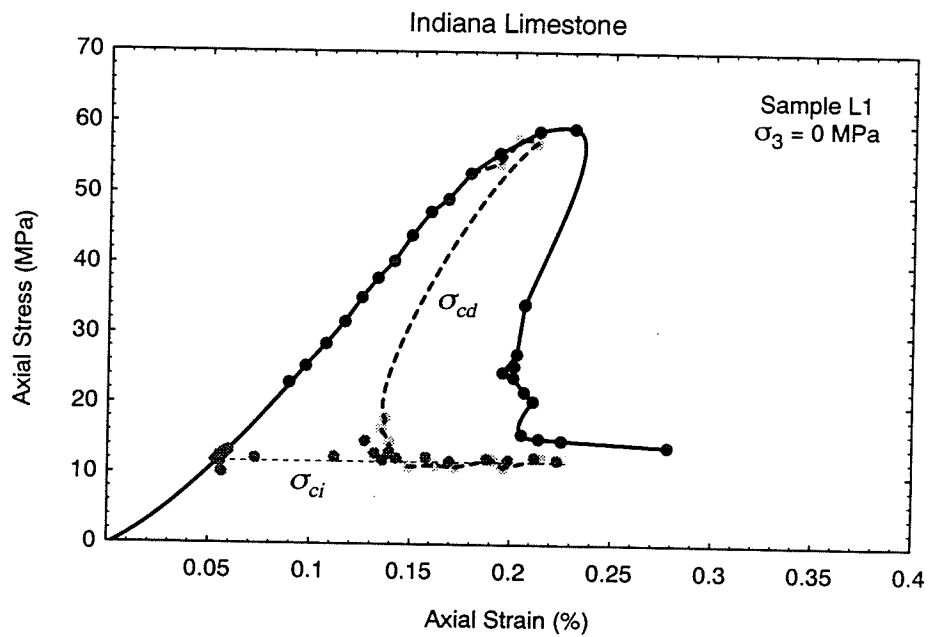
Figure 4.35: Damage-controlled test results for an unconfined sample of Indiana Limestone. Note the increase in the amount of axial strain required to cause the crack damage locus to decrease to the crack damage threshold compared to the brittle sample of Lac du Bonnet granite from Cold Spring Quarry (see Figure 4.33).
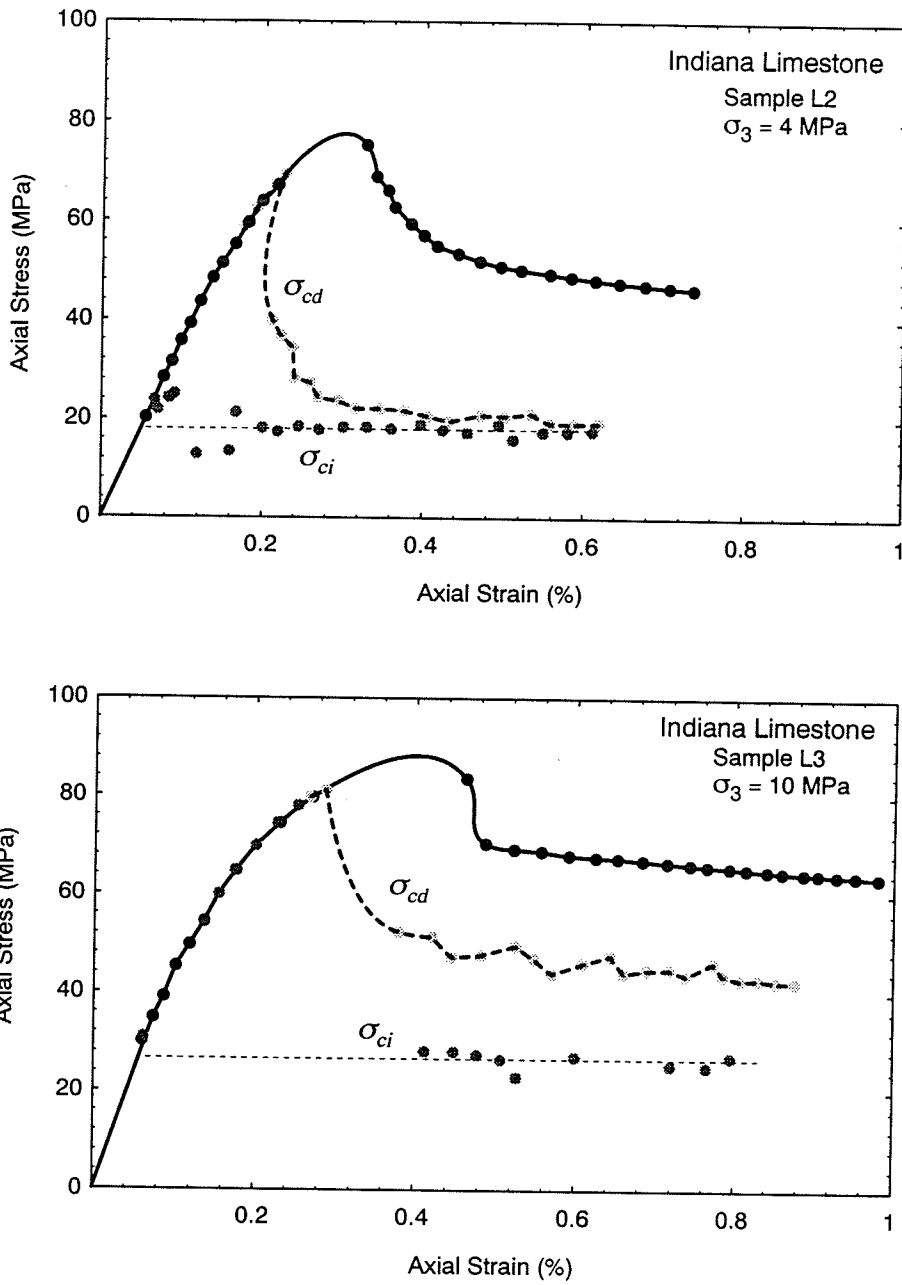
Figure 4.36: Damage-controlled test results for two samples of Indiana Limestone at different confining stress. Note the increase in the crack damage threshold above the crack initiation stress as the confining stress increases.
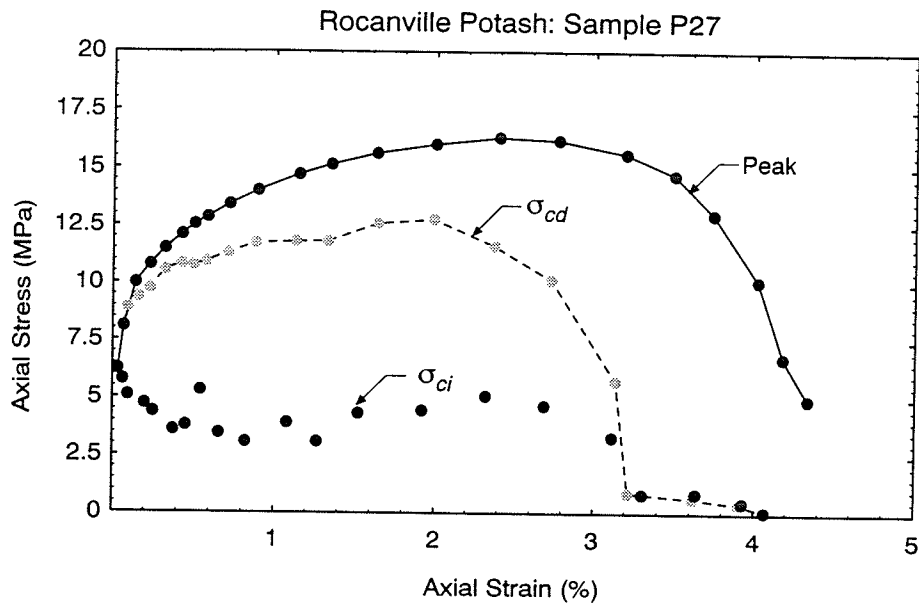
Figure 4.37: Damage-controlled test results for an unconfined sample of Rocanville potash. Note the increase in the amount of axial strain required to cause the crack damage locus to decrease to the crack damage threshold compared to the brittle sample of Lac du Bonnet granite from Cold Spring Quarry (see Figure 4.33).

Under ordinary temperature and pressure, most rocks are brittle. Salt rocks are no exception. Despite being more ductile than the typical rock, microcracking is common in salt rocks. Specimens of Rocanville potash salt rock (Rocanville, Saskatchewan, Canada), dilate during uniaxial compression and the growth of cracks is obvious to the naked eye. The rock has a strength that is only one tenth of that of Lac du Bonnet granite although the modulus is about 16 GPa or about 1/3 to 1/4 of the Young's modulus of a granite. In a damage-controlled test, the crack damage stress seems to follow a course that is very similar to that observed for the granite (Figure 4.37). The most significant difference between the Lac du Bonnet granite and this salt rock is the significant amount axial strain required to cause the crack damage to decrease to a threshold value.

In examining the damage-controlled test results from the granite, limestone and potash the slope of the crack damage locus, during its rapid descent to the crack damage threshold,

is seen to shift from a positive slope for the granite to a negative slope for the potash. In terms of the Griffith locus this implies that the softer material cannot produce unstable crack growth. Hence crack growth can only occur by increasing the loads. In potash time-dependent deformations also occur.

4.6 Crack Damage Stress in the Brazilian Test

In the previous sections failure in compression tests on cylindrical samples was analyzed. Those tests showed that the cohesion limit, in compression, could be equated to the crack damage stress, i.e., the stress level at which crack propagation occurs, and this stress level was defined by the volumetric strain reversal on the volumetric strain versus axial strain curve. In this section compression loading of circular discs (Brazilian test) are analyzed to determine if the crack damage stress can also be used to define the tensile cohesion limit.

The tensile strength of rock is also commonly determined using the Brazilian tensile test (Figure 4.38). The Brazilian tensile test is an indirect method of determining the tensile strength in which the tensile strength σ_{Bt} is given by

$$\sigma_{Bt} = \frac{2P}{\pi D t} \tag{4.21}$$

where P is the load at failure, D is the diameter and t is the thickness of the disc-shaped sample.

The tensile strength of rock is found from a direct tension test and for this test setup the stress at failure is equal to the tensile cohesive strength. It is well known that the tensile strength obtained from direct tension tests is less than the tensile strength obtained from the Brazilian test. The reason for this discrepancy is usually attributed to stress gradients, although the modulus ratio between compression and tension may also play a role [28].

In an effort to determine if the crack damage stress obtained from the Brazilian tests gave a more reliable indication of the tensile cohesive strength, twenty Brazilian tests were carried out. Each sample was instrumented with an axial and lateral electrical resistance
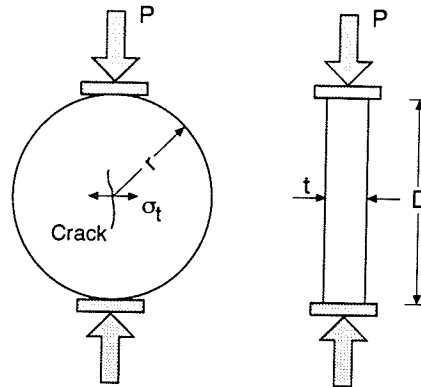
Figure 4.38: Experimental setup for a Brazilian test.

strain gauge and strain monitored throughout the test. A typical plot of the measured axial and lateral strains, and the calculated volumetric strain given by

$$\Delta V/V = \epsilon_{axial} + \epsilon_{lateral} \qquad (4.22)$$

versus σ is given in Figure 4.39. σ in Figure 4.39 is calculated using equation 4.21.

The samples of Lac du Bonnet granite, from Cold Spring Quarry, used in the testing program were taken from both ends of samples that were used to measure the direct tensile strength (see Table C.1 in Appendix C. Hence, the scatter due sample variation was minimized. A summary of the results from the twenty Brazilian tests is given in Table 4.3. The mean Brazilian tensile strength is 8.8 MPa and the mean crack damage stress is 7.4 MPa, giving a ratio of 0.84. This ratio of 0.84 is very similar to the ratio between crack damage stress and peak strength found in uniaxial compression. More, importantly the crack damage stress of 7.4 MPa is considerably closer to the direct tensile strength of 6.9 MPa than the Brazilian strength of 8.8 MPa. A summary of the comparison is given in Figure 4.40. Thus it seems reasonable to conclude that the crack damage stress in the Brazilian test represents tensile cohesive strength.
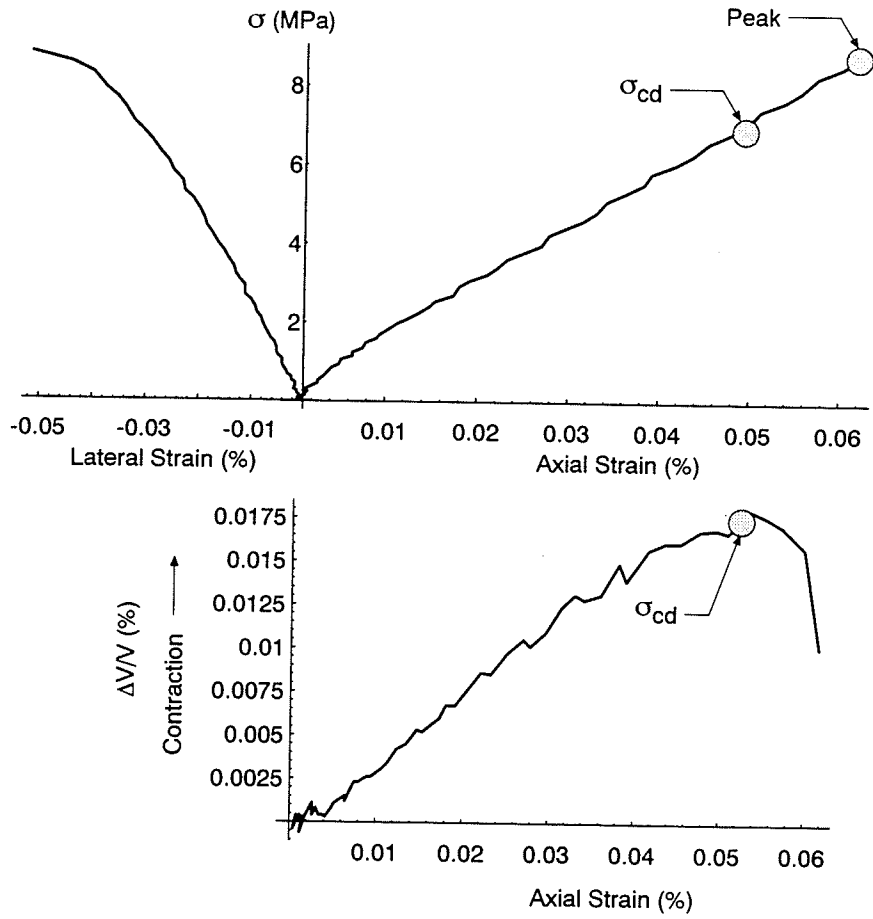
Figure 4.39: The stress strain curves obtained from a Brazilian test.

Table 4.3: Summary of the tensile strengths obtained from the Brazilian test.

Sample Number	Diameter (mm)	Thickness (mm)	σ_{cd} (MPa)	Peak (MPa)	Ratio σ_{cd}/Peak
34.134A	44.97	20.73	7.67	8.80	0.87
34.134B	44.97	22.50	6.54	9.11	0.72
34.449A	44.98	22.97	9.65	9.65	1.00
34.449B	44.98	21.87	5.73	8.34	0.69
34.763A	44.97	22.96	7.50	9.63	0.78
34.763B	44.97	22.64	5.05	8.48	0.60
34.133A	44.98	22.38	6.73	6.73	1.00
35.133B	44.98	22.15	6.80	7.80	0.87
35.533A	44.98	23.44	7.60	9.11	0.83
35.533B	44.98	21.84	6.12	8.35	0.73
35.860A	44.98	22.06	10.01	10.67	0.94
35.860B	44.98	22.06	9.16	9.16	1.00
38.030A	44.98	22.85	8.06	9.85	0.82
38.030B	44.98	22.99	7.07	9.39	0.75
38.517A	44.99	23.28	7.12	7.12	1.00
38.517B	44.99	22.32	4.32	7.49	0.58
41.043A	44.91	22.86	9.97	9.97	1.00
41.043B	44.91	21.74	7.21	8.97	0.80
41.362A	44.92	22.72	9.04	9.42	0.96
41.362B	44.92	22.05	7.36	9.06	0.81
mean			7.42	8.80	0.84
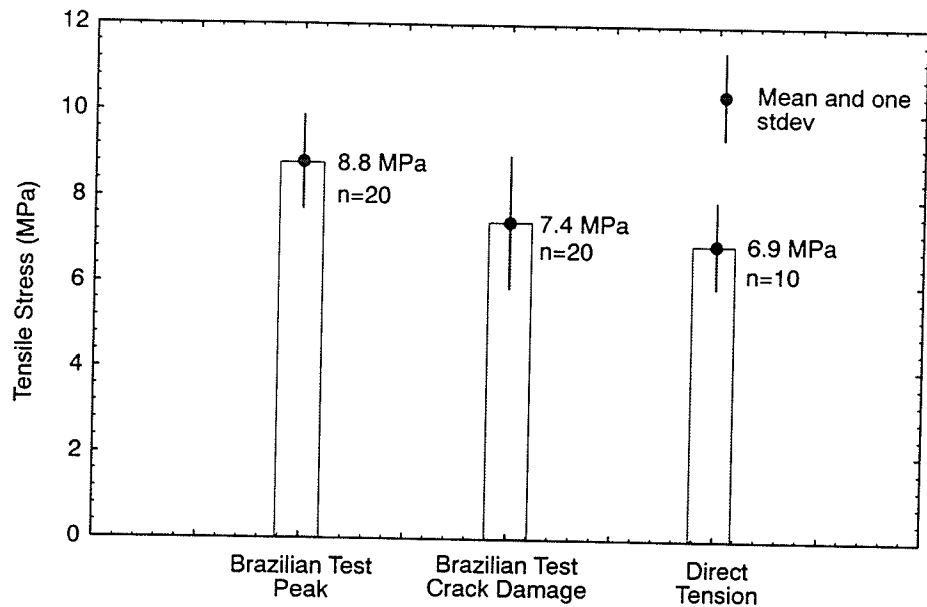
Figure 4.40: Comparison of the results from the direct tension tests and the Brazilian tension tests. Note that the crack damage stress gives nearly the same tensile strength value as the direct tensile test.

4.7 Application of the Griffith Locus

The Griffith crack damage locus can be readily applied to the rock surrounding an underground opening. As the face of the opening approaches and passes the volume of rock which eventually becomes part of the tunnel surface, the principal stresses associated with this rock will change significantly in both magnitude and direction. Stresses in excess of the crack damage, σ_{cd}, locus occurring at any period in the rock's loading history around the opening will result in a localized increase of damage to the rock and a corresponding loss of cohesion. The degree of damage will be highest at the surface of the opening where confinement is zero and stress concentrations are greatest, and this damage will decrease with increasing distance into the rock. From equations 4.15 or 4.16 it is clear that when $\sigma_3 = 0$ the frictional component of the rock's strength plays essentially no role in determining the strength around an underground opening. The strength, is determined by the cohesion which is a function of crack damage. Hence the strength around an underground opening,

in a high stress environment, will be lowest at the tunnel surface. In such situations, back analysis of the failed or damaged openings would suggest much lower strength than that found from routine laboratory testing. For our test results the cohesion loss was greater than 50% of the unconfined compressive strength. This low strength material would only be present in a local area around the tunnel which has experienced the damage and the rock mass outside this damaged zone would still have the undamaged strength.

This concept of cohesion loss through damage would imply that the failure envelope for damaged rock around a tunnel would be quite different from that normally assumed. Figure 4.26 showed the three failure envelopes, one for peak strength, one for the initial crack damage and one for the crack damage threshold. Earlier it was shown that when $\sigma_3 = 0$ the peak strength is a function of time, and that even for short periods of one day cannot be relied on. It is assumed that this would also apply when $\sigma_3 > 0$, although the time to failure would probably increase. Thus it is proposed that when the stress level has not exceeded the initial crack damage stress, i.e., $\omega = 0$, the true strength of the intact rock mass is given by the initial crack damage envelope. In the damaged zone, i.e. $\omega > 0$, near the tunnel wall where $\sigma_3 \simeq 0$, the strength would equal the crack damage threshold. However, where $\sigma_3 > 0$ and damage has not occurred, i.e., $\omega = 0$, the initial crack damage strength would still be available. Thus the failure envelope would be extremely steep in the region close to the tunnel wall (see Figure 4.41). Hence the traditional failure envelope would not apply in such circumstances.

A similar analogy to the one above could be used to explain the sample disturbance phenomenon described in Section 2.3. It was shown in Section 2.3 that sample disturbance causes a loss in strength (cohesion) of the samples taken from the 420 Level of the URL and that this loss in cohesion is progressive with depth from the surface. Hence, by plotting the crack damage stress of samples taken from the three *in situ* stress domains at the URL one should be able to map the Griffith locus of the damaged samples. The crack damage stress of samples from the three stress domains is plotted in Figure 4.42. It is clear from
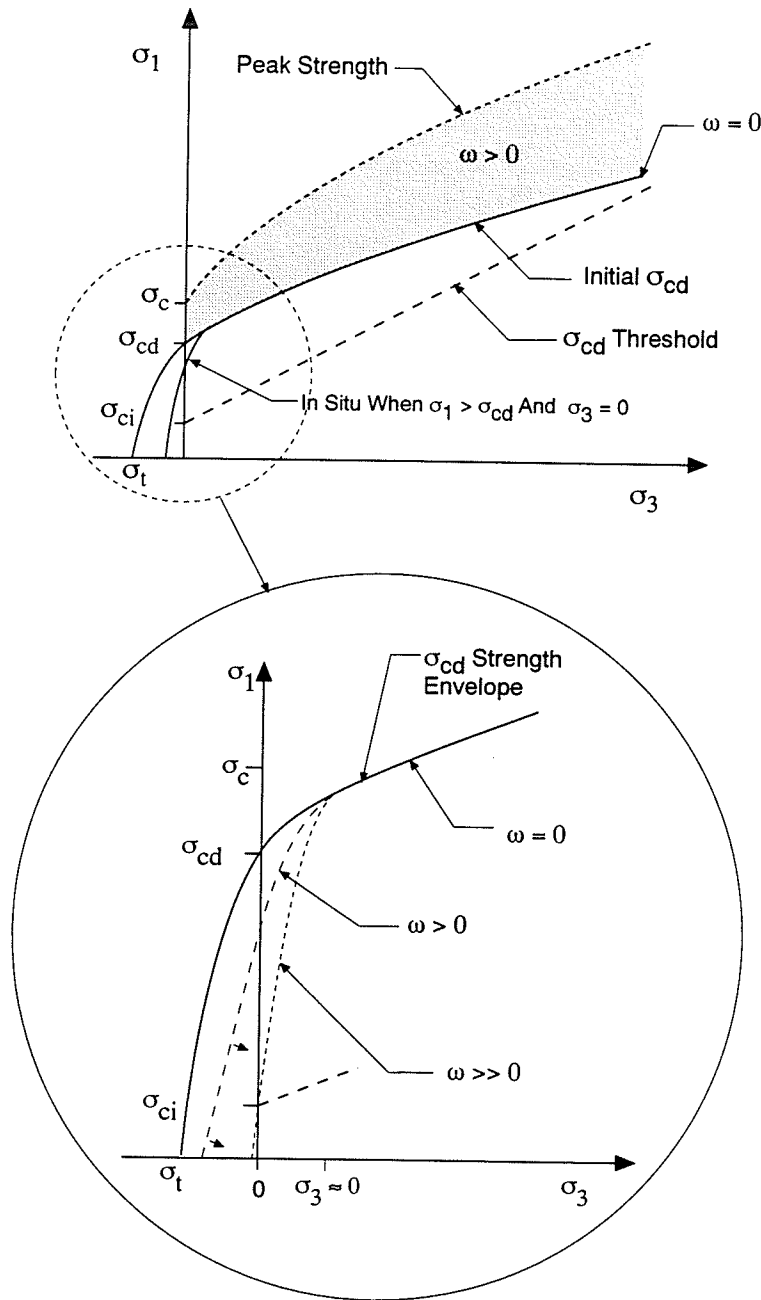
Figure 4.41: Proposed *in situ* failure envelope for damaged rock around an underground opening.
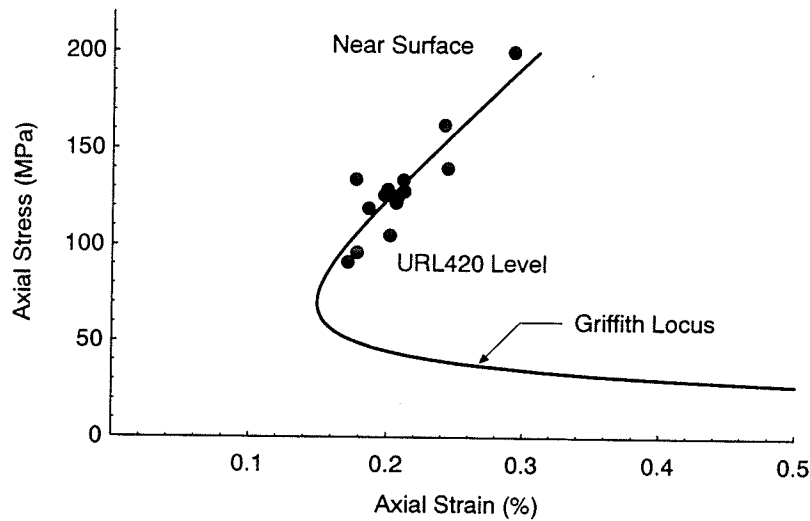
Figure 4.42: Calculated Griffith locus compared with crack damage locus obtained from uniaxial tests on samples from different depths.

Figure 4.42 that the crack damage stress obtained from the samples is very similar to the predicted Griffith locus. The sliding portion of the Griffith locus is not available from the samples and it is suggested that this portion of the locus may coincide with core discing.

It was illustrated in Figure 4.1 that the crack volumetric strain could be determined from the measured axial and lateral strains. It was also shown in Figure 4.1 that if a sample contains an initial crack density, this crack volume is reflected in the crack closure portion of the crack volumetric strain. The initial crack volumetric strain was determined on samples obtained from the three stress domains at the URL. Figure 4.43 is a plot of the initial crack volumetric strain calculated for each sample versus the corresponding unconfined crack damage stress for that sample. At present there is no way to relate crack volumetric strain to crack length without making many assumptions related to the shape of the cracks. As a first approximation, the relationship between crack length and the crack damage stress given in equation4.15, for an unconfined sample, is also plotted in Figure 4.43. The results are encouraging and indicate that a relationship may exist between crack volumetric strain and crack length. However, before any conclusions can be drawn considerably more testing
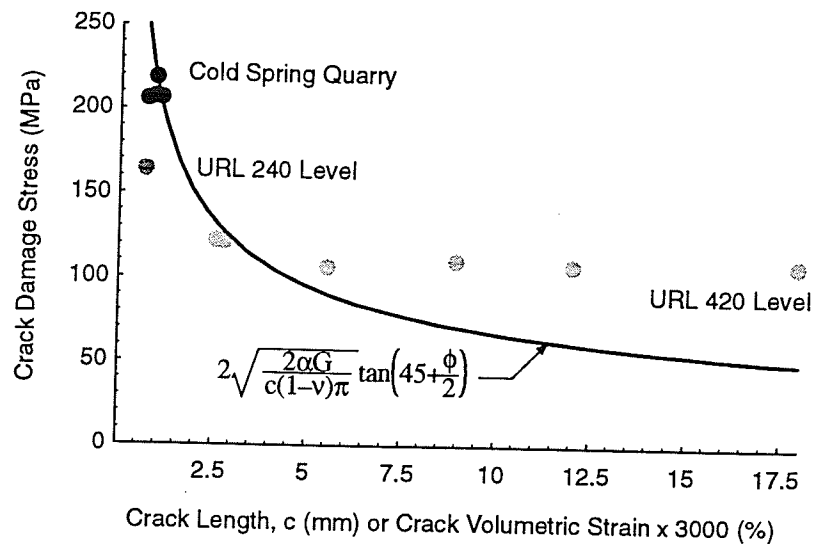
Figure 4.43: Crack damage stress versus crack volumetric strain compared to the predicted change in strength (crack damage stress) versus crack length.

would have to be carried out.

4.8 Summary

The progressive failure of Lac du Bonnet granite has been demonstrated by damage-controlled testing. It is well known that the strength of intact rock is made up of two components, cohesion and friction. It is proposed that as the granite is loaded in compression its strength is derived from only the cohesion component. When the load exceeds the cohesion, which occurs at about 0.7 to 0.85 (≈ 0.8 in Figure 4.29) of the compressive strength, the strength now consists of a reduced cohesion and mobilized friction. However, as friction is mobilized some of the initial cohesion is lost. This concept of cohesion loss is well recognized in soil mechanics [115] and has also been suggested by Charlez [27] for rock.

The loss in cohesion was traced using the crack damage locus. The locus of cohesion, at various stages in the failure process was mapped by determining the stress level required for the onset of sliding (σ_{cd}). Initially, in an undamaged sample and at the onset of sliding, the strength of the sample consists of 100% cohesion. At this stage friction is not mobilized

in the sample. With increasing loads above this initial cohesion limit, the sample becomes damaged. This damage results as sliding occurs along preferred planes within the sample. As a result of this mobilization of friction, cohesion is rapidly lost, such that by the time the sample reaches its peak strength the cohesion has decreased to a threshold value. At this stage the strength of a uniaxial sample is composed of $\approx 30\%$ cohesion and $\approx 70\%$ friction. With further damage beyond the peak strength, i.e., more sliding, the frictional component of the strength also decreases rapidly. By the end of the test the frictional strength component reaches its residual value, which corresponds to a friction angle of $\approx 42°$.

The crack damage locus was modelled using the Griffith locus based on a sliding crack. The predicted loci agreed very closely with the measured crack damage loci obtained from the damage-controlled tests. This agreement between the predicted and measured loci supports the notion that the crack damage stress can be used to predict the onset of sliding and must therefore also represent the cohesion limit in the sample.

Chapter 5

Failure Around Openings in Massive Rocks

In Chapter 2 it was shown that the in situ stresses on the 420 Level of the URL were relatively uniform and that the rock mass was homogeneous, massive and fracture free. Thus elastic analyses of openings on the 420 Level should provide an accurate estimate of the tangential stresses on the boundary of the excavations. The stability of the tunnels on the 420 Level can then be assessed by comparing the calculated stresses to the unconfined compressive strength of the rock.

5.1 Initial Back-Analysis of the 420 Level Tunnels

The excavations on the 420 Level were created using full-face drill and blast techniques and are shown in Figure 5.1. In addition to the drill and blast excavations, a special 3.5-m-diameter test tunnel was also excavated using a combination of line drilling and mechanical rock breaking using hydraulic splitters [122]. The major excavations, called Rooms, on the 420 Level have been aligned with the general direction of the principal stresses, such that Room 405 and the test tunnel are parallel to σ_2, and Rooms 409 and 413 are parallel σ_1.

The design excavation profiles for Room 405 and Room 413 were analysed using the boundary element program Examine^{2D}. The maximum tangential stress on the boundary of the excavation, obtained from the numerical analysis, was 130 MPa for Room 405 and 110 MPa for Room 413 (Figure 5.2). The excavation geometry used in the modelling has

141
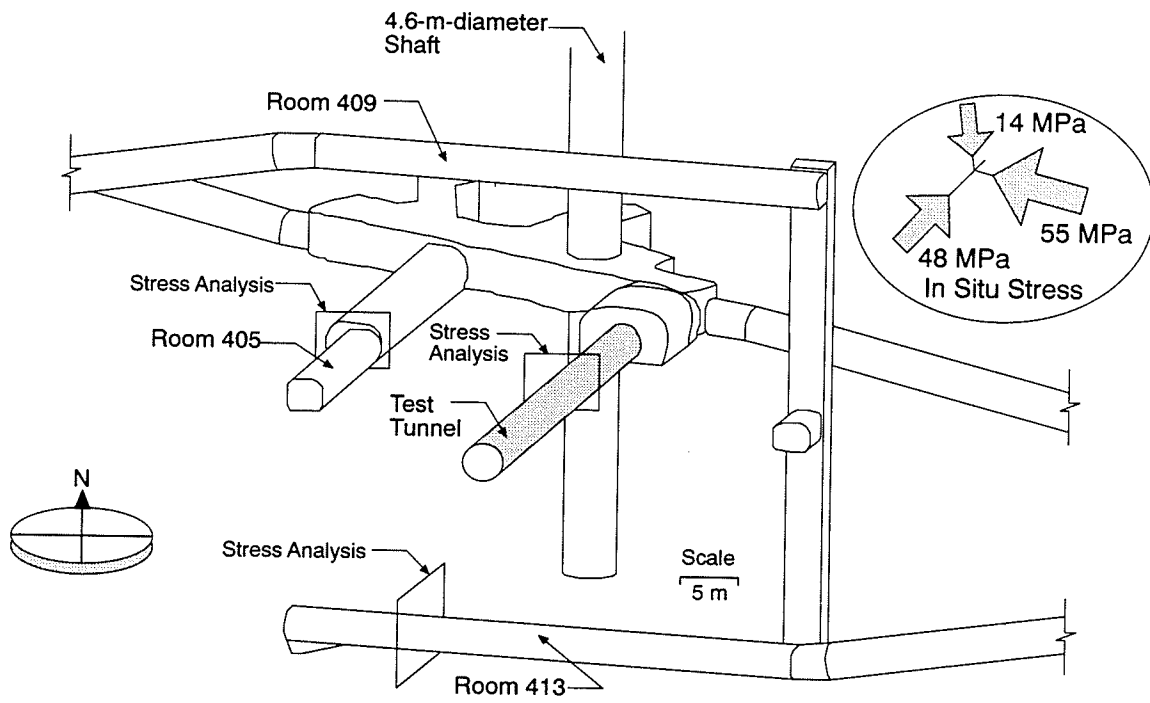
Figure 5.1: Layout of the excavations on the 420 Level of the URL and the locations of the profiles used in the numerical stress analyses.

some influence on the stress magnitudes, hence extreme stress magnitudes concentrated at sharp corners in Figure 5.2 should be ignored.

The excavations were carried out using drill-and-blast techniques. Hence, drill-hole traces or half-barrels on the perimeter of the excavation mark the as-built profile of the excavation. The lack of half-barrels indicates either the rock was damaged during blasting or the rock has failed since excavation. Traditionally there are no half-barrels found on the floor of the excavations at the URL because additional blasting agent is placed in the floor blast holes to "lift" the muck, resulting in increased blast damage to the excavation floor. However it is routine at the URL to maintain all the half-barrels on the walls and roof of the excavation. Figure 5.3 shows the half-barrels found in Rooms 413 and 405. Room 413 was excavated parallel to σ_1, and it was subjected to a maximum in-plane stress ratio of 3.4. The half-barrels are visible nearly everywhere around the perimeter (Figure 5.3) except at one location in the roof. Thus, very little failure has taken place in Room 413. In Room 405 however, the perimeter blast hole traces (half-barrels) are only observed on the side walls and the roof contains the classic v-shaped notch characteristic of spalling failure. The in-plane stress ratio for Room 405 is 3.9.

The spalling failure observed in Room 405 was found in all tunnels excavated parallel or near parallel to Room 405, i.e., parallel to σ_2. The stable conditions found in Room 413 were also found in all excavations on the 420 Level parallel to Room 413, i.e., parallel to σ_1. The difference in magnitude between σ_1 and σ_2 is only 7 MPa, yet the difference in excavation response is dramatic.

In Section 2.3 it was shown that the samples from the 420 Level are not representative of *in situ* conditions because of sample disturbance and that the properties of Lac du Bonnet granite from Cold Spring Quarry are probably close to *in situ* conditions. In Chapter 3 the long-term strength of Lac du Bonnet granite from Cold Spring Quarry was given as 161 MPa after one year [140]. However, it was shown in Chapter 4 that the cohesive strength of Lac du Bonnet granite is about 0.7 of the short-term unconfined compressive
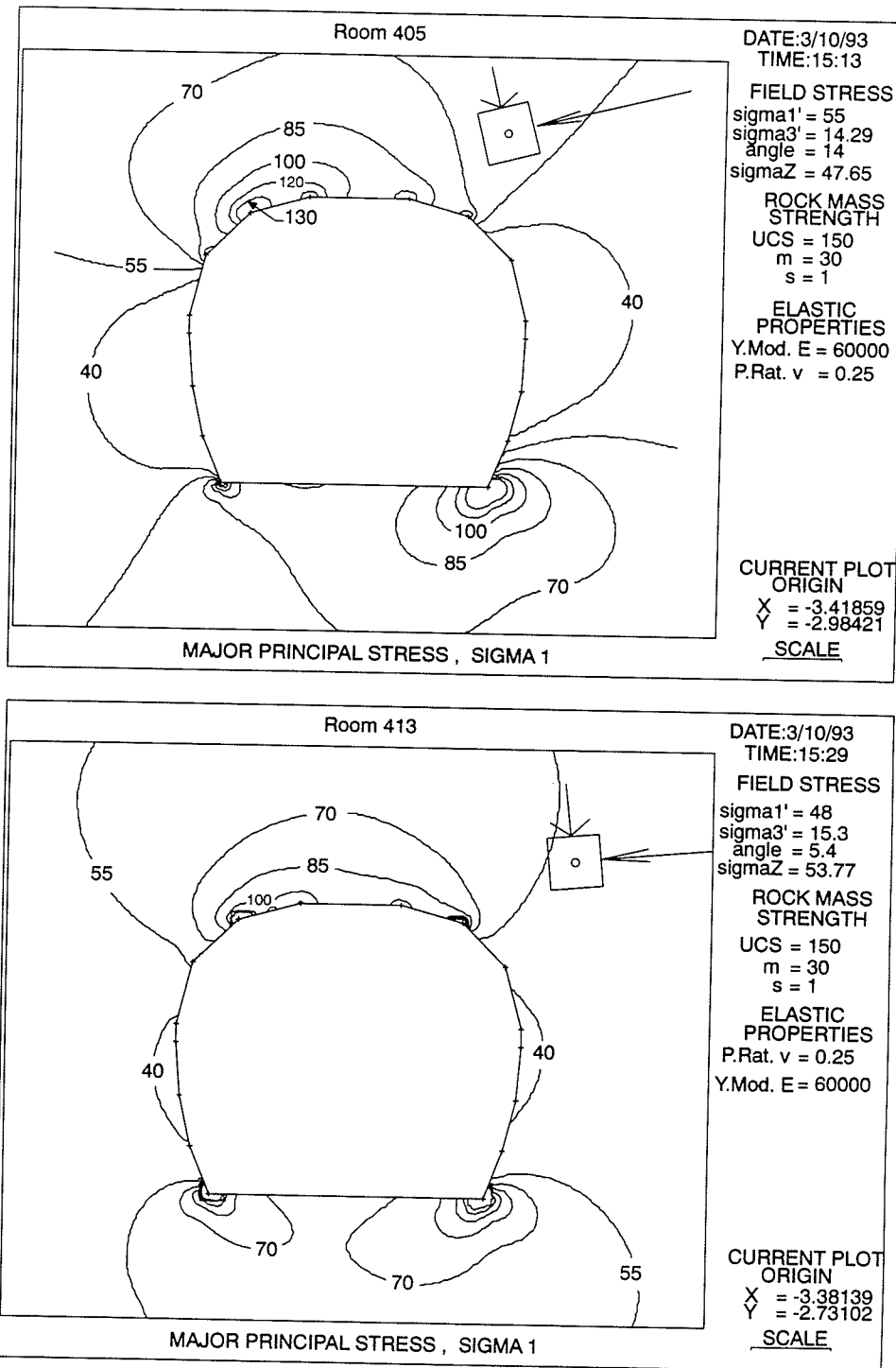
Figure 5.2: Results of the stress analysis for Room 413 and Room 405. The maximum tangential stress for Rooms 405 and 413 is 130 MPa and 110 MPa, respectively.
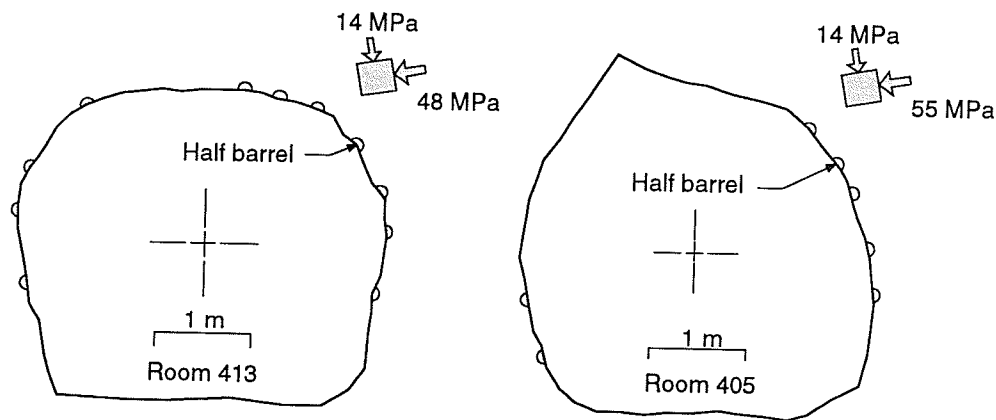
Figure 5.3: As-built profiles of Room 413 and Room 405. Note the classic v-shaped notch in the roof of Room 405 indicating spalling-type faliure.

strength σ_c, (220 MPa) or about 155 MPa. Hence, the long-term unconfined strength *in situ*, $\sigma_{c_{lt}}$, will be taken as 150 MPa which is slightly lower than the lowest failure load of 155 MPa found by Schmidtke and Lajtai [140]. This is considerably lower than the short-term unconfined compressive strength, σ_c, of 220 MPa which is considered representative of Cold Spring Quarry samples. The $\sigma_{c_{lt}}$ value of 150 MPa, is also very close to the unconfined compressive strength of "disturbed samples" from the 420 Level of the URL.

If we compare the calculated, maximum tangential stresses on the boundaries of Rooms 405 and 413 to the *in situ* strength value, $\sigma_{c_{lt}}$ of 150 MPa, one could safely assume that the tunnels are completely stable. Unfortunately, this is not the case as described above. If we take the tangential stress of 110 MPa for Room 413 as the limiting stress for failure we would conclude that the strength around the underground openings at the 420 Level of the URL is $\approx 0.5\sigma_c$ or $\approx 0.7\sigma_{c_{lt}}$.

Pelli et al. [125] also concluded from their analysis of the Donkin-Morien tunnel, a 7.6 m-diameter tunnel excavated in massive sedimentary rocks, that the strength in the local failure zones around the tunnel was about 0.5 to $0.6\sigma_c$. Similar findings have been reported elsewhere [117, 69], although in those cases it was not clear that the rock masses were free of fractures. Thus it appears that the experience at the URL is not unique, in that, failure

around the underground openings at the 420 Level occurs when the tangential stress around the openings is well below the short-term unconfined compressive strength, σ_c.

In the next section, the tunnelling experience at the 420 Level of the URL is compared with the tunneling experience from South Africa in massive brittle rocks.

5.2 South African Experience

Several attempts have been made in South Africa to quantify the stability of underground openings in massive brittle rock. Ortlepp et al. [123] used a simple far-field stress criterion and showed that for the case of 3- to 4-m diameter tunnels in quartzites minor spalling was first observed when the maximum far-field stress exceeded 0.2 of the uniaxial compressive strength (σ_c) and that heavy support was required if the far-field stress exceeded 0.4 of the uniaxial compressive strength. In the case of a circular tunnel in a hydrostatic far-field stress conditions the tangential stress concentration factor for the stress at the boundary of an excavation is 2. Here spalling will initiate when the tangential stress reaches about $0.4\sigma_c$.

Wiseman (see [151]) improved on this criteria by using the maximum and minimum in-plane stresses acting on the excavation and the uniaxial compressive strength to determine a relationship between the stress concentration factor (SF) and strength where

$$SF = \frac{3\sigma_1 - \sigma_3}{\sigma_c} \tag{5.1}$$

Wiseman noted that if the stress concentration factor exceeded 0.8 the amount of spalling around an excavation increased rapidly. At the excavation boundary $\sigma_3 = 0$ and Wiseman's criterion for spalling initiation reduces to $\sigma_1 = 0.25\sigma_c$.

Stacey [128] developed an extensional strain criterion to predict the failure based on

$$\epsilon_3 = \frac{1}{E}(\sigma_3 - \nu(\sigma_1 + \sigma_2)) \tag{5.2}$$

where E is the Young's modulus and ν is Poisson's ratio.

Solving for σ_1 gives

$$\sigma_1 = -\epsilon_3 \frac{E}{\nu} + \sigma_3 \left(\frac{1-\nu}{\nu} \right)$$

This gives a linear failure envelope similar to Mohr-Coulomb with the cohesion given in terms of E and ν. Stacey noted that the critical extensional strain at failure, ϵ_{cr}, could be found in laboratory samples by plotting axial strain against lateral strain. Stacey noted that such a plot produced an inflection point which represented the critical strain. Figure 5.4 is a plot of the axial and lateral strain for a sample of Lac du Bonnet granite from Cold Spring Quarry. Unfortunately it is difficult to determine an inflection point in this plot. Nonetheless Stacey was simply pointing out that crack initiation is first registered by the lateral strain gauge and not by the axial gauge. Thus under ideal conditions, i.e., the sample is essentially crack free, it may be possible to determine the crack initiation point by plotting the strains as Stacey suggested. It was demonstrated in Chapter 4 that the crack initiation stress can be easily determined by calculating the crack volume as shown in Figure 4.1. Stacey's values for critical strain typically occurred at 1/3 of the maximum strength obtained from the uniaxial compressive strength test, which implies that around the boundary of the opening failure would be observed at about $0.3\sigma_c$.

What is most interesting from the three South African criteria noted above is that all three indicate that spalling around an excavation will occur if the boundary stress is greater than about 1/4 to 1/3 of the uniaxial compressive strength.

Hoek and Brown [75] compiled case histories from South Africa where sidewall failures were observed in square tunnels in massive quartzite. They developed a simple classification based on the ratio of the far-field maximum stress (σ_1) to the short-term unconfined compressive strength σ_c. A $\sigma_1/\sigma_c = 0.1$ represented a stable unsupported tunnel, whereas a $\sigma_1/\sigma_c = 0.5$ represented possible rock burst conditions. Sidewall spalling was found to occur when $\sigma_1/\sigma_c > 0.2$. Their results are summarized in Figure 5.5. The stability of the openings on the 420 Level of the URL was assessed using the South African criterion
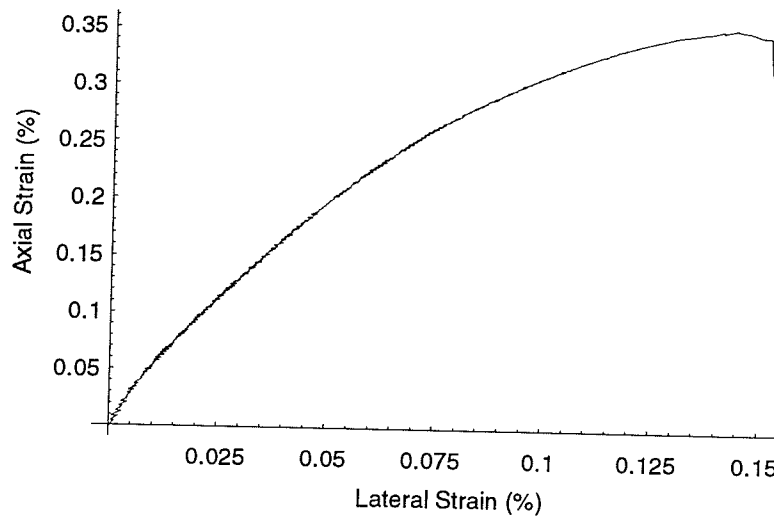
Figure 5.4: Plot of axial strain versus lateral strain for a sample of Lac du Bonnet granite from Cold Spring Quarry.

of Hoek and Brown, with $\sigma_c = 220$ MPa and the *in situ* stress $\sigma_1 = 55$ MPa, which gives $\sigma_1/\sigma_c = 0.25$. Thus, according to this criterion the openings on the 420 Level of the URL should experience minor to severe spalling (Figure 5.5) which agrees with the 420 Level observations.

5.3 Failure Processes in Physical Models

It is clear from the South African experience and from the experience at the URL, that the stability of underground openings cannot be assessed by comparing the laboratory unconfined compressive strength to the calculated tangential stress. In Chapter 3 it was shown that the strength around circular openings in the laboratory matches quite well the short-term unconfined compressive strength. Thus it appears that the laboratory tests do not replicate the loading path followed by the *in situ* rock mass. However, before this aspect is explored, it is instructive to examine the fracture patterns that develop around circular openings in laboratory physical model tests.

The stress distribution around a circular opening [84], for the conditions in Figure 5.6, is given by
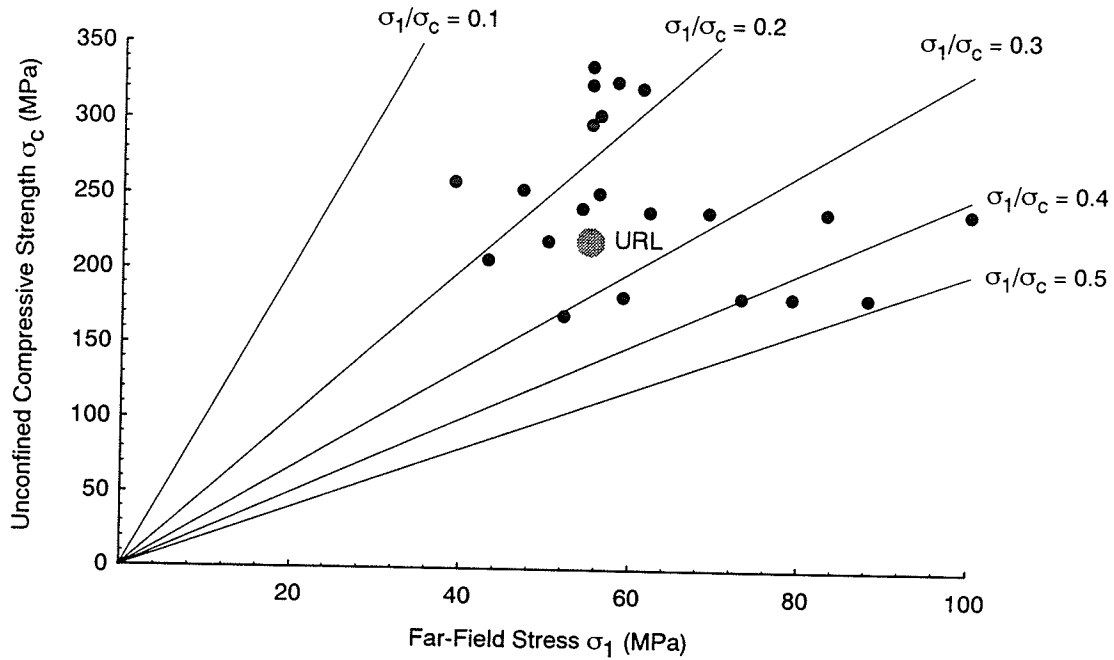
Figure 5.5: Stability of square tunnels in very good quality massive quartzite (after [75]).

$$\sigma_{\theta\theta} = \tfrac{p}{2}\left[(1+K)\left(1+\tfrac{a^2}{r^2}\right) + (1-K)\left(1+3\tfrac{a^4}{r^4}\right)\cos 2\theta\right]$$
$$\sigma_{rr} = \tfrac{p}{2}\left[(1+K)\left(1-\tfrac{a^2}{r^2}\right) - (1-K)\left(1-4\tfrac{a^2}{r^2}+3\tfrac{a^4}{r^4}\right)\cos 2\theta\right] \qquad (5.3)$$
$$\tau_{r\theta} = \tfrac{p}{2}\left[(1-K)\left(1+2\tfrac{a^2}{r^2}-3\tfrac{a^4}{r^4}\right)\sin 2\theta\right]$$

At the boundary of the opening $r = a$, and equation 5.3 reduces to

$$\sigma_{\theta\theta} = p\left[(1+K) + 2(1-K)\cos 2\theta\right]$$
$$\sigma_{rr} = 0 \qquad (5.4)$$
$$\tau_{r\theta} = 0$$

Thus, for the unconfined case $K = 0$ and the tangential stress at the zone of spalling in the sidewall is $3p$ and the tangential stress in the zone of tension in the roof is $-p$.

The failure process around the an underground opening in brittle rock is usually described as spalling or slabbing, and the shape of the failed zone is commonly called, well-bore breakout, "dog-ear" or v-shaped notch. Researchers [72, 54, 55] using physical model studies demonstrated that the spalling fracture initiates a complex process of progressive
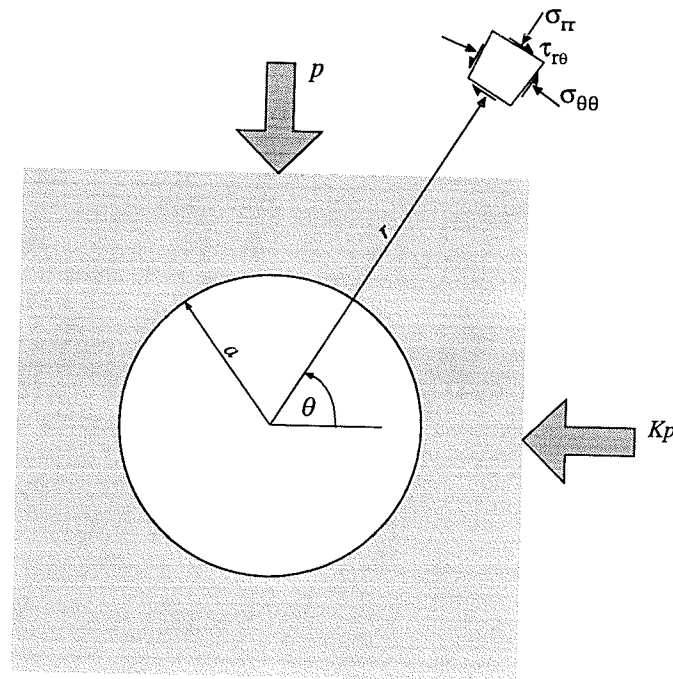
Figure 5.6: Notation for equations 5.3 for a circular opening in a biaxial stress field.

failure which can lead to the collapse of an opening. This failure process occurs in the zone of maximum compression around the opening and is the process mostly common observed in underground openings. However, investigations in the laboratory have identified two other types of fractures around circular openings: tensile or primary fractures and secondary or remote fractures (Figure 5.7). Hoek [72] carried out biaxial compression tests on chert and noted all three types of fractures around a 19 mm diameter circular opening. Hoek [72] also demonstrated that the primary fracture only propagated a short distance from the opening because the stresses at the tip of this fracture become compressive a short distance away from the opening. However, the initiation and propagation of the primary fractures do cause local stress redistribution which means that it is not possible to predict the final fracture configuration from an examination of the elastic stress distribution around the unfractured opening. Hoek found that the remote fractures form after the primary cracks initiate and are found in the regions of tensile stress. Hoek suggested that these remote fractures result
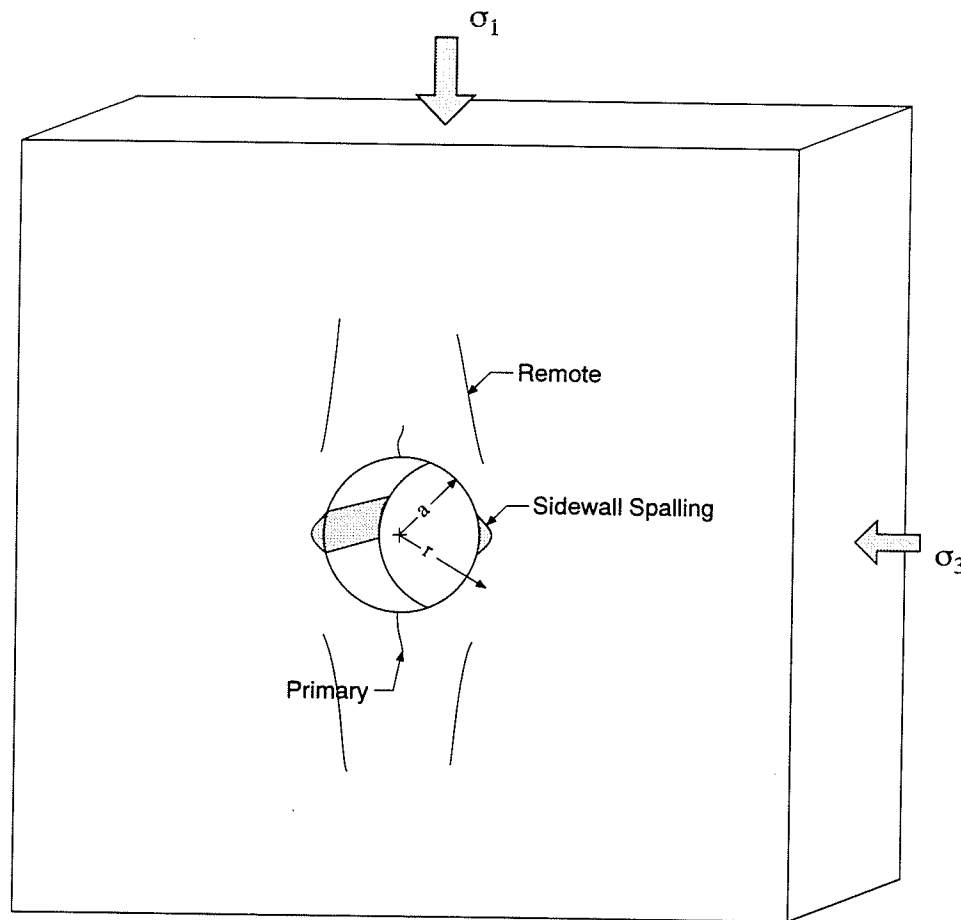
Figure 5.7: Types of fractures found around circular openings in laboratory model tests.

from the stress redistribution caused by the primary fractures.

Hoek [72] found that the remote fractures occurred after the primary fractures but before the sidewall fractures. However, other researchers [119, 99] have found that the remote fractures occur after the sidewall fractures provided the samples are subjected to a biaxial stress (Figure 5.8). Carter et al. [25, 22] also found, for the unconfined case, that the remote fractures occur before the sidewall fractures. The unconfined model studies reported in Chapter 3 also support the notion that the remote fracture occurs after the primary fracture has developed but before the spalling fracture initiates (see Table 3.3).

One block of Lac du Bonnet granite from the 420 Level of the URL was tested with
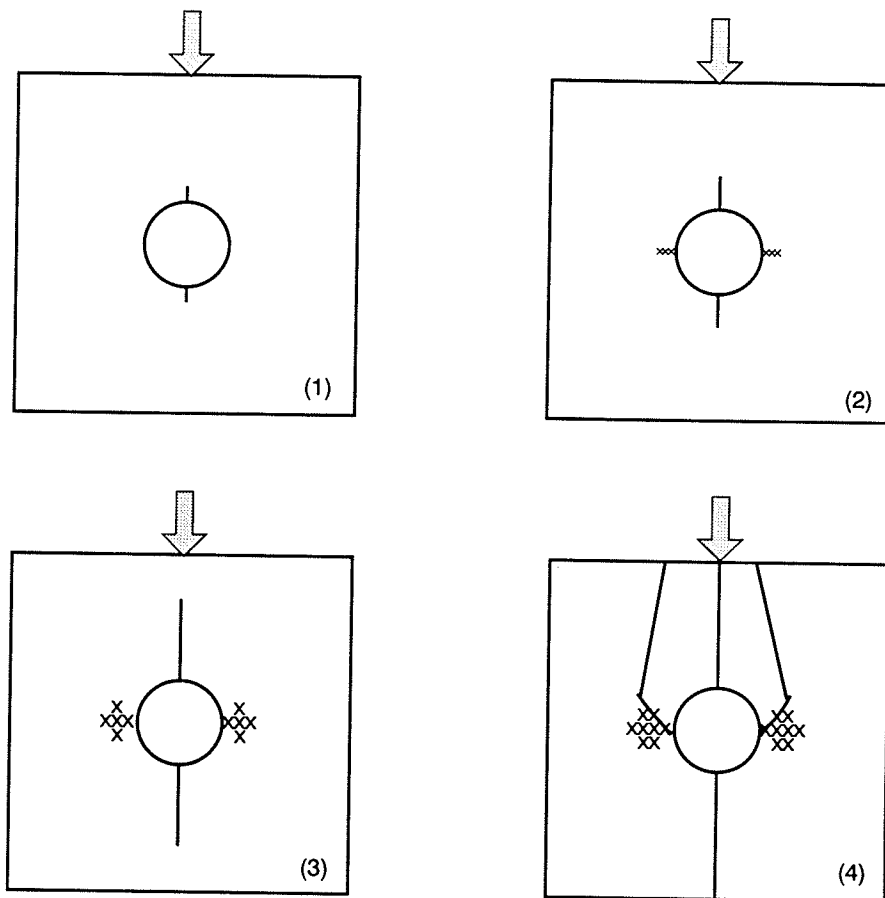
Figure 5.8: Evolution of primary, sidewall and remote fractures around circular openings in laboratory model tests at low confining stress. The "x" pattern at the sidewall of the opening denote the area where crushing occurred (after [99]).

a confining stress close to the 14 MPa minimum stress found *in situ* to investigate the formation of fractures around a biaxially loaded opening. The block dimensions had to be selected taking regard of the limitations of the 5.3 MN capacity loading frame. Hence the opening diameter was also constrained in size, because the distance from the opening to the edge of the block needed to be sufficient to minimize boundary effects. Based on the results from the unconfined tests a hole diameter of about 60 mm produced only modest scale effects. These constraints gave a block dimension of 343 × 345 × 103 mm with a hole diameter of 60.7 mm (Figure 5.9). The block was biaxially loaded but unconfined in the direction perpendicular to the opening axis and the strain gauges used to detect sidewall spalling and tensile fracturing placed inside the opening.

The block was initially loaded by increasing the axial load and the confining load simultaneously to 15 MPa. The confining stress was maintained at 15 MPa using a manually operated hydraulic ram as the axial load increased. The deviatoric load on the block at which spalling initiated was about 66 MPa (Figure 5.10). Using equation 5.3, the stress at the sidewall of the opening where failure is occurring is about 228 MPa. This value is about 1.5 times greater than the unconfined compressive strength of 149 MPa given in Table 2.3 for the 420 Level granite. This is in keeping with the maximum scale effects found in the unconfined model study for a 60 mm diameter hole (see Figure 3.15). It should be noted however, that the 66 MPa deviatoric load represents the initiation of yielding and that the sample was subjected to deviatoric loads greater than 110 MPa without collapsing the opening. At a deviatoric load of 86 MPa sidewall spalling was clearly visible. The final shape of the opening is given in Figure 5.11.

The strain gauge pattern used to monitor the sample provided sufficient information to determine the sequence of fracturing while applying the load. An example of the strain gauge response is given in Figure 5.12. In this case the remote fractures occur after the sidewall spalling. This is opposite to the situation for the unconfined blocks where the remote fractures occur before the sidewall spalling. The major difference between the unconfined
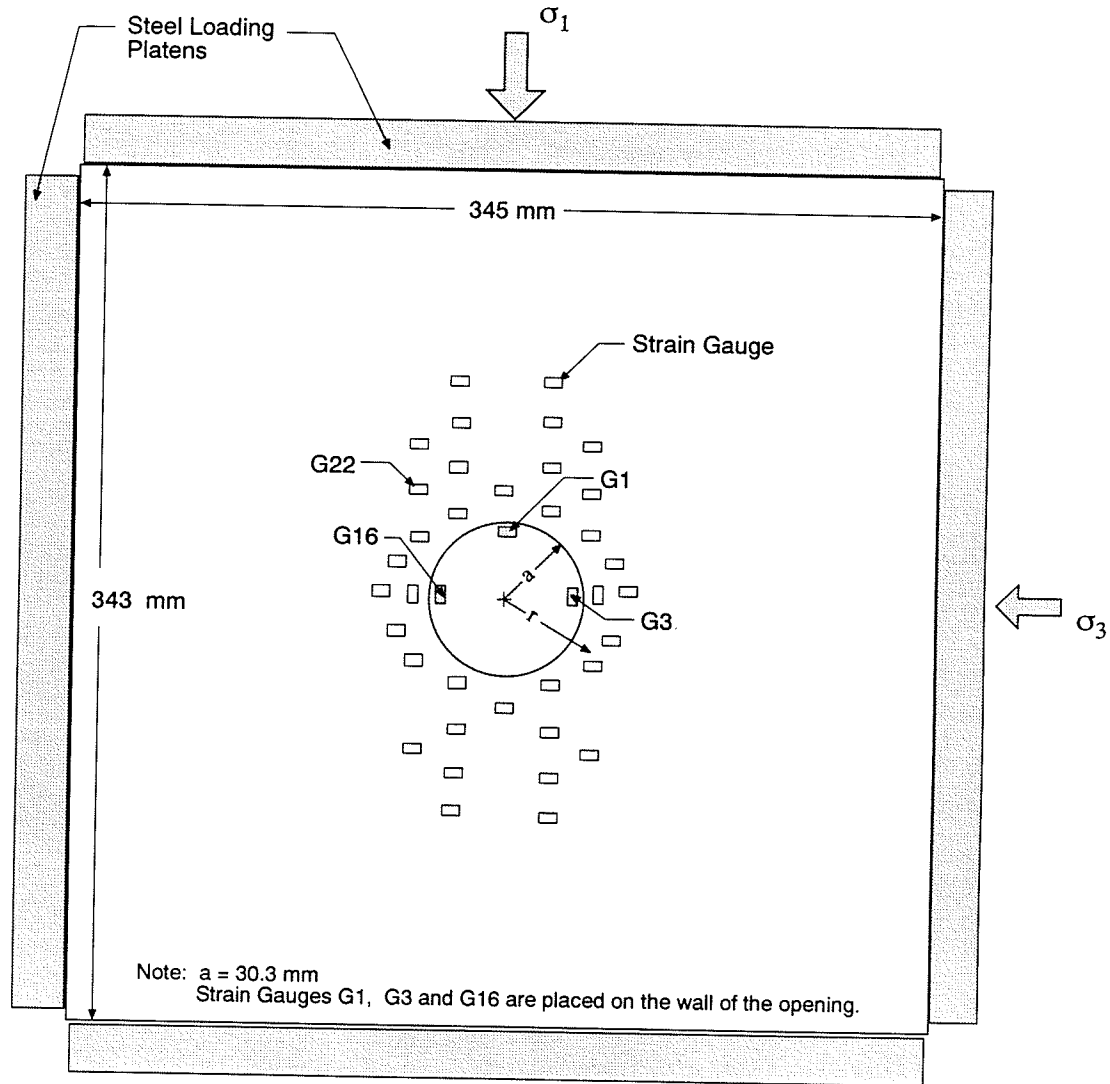
Figure 5.9: Test set up for confined block ($\sigma_3 = 15$ MPa) of Lac du Bonnet granite taken from near the entrance of the Mine-by test tunnel at the 420 Level of the URL.
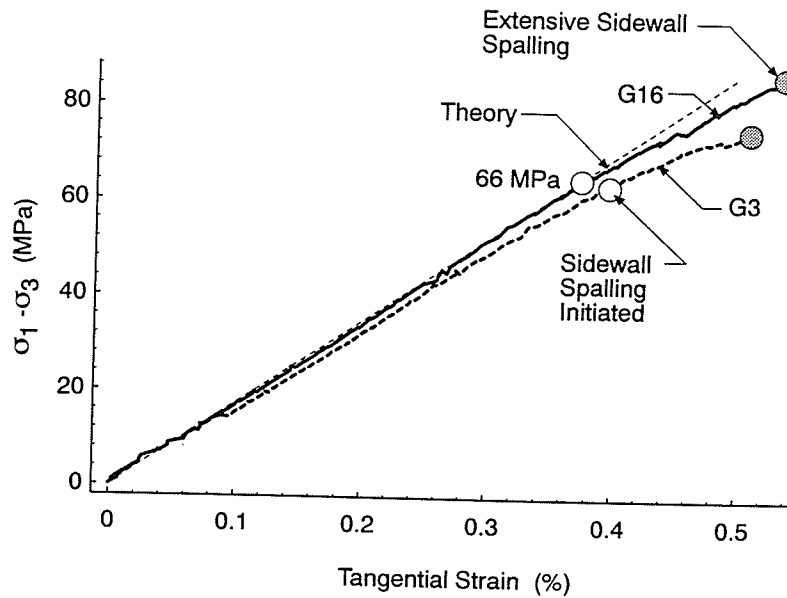
Figure 5.10: Tangential strains versus the deviatoric loads for a block with $\sigma_3 = 15$ MPa. See Figure 5.9 for the the strain gauge locations.
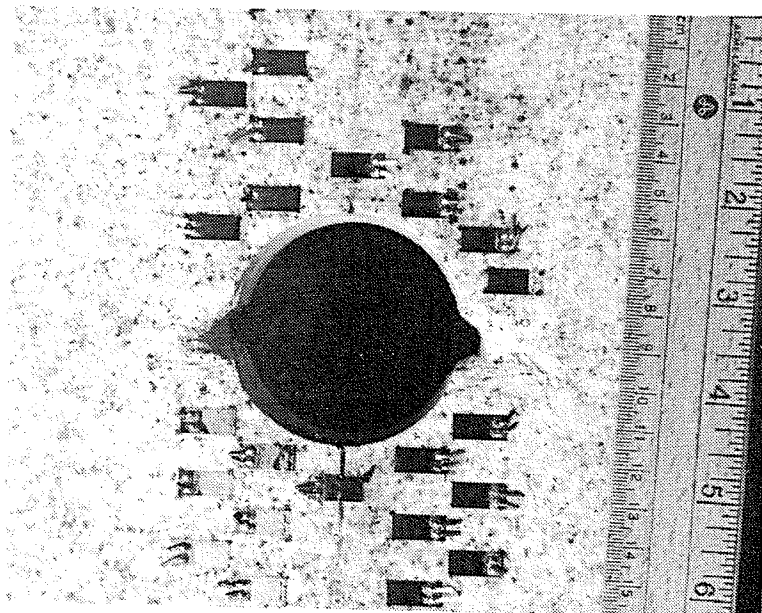
Figure 5.11: Shape of the opening after axial loading to 110 MPa. Sidewall spalling initiated at axial loads of 66 MPa but collapse of the opening did not occur. Note the characteristic "dog ear" shape of the zone subjected to sidewall spalling.
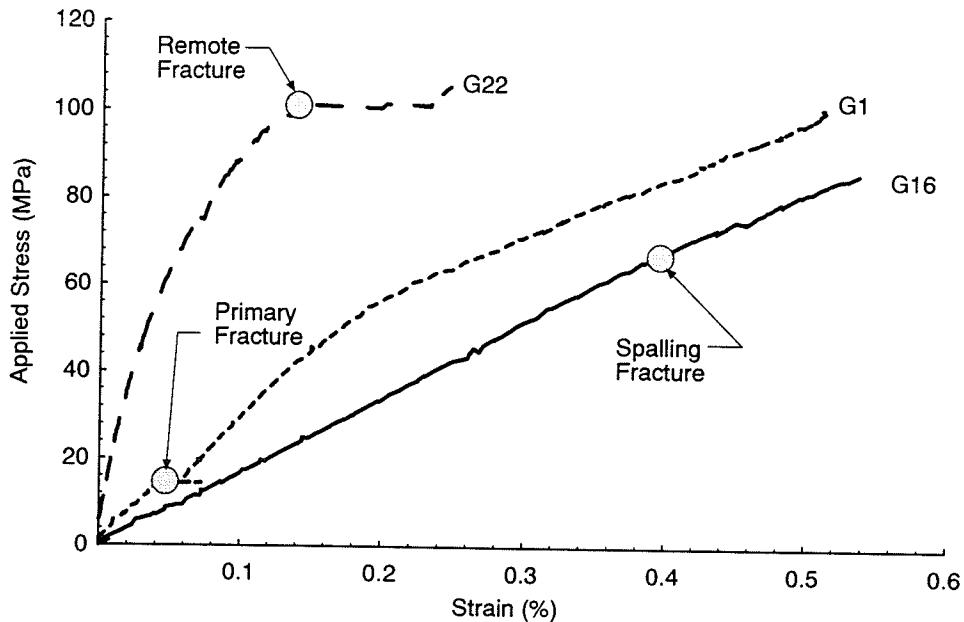
Figure 5.12: The fracture sequence found during the testing of the confined sample. Note that the remote fracture occurs after the sidewall spalling.

and confined tests is that in the confined case the primary fractures only extend a short distance, about $1a$, beyond the opening whereas in the unconfined blocks the primary fracture extends about $4a$. Thus, the stress redistribution caused by the primary fractures plays a role in controlling the sequence of the remote and sidewall fractures. These laboratory results may explain why remote fractures have not been reported found *in situ*.

The model studies carried out on samples of Lac du Bonnet granite illustrate two important points.

- The strength around the circular openings, in both the confined and unconfined tests, is slightly above the measured short-term unconfined compressive strength and therefore offers no solution to the observed stability issue discussed earlier.

- The occurrence of fracture patterns around an underground opening may be influenced by local stress redistribution caused by the formation of the first fractures.

In the laboratory the fracture patterns are mapped by strain gauges. However, *in situ*

other techniques, such as microseismic monitoring, are used to map fracture locations. In the next section, this technique was used to locate fractures around a circular tunnel on the 420 Level.

5.4 Microseismic Monitoring

It is well known that cracking, i.e., damage, occurs around an opening excavated in a highly stressed brittle medium [35, 34]. Two examples, of extreme scales, are the process zone around the tip of an advancing crack [127, 94] and the cracking associated with deep-level mining [1, 85]. The energy released by this cracking process underground is referred to as excavation-induced seismicity. Earlier work at the URL had established that considerable microseismic activity was associated with the sinking, by drill and blast techniques, of a circular shaft from the 240 Level to the 420 Level [149]. In order to determine if the microseismic activity was caused by the blasting or simply related to stress redistribution, a test tunnel for the Mine-by Experiment was excavated without the use of blasting on the 420 Level of the URL.

5.4.1 Test Tunnel Excavation

The 3.5-m-diameter test tunnel had a circular profile and was excavated parallel to σ_2 (Figure 5.13). This configuration provided the maximum stress concentration in the roof and floor of the tunnel. The tunnel was excavated in 1-m and 0.5-m increments (Figure 5.14) using perimeter line drilling and mechanical breaking of the rock stub [122]. Excavation of each increment could be completed in two 8-h shifts, but experimental activities constrained progress to 1 round about every 3 days. The temperature of the test tunnel was maintained at the ambient rock temperature of 10.5°C ±0.5° and > 90% relative humidity by an air conditioning unit. Extensive state-of-the-art geomechanical instrumentation was installed prior to the start of the excavation, and was used to monitor the complete mechanical response of the rock mass around the tunnel [129].
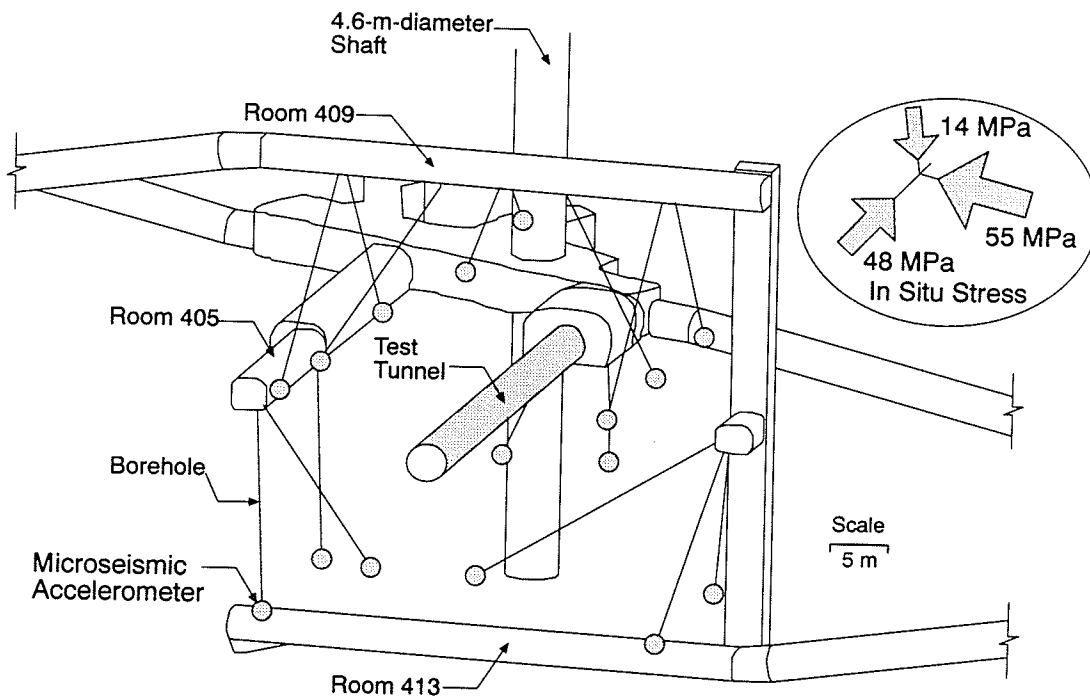
Figure 5.13: Location of the Mine-by test tunnel and the microseismic triaxial accelerometers on the 420 Level.
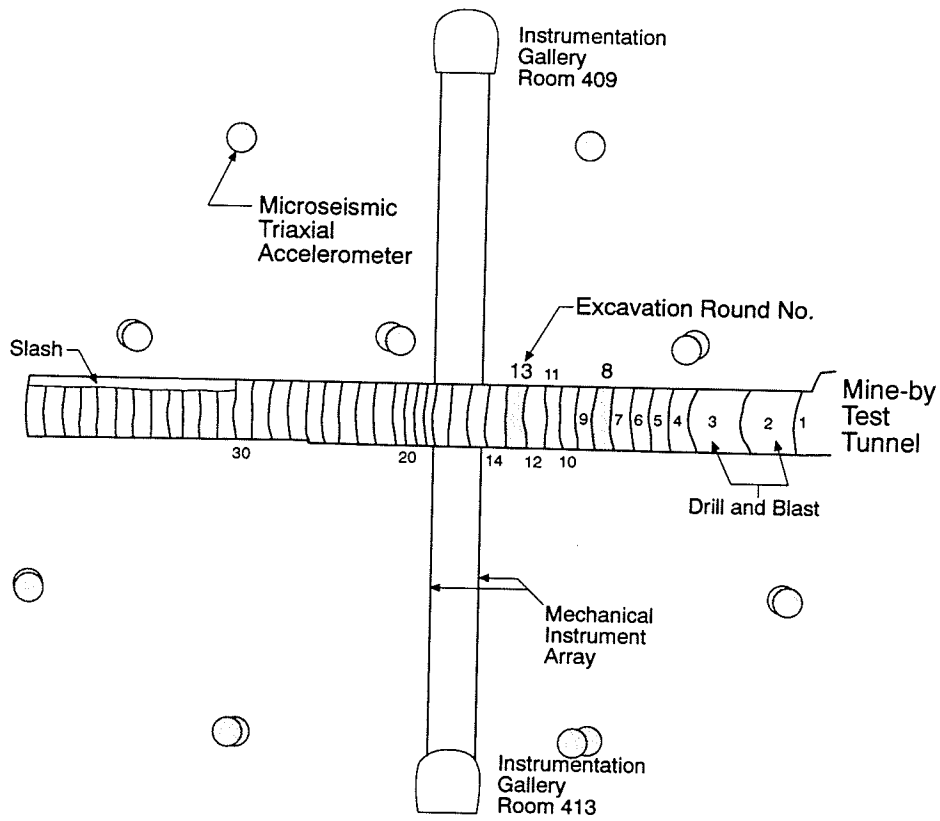
Figure 5.14: Vertical cross section through the test tunnel showing the location of microseismic triaxial accelerometers and the location of Rounds 8 and 13. The spatial distribution of the accelerometers can be seen in Figure 5.13.

The Mine-by test tunnel was excavated over a six month period. Failure in the roof and floor was observed immediately as each excavation round was taken and progressed as the test tunnel was advanced. Figure 5.15 illustrates the development of the notch in the roof over about a five month period. The progressive development of the notch in the floor is not available because the floor always contained "tunnel muck" until the tunnel advance was completed. However, the final shape of the notch in the floor is very similar to the notch in the roof. The dates given in Figure 5.15 do not reflect the actual times required for the notch to develop but the dates of the actual notch survey. The thickness of the spalling slabs which created the notch varied from a few mm to tens of mm and there did not appear to be any preferred direction of slabbing, i.e., the slabs formed on both sides of the notch. Regardless of the process causing the notch development the orientation and geometry of the notch was consistent from the start of the test tunnel to the end of the test tunnel and this orientation is consistent with the 14° plunge of σ_1 (Figure 5.16).

5.4.2 Microseismic Events and Observations

An array of 16 triaxial accelerometers was also installed to monitor the microseismic events associated with the excavation [111]. The accelerometers, with a frequency response from 50 Hz to 10 kHz (±3 dB), were grouted in place at the end of diamond-drilled boreholes (Figure 5.13). The accelerometer array was designed for focal sphere coverage and a source location accuracy of about ±0.25 m near the centre of the tunnel. The sampling rate was set to 50 kHz, allowing the study of seismic events with moment magnitudes as small as -6. The sequencing of the construction schedule for the test tunnel provided about 12 h of quiet time for monitoring after the initial perimeter drilling and about 12 h of quiet time for monitoring after mechanical breaking of the rock stub. This provided a total of about 24 h of monitoring per round of tunnel advance.

Preliminary processing of the microseismic data was carried out in the field using automated source location computer software developed at Queen's University [31]. Some 25000
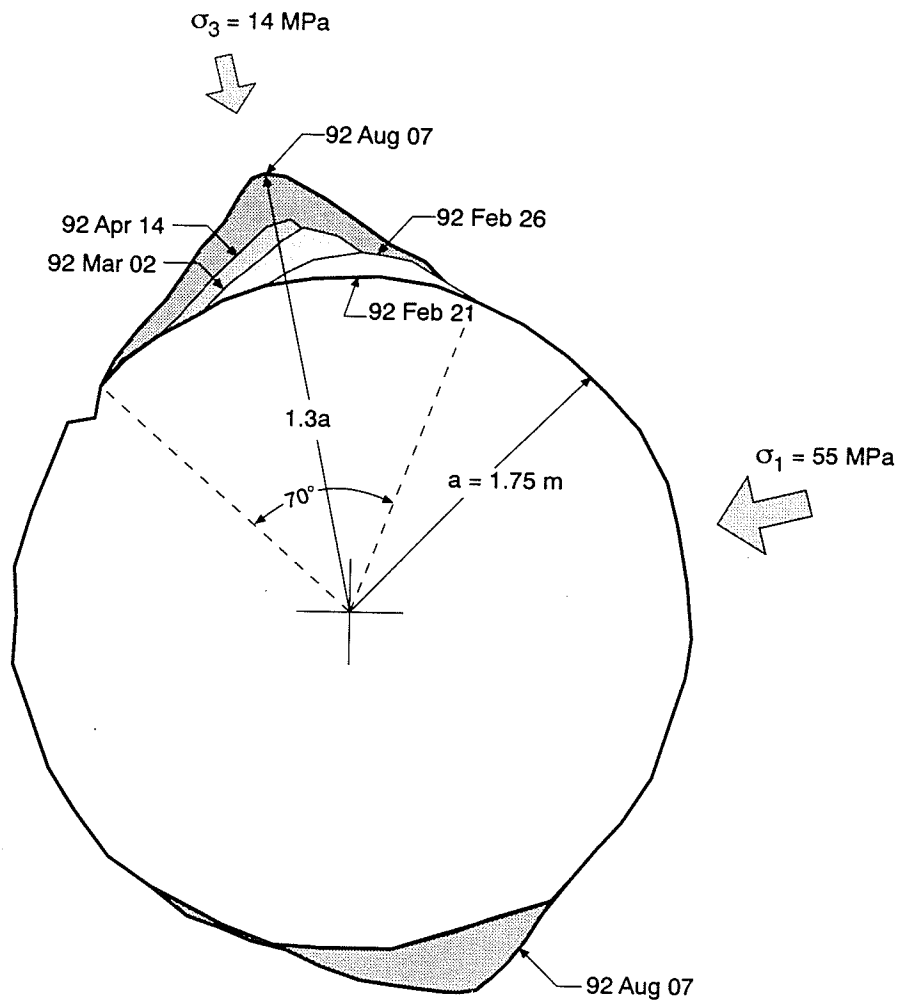
Figure 5.15: Progressive development of the notch geometry in the roof and floor of the Mine-by test tunnel over a five month period.

Figure 5.16: Mine-by test tunnel after excavation. The notch geometry observed in the roof and floor was caused by the spalling process.

events were source located. Inspection of all 46 rounds showed similar trends. Figure 5.17 is an example of the spatial location of the microseismic events recorded at the end of one round. Note the clustering of microseismic events in the areas where the spalling will eventually occur.

A detailed analysis of Round 13, located near the centre of the tunnel, was carried out by manual picking of the first P and S wave arrivals [111]. This process improves the source location accuracy considerably. In addition to the microseismic data, detailed survey information on the development of the notch geometry is also available for this round. The location of Round 13 is shown in Figure 5.14.

The perimeter drilling was carried out in the pattern shown in Figure 5.18 for Round 13. The perimeter drilling started at the bottom of the tunnel at point A, and went clockwise to point B. The perimeter drilling then started at point A and went counter clockwise to point C. During the perimeter drilling, cracking was commonly observed as the drilling approached the roof where the maximum stresses were concentrated. Figure 5.18 shows the 47 microseismic events recorded over a 10-h period immediately after the perimeter drilling was completed. During this period the events do not show strong clustering, although there is a slight grouping of events where the notch is eventually first observed. Note that the first notch is near vertical, yet the stress orientation would suggest that the notch should be off-centre by 14° (Figure 5.18). It appears that the sequencing of the perimeter drilling may play some role in defining where the notch initiates.

After the initial microseismic monitoring period the rock stub shown in Figure 5.18 was broken out, from the bottom to the top, using mechanical hydraulic rock splitters. This process took about 6 h. After the rock stub was removed, 52 new microseismic events were recorded during a 16-h monitoring period (Figure 5.19). These events show strong clustering in the roof, slightly ahead of the existing notch and particularly where the notch eventually occurred. Feignier and Young [51] analyzed the microseismic events from Round 3 of the test tunnel and found, using a moment tensor inversion technique, that all of the events
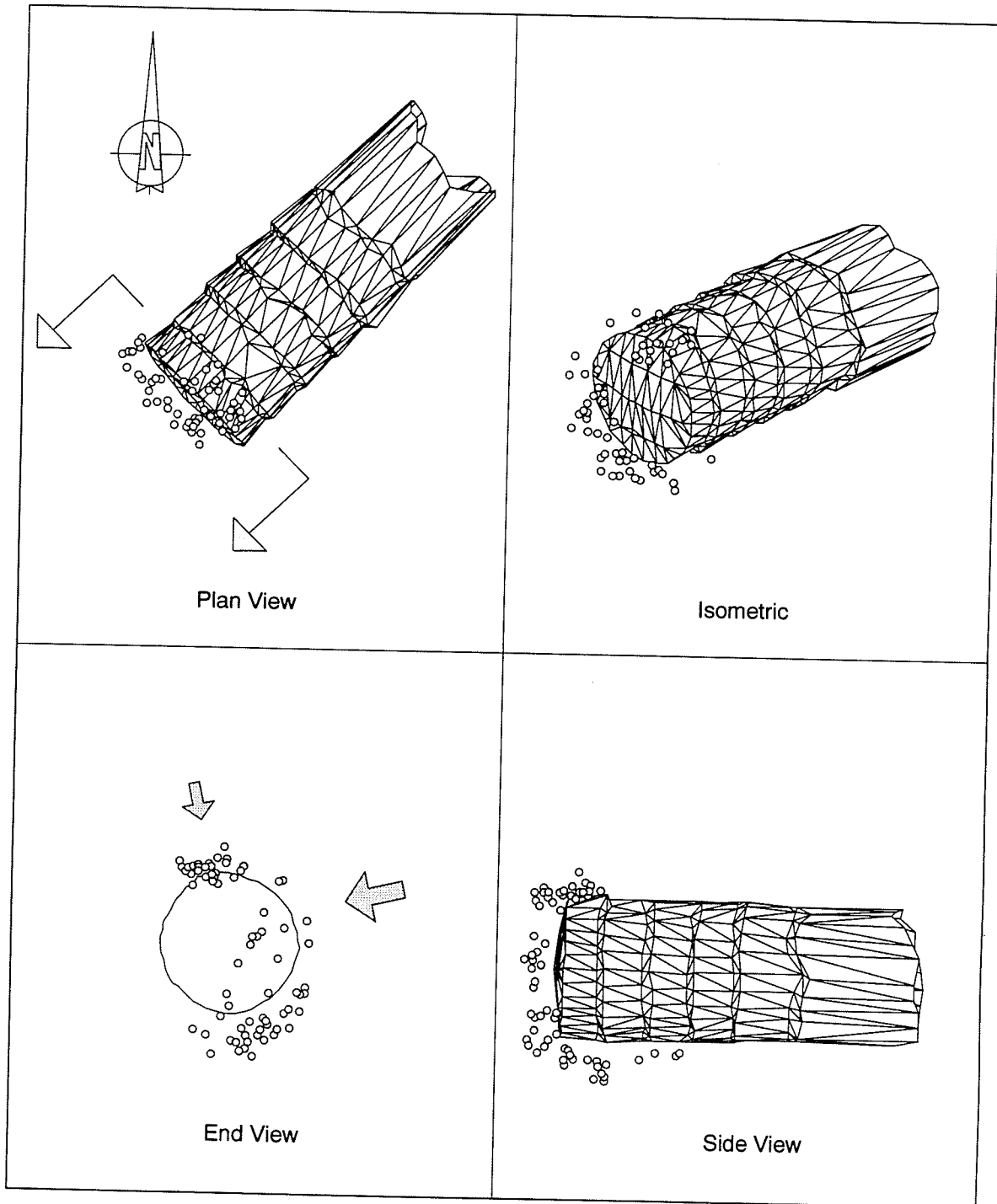
Figure 5.17: Location of microseismic events at the end of Round 8. Note that cracking is occurring ahead of and around the advancing face.
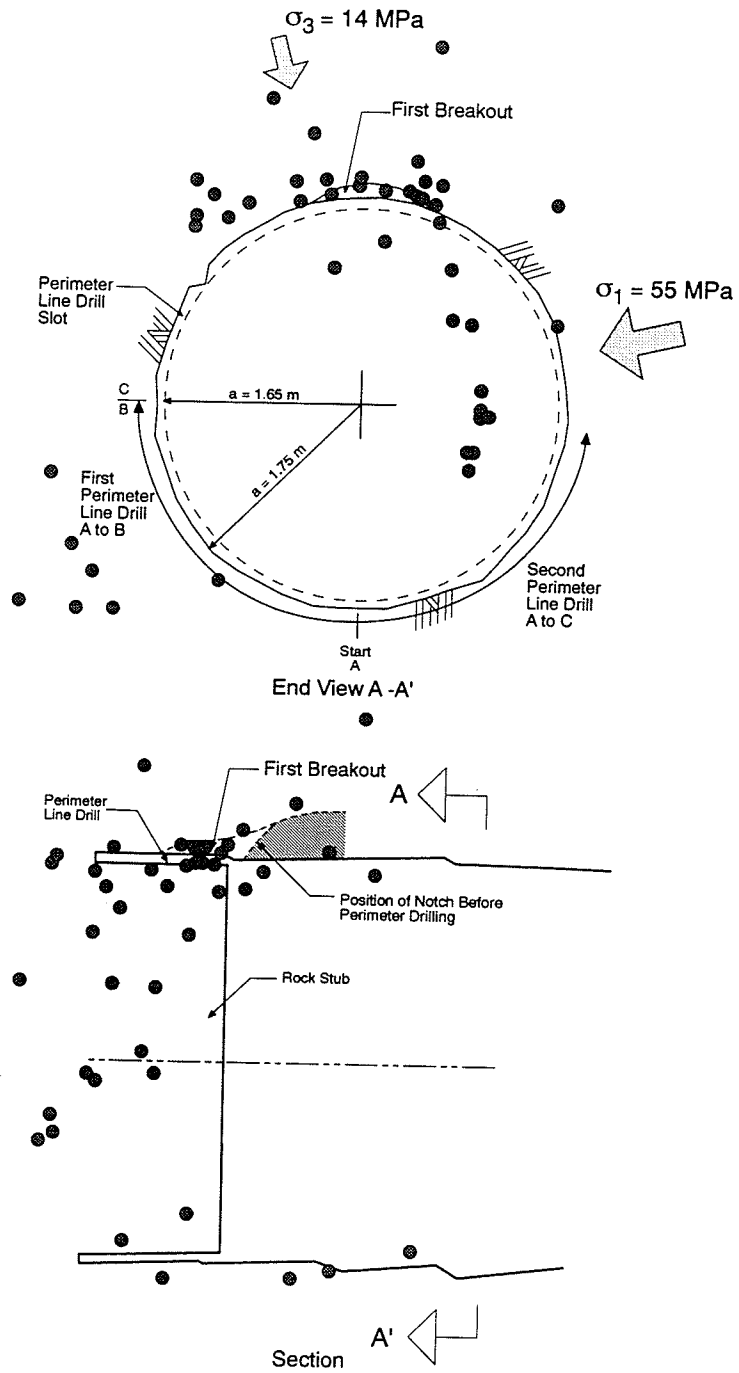
Figure 5.18: Location of microseismic events at the end of perimeter drilling of Round 13. Note the slight clustering of events in the roof where the first notch eventually appears.

located where the notch eventually occurred were dilational (see Figure 5.14 for location of Round 3).

It would appear that the concentration of induced seismic events near the tunnel face is defining the region where the notch geometry will appear. This concentration of events might be considered similar to the process zone ahead of an advancing crack tip [94]. Visual observations during notch development indicate a process zone does develop at the apex of the notch. Note that the dates in Figure 5.19 do not reflect the actual times required for the notch to develop but the dates of the actual notch survey. The development of the notch was related to the advancement of the tunnel and to the scaling carried out for safety reasons. It should also be noted that the formation of the notch is not evident at the tunnel face because of the 3D geometry, but starts forming about 0.75 to 1 m back from the tunnel face, and is fully developed 2 m back from the face.

It should be noted that in the preceding discussion and in Figures 5.18 and 5.19, the majority of the microseismic events are concentrated only in the roof of the tunnel. In fact microseismic events also show the same clustering in the floor but it occurs after the tunnel has advanced another round. Thus the clustering in the roof and floor is offset by about 1 m along the tunnel axis. This time lag for the floor events is due to the confining stress provided by the weight of the tunnel muck in the floor.

Another feature of the excavation rounds investigated is the induced seismicity occurring ahead of the tunnel face (Figure 5.19). Presumably this damage is occurring because of the stress concentrations caused by the tunnel face. The moment magnitudes for the events associated with Figure 5.19 ranged from -6 to -4 (Figure 5.20). It should be noted that the microseismic events in Figures 5.19 and 5.18 are not the only crack related events taking place around the test tunnel, but merely the events recorded by the 16 triaxial accelerometers. For example, Carlson and Young [21] recorded, using 1 MHz transducers, over 720 microseismic events in the sidewall of the test tunnel during a 13 h monitoring period. Hence, the damage is probably associated with microseismic events that have a
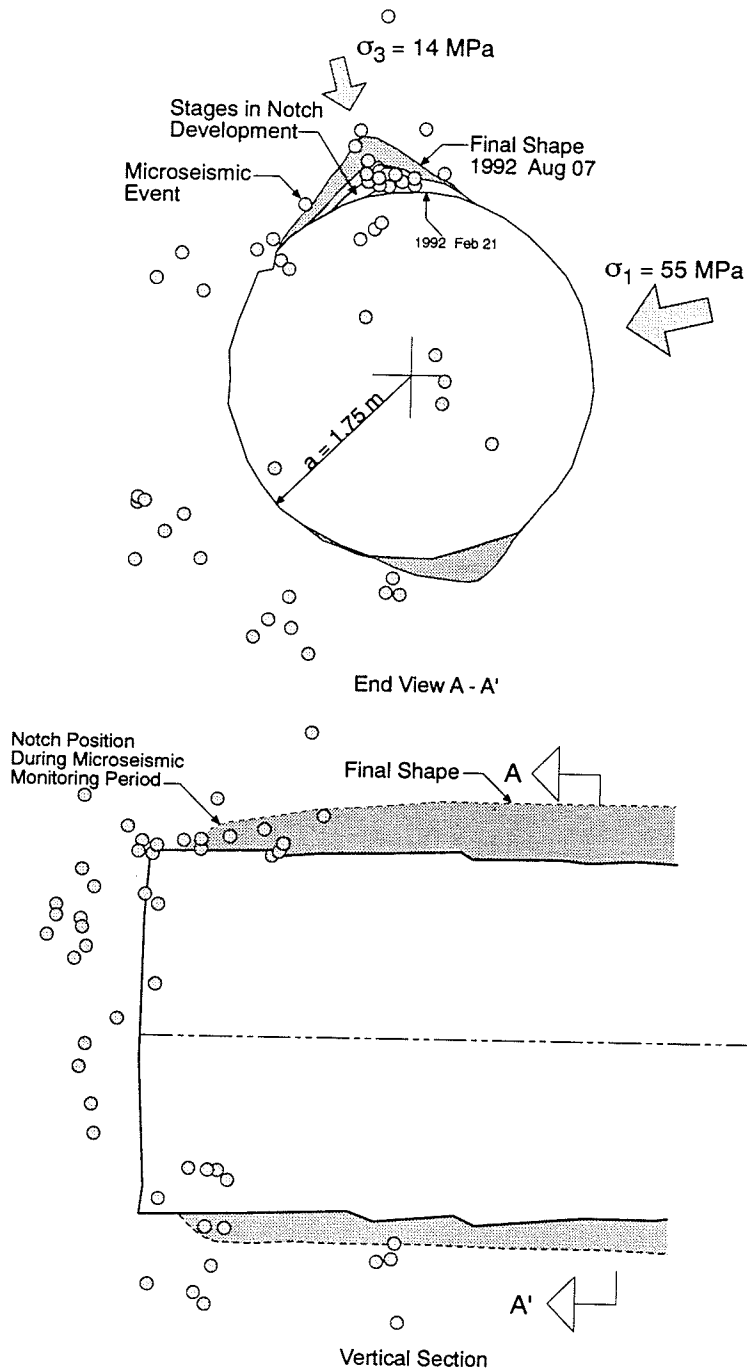
Figure 5.19: Location of microseismic events at the end of Round 13. Note the strong clustering of events in the roof where the notch will eventually develop. Also note the cracking occurring ahead of the face.
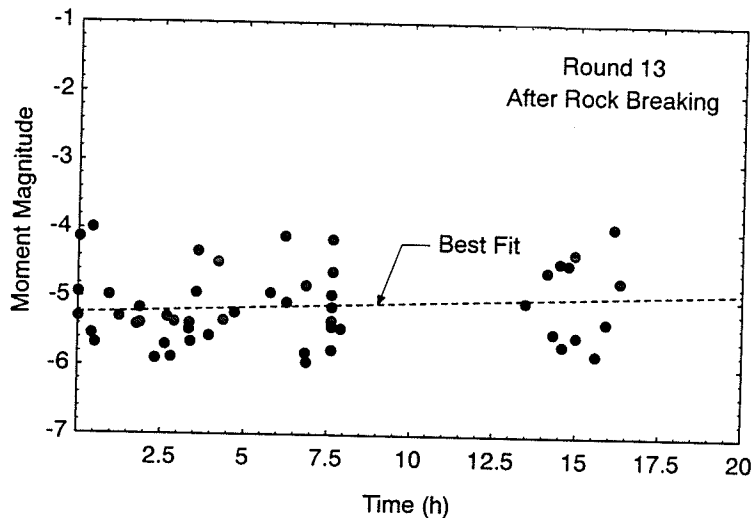
Figure 5.20: Moment magnitudes for the microseismic events recorded at the end of Round 13.

wide range of moment magnitudes. Similar cracking has been observed in the deep mines of South Africa [85], although the damage at the URL is small by comparison.

The microseismic monitoring has shown that cracking in the regions of maximum tangential compression starts ahead of the advancing tunnel and continues until the tunnel stabilizes, i.e., until the spalling stops. Unexpectedly, no microseismic events were recorded in the areas of tensile cracking or remote cracking as seen in the physical model studies. Also, the tensile fracture was not visually observed on the wall of the test tunnel. It is possible that the tensile strains in the sidewall of the tunnel are accommodated by existing flaws such that no single tensile crack appears. Another possibility is that the damaged skin has a $E_c/E_t = 2$ [28] where E_c is the Young's modulus in compression and E_t is the Young's modulus in tension. This could result in reduced tensile stresses. However, in the case of the remote fracture it is likely that the stresses are simply not large enough to produce the remote fractures *in situ*.

In Section 5.1 it was demonstrated that the strength around the underground openings at the 420 Level of the URL is considerably less than that measured in the laboratory.

However, it was also shown in Chapter 4, that the strength of intact rock is a function of its loading history. For example, if the rock around an underground opening has been damaged by the advancing tunnel, then according to the Griffith locus of sliding the cohesion of the intact rock will be considerably less than that given by the undamaged samples. In the laboratory testing program in Chapter 4 the cohesion was found to reduce to about 25% of its initial value after small amounts of damage. It is now clear that considerable damage is occurring around the underground openings at the 420 Level of the URL as the tunnels are excavated.

5.5 In Situ Crack Initiation

The microseismic monitoring provides a means of determining where cracking is occurring *in situ*. It also provides an opportunity to determine an in situ failure envelope. A three dimensional stress analysis was carried out using Examine^{3D} to determine the stress state at the event source (Figure 5.21). Figure 5.22 shows the calculated stress magnitudes at the microseismic events for Round 8 (see Figure 5.14 for location). The σ_1 magnitude at which cracking is occurring is fairly low, about 73 MPa, and appears to be only slightly dependent on σ_3. The laboratory testing showed that the crack initiation stress which was the first sign of cracking in compression loading occurred at about 49 MPa and was only slightly dependent on the confining stress (see Figure 4.14). The crack initiation stresses obtained from the laboratory tests is also shown in Figure 5.22 and shows the same general trend as the stresses calculated at the microseismic events but at a lower intercept. It was pointed out in Chapter 2 that the samples from the 420 Level are disturbed. Hence, it is suggested that the lower crack initiation stress in the laboratory, compared to the crack initiation *in situ*, is caused by this sample disturbance, i.e., the *in situ* material is stronger.

The Griffith [60] failure criterion is one of crack initiation and is given by

$$(\sigma_1 - \sigma_3)^2 = 8\sigma_t(\sigma_1 + \sigma_3) \tag{5.5}$$
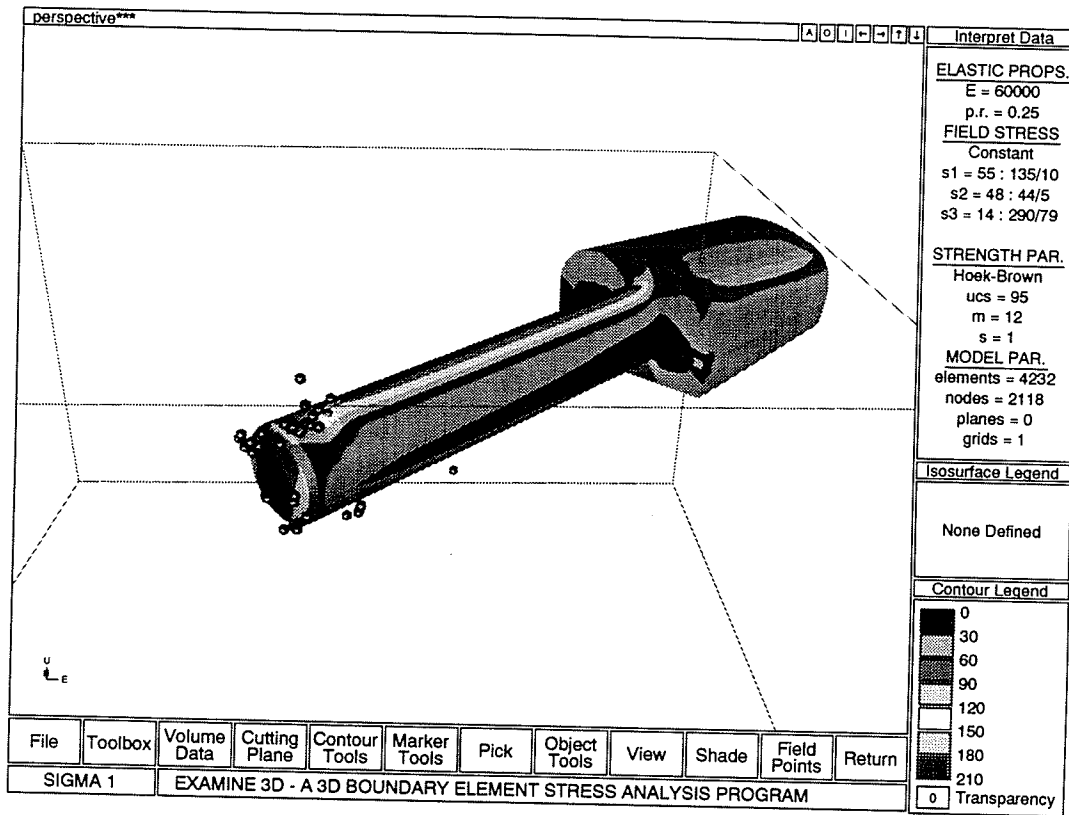
Figure 5.21: Example of the Examine³D model used to determine the stress state at the microseismic event locations. The microseismic events are shown as small spheres near the face of the tunnel.
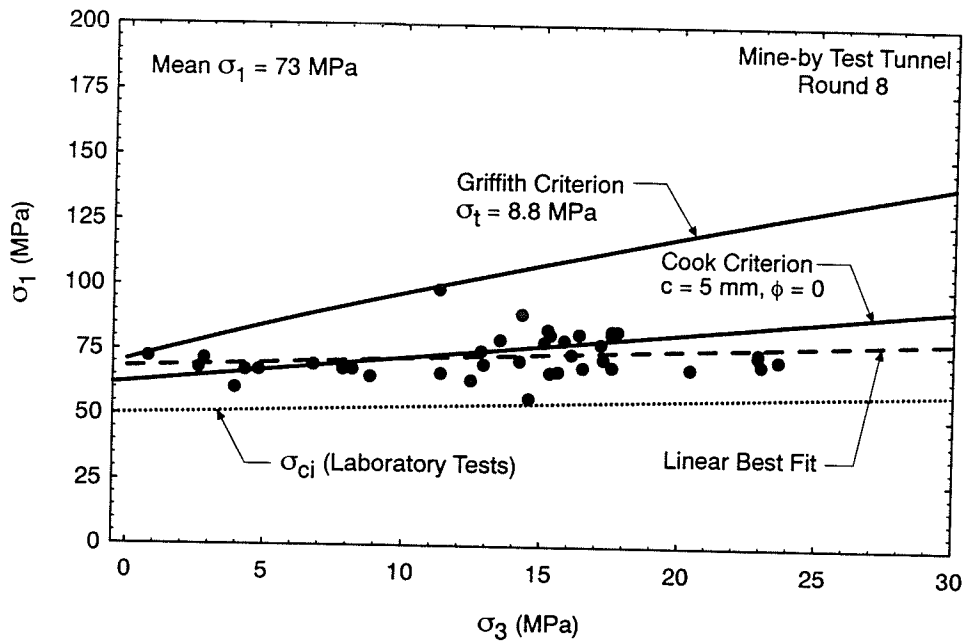
Figure 5.22: The stress state at the microseismic events recorded for Round 8 from the Mine-by test tunnel. The data are compared to the Griffith and Cook failure envelopes and the σ_{ci} locus from the damage-controlled laboratory tests.

where σ_t is the tensile strength. Hence the cracking events examined were not coming from the notch but from events ahead of and very close to the tunnel face, consequently, this cracking could be considered crack initiation. Figure 5.22 shows the Griffith failure envelope for a tensile strength of 8.8 MPa. The Cook failure envelope, equation 4.14, is also provided in Figure 5.22. In this case the friction component of the failure envelope is set to $\phi = 0$ to indicate that friction has not been mobilized. A crack length of 5 mm for the Cook failure envelope gives a much better fit to the data than the Griffith failure envelope. The results imply that only the cohesion portion of the failure envelope is affected by this cracking and that this cracking is only slightly dependent on confining stress.

A similar analysis was carried out for Round 13 from the Mine-by test tunnel. In this case the microseismic events were divided into two groups, the events which occurred ahead of the tunnel, and the events which occurred around the tunnel. It should be noted that

for both round 8 and 13 the events are all located with about ± 2 m of the tunnel face. Figure 5.23 shows a similar pattern to Figure 5.22 and again suggests that the cracking registered by the microseismic events is only affecting the cohesion component of the failure envelope, i.e., friction is not being mobilized in this early stage of the failure process.

The stress analyses presented in this section show that the failure process begins by crack initiation, and it appears that this initiation is only slightly dependent on confining stress. This finding is in many way similar to the laboratory findings presented in Chapters 3 and 4 where it was also shown that crack initiation was the first stage in the failure process and that it also was only slightly dependent on confining stress. It should also be noted that the microseismic events, i.e., crack initiation, are located in the regions of maximum deviatoric stress which are shown in Figure 5.24.

5.6   Mechanisms Causing In Situ Damage

Creating an underground excavation causes the rock near the face of the advancing excavation to follow a complicated loading path. In many situations the maximum stress at a point will increase, unload and subsequently increase again as the tunnel advances towards the point and passes it, while at the same time the minimum stress goes to zero. The loading path near the tunnel face cannot be duplicated in the laboratory at any reasonable scale because in addition to the change in stress magnitude near the face the principal stress directions are also changing. In the preceding section it was shown that cracking is occurring around the face of an advancing tunnel. In this section two possible factors are explored to explain the causes for the *in situ* cracking: face effects and stress rotation.

5.6.1   Face Effects

Numerical analyses using the three dimensional boundary element programs MAP3D [157] and Examine^{3D} [36] were carried out to investigate the change in stress magnitude near the face of an advancing tunnel. All numerical analyses were carried out on a 486 PC and the
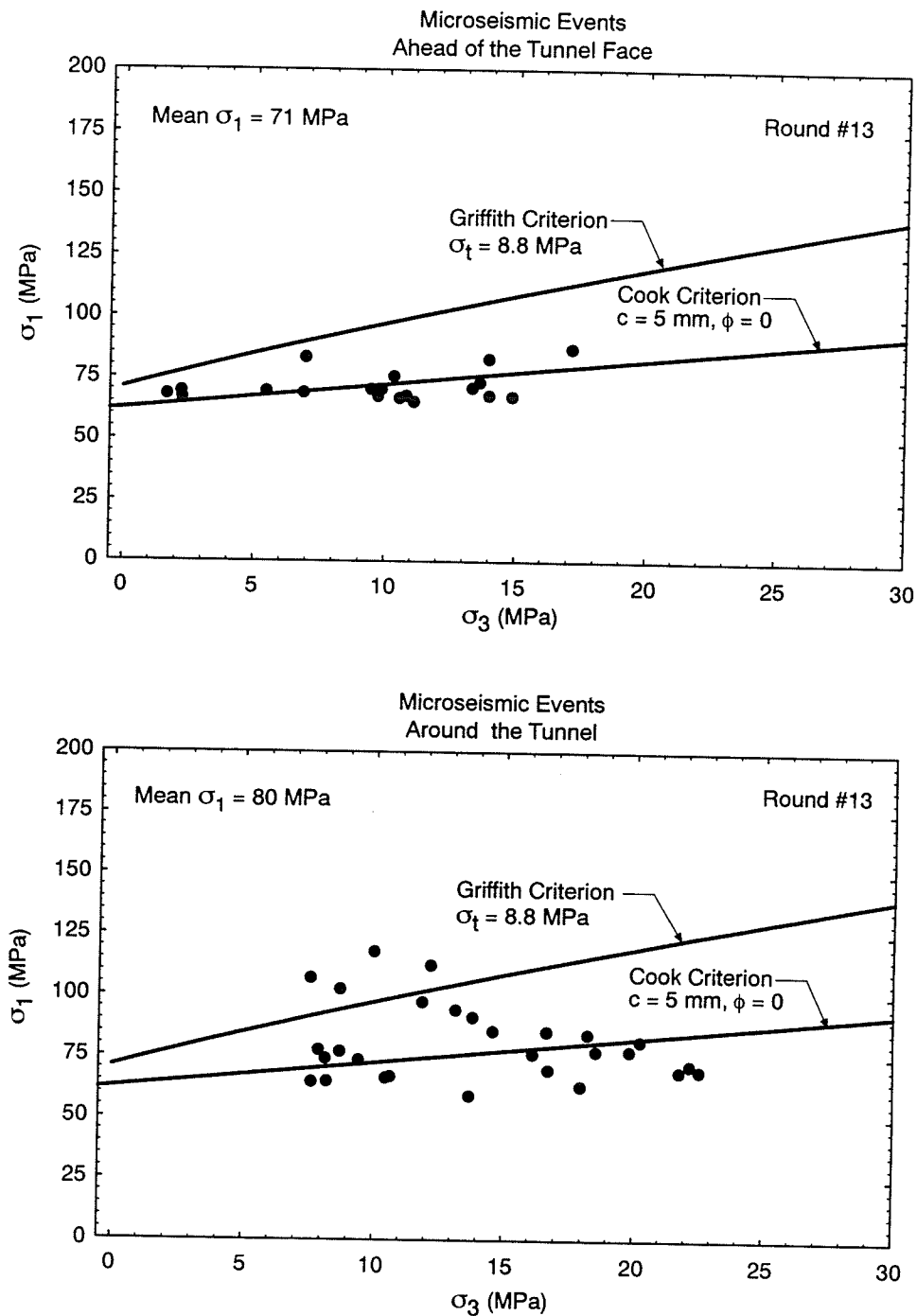
Figure 5.23: The stress state at the microseismic events recorded for Round 13 from the Mine-by test tunnel. The data are divided into events that occurred ahead of the tunnel face and events that have occurred near the the tunnel, and compared to the Griffith and Cook failure envelopes.
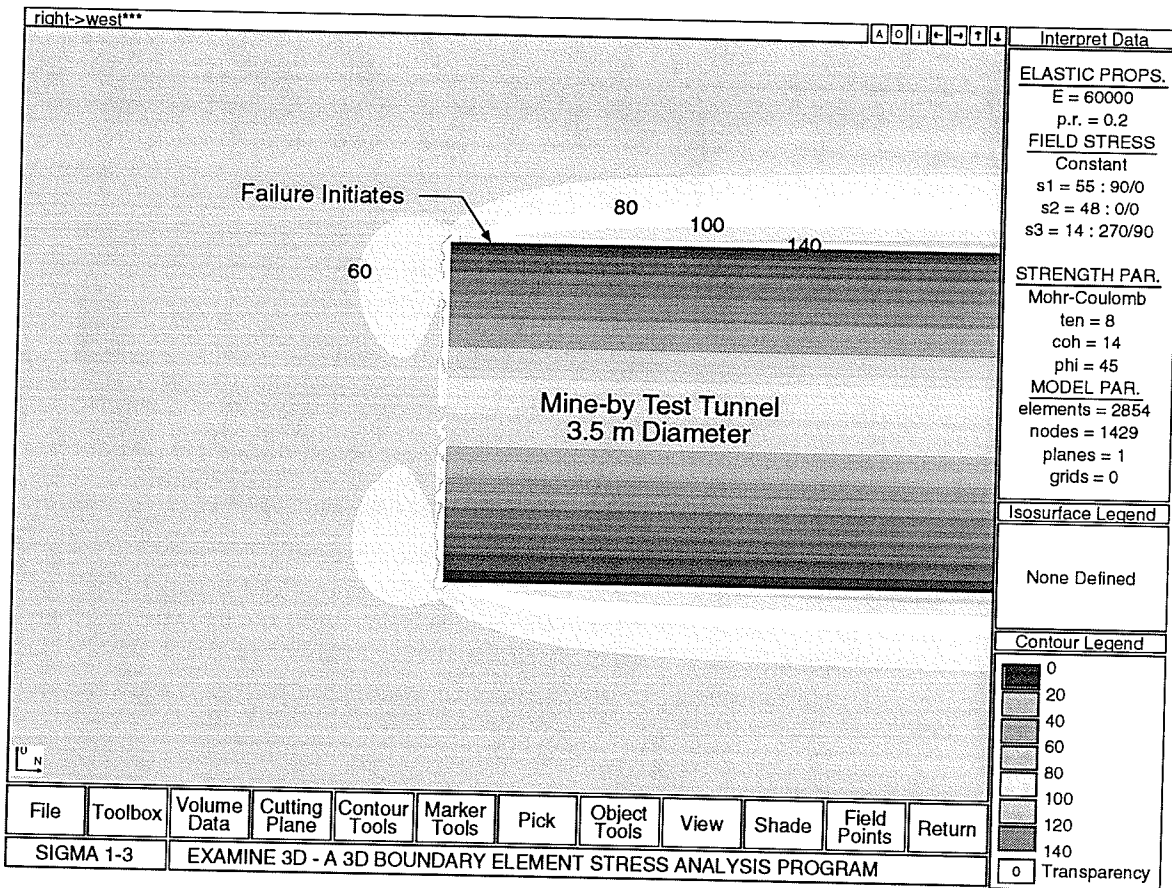
Figure 5.24: Section through the Mine-by test tunnel showing the location of the initiation of failure and the σ_1-σ_3 contours. Note that the microseismic events are concentrated in the areas of maximum deviatoric stress (see Figure 5.19).

data processing carried out using the commercial software Mathematica[TM] [160]. The first step was to establish the numerical parameters required to provide a reasonably accurate solution. A flat face tunnel creates singularities near the face, consequently the number of boundary elements and the distance from the excavation boundary dictate the accuracy of the solution. The circular geometry of the Mine-by test tunnel also provides an analytical check on the accuracy of the results for the plane strain case, which occurs about 1 to 2 diameters away from the face. Thus for the test tunnel the maximum tangential stress concentration at the boundary of the tunnel, for plane strain conditions, is 151 MPa using $\sigma_1 = 55$ MPa and $\sigma_3 = 14$ MPa (see Table 2.2) and equation 5.3. The complete stress distribution around the tunnel is given in Figure 5.25.

The numerical model used to simulate the tunnel advance is shown in Figure 5.26. Figure 5.27 illustrates the change in principal stress magnitudes at a point A as the tunnel face approaches and then advances beyond the point. Approximately 200 data points were extracted from the numerical analyses to produce each line in Figure 5.27. For this case the numerical accuracy was sacrificed, as shown by the $\sigma_3 > 0$ inside the tunnel near the tunnel face. The objective of this exercise was to only identify areas with the greatest stress changes, consequently this was considered acceptable. It is clear from Figure 5.27 that the face causes the stress magnitudes to increase and decrease at all positions around the tunnel boundary. However, it is only in the roof that the σ_1 magnitude increases to a greater value, after the tunnel has passed by, than that which occurred at the face. The microseismic data showed that most of the cracking was occurring in the roof of the test tunnel, consequently a more accurate analysis was carried out at the maximum stress concentration in the roof.

For this case, the same geometry was used as shown in Figure 5.26, with lines at 10, 100, 200 and 300 mm into the tunnel roof. However in this case the element density was increased such that at 10 mm from the boundary of the tunnel the maximum tangential stress was about 150 MPa which is very close to the plane strain analytical solution of 151 MPa. Figure 5.28 shows the results from this analysis and clearly indicates that a sharp
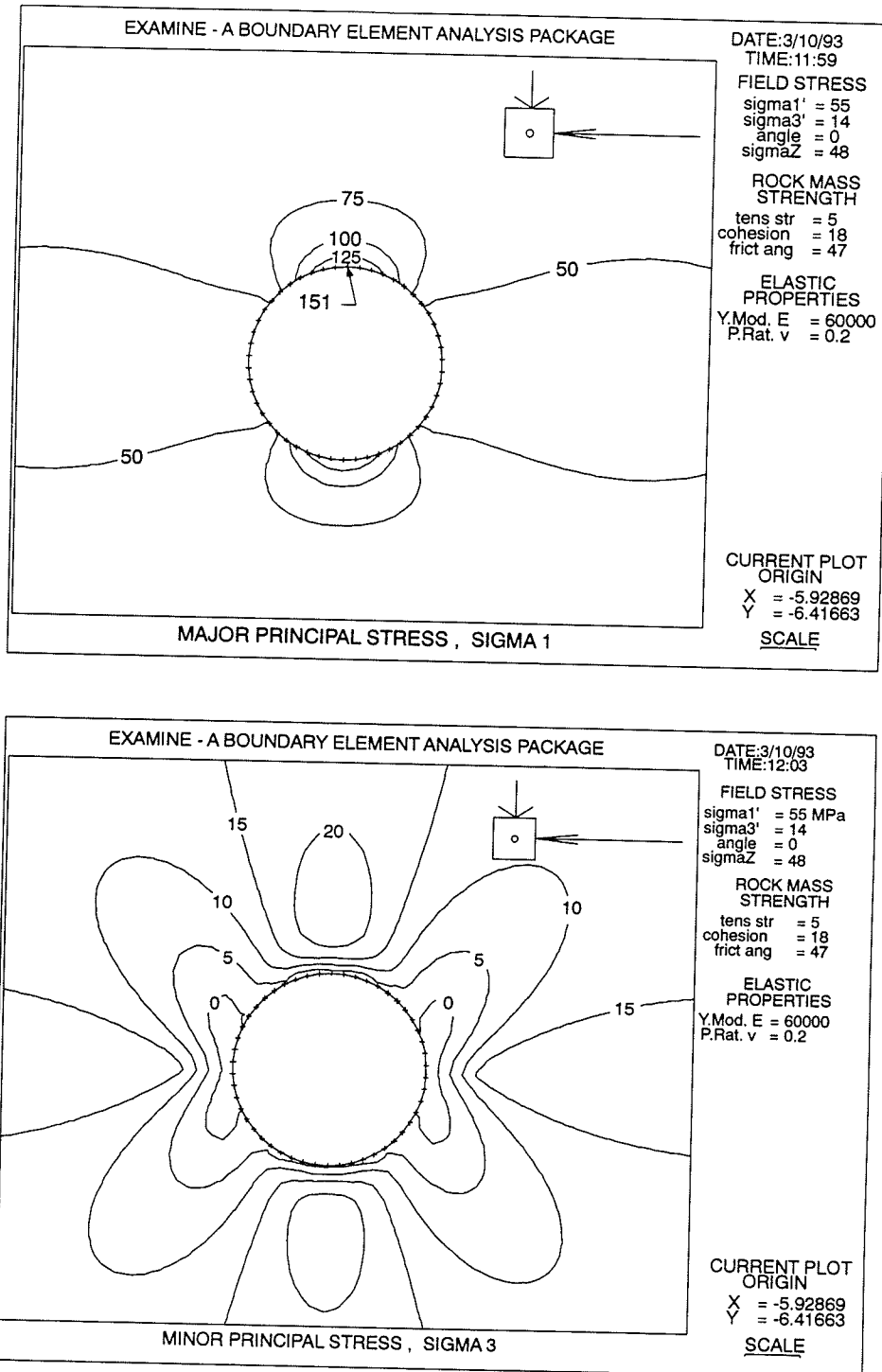
Figure 5.25: Two-dimensional stress distribution around the 3.5-m diameter test tunnel.
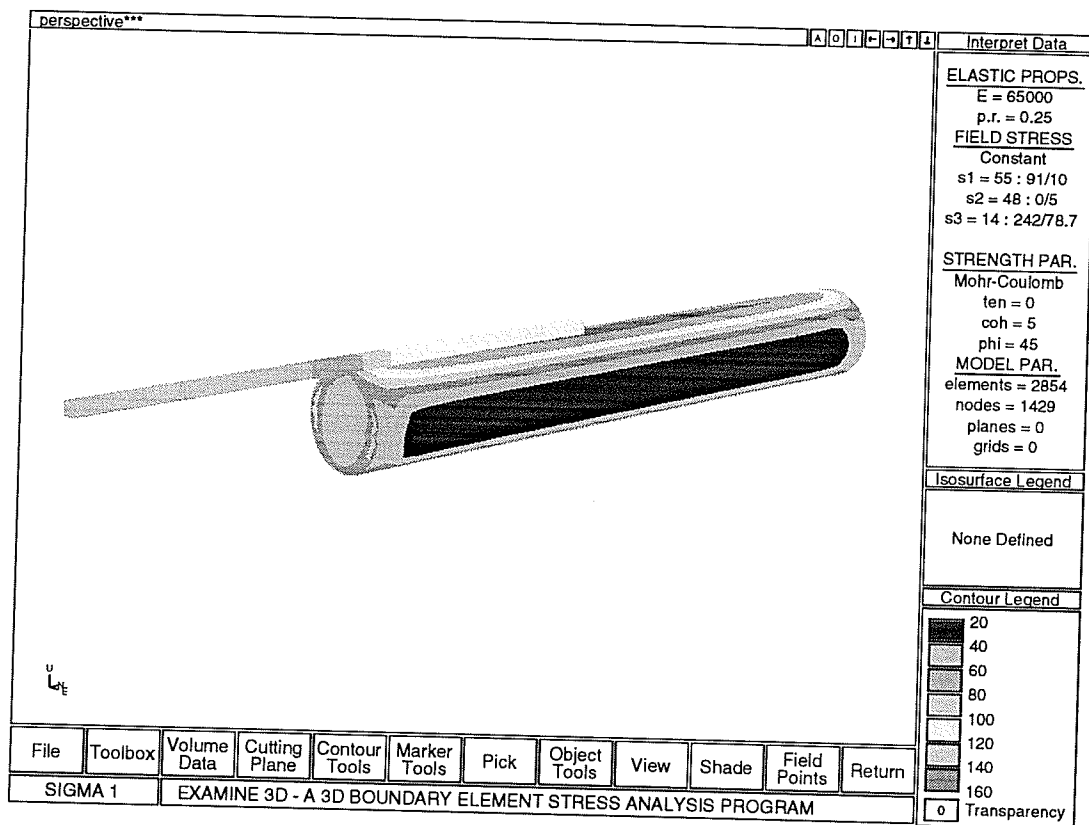
Figure 5.26: Model in Examine^{3D} used to calculate the stresses at points near the tunnel face. The points (200) appear as a line along the roof of the tunnel and a line projecting ahead of the face. The contours on the surface of the tunnel are for σ_1.
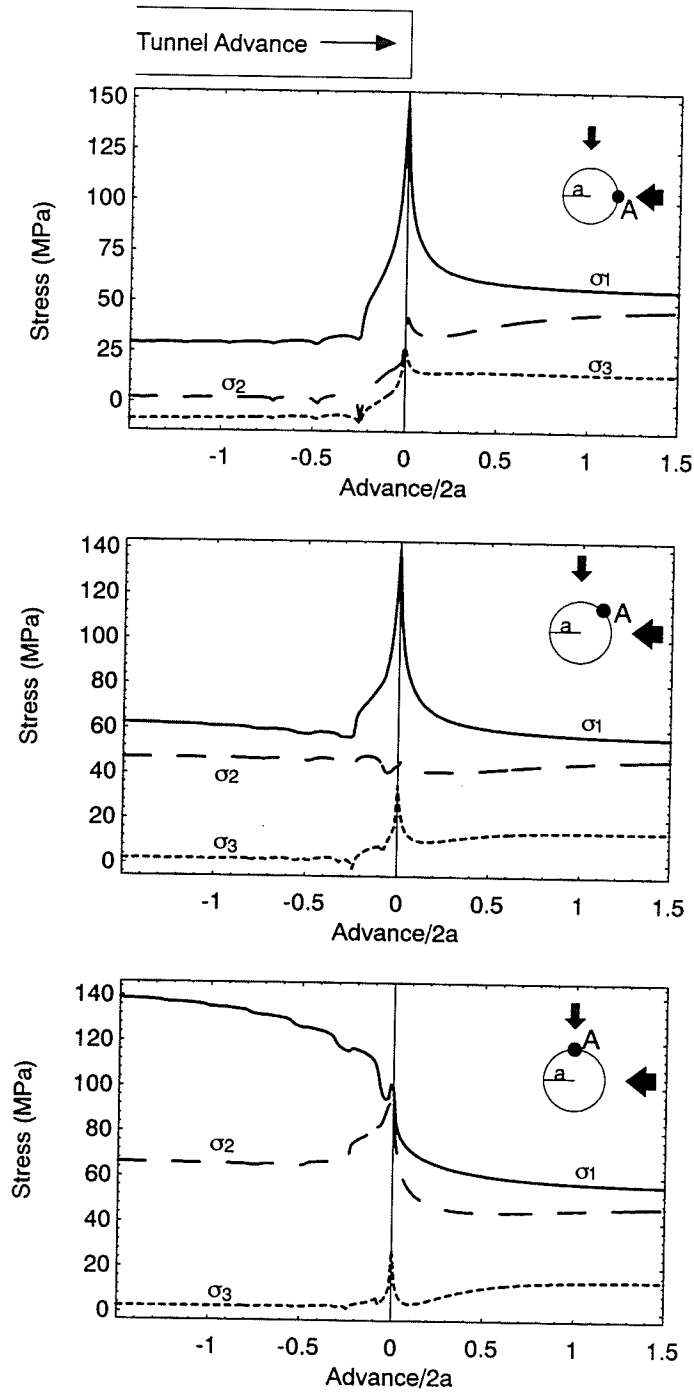
Figure 5.27: Change in principal stress magnitudes around a flat face tunnel as tunnel advances.
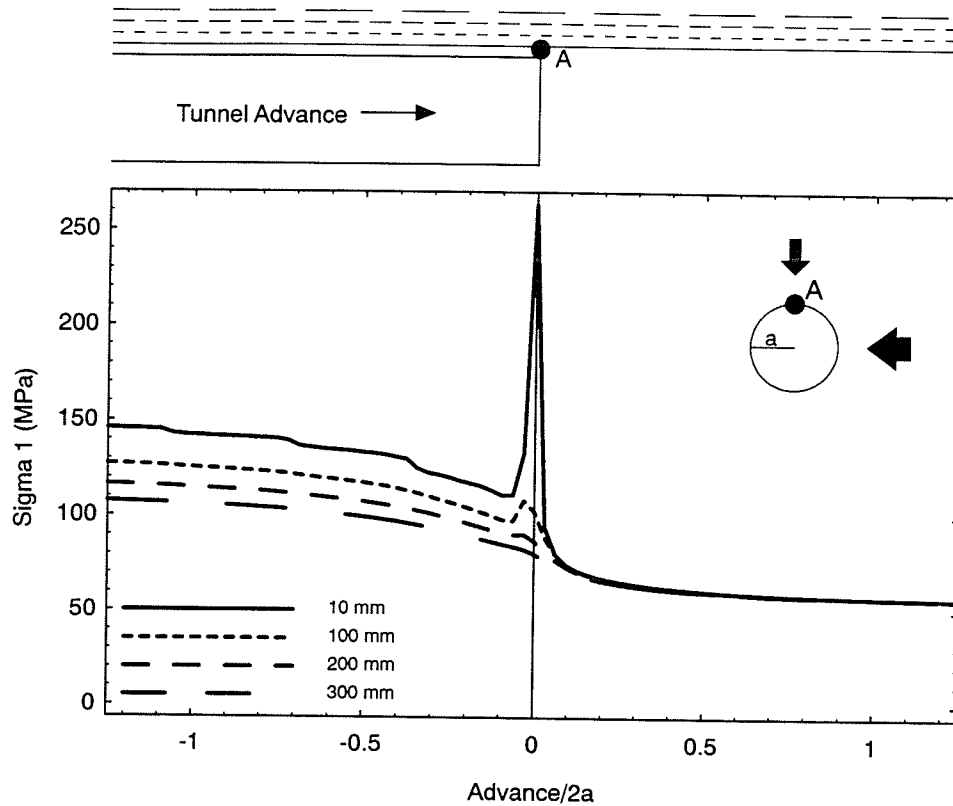
Figure 5.28: Change in σ_1 magnitudes at various distances into the tunnel roof at A as the tunnel advances.

rise in σ_1 occurs at the face position at 10 mm from the tunnel boundary. However, at 100 mm from the tunnel boundary this stress spike is essentially absent and σ_1 shows only a gradual increase from the far-field magnitude of 55 MPa to the plane strain condition. Thus it seems likely that the stress spike seen at 10 mm is only an artifact of the stress singularity caused by the flat face.

In Chaper 4 the damage to the laboratory loaded samples did not occur until after the cohesion, i.e., the initial σ_{cd}, of the material was exceeded. Thus, based on an *in situ* strength (cohesion) of 150 MPa this would occur only as the tangential stress around the tunnel reached the plane strain conditions of 151 MPa. In Figure 5.28 plane strain conditions are reached at about 1 diameter away from the face or at 3.5 m in the case of
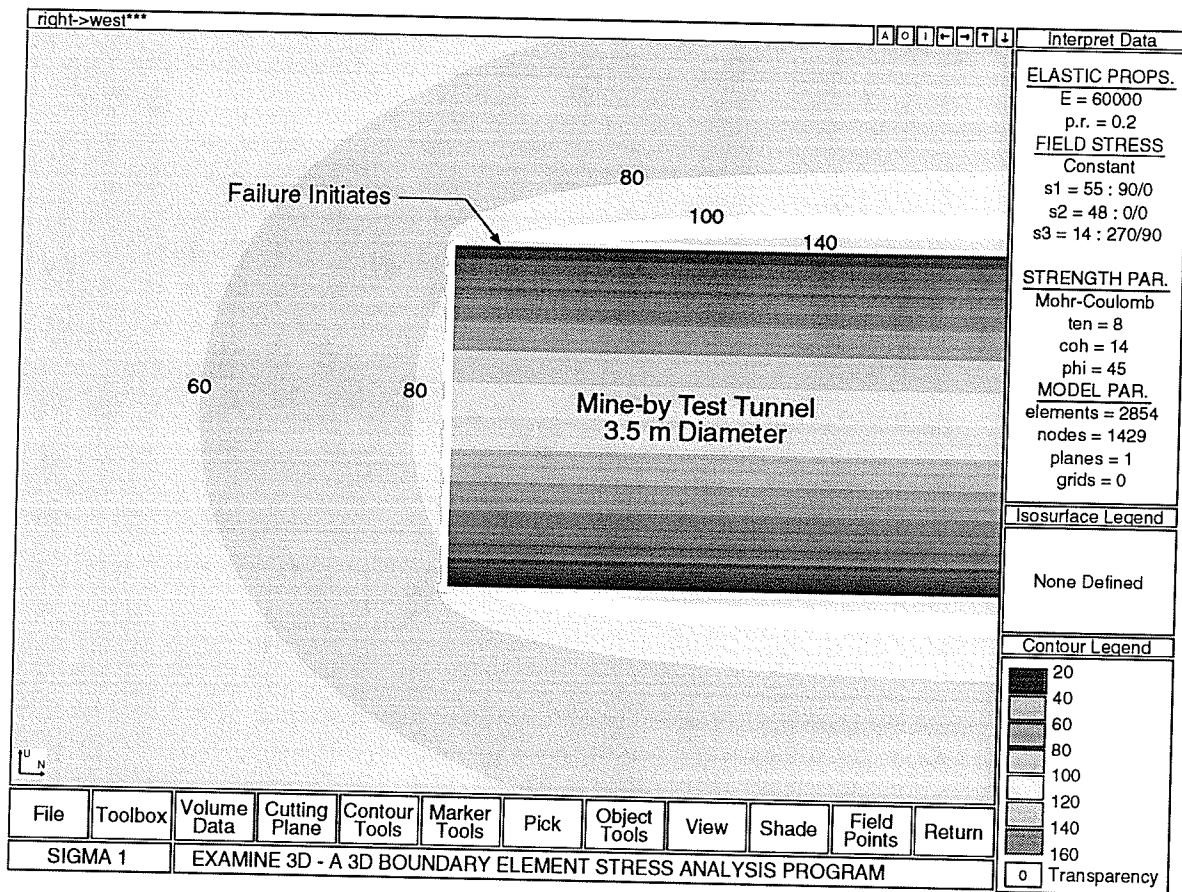
Figure 5.29: Section through the Mine-by test tunnel showing the location of the initiation of failure and the σ_1 contours. Note that the failure starts when the maximum tangential stress is about 80 to 100 MPa.

the test tunnel. However, as shown in Figure 5.29 failure actually initiates (based on visual observation) much closer to the tunnel face, where the maximum tangential stress is in the range of 80 to 100 MPa. This visual observation is also supported by the microseismic events which shows that the notch develops within about 0.5 m from the tunnel face (see Figure 5.19). Thus it is suggested that some other mechanism must be responsible for degrading the rock strength near the tunnel face.

5.6.2 Stress Rotation

The tunnel face not only causes the stress tensor to change in magnitude but it also causes the stress tensor to rotate. New analyses were carried out using the boundary element program Examine^{3D} to investigate stress rotation. As before the number of boundary elements was optimized to give the plane strain solution of 151 MPa for the maximum tangential stress. In this case lines with 200 monitoring points were selected parallel to the tunnel axis at the $0°$, $20°$, $40°$, $60°$, $80°$ and $90°$ (roof). The results are given in Figures 5.30 and 5.31. Only the rotation of σ_3 is plotted in Figures 5.30 and 5.31 because any crack would grow in the plane perpendicular to σ_3. Thus, the rotation of σ_3 represents the rotation of the pole normal to the crack surface.

Figures 5.30 and 5.31 indicate that rotation of σ_3 occurs everywhere around the tunnel. However, in the roof the rotation ahead of the face is at a maximum and a rotation of about $23°$ occurs. Wu and Pollard [161] conducted tensile tests on a brittle material to investigate the influence of the orientation of existing cracks on crack growth in tension. By rotating the applied tensile stress relative to the orientation of the existing cracks they demonstrated that the existing cracks influenced the growth of new cracks (Figure 5.32). They also demonstrated that by simply keeping the stress constant but rotating its direction they could generate crack patterns in different directions (Figure 5.32). At rotation angles from about 0 to $45°$ the new cracks tended to grow from the tips of existing cracks. Beyond $45°$ two separate fractures formed. Thus, it is suggested that because the σ_1 magnitude starts increasing, above the crack initiation stress of ≈ 70 MPa, and rotating near the tunnel face, a similar form of crack growth could be occurring close to the tunnel where the microseismic activity was recorded. This form of crack growth would result in a loss in cohesion of the rock strength, because it is causing the crack length to extend.
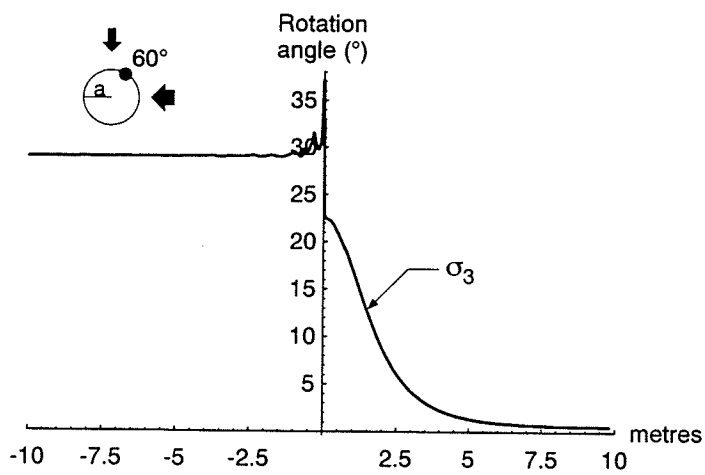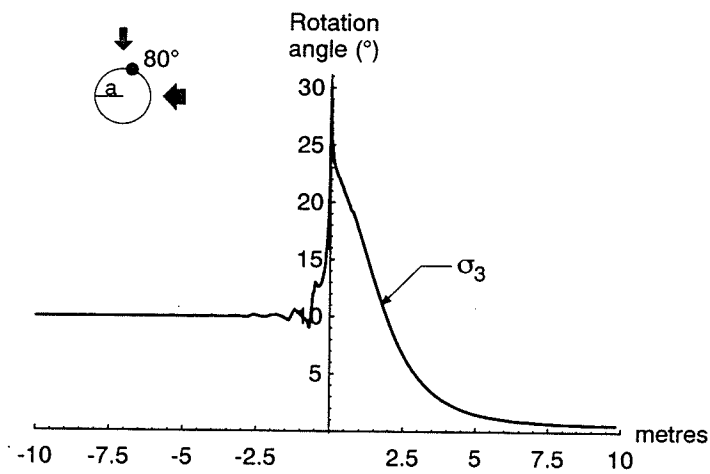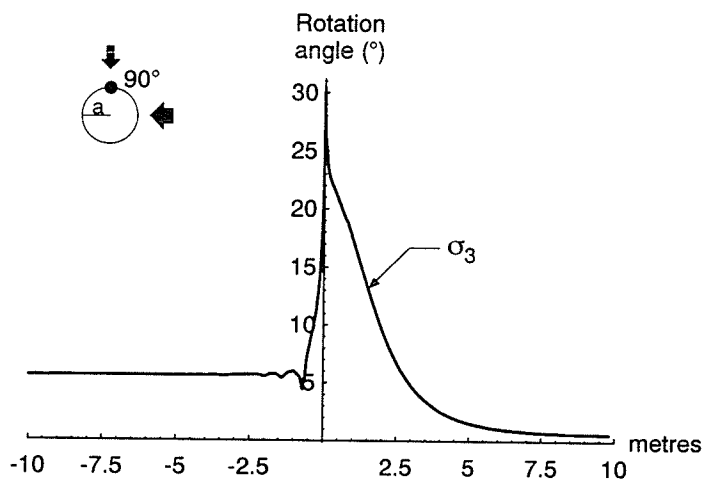
Figure 5.30: Rotation of σ_3 compared to its far-field position. The face of the tunnel is at 0 with the far-field stress conditions at 10 m.
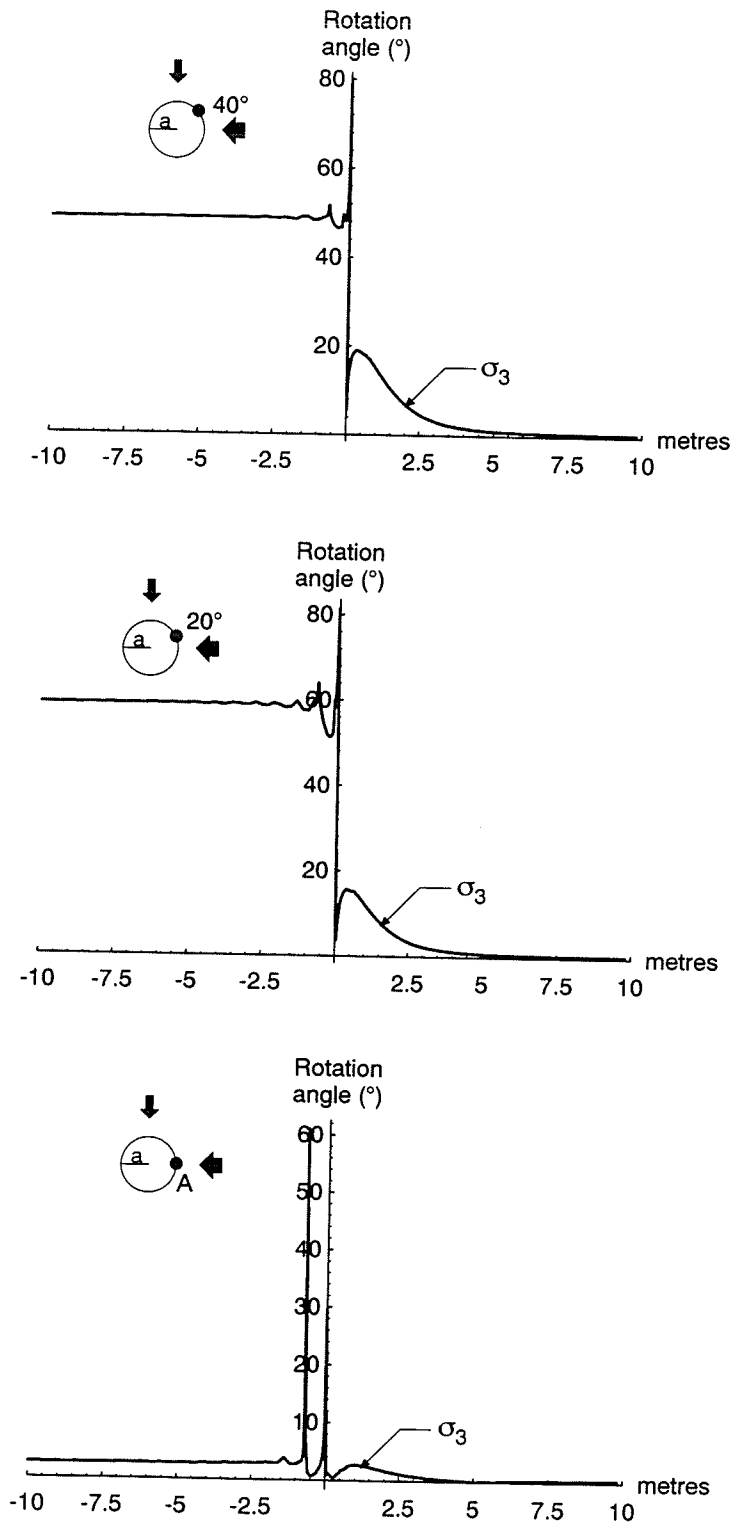
Figure 5.31: Rotation of σ_3 compared to its far-field position. The face of the tunnel is at 0 with the far-field stress conditions at 10 m.
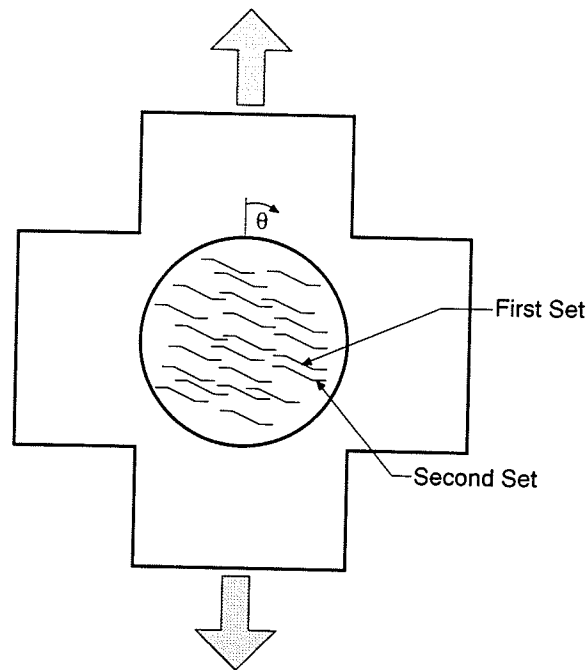
Figure 5.32: Illustration of the influence of existing cracks on the orientation of secondary crack growth, after [161].

5.6.3 Combined Stress Rotation and Face Effects

The stress analyses above have indicated that the advancing face of the Mine-by test tunnel is subjected to a complicated loading path, involving both increasing and decreasing stress magnitudes, and stress rotation. A series of 3-dimensional stress analyses was carried out to follow the loading path of various reference points ahead of the tunnel and as the tunnel advances towards and passes the reference point (Figure 5.26). In each case, the reference point starts 10 m ahead of the tunnel and is referred to as the "far-field" and its stress path is followed until the tunnel has passed the reference point by 10 m and is referred to "inside tunnel".

As shown previously the maximum tangential stress occurs in the roof where failure is observed. Figure 5.33 illustrates the stress path for a point 10 mm from the tunnel boundary in the roof. Also shown on Figure 5.33 is the peak strength failure envelope of the URL

near-surface granite (Figure 3.3), the peak strength failure envelope from the URL 420 Level granite (Figure 4.26), the crack damage threshold envelope (Figure 4.26), the crack initiation line from the microseismic monitoring (Figure 5.22) and the crack initiation line from the laboratory testing (Figure 4.14). Figure 5.33 indicates that the loading path occurring at the point *in situ* exceeds even the laboratory crack initiation stress. Figure 5.33 also shows that the loading path does not exceed the peak failure envelope of the 420 Level granite, although the 150 MPa tangential stress is very close to the failure envelope. However, failure is first observed when the loading path reaches point B in Figure 5.33 or about 100 MPa, as described previously. At this point, when σ_1 reaches 100 MPa, the loading path is well above the crack damage threshold. However, from the damage-controlled testing program described in Chapter 4, recall that the only way to create the crack damage threshold was to do damage to the rock at stress levels above its cohesion strength of 150 MPa. Thus, in order to apply the crack damage threshold as a failure criterion the loading path for the rock, at some point in its loading history, must have exceeded 150 MPa. From Figure 5.33 this only occurs after failure is observed, i.e., failure is observed long before the loads reach the critical value of 150 MPa. It appears that the rock *in situ* is damaged but that the damage is not created by loads exceeding 150 MPa. It is suggested that the damage occurs because the loads are above the crack initiation stress and are rotating, as described previously. Thus, the rotation angle of σ_3 relative to its orientation at the far-field reference point is also determined and shown adjacent to the loading path.

Figures 5.34 and 5.35 illustrate the stress path for three points, one at the maximum compressive stress in the roof, one at the sidewall located at 60° from σ_1 and one at the sidewall located 0° from σ_1. The effect of the tunnel face , as the reference point is passed, is shown on Figure 5.34 and 5.35 where loading path moves sharply to the right and subsequently sharply to the left. It should be noted that some of the high stress magnitudes near the tunnel face result from the stress singularity caused by the tunnel face. Also shown on Figures 5.34 and 5.35 is the crack initiation envelopes and the crack damage threshold
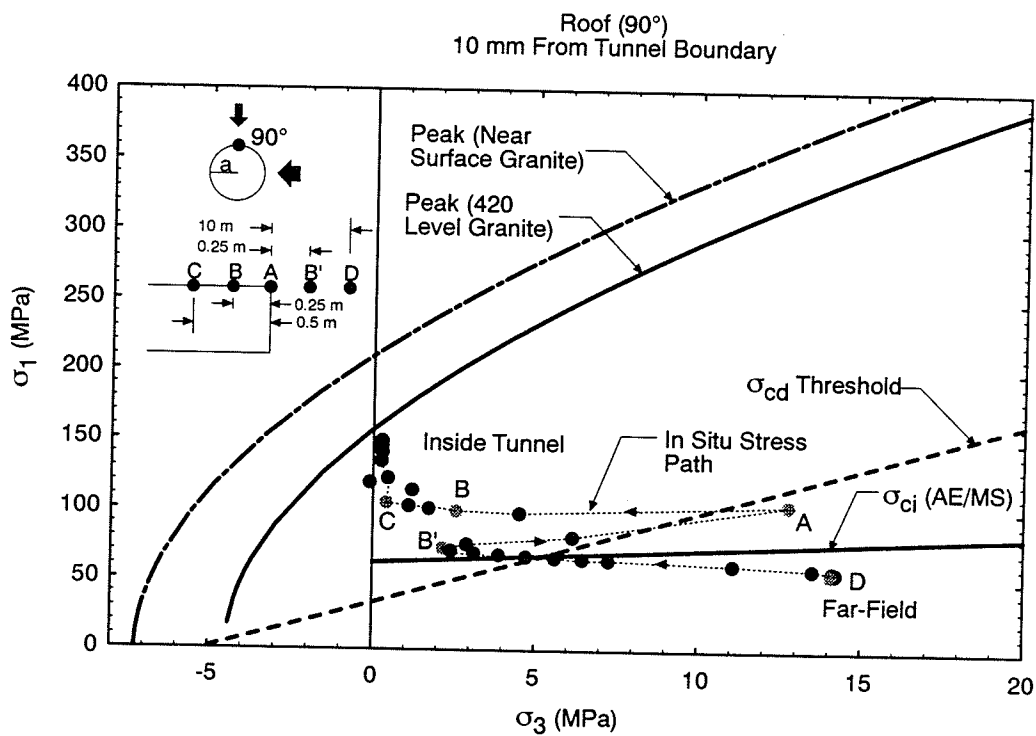
Figure 5.33: Stress path for a point located 10 mm from the tunnel boundary at the maximum compressive stress concentration in the roof. The "far-field" point in the figure is located 10 m ahead of the face.

described above. Examination of Figures 5.23 reveals that at all positions around the tunnel the stress path exceeds the crack initiation envelope and the crack damage envelope. Thus if failure is defined by the crack damage stress then failure should be observed every where around the tunnel. However, as shown in Figure 5.15 failure is only observed over a small region of the tunnel perimeter. Therefore the crack damage envelope, alone cannot be used to define the limits of failure. The major reason for the limited failure zone may be the combination of stress rotation and loading path. The major difference between the sidewall and the roof is that it is only in the vicinity of the roof, where the loading path reaches its maximum stress, that the stress direction goes through a complete cycle of rotating to its maximum of 25° at the tunnel face and then rotating back, almost to its original direction. It is proposed that this reversal of the rotation angle is responsible for the crack damage because now the increasing stress can take advantage of the cracks initiated at lower stresses and different orientations. In effect the maximum stress initiates a crack at about 70 MPa and then inclines the crack relative to its direction and exploits the plane of weakness it initially created.

Similar stress analyses, to those described above, were carried out at distances of 0.25 m and 0.5 m from the tunnel boundary. These results are given in Figures 5.36 and 5.37. It is clear from Figures 5.36 and 5.37 that from 0.25 m and beyond from the tunnel boundary the loading path exceeds the crack initiation stress but remain well below the crack damage stress. Interestingly, the stress rotation has decreased to less then 10° at 0.5 m. Thus at 0.5 m from the tunnel boundary it is not likely that the rock strength has been degraded from its *in situ* value by the advancing tunnel face.

The conclusion that the damage around the Mine-by test tunnel only extends to about 0.5 m from the tunnel boundary is in part supported by the microseismic data and by the depth of the notch in the roof. If we use 0.5 m as the limit of the damaged rock then the notch depth would be 2.25 m from the centre of the tunnel or $1.3a$, where a is the tunnel radius of 1.75 m. Figure 5.15 shows that the notch does grow to a depth of $1.3a$.
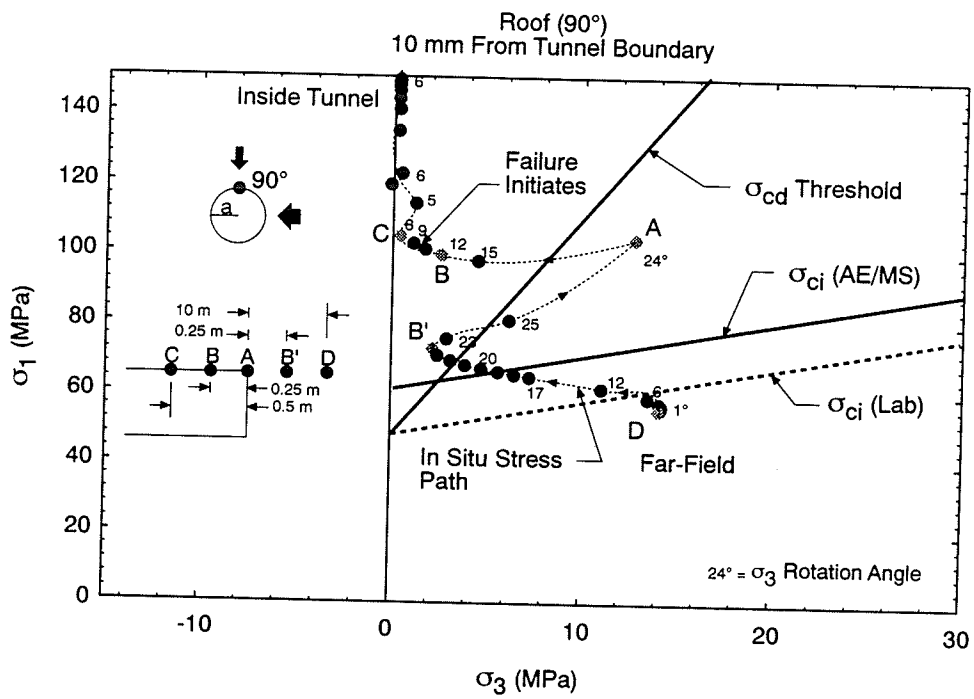
Figure 5.34: Stress path for a point located 10 mm from the tunnel boundary at the maximum tangential stress concentration.
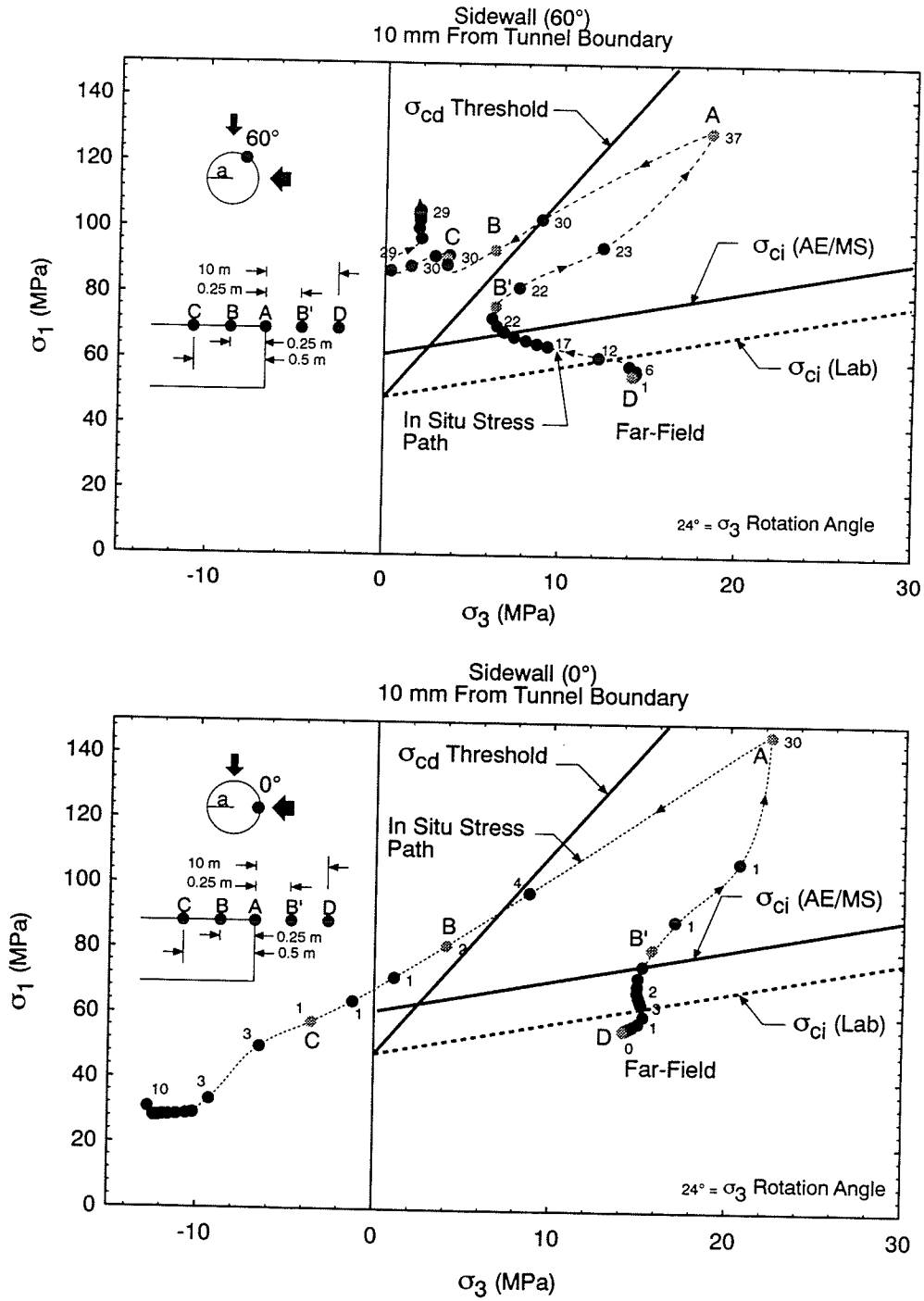
Figure 5.35: Stress path and σ_3 rotation for a point located 10 mm from the tunnel boundary at 60° and 0°.
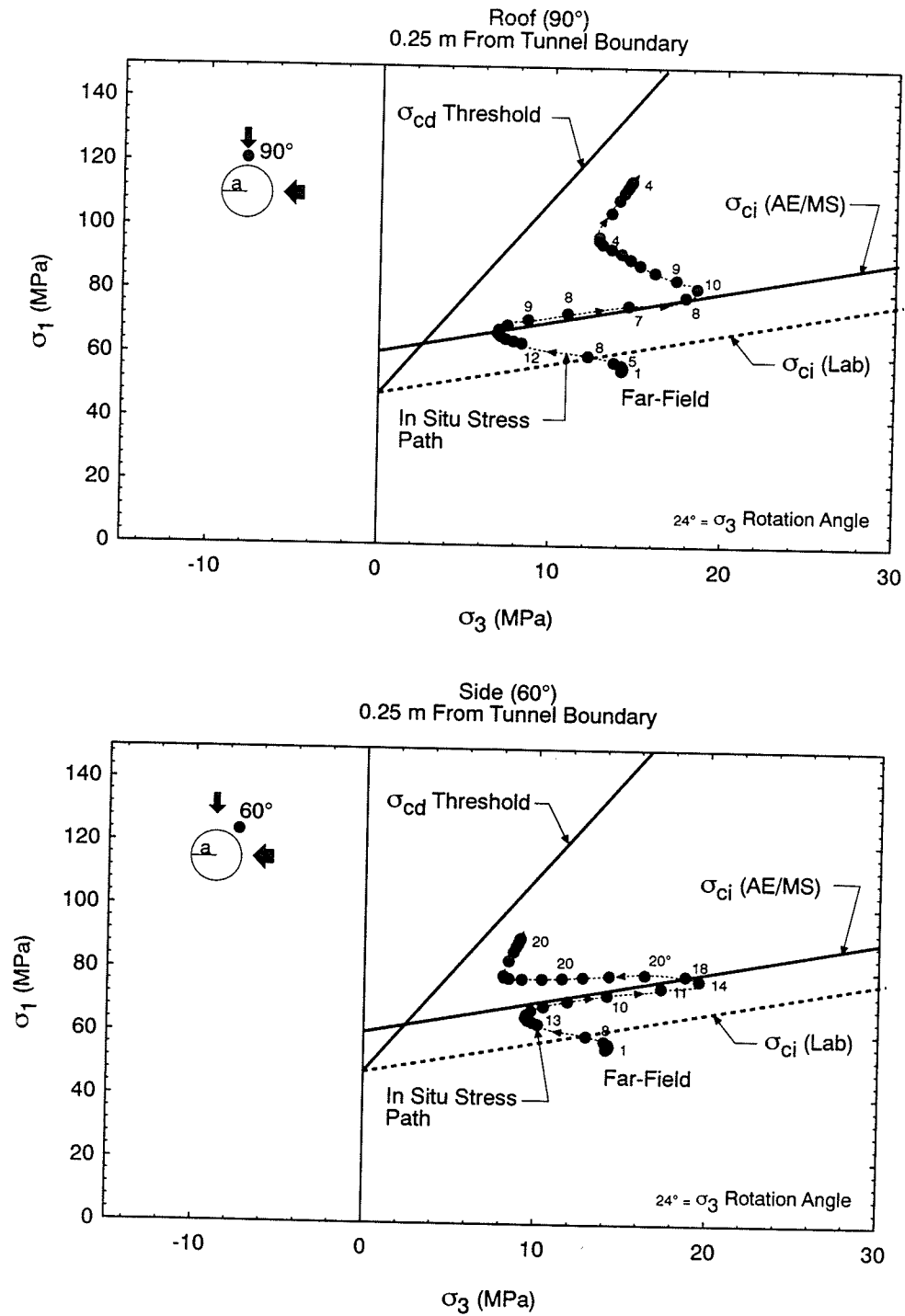
Figure 5.36: Stress path and σ_3 rotation for a point located 0.25 m from the tunnel boundary at 90° and 60°.
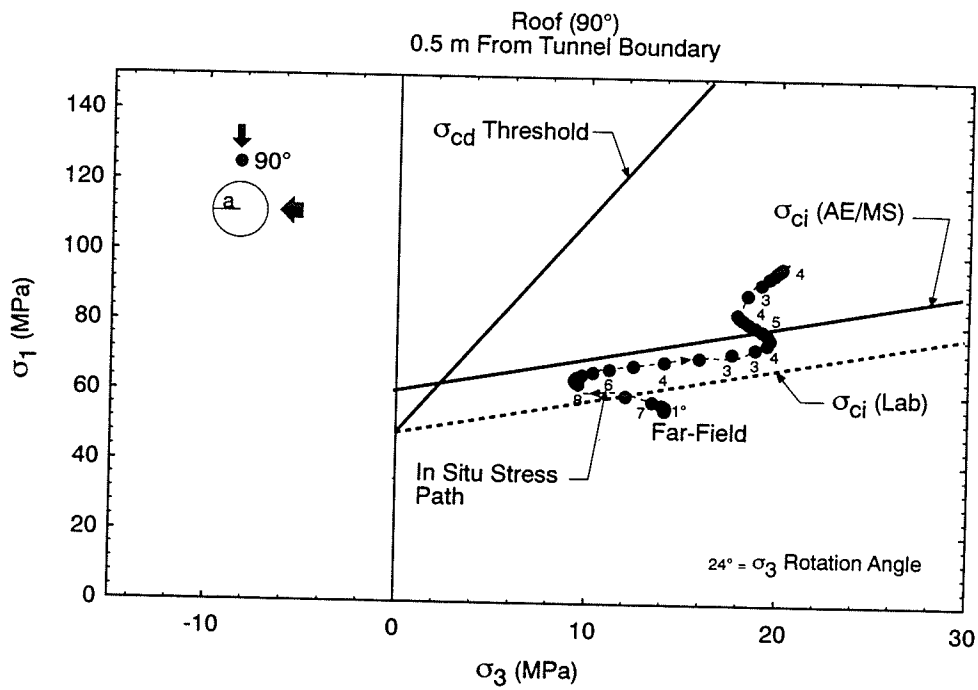
Figure 5.37: Stress path and σ_3 rotation for a point located 0.5 m from the tunnel boundary at 90° and 60°.

5.7 Failure Process Observations

The excavating method used in the Mine-by test tunnel allowed detailed inspection of the failure process. In Section 5.4.1 the microseismic monitoring indicated where damage was concentrated around the tunnel. Once the tangential stress at the boundary of the tunnel reaches the strength of this damaged material the failure process commences. The spalling process generally started at a distance of about 0.5 to 1 m back from the face where the tangential stress is about 100 MPa. Initially the spalling zone is relatively small, measuring only about 100 to 200 mm along the tunnel perimeter. The material in this zone turns a milky colour when it starts to fail as if the material is being crushed. The process continues until plane strain conditions are reached down the tunnel. This intervening period is the most violent time in the tunnel advance. Once plane strain conditions are reached the violent spalling quickly decreases. Stability is eventually achieved, although the process may take several months.

One of the observed phenomena which is consistently associated with the spalling process is the "process zone". The process zone is the crushed zone referred to above and the intensely crushed material within this zone gives rise to considerable dilation (Figure 5.38). Initially, this process zone seems only to provide a nucleus for the initiation of the notch and the dilation is accommodated by small flakes of material, < 50 mm in diameter, falling from the crushed area. However, as the notch develops the process zone is more contained at the notch tip and the dilation now expresses itself as small-scale buckling at the tip of the notch (Figure 5.39). The small-scale buckling has been observed to take several weeks to several months to develop and is generally observed as the notch becomes stable.

Another failure process initiated by the development of the process zone is curved slabbing (Figure 5.38). In this case it appears as if the curved slabs form as the process zone is growing. This slabbing might be considered equivalent to core discing, i.e., each core disc forms as the drill bit is advanced a certain distance, only in this case the drill bit is the
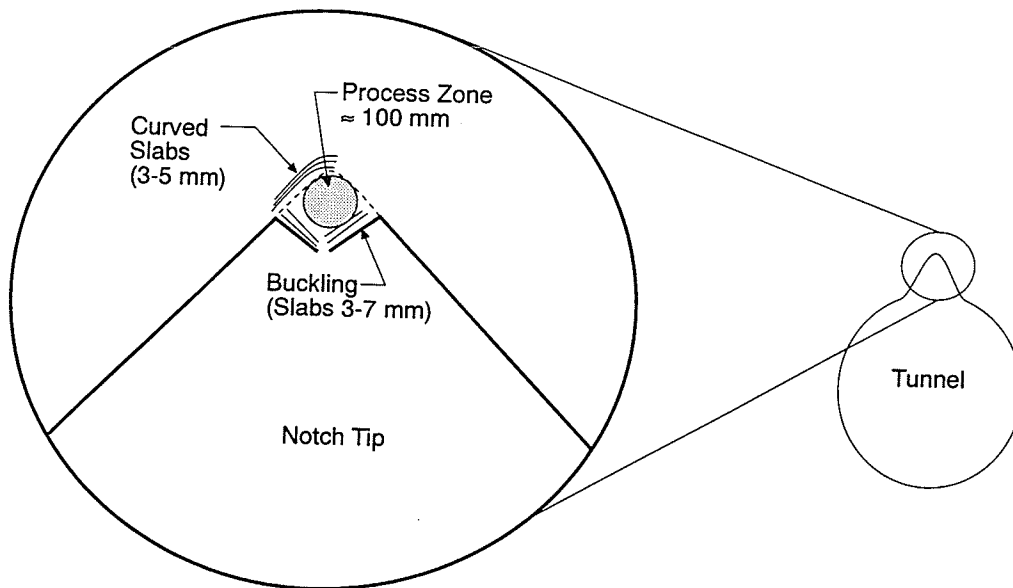
Figure 5.38: Illustration of the process zone at the tip of a notch.
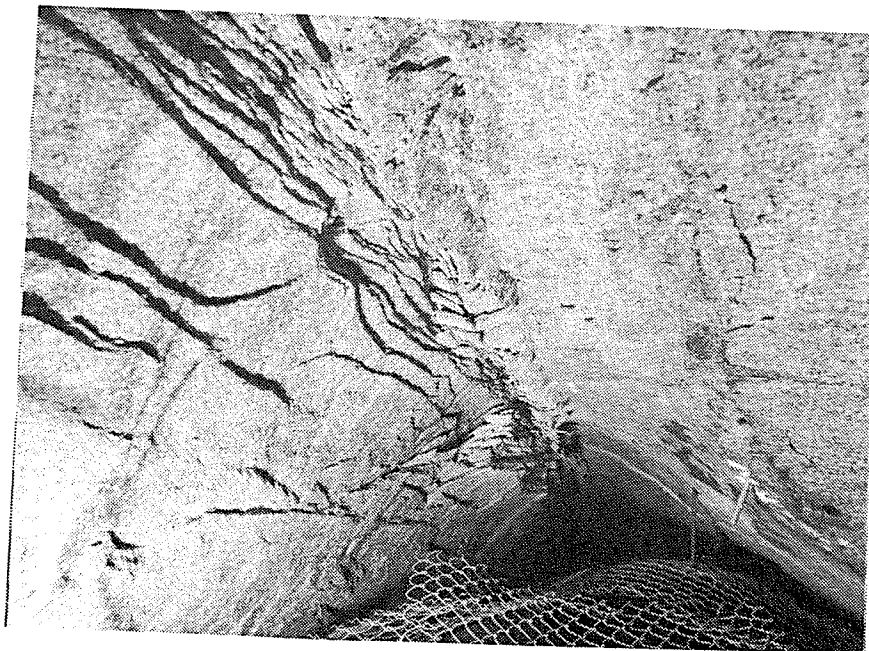
Figure 5.39: Photo of the buckling observed at the notch tip. Note the pen for scale.
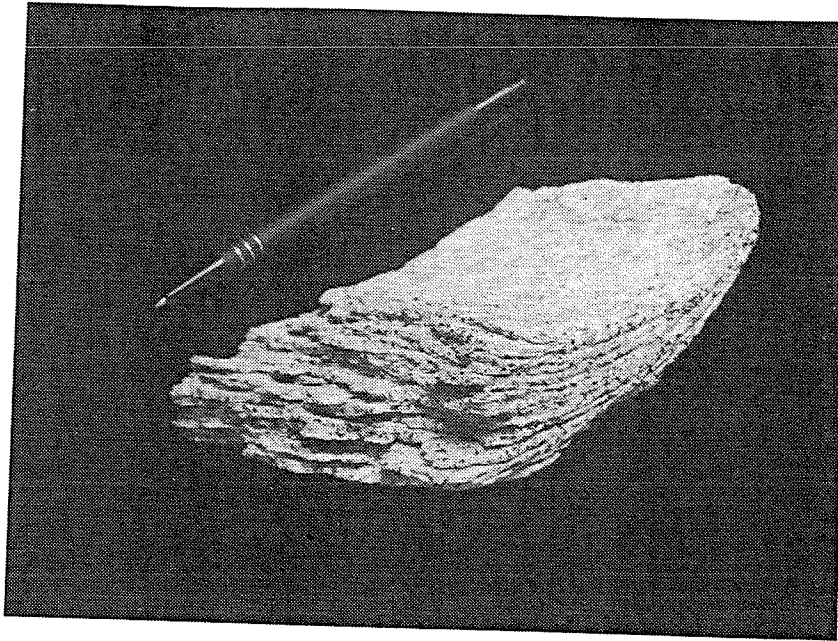
Figure 5.40: Photo of the curved slabbing observed at the notch tip. Note the thickness of the slabs is about equal to the grain size ($\approx$ 4 mm).

process zone. An example of this phenomena is given in Figure 5.40.

An attempt was made to examine the process zone *in situ*. A slot was cut by drilling a series of boreholes in the apex of the notch radial to the tunnel. Figure 5.41 shows the location of the process zone at the tip of the notch and also shows some of the features associated with the process zone. Note in Figure 5.41 the curved thin slabs, localized buckling and the large amount of dilation associated with the process zone.

The development of the notch is extremely complex. However, from the observations made at the URL several features stand out:

- The failure process starts over a small region (50-100 mm) on the boundary of the tunnel.

- The failure process is initiated by crushing the rock in this region.

- The crushing process produces dilation.
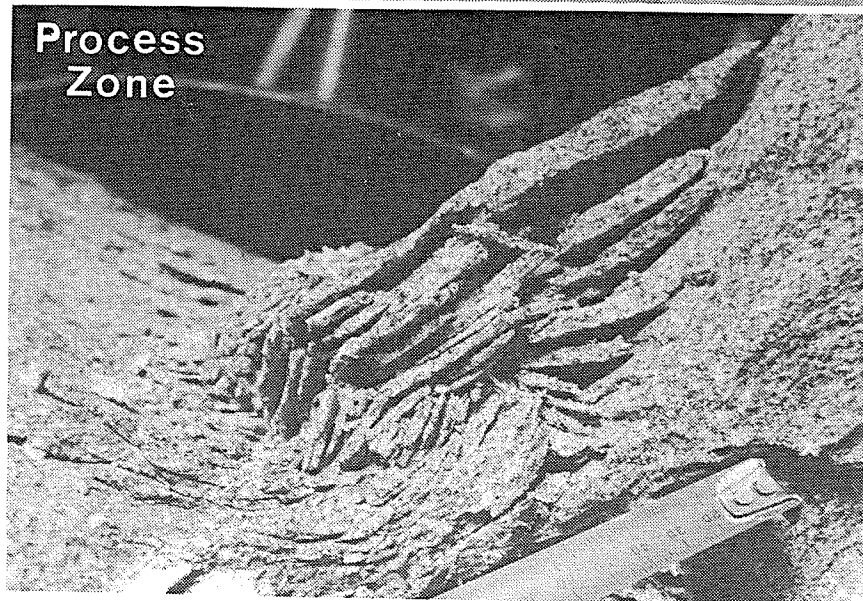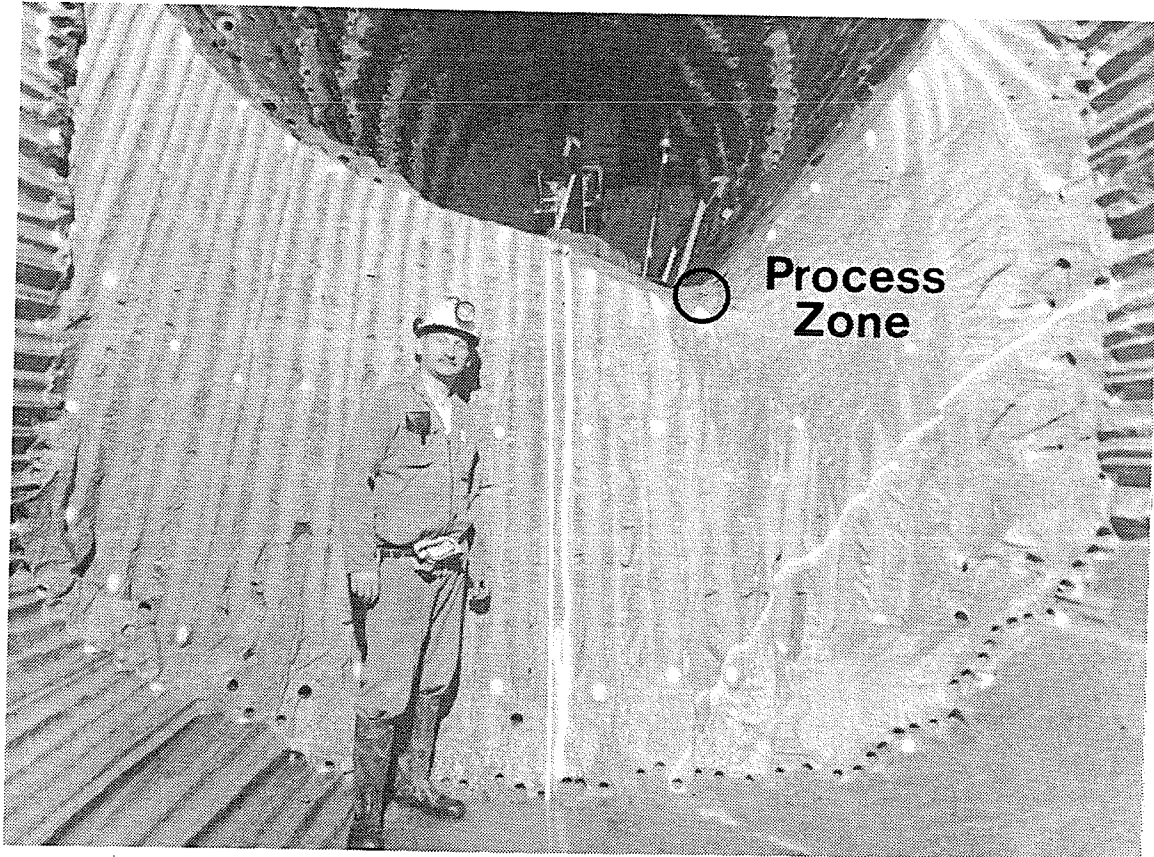
Figure 5.41: Photo of the process zone at the notch tip. Note the convex shape of the notch, and the thin curved slabs and the large amount of dilation in the process zone.

- The dilation leads to slabbing and buckling.

Figure 5.42 is an attempt to illustrate the major processes in the development of a notch. In the early stages it appears the slabs are long (460 mm) but relatively thick ($\approx$ 20 mm), giving an aspect ratio of $\approx$ 20 : 1. However as the notch develops the thickness of the slabs decreases to < 10 mm, and in some cases approaches the size of the mineral grains, 3-5 mm. In all cases, a process zone is present. This process zone could be considered equivalent to the small scale process zone found around a crack tip [127, 94].

Stage I - Initiation
Critically oriented grain boundaries start to crack in region of maximum stress concentration.

Stage II - Dilation
Shearing and crushing along grain boundaries develop causing dilation.

Stage III - Slabbing & Spalling
The process of crushing and shearing causes dilation. Dilation leads to formation of thin slabs by splitting and creating loads parallel to the free surface which results in extensional unstable cracking. Once the slabs form this allows the crushing process to continue and create new slabs.

Stage IV - Stabilization
The slabbing process will stop when the the geometry of the notch has changed enough to provide confinement at the notch tip. This ususally means there is a slight convex curvature to the notch shape. Alternatively, if the slabs from the side of the notch are held in place by support mechanisms then the notch will also stop developing.

Figure 5.42: Illustration of the major processes found in the development of a notch.

Chapter 6

Modelling the Failure Process

In simulating the failure process one is faced with having to choose a material model which best represents the physical process. With material such as rock, some type of strain-softening model is generally used (Figure 6.1). The strength of the rock in the strain-softening model reduces as the load exceeds a critical value but the rock is still able to carry a reduced load. By this process of strain softening, load is redistributed from the region of failed material to other regions around the opening below the critical load.

As shown in Section 5.7, the failure process in brittle rock at the 420 Level involves a series of slabs spalling off as the notch developed. Thus, the amount of strain softening involved in the failure process is minimal except perhaps in the process zone. It is suggested, based on observations, that an elastic brittle model (Figure 6.1) is more representative of the failure process than a strain-softening model. With this model, once the load capacity of the material is exceeded the material can no longer carry load and in the numerical simulations must be removed. The removal of the material is simulated by modifying the geometry of the opening to reflect that a slab of rock has been eliminated. Thus, a complete simulation will require several runs, each with a slightly different geometry.

6.1   Notch Development

For the Mine-by test tunnel, stability occurred when the notch reached a depth of $1.3a$, where a is the tunnel radius measured from the center of the tunnel. One of the reasons

198
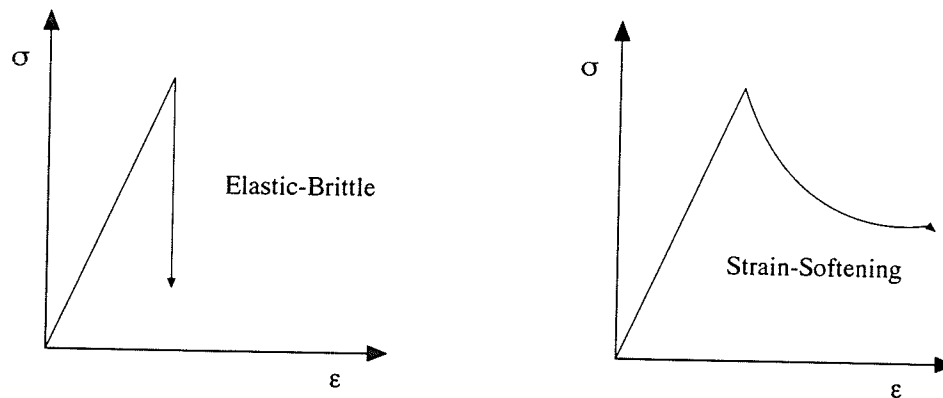
Figure 6.1: Types of material behaviour generally used to model failures around underground openings.

stability is achieved as the notch grows, is illustrated in Figure 6.2. Assume a circular tunnel subjected to a biaxial stress state of 55 and 14 MPa. Numerical analyses were carried out in a series of steps to investigate the stress history at point B, located some distance from the tunnel boundary, as the notch develops (Figure 6.2). At the instance the tunnel is excavated, the maximum stress at B is less than that at the boundary of the tunnel. At the boundary of the tunnel the tangential stress exceeds the strength of the material and hence the notch starts to develop. As the notch develops, the Mohr circle of stress for point B moves further from the failure envelope (Figure 6.2). When the notch has developed to within 10 mm from B, the stress state at B is far from the failure envelope and notch growth cannot continue. Obviously, this is an approximation to the process. However, the notch growth causes a change in the geometry which results in a new stress distribution that is entirely different from that for the original circular tunnel. This change in the geometry is a key element in order for the notch to achieve stability [162, 48].

It appears that the final shape, as well as the depth of the notch, is determined by stress redistribution as the notch develops. Figure 6.3 illustrates the concave and triangular notch shapes commonly used in numerical modelling of the failure process [48, 162]. The notch shape observed *in situ* at the URL varies from the triangle to the convex shape. At the
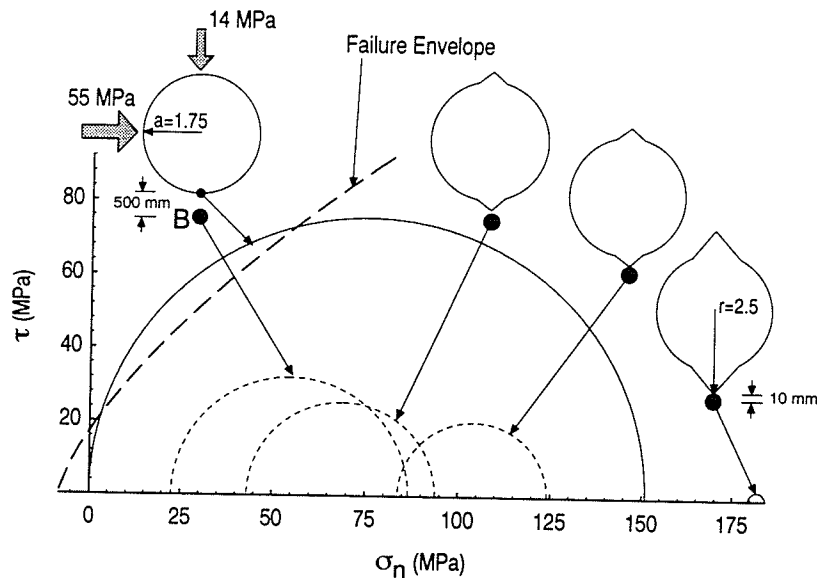
Figure 6.2: Stress history of a point as the notch develops.

URL the stable notch shape indicates a slight amount of convex curvature (see Figures 5.3 and 5.15). However, in South Africa where the *in situ* stresses are much higher than at the URL, the convex shape in Figure 6.3 is commonly observed (D. Ortlepp, personal communication). Thus, it appears that the amount of convex curvature observed is related to the stress level causing the failure.
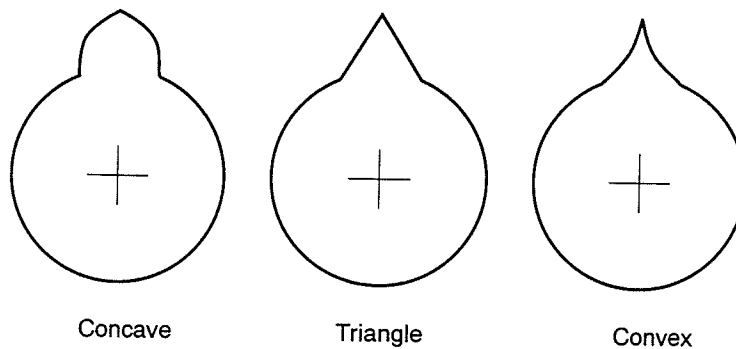
Figure 6.3: Various notch shapes. The concave and triangle shapes are generally used in modelling. Varying degrees of the convex shapes are generally observed *in situ*.

6.2 Phenomenological Modelling

An elastic numerical stress-strength analysis to determine the stability of an underground opening requires knowledge of the stress state, the geometry of the problem and the strength of the material. The *in situ* stresses for the 420 Level were given in Section 2.2.5 and the shape of the excavations on the 420 Level provide geometry. The remaining unknown is the strength of the rock mass. Analyses of Rooms 413 and 405 were carried out to evaluate the strength of the rock mass.

The design excavation profiles for Room 405 and Room 413 were analysed using the boundary element program Examine^{2D}. The first series of analyses used the traditional laboratory peak strength obtained from laboratory triaxial tests. No signs of instability were evident from this analysis.

It was shown in Chapter 4 that the cohesion decreases as damage accumulates in the rock. In Chapter 5 it has also been shown that damage, in the form of cracking, is occurring near the face of the tunnel as the tunnel is advancing. Thus, it is likely that locally around the tunnel, where the damage is accumulating, some cohesion, i.e., strength, is lost. Recall from Section 2.3 samples taken from the 420 Level of the URL showed a reduced strength due to sample disturbance. It is suggested that the process causing the sample disturbance is similar to the process causing the damage around the tunnel and therefore, as a first step, the initial crack damage stress of the disturbed samples will be used to estimate the damaged strength around the tunnel (see Figure 4.26). A second series of analyses was carried out for the same conditions as above but using the Hoek-Brown failure envelope for the initial crack damage stress given in Figure 4.26 with $\sigma_c = 100$ MPa, $m = 20$, and $s = 1$. σ_c was degraded from the $\sigma_c = 114$ MPa measured for the laboratory samples to $\sigma_c = 100$. This reduction in σ_c was made in light of the other evidence that indicated that failure occurred when the maximum tangential stress reached about 100 MPa. From this analysis, failure is evident in Room 405 as indicated by the 1.0 strength-to-stress contour

line (Figure 6.4). Room 413 however is marginally stable. Recall that the half-barrels on the roof of Room 413 indicate that the room is stable, which correlates with the numerical results (see Figure 5.3).

The failure criterion for damaged rock used above satisfies the observation that openings excavated parallel to σ_1 show greater stability than openings excavated parallel to σ_2. However, if the damaged failure criterion is correct, then the final geometry of Room 405 must also be stable, because all spalling activity stabilized shortly after plane strain conditions were achieved. To simulate the failure process in Room 405, the excavation profile in the model was modified by removing the rock within the contour where the strength/stress ratio equals 1. The simulation started with the design profile and progressed through four excavation steps (Figure 6.5).

A final analysis is carried out on the excavated profile. Note the general agreement between the shape of the opening in the roof predicted by the model and the actual excavation profile. Also note that in the model the excavated profile in the roof is stable except at the very tip of the v-shaped notch. Boreholes were drilled in the roof and floor to determine if fracturing existed outside the measured profile (Figure 6.5). In the roof, fracturing was not evident, although the stresses were high enough to cause 300 mm of well-bore breakouts to extend along the walls of the borehole drilled in the v-shaped notch. In the floor, fracturing was more pervasive and extended to a depth of about 300 mm.

The process described above is phenomenological, i.e., no effort is made to follow the failure process except to reduce the rock strength. Obviously, this approach has practical merit because it is easily modelled by available numerical techniques and it provides a reasonable approximation to the problem. However, the limitation of this approach is that it assumes the rock strength everywhere around the opening has been damaged. Clearly, from the microseismic data, the most extensive damage is only occurring in limited areas around the tunnel, i.e., areas of maximum tangential stress concentrations. Also, from the laboratory test results it is seen that the cohesion depends entirely on the amount of damage.
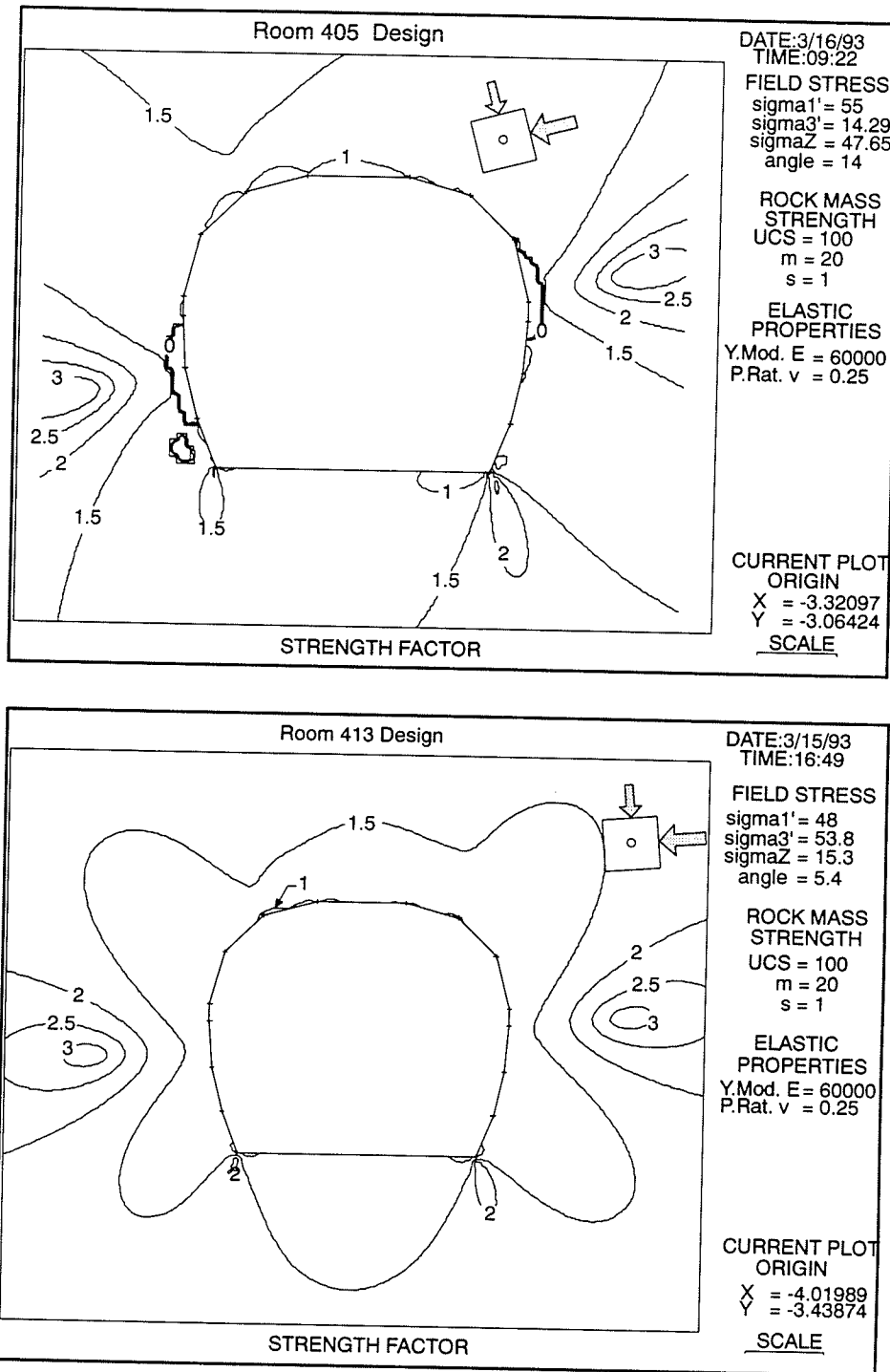
Figure 6.4: The strength to stress ratio for Room 405 and 413 when $\sigma_c = 100$ MPa, $m = 20$ and $s = 1$. Compare the stability to Figure 5.3.
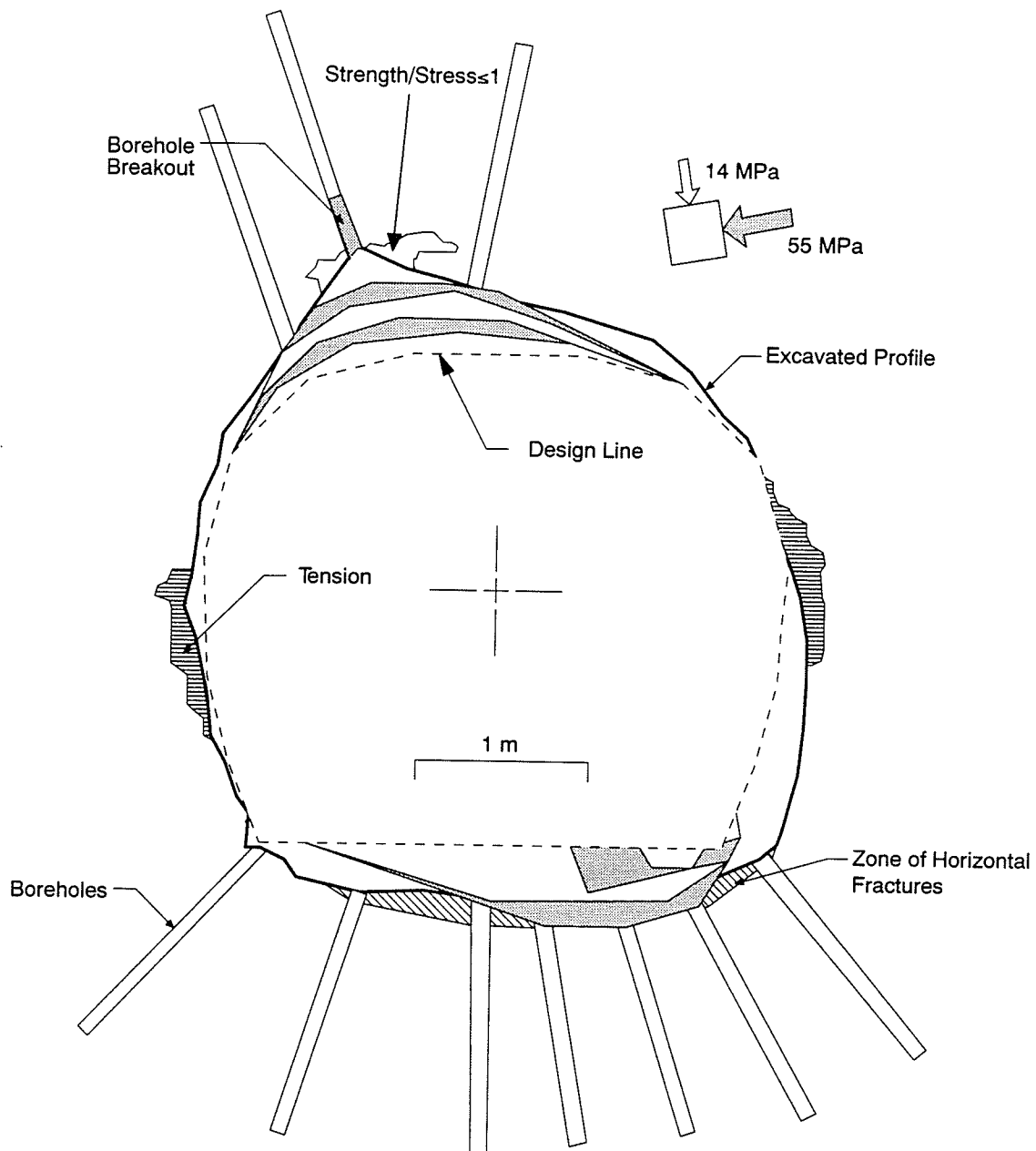
Figure 6.5: Progressive failure of Room 405 using the phenomenological approach.

Thus the strength around the openings will vary from a maximum value (undamaged) to a minimum value (maximum damage).

In the example above, the <u>excavated shape</u> of the opening was known and provided the profile for the final analysis. However, in some cases this information may not be available. If this information had not been available at the URL, the predicted depth of the notch would have been much larger. This problem arises because the model is a 2-dimensional analysis of a 3-dimensional failure process. For example, a plane strain stability analysis of a circular opening shows the failure zone as a thin layer in the roof (Figure 6.6). If this layer is removed in an attempt to represent the progressive nature of the spalling process, stability can only be achieved when the notch reaches a depth of about $2a$ from the centre of the opening [162]. This occurs simply because too much material has been removed in the initial modelling step. If, on the other hand, when only a small amount of material is removed to simulate the actual observations, stability is achieved with a much smaller notch. It is clear that any attempt to model the progressive failure must account precisely for the actual failure sequence.

The phenomenological approach can only approximate this complexity. In the next section a modelling approach based on crack growth is used to investigate the failure process.

6.3   Discrete Fracture Modelling

Modelling of discrete fracture propagation has received considerable attention over the past ten years. In most cases linear elastic and nonlinear elastic fracture mechanics are employed using some form of a sliding crack model [118, 137, 77, 48, 87, 89]. More recently Bažant et al. [5] used strain energy of a splitting crack to model the notch development around a circular opening. One of the difficulties with the formulation of models based on fracture mechanics is that when the stresses are compressive a shear mode stress intensity factor is used for which the predicted angle of crack propagation is different from that observed in rock where fractures tend to follow the direction of the maximum compressive stress.
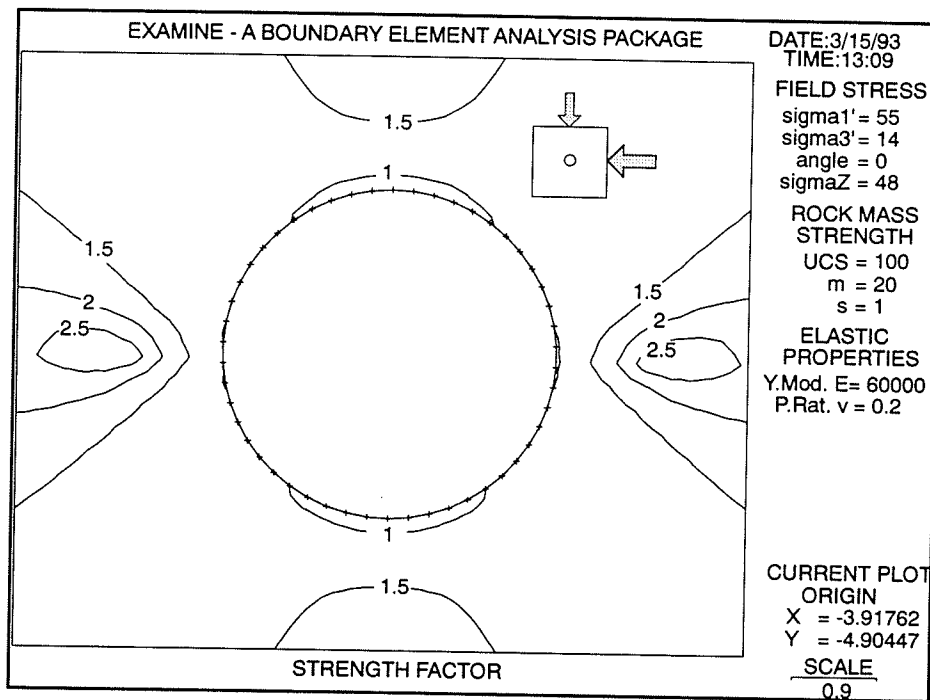
Figure 6.6: Stability around a circular tunnel. Note the thin layer of material (≤ 1) which has failed. In situ failure initiates at a point not as a thin layer.

Since fractures in compression tend to follow the direction of the maximum compressive stress, this problem can be overcome by avoiding fracture propagation models based on a sliding crack. A compressive fracture model which has this feature is described by Lajtai et al. [97, 96].

It was shown in Section 5.7 that the failure process involves localized crushing, leading to dilation and subsequent slabbing. In order to simulate this process a linear elastic finite element program InSight[2D] [44], currently being developed at the University of Manitoba, was used. This finite element code runs on a 486 IBM compatible personal computer and is completely user-friendly. Presently, the program is linear elastic and has the capability to have multiple material types and to assign a specific material type to an individual finite element. Various failure criteria are available within InSight[2D] to compute factors of safety. The program also contains the empirical compressive crack model developed at the University of Manitoba [97, 96]. With this model a crack is represented by an open ellipse and the growth of the crack is controlled by a stress averaging technique at the crack tip. This empirical fracture model can model the growth of cracks parallel to the direction of the maximum load. A complete discussion of the merits of this crack modelling approach is given by Carter [22]. It should be noted that the program InSight[2D] is in the development stage and that the compressive crack model currently in the program is presently being verified against laboratory results. Although the program has not been rigorously tested, its use is considered justified in this thesis because the program has many features which make it well suited for modelling the failure process.

It has been shown by Carter et al. [24] that most failure criteria have difficulty accurately describing both the tensile and unconfined compressive strength of rock as well as the confined strength. They showed that a three parameter function, called the Rocker function, best described the strength envelope of Lac du Bonnet granite, particularly when $\sigma_3 \approx 0$. The Rocker function is given as

$$\sigma_{1f} = \sigma_c \left(1 - \frac{\sigma_3}{\sigma_t}\right)^R \tag{6.1}$$

where σ_{1f} is the maximum principal stress at failure, σ_c is the unconfined compressive strength, σ_t is the tensile strength and R is the curve fitting exponent. The Rocker function has been implemented in InSight^{2D} in a special form of the strength to stress ratio called the USR [97] which can be used to define where fracture occurs. The USR, which can be considered equivalent to a factor of safety, is defined as

$$USR = \frac{\sigma_t}{\frac{\sigma_3}{2} - \sqrt{\left(\frac{\sigma_3}{2}\right)^2 + \left(\frac{\sigma_1 \sigma_t}{\sigma_c}\right)^2}} \tag{6.2}$$

The condition for fracture occurs when $USR = 1$. The parameters used to define the Rocker function for the undamaged Lac du Bonnet granite are $\sigma_c = 150$ MPa, $\sigma_t = 8$ MPa and $R = 0.8$.

The first step in the modelling process was to establish that the automatic mesh generator in InSight^{2D} provided enough accuracy to predict correctly the maximum tangential stress of 151 MPa for the plane strain solution (Figure 6.7). With the boundary of the tunnel discretized into 100 elements the plane strain analytical solution was achieved.

It was noted in Chapter 5 that failure initiated when the maximum tangential stress reached 100 MPa. Thus, the first step in modelling the failure process was to select far field stresses which produced the 100 MPa tangential stress in the crown of the tunnel. To achieve this tangential stress at the boundary of the tunnel the far-field stress was set to 40 MPa and 14 MPa. This approach approximates the 3-dimensional effect of the face on the tunnel tangential stresses, i.e., when the tunnel section is within 1 m of the tunnel face. With these stress conditions, a small region in the crown of the tunnel was assigned a Young's modulus which was lower than the Young's modulus for the rest of the rock mass. The purpose of this region of lower modulus was to simulate the damage due to crack initiation and stress rotation, which had occurred near the tunnel face, and the crushing of this damaged rock which occurs at about 100 MPa. The modulus of the crushed region was gradually lowered from 60 GPa, i.e., the uncrushed rock, to 5 GPa to simulate the crushed
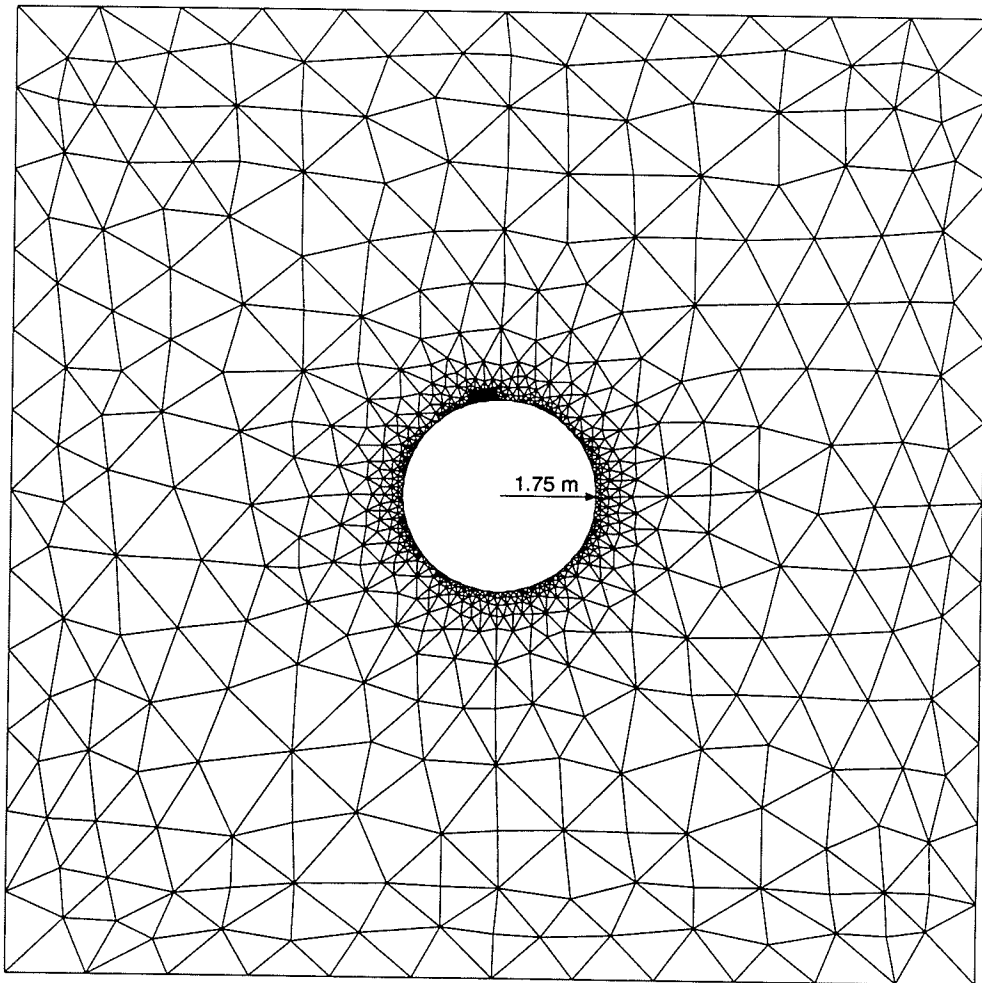
Figure 6.7: Finite element mesh generated by the automatic mesh generator in the program InSight^{2D}.
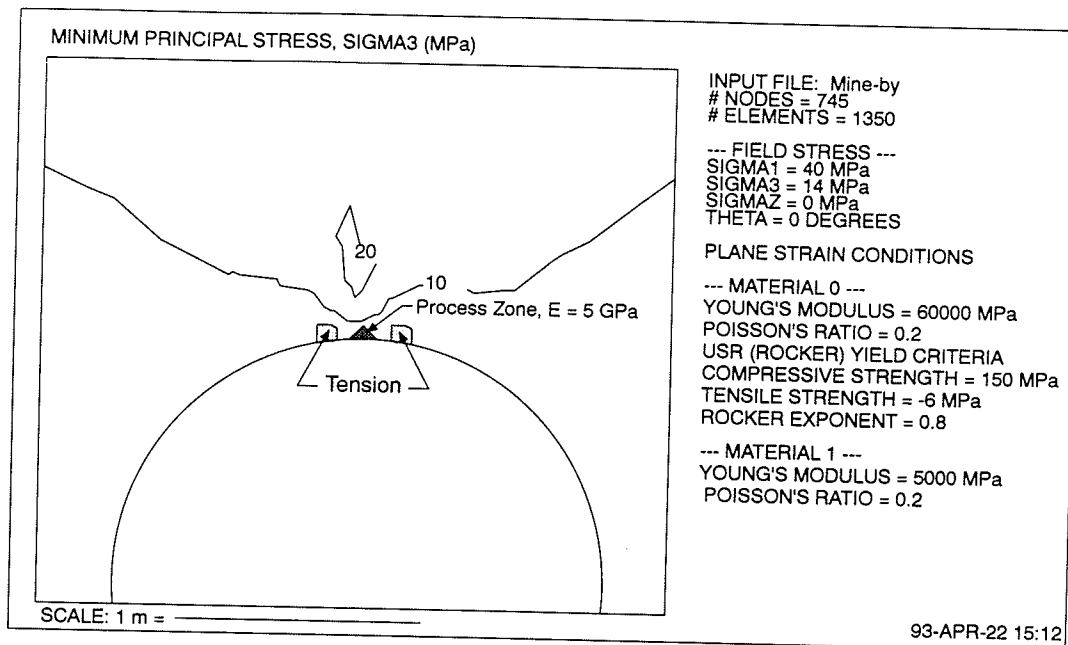
Figure 6.8: Tension on both sides of the process zone when the maximum tangential stress is 100 MPa.

process zone. During the course of reducing the modulus to 5 GPa, tension was observed near the boundary of the tunnel on both sides of the crushed zone (see Figure 6.8). This tension was first observed when the reduced modulus reached 30 GPa. Interestingly, the physical model studies also showed that when spalling initiated in the zone of maximum tangential stress, tension was observed remote from the boundary of the tunnel but close to the zone of spalling.

In Section 5.4 the microseismic data showed that cracking had initiated in the region that is now in tension in Figure 6.8. It was therefore considered reasonable that a fracture could propagate from this tensile region. An elliptical fracture about 70 mm long with a width of 1 mm was manually inserted in this tensile region with the long axis of the fracture in the direction of the maximum principal stress trajectory. After the fracture was inserted the mesh was rediscretized and the maximum *in situ* stress raised from 40 to 55 MPa to represent the tunnel advancing to the point where the maximum tangential stress reached

the plane strain condition of 151 MPa. This analysis indicated that the fracture was unstable (Figure 6.9). The fracture was subsequently extended and the analysis repeated. Again the longer fracture was found to be unstable and hence the fracture length increased again. Each time the fracture was lengthened the direction of extension followed the maximum principal stress trajectory. Eventually the fracture tip reached the process zone and became stable. However, the other fracture tip still remained unstable (Figure 6.10). At this stage in the process the crack tip farthest from the maximum tangential stress concentration should start to move towards the boundary of the tunnel to produce a slab with a thin edge as shown in Figure 5.42. Inspection of the maximum principal stress trajectories near the crack tip shows that they are oriented towards the tunnel boundary and that a failed zone is induced ahead of the crack closer to the tunnel perimeter (Figure 6.10). These features suggest that the crack should now start to curve towards the tunnel boundary. Unfortunately, the thickness of the slab between the crack and the tunnel is so thin that the analysis cannot be extended because numerical problems arise and the numerical simulation for this slab is therefore completed. Interestingly, the crack tip near the process zone also starts to curve around the process zone because the maximum principal stress trajectories tend to flow around the softened zone. This phenomenon could account for the curved slabs shown in Figure 5.40 which were found close to the notch tip.

The physical model studies in Chapter 5 demonstrated that once a crack formed at the boundary of a circular opening the resulting stress distribution could not be predicted based on closed-form solutions from elastic theory. Figure 6.11 shows the distribution of the maximum principal stress for a crack located in the region of maximum tangential stress. Clearly, the stress distribution is quite complex and completely different than the stress distribution in the absence of the crack.

It is now assumed that a similar slab has formed on the other side of the region of the crushed process zone and so the geometry of the tunnel is modified in the shape of a small notch to reflect the removal of two thin slabs. The modulus is now reduced in a new region
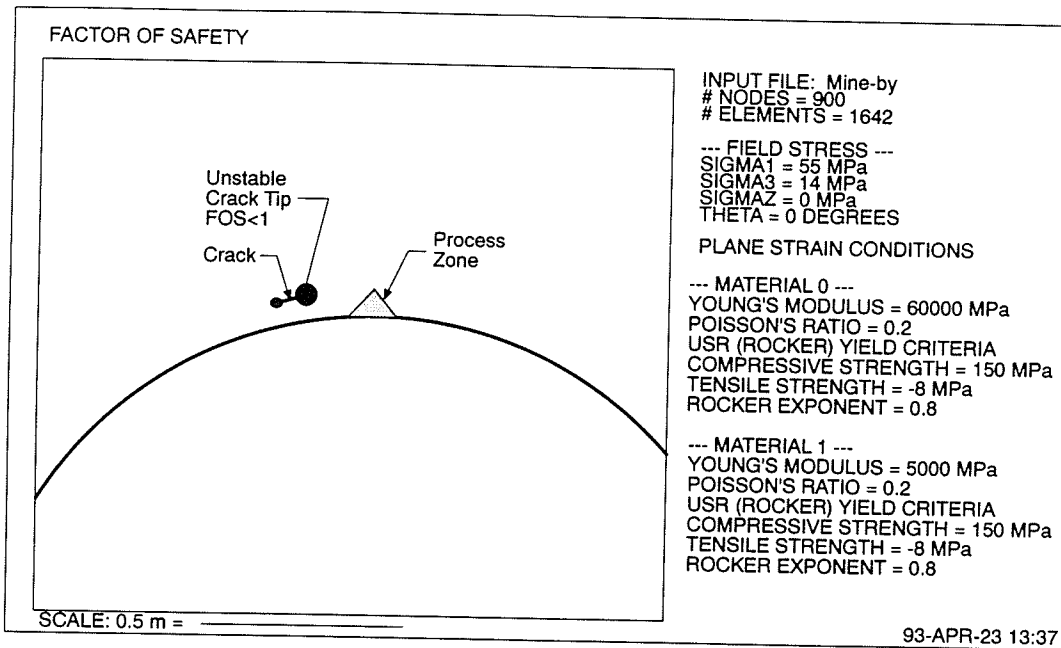
Figure 6.9: The crack with an unstable crack tips. Note that the tip nearest the process zone has the largest unstable area.
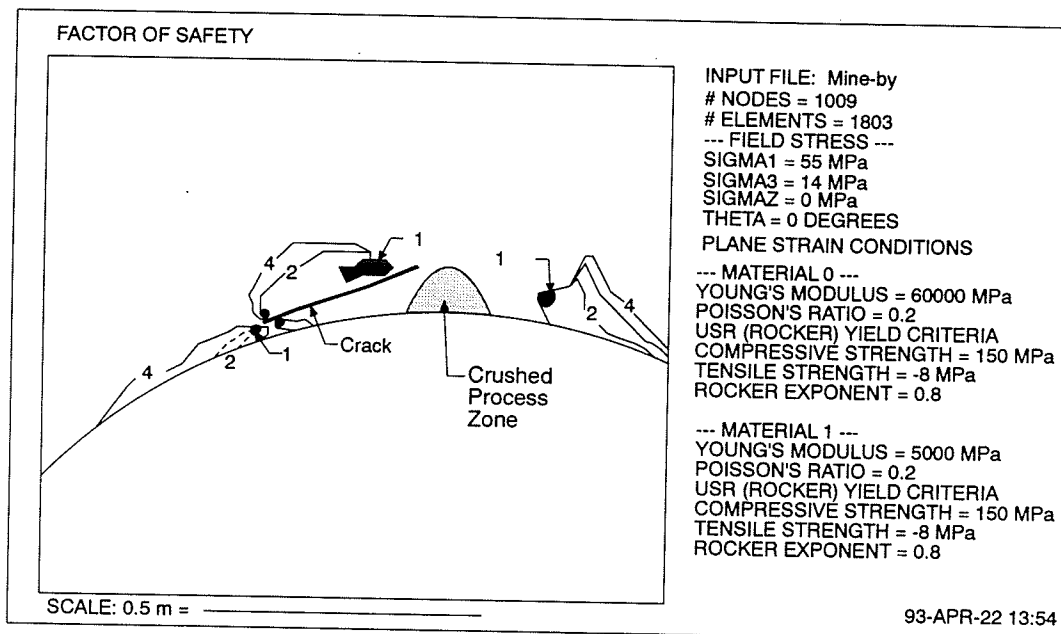
Figure 6.10: The crack has been extended until one crack tip reached the process zone. At this point the crack tip closest to the tunnel perimeter is still unstable. Also note other zones of instability around the process zone now appear.
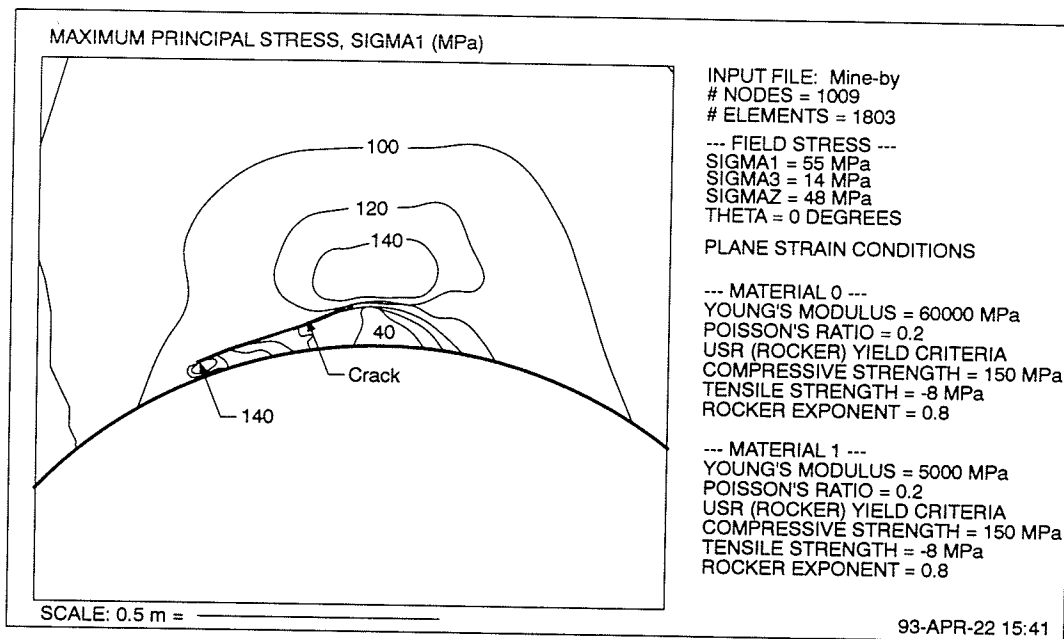
Figure 6.11: Distribution of the maximum principal stress around a crack located in the region of maximum tangential stress.

at the notch tip to simulate that the change in geometry has caused a stress concentration at the apex of the notch which leads to more crushing of the damaged rock. Hence the process repeats itself. As a result of the softened process zone at the notch tip tension again develops on either side of the notch. A compressive crack in this region is unstable and grows parallel to the maximum principal stress trajectory. Interestingly, if the crack is place at an angle to the maximum principal stress trajectory, the failure does not occur near the tip of the crack, but off to the side, suggesting that the crack would not extend but that an offset or en echelon crack would form. It is only when the crack is parallel to the maximum principal stress direction that the crack tips become unstable. Thus, it appears that the compressive fracture will propagate parallel to the tunnel boundary until it reaches a critical length, relative to the geometry of the opening, at which time it will tend to move towards the tunnel boundary.

This procedure of creating a softened process zone followed by discrete fracturing into

thin slabs would continue until a stable notch forms. At present, this iterative process in InSight^{2D} is completely manual and requires considerable judgment for successful execution. However, the major advantage of the discrete fracture approach is that it appears to capture the overall failure process, and avoids having to artificially degrade the rock strength around the tunnel, as with the phenomenological approach. Interestingly, the process of notch development using the discrete fracture model becomes more a problem related to geometry rather than rock strength.

The "as-built" shape of the Mine-by test tunnel was analyzed using InSight^{2D} to determine the effect of the process zone on stability. The surveyed geometry, obtained about 4 months after the tunnel was excavated, was used without modification. The tensile principal stress around the tunnel is shown in Figure 6.12. Note that tension occurs on the sidewall of the tunnel and that localized tension also occurs where the tunnel geometry is slightly irregular. Even in the areas where the geometry is irregular the tensile stress is only about -1 MPa. A process zone with the same modulus used in the previous analyses was inserted at the tip of the notch in the Mine-by tunnel and the analysis repeated (Figure 6.13). Unlike the results in Figure 6.8, now the "process zone" has no effect on the tensile stress distribution around the notch (compare Figures 6.12 and 6.13). The geometry of the notch in the roof was then modified in an attempt to smooth out the surveyed geometry and to extend the notch tip to a point. The results from this geometry modification are shown in Figure 6.14. The geometry modifications do remove some of the tensile stresses on one side of the notch but the overall change is quite minor. These analyses illustrate that the final stress distribution around the Mine-by test tunnel is now rather insensitive to minor geometry changes. This is quite different from when the tunnel was initially circular.

A final analysis of the Mine-by test tunnel was carried out to calculate the factor of safety using equation 6.2 (Figure 6.15). The results in Figure 6.15 indicate the tunnel is now stable except for minor tensile failure in the sidewall.

MINIMUM PRINCIPAL STRESS, SIGMA3 (MPa)

INPUT FILE: Mine-by
NODES = 1212
ELEMENTS = 2177

--- FIELD STRESS ---
SIGMA1 = 55 MPa
SIGMA3 = 14 MPa
SIGMAZ = 48 MPa
THETA = 14 DEGREES

PLANE STRAIN CONDITIONS

--- MATERIAL 0 ---
Y. MOD. = 60000 MPa
POISSON'S RATIO = 0.2
USR FAILURE CRITERIA
UCS = 150 MPA
TENSILE ST.= -8 MPa
ROCKER EXP. = 0.8

CONTOUR INTERVAL = 1
CONTOURS X 10**0

-1.00
-1.00
-1.00
-14
-14
-1.00
-1.00

SCALE: 1 m =

93-APR-28 14:32
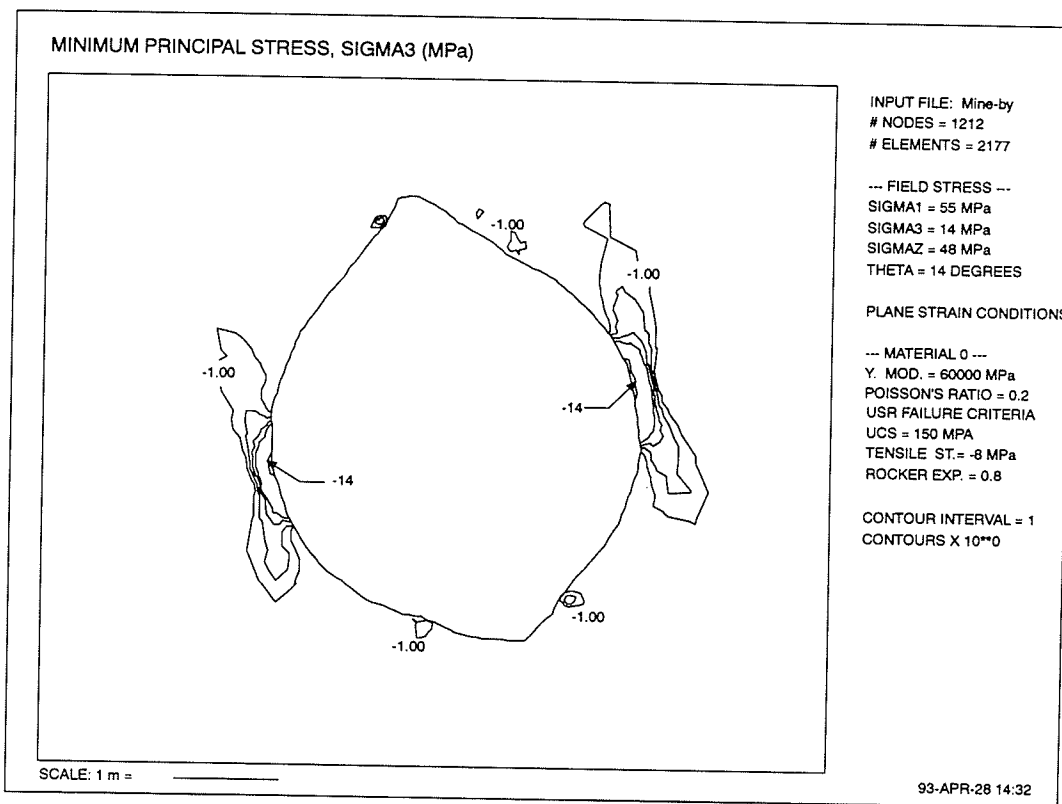
Figure 6.12: Distribution of the tensile principal stress around the Mine-by test tunnel.
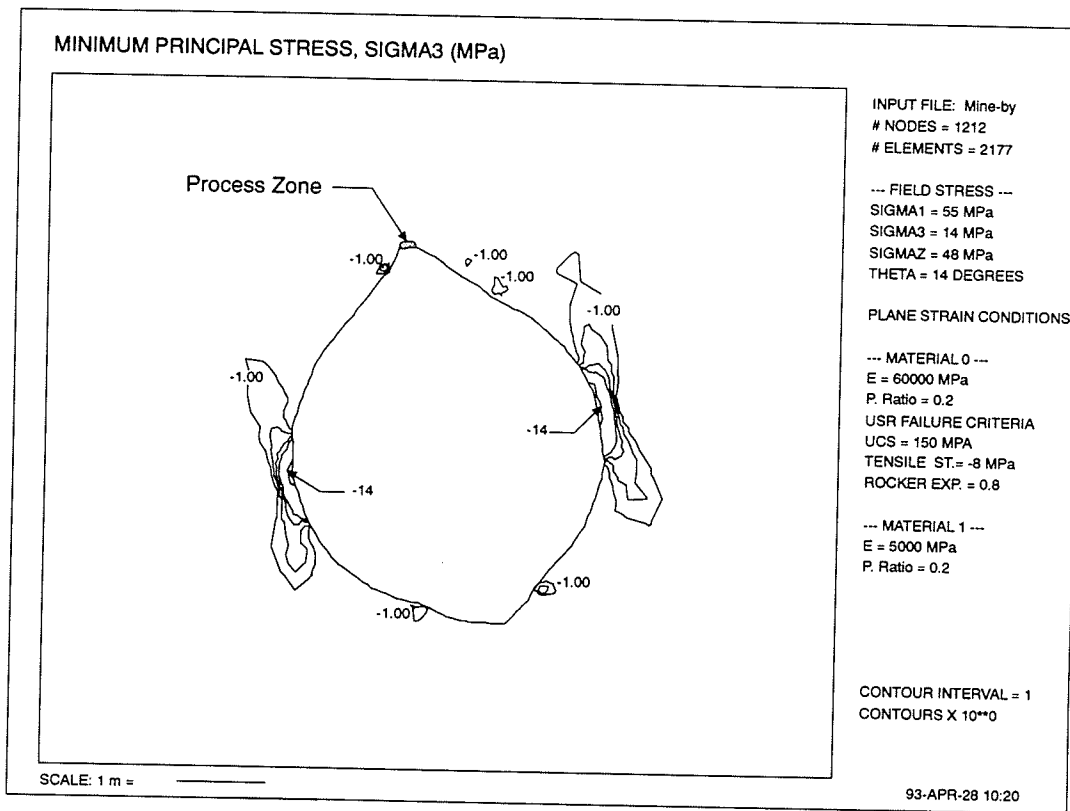
Figure 6.13: Distribution of the tensile principal stress around the Mine-by test tunnel after a "process zone" has been inserted in the notch tip.

MINIMUM PRINCIPAL STRESS, SIGMA3 (MPa)

INPUT FILE: Mine-by
NODES = 1215
ELEMENTS = 2183

--- FIELD STRESS ---
SIGMA1 = 55 MPa
SIGMA3 = 14 MPa
SIGMAZ = 48 MPa
THETA = 14 DEGREES

PLANE STRAIN CONDITIONS

--- MATERIAL 0 ---
YOUNG'S MODULUS = 60000 MPa
POISSON'S RATIO = 0.2
USR (ROCKER) YIELD CRITERIA
UCS = 150 MPa
TENSILE STRENGTH = -8 MPa
ROCKER EXPONENT = 0.8

CONTOUR INTERVAL = 1
CONTOURS X 10**0

SCALE: 1 m =   93-APR-28 10:17

Figure 6.14: Distribution of the tensile principal stress around the Mine-by test tunnel after some of the irregular geometry of the notch tip in the roof was removed.

FACTOR OF SAFETY

FOS ≤ 1

Tensile Failure

INPUT FILE: Mine-by
NODES = 1212
ELEMENTS = 2177

--- FIELD STRESS ---
SIGMA1 = 55 MPa
SIGMA3 = 14 MPa
SIGMAZ = 48 MPa
THETA = 14 DEGREES

PLANE STRAIN CONDITIONS

--- MATERIAL 0 ---
Y. MOD. = 60000 MPa
POISSON'S RATIO = 0.2
USR YIELD CRITERIA
UCS = 150 MPa
TENSILE STRENGTH = -8 MPa
ROCKER EXPONENT = 0.5

CONTOUR INTERVAL = 1
CONTOURS X 10**-1

SCALE: 1 m =   93-APR-28 14:36
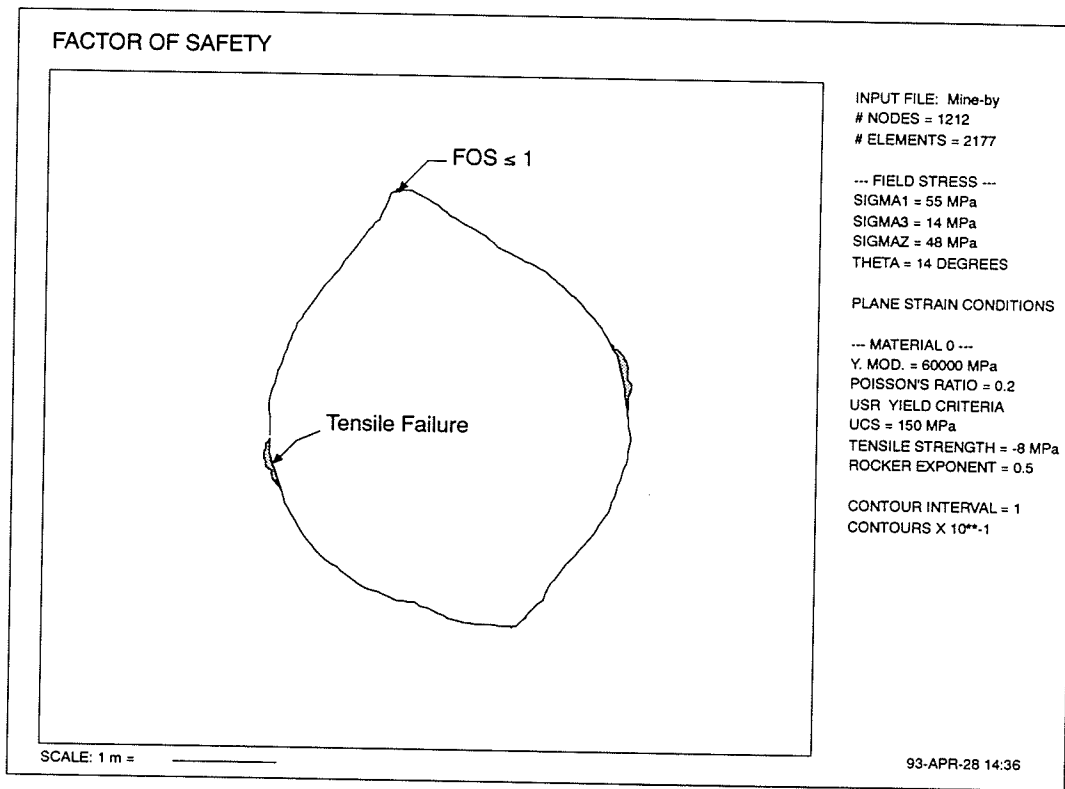
Figure 6.15: Stability of the Mine-by test tunnel. Only tensile failure in the sidewalls is indicated.

Chapter 7

Summary and Conclusions

The major objective of this thesis was to investigate why the strength of massive granite from back analysis of tunnels excavated at the 420 Level of the Underground Research Laboratory was about 100 MPa when the reported laboratory unconfined compressive strength, σ_c, of the granite was around 200 MPa. In the past, strength reductions found around underground openings have generally been attributed to scale effects, i.e., the strength decreases as the volume of the sample increases. At the URL it was obvious that scale effects could not explain the strength reduction because a 100-mm diameter borehole displayed the same failure as a 3.5-m diameter tunnel.

The testing programs carried out as part of this thesis revealed that excavating tunnels at the 420 Level causes damage around the advancing tunnel face and that this damage reduces the rock strength. The following is a summary of the progressive damage/failure process found around the underground openings at the URL.

7.1 Laboratory Progressive Failure

Analyses of unconfined compression test results revealed that cracking in compression begins at about $0.4\sigma_c$. This cracking continues as the load increases until the crack damage stress is reached at about $0.8\sigma_c$, at which point the sample starts to dilate. The load can be temporarily increased above this stress level but rock cannot sustain this load for any significant length of time. Thus, the crack damage stress is the true strength or cohesion

of the rock in unconfined compression. This concept is in complete agreement with the concrete industry which defines the long-term strength of concrete at the crack damage stress.

The laboratory properties of Lac du Bonnet granite were reviewed in Chapter 3. In Chapter 4 it was shown that the crack damage stress of Lac du Bonnet granite was not significantly influenced by scale effects and that properly conducted laboratory tests would fail at the crack damage stress, again supporting the notion that the traditional peak strength is an artifact of the test loading conditions. Also, it was shown that although the initial cracks during a compression test form parallel to the direction of the maximum applied load, the final failure surface is one which is inclined at about 23° to the direction of the applied load. This inclined failure surface was more pronounced in the tests which failed near or at the crack damage stress, suggesting that the axial splitting mode of failure may also be an artifact of the test conditions.

Damage-controlled laboratory tests were carried out to investigate the influence of crack volume on the crack damage stress. The testing program demonstrated that the crack damage stress decreased significantly to a crack damage threshold as damage accumulated in the sample. This threshold value coincided with the crack initiation stress for unconfined tests but as the confining stress increased the crack damage threshold value was always above the crack initiation stress.

The locus of crack damage stress with increasing damage was modelled using the Griffith locus of sliding and found to be in excellent agreement. The Griffith locus, which is based on fracture mechanics, was first introduced by Berry [6, 7] for tension and Cook [32] for compression. In developing the Griffith locus for triaxial compression, it became obvious that the strength of the material described by the Griffith locus had two strength components — cohesion and friction, but only the cohesion was controlled by the fracture mechanics properties such as fracture surface energy and crack length.

It is generally assumed that cohesion and friction are mobilized at the same displacements. The damage-controlled tests and the Griffith locus provided a means of separating the portion of the strength due to cohesion, basic friction and friction caused by roughness. At the instant the crack damage stress is first reached in a compression test the strength is essentially cohesion. At loads beyond the crack damage stress, friction becomes mobilized. Unfortunately, in the process of mobilizing friction, some cohesion is lost. When displacements are large this cohesion loss can amount to 50% or more of the initial cohesion.

Damage-controlled tests of Indiana limestone and Rocanville potash showed similar results to those from the granite testing program, the major difference being the slope of the Griffith locus in the softer rocks. It appears that the loss in cohesion in potash would not be nearly as rapid as in granite.

The concept of cohesion loss as a rock is damaged suggests that the traditional failure envelopes for rock around underground openings are not adequate. At the boundary of the openings the strength could be reduced to less than 50% or more of the initial cohesion. However, at some distance from the boundary, where $\sigma_3 > 0$ the strength of the undamaged rock is not degraded. Thus around the opening the failure envelope is very steep, being equal to $\approx 0.3\sigma_c$ at $\sigma_3 = 0$ and rising steeply to the initial crack damage stress when σ_3 is slightly greater than zero.

7.2 In Situ Progressive Failure

The concept of reducing cohesion with increasing damage was explored through the phenomenon of sample disturbance. The process of extracting a sample from a medium stressed above a critical level causes stress-induced microcracking which in the extreme case produces core discing. It was shown that the strength, i.e., cohesion, of samples with extensive microcrack damage, is significantly reduced when compared to undamaged samples. What is most important is that it is only the cohesion component of the strength envelope which is affected by the damage and that this cohesion cannot be regained by applying a confining

stress. The laboratory testing program revealed that the properties of Lac du Bonnet granite varied, depending on the location of the samples and that the strength of the samples from Cold Spring Quarry was noticeably higher than the strength of the near surface samples from the URL. This variation in rock properties was attributed to the crack density of the laboratory samples and not to the crack density in situ.

Physical models of openings of various diameters were loaded in uniaxial and biaxial compression. These model studies were carried out to examine the strength around circular openings. In the physical model studies the tangential stress required for spalling failure to occur around circular openings was about 220 MPa. This is considerably higher then the observed *in situ* strength. Thus physical model studies could not replicate the reduced strength observed *in situ*. Hence it was concluded that the reduced strength must be caused by something which is unique to the tunnel excavation *in situ*.

Microseismic monitoring of a 3.5-m diameter test tunnel revealed that considerable cracking was occurring around the face of the advancing tunnel. This cracking was found to occur to a depth of about $1.3a$ relative to the centre of the tunnel, where a is the tunnel radius. The microseismic events ahead of the tunnel face represent the initiation of cracking and not the failure strength. Stress analysis revealed that the stress magnitudes at the location of these microseismic events agreed very well with the crack initiation stress obtained from the laboratory testing program. The crack initiation stresses for the microseismic events also fitted the Cook envelope with $\phi = 0$, again suggesting friction had not been mobilized. Although the Griffith failure envelope for compression is suppose to represent the initiation of fracture, it gave a poor fit to the *in situ* microseismic cracking stress.

The *in situ* crack initiation envelope developed from the microseismic events was then used to evaluate the stress path at various locations around the tunnel as the tunnel face advances. It was shown that the stresses around the tunnel did not exceed the crack initiation envelope beyond about $1.5a$ from the center of the tunnel, where a is the tunnel radius. Thus at distances less then $1.5a$ cracking should be occurring. This agreed quite

closely with the locations of the microseismic events and the measured depth of spalling around the Mine-by test tunnel.

The unconfined *in situ* compressive strength of Lac du Bonnet granite is estimated at 150 MPa. This is considerably less than the short-term unconfined compressive strength, σ_c, of 220 MPa for undamaged samples from Cold Spring Quarry and has been degraded to reflect the laboratory findings discussed in Chapter 4. The 3-dimensional numerical analyses showed that the tunnel stresses near the face of an advancing tunnel did not exceed 150 MPa and at the point on the tunnel boundary where failure was observed the calculated maximum tangential stress was only about 80-100 MPa. Thus from the numerical analyses and the best estimate of the *in situ* strength it appeared that the loading path followed in the laboratory tests was not the loading path followed *in situ*, because according to the laboratory results failure should not have occurred.

In addition to the stress path around the tunnel, the effects of stress rotation were also considered. Wu and Pollard [161] demonstrated, for tension, that a stress rotation could influence the direction and origin of crack growth and cause additional crack growth without increasing the load. It was shown that the compressive stress near the tunnel face also rotates and it is proposed that this stress rotation contributes to the loss in cohesion. In the Mine-by test tunnel the σ_1 stress magnitude increases above the crack initiation stress of 70 MPa at 0.25 m ahead of the tunnel face, to about 100 MPa at 0.5 m inside the tunnel. Because the stress directions were rotated by the advancing tunnel, it is postulated that the crack length is increased above what would be expected with no rotation. The result of this additional crack growth is reduced cohesion. Interestingly, it is only at the maximum tangential stress concentration that the stress rotates to its maximum value ($\approx 25°$) at the tunnel face and then rotates back to its original position as the tunnel advances. At other positions around the tunnel perimeter the stress either does not rotate or does not rotate back to its original position. It is suggested that this complex loading path is responsible for the damage, i.e., loss in cohesion, in the region of the maximum

tangential stress concentration.

Observations made during the excavation of the Mine-by test tunnel revealed the failure process initiated at the maximum tangential stress concentration and that in this zone the rock failed by crushing. After this crushing occurred thin slabs were released violently from around the crushed zone. This crushed zone can be considered equivalent to the "process zone" at the tip of an advancing crack. Once the slabbing process initiates, it continues as the tunnel face is advanced. When the notch finally stabilizes the geometry of the notch displays a characteristic convex shape with the process zone at the tip of the notch.

7.3 Modelling the Failure Process

Physical model studies of a circular hole in blocks of Lac du Bonnet granite were carried out with and without confining stress. The unconfined samples revealed that three types of cracks occurred around the circular openings: primary crack, remote crack and the spalling crack. The primary crack occurred first followed by the remote crack which was subsequently followed by the spalling crack. The sequencing of the remote and spalling cracks was reversed for the confined case. This change in fracture sequence for the confined case occurs because the primary crack does not grow very far compared to the unconfined case. Thus the sequence of fracturing is influenced by the stress redistribution which occurs as a result of the initial primary crack. In both the unconfined and confined physical models the spalling cracks formed when the maximum tangential stress on the boundary of the circular hole was slightly greater then the unconfined compressive strength.

Two approaches were used in the modelling of the failure process around underground openings: the phenomenological approach and the discrete fracture approach. The phenomenological approach made no assumption of the mechanisms involved in the failure process. It simply assumes a degraded rock strength everywhere around the opening. In this case the strength was assumed to be approximately equal to the initial crack damage stress envelope obtained from the testing of the damaged samples from the 420 Level of the

URL. It was reasoned that the damage process around the tunnel is similar to the damage process in extracting a sample, and therefore, the initial crack damage stress of the damaged samples would be a reasonable estimate of damaged *in situ* strength. A strength to stress ratio is used to locate the "failed zones". In this modelling approach an elastic-brittle material behaviour is assumed such that once the failed zones are located, then the tunnel shape is modified to reflect the removal of this failed material, i.e., the slabbing process. After the geometry is modified the elastic analysis is rerun. The process is repeated until a reasonably stable geometry is achieved. For this modelling approach to work, some idea of the final stable shape is required. Also, the approach is sensitive to the amount of the material removed in each step. In this simplified approach, a notch which extends about $2a$ from the tunnel centre is produced. This is considerably deeper than the notches observed at the URL.

After observing the crack growth in the physical models, it was postulated that the process zone must be a key factor in modelling the notch development. The 2-dimensional finite element program InSight^{2D}, containing an empirical compressive crack model, was used to investigate the spalling process. The initial far-field stresses were set to provide a maximum tangential stress of 100 MPa, the stress level at which failure was first observed. The process zone, which was observed *in situ*, was represented in the InSight^{2D} model by assigning a small region in the zone of maximum tangential stress a reduced modulus equivalent to about 1/12 of the undamaged modulus of 60 GPa. This softened process zone caused tension to appear near the boundary of the tunnel on both sides of the process zone. A compressive crack was then manually inserted into this region of tension, parallel to the direction of the maximum principal stress. The far-field stress was then increased to provide the maximum tangential stress given by the plane strain conditions. The compressive crack, with the new stress conditions, became unstable. The crack was then extended until it reached the process zone, at which point the other crack tip still remained unstable. Crack propagation continued until the crack tip approached the boundary of the tunnel. Although

the crack propagation in InSight[2D] is entirely manual, the program appears to capture all the key elements observed during the failure process *in situ*: a process zone, slabbing, and convex curvature near the notch tip. The major advantage of the discrete fracture approach is that the rock mass strength is not degraded as with the phenomenological approach.

7.4 Conclusions

Listed below is a brief summary of the key contributions and conclusions of this thesis towards an advancement in the understanding of rock failure and rock strength around underground openings.

1. The broad distribution of stresses in a large rock mass can be explained using elastic theory.

2. Samples obtained from a pre-stressed medium may be damaged by the sampling process. This damage, which starts to occur when the far field stress exceeds about $0.15\sigma_c$, affects the strength of the sample. In particular, the damage reduces the cohesion but does not affect the friction. Thus intact samples obtained from a pre-stressed rock mass may not necessarily represent the *in situ* intact strength.

3. The effects of scale, loading-rate and moisture on intact strength of granite is minimal and do not explain the observed strength reduction investigated in this thesis.

4. The laboratory unconfined compressive strength (σ_c) of granite is not a material property but is dependent on the loading conditions. The crack initiation and crack damage stress were found to be essentially independent of loading conditions and are considered material properties.

5. Cracking initiates in laboratory samples at about $0.4\sigma_c$ as stable crack growth parallel to the direction of the maximum applied load.

6. Sliding in a sample occurs at about 0.7-$0.8\sigma_c$ when the crack damage stress exceeds the cohesive strength. Initially, as sliding first starts the mechanism is unstable.

7. Damage-controlled tests can be used to map the locus of stress associated with crack initiation and sliding. The Griffith locus of sliding was applied to the sliding locus obtained from the damage-controlled tests and gave excellent agreement.

8. The results from the damage-controlled tests and the application of the Griffith locus demonstrated that friction and cohesion are not mobilized equally as a sample is strained. By the time the friction is fully mobilized a significant portion of the initial cohesion in the sample is lost. This implies that the prediction of failure around tunnels which are experiencing damage cannot be based on strength envelopes derived from traditional laboratory tests.

9. The Cook failure criterion was extended and the extension separated the Cook failure envelope in σ_1-σ_3 space into cohesion and friction with the cohesion as a function of crack length and fracture surface energy.

10. Cracking around underground openings initiates at about the same stress level as crack initiation in the laboratory tests. Like the laboratory test results, the crack initiation *in situ* suggests that the cracking is only affecting the cohesion of the rock mass. The zone of the crack initiation, with $\phi = 0$, appears to define the limit of progressive failure around the openings at the 420 Level of the Underground Research Laboratory.

11. The loading path of rock near the tunnel face suggests that stress rotation in the areas of maximum tangential stress concentration is a significant contributor to the localized degradation of the rock mass cohesive strength. Failure initiates in these locally damaged areas when the maximum tangential stress reaches about 100 MPa which is approximately 50% of σ_c.

12. Failure around the underground openings at the 420 Level of the Underground Research Laboratory initiates at a point, called the process zone, and is progressive. Failure occurs as a slabbing mechanism and stops when the geometry of the notch becomes convex and the process zone becomes contained. The depth of this type of failure at the Underground Research Laboratory is about $1.3a$, where a is the tunnel radius.

13. Modelling of the extent of failure cannot be captured by plane-strain modelling unless some effort is made to account for the initiation of failure at a point near the tunnel face before plane strain conditions are reached.

7.5 Future Research

In any new approach to an old problem there are always areas that require further research. The two areas which need additional research for the problem posed in this thesis are

- the effect of stress rotation on crack growth in compression

- numerical modelling of the failure process

Laboratory tests to investigate the effect of stress rotation on crack length would be difficult to perform because to truly simulate the advancing tunnel the load would have to be maintained while the sample is rotated. There does not appear to be any simple test configuration for this problem. However, this issue is very important because in any underground situation stress rotation occurs in advance of the excavation. If the rock strength can be degraded by simply holding the stress constant above the crack initiation stress and rotating the direction of application it could have a direct impact on the sequence of excavation, e.g., where multiple openings occur.

The process zone appears to be the key to the failure process. A numerical model which simulates the behaviour of the process zone, i.e., dilation, may provide a better

understanding of the failure process. The current version of InSight^{2D} greatly enhances our ability to quickly explore excavation-related problems. Future versions need to automate the crack growth and spalling process, and simulate tunnel advance.

Bibliography

[1] G. R. Adams, A. J. Jaegar, and C. Roering. Investigations of rock fracture around deep level gold mine stopes. In H.H. Einstein and D. P. Scandariato, editors, *Proc. 22nd US Symposium on Rock Mechanics, M.I.T.*, pages 227–236. Massachusetts Institute of Technology, 1981.

[2] M. F. Ashby and C. G. Sammis. Damage mechanics of brittle solids in compression. *Pure and Applied Geophysics*, 133(3):489–521, 1990.

[3] B. K Atkinson and P. G. Meredith. The theory of subcritical crack growth with applications to minerals and rocks. In B. K Atkinson, editor, *Fracture Mechanics of Rock*, pages 111–166. Academic Press, New York, 1987.

[4] N. R. Barton, R. Lien, and J. Junde. Engineering classification of rock masses for the design of tunnel support. *Rock Mechanics and Rock Engineering*, 6:189–239, 1974.

[5] Z. P. Bažant, F.-B. Lin, and H. Lippmann. Fracture energy release and size effect in borehole breakout. *Int. J. for Numerical and Analytical Methods in Geomechanics*, 17:1–14, 1993.

[6] J. P. Berry. Some kinetic considerations of the Griffith criterion for fracture I: Equations of motion at constant force. *J. Mech. Phys. Solids*, 8:194–206, 1960.

[7] J. P. Berry. Some kinetic considerations of the Griffith criterion for fracture II: Equations of motion at constant deformation. *J. Mech. Phys. Solids*, 8:207–216, 1960.

[8] Z. T. Bieniawski. Mechanism of brittle fracture of rock, parts I, II and III. *Int. J. Rock Mech. Min. Sci. & Geomech. Abstr.*, 4(4):395–430, 1967.

[9] Z. T. Bieniawski. Engineering classification of jointed rock masses. *The Civil Engineer in South Africa*, pages 335–343, December 1973.

[10] E. Bombolakis. Study of the brittle fracture process under uniaxial compression. *Tectonophysics*, 18:231–248, 1973.

[11] W. F. Brace. Brittle fracture of rocks. In W.R. Judd, editor, *Proc. Int. Conf., State of Stress in the Earth's Crust*, pages 111–178, 1964.

[12] W. F. Brace and J .D. Byerlee. Recent experimental studies of brittle fracture of rocks. In C. Fairhurst, editor, *Proc. 8th U.S. Symp. on Rock Mechanics, Minneapolis*, pages 58–81. American Institute of Mining Engineers, 1968.

[13] W. F. Brace, B. Paulding, and C. Scholz. Dilatancy in the fracture of crystalline rocks. *Journal of Geophysical Research*, 71:3939–3953, 1966.

[14] W. F. Brace, E. Silver, K. Hadley, and C. Goetze. Cracks and pores: A closer look. *Science*, 178:162–164, 1972.

[15] B. H. G. Brady and E. T. Brown. *Rock mechanics for underground mining*. George Allen & Unwin, London, first edition, 1985.

[16] D. Brock. *Elementary engineering fracture mechanics*. Kluwer Academic Publishers, Dordrecht, fourth edition, 1986.

[17] A. Brown, N. M. Soonawala, R. A. Everitt, and D. C. Kamineni. Geology and geophysics of the Underground Research Laboratory Site, Lac du Bonnet Batholith, Manitoba. *Can. J. Earth Sci.*, 26:404–425, 1989.

[18] E. T. Brown. Strength-size effects in rock material. In *In Proc. ISRM Symp. Rock Fracture*, pages 2–11, Nancy, 1971.

[19] E. T. Brown, editor. *Rock characterization testing and monitoring, ISRM suggested methods*, pages 107–127. Pergamon Press, Oxford, 1981.

[20] N. P. Cannon, E. M. Shulson, T. R. Smith, and H. J. Frost. Wing cracks and brittle compressive fracture. *Acta metall. mater.*, 38(10):1955–1962, 1990.

[21] S. R. Carlson and R. P. Young. Acoustic emission and ultrasonic velocity study of excavation-induced microcrack damage in the Mine-by tunnel at the Underground Research Laboratory. Atomic Energy of Canada Ltd. RP015AECL, Engineering Seismology Laboratory, Queen's University, Kingston, Canada, 1992.

[22] B. J. Carter. *Physical and numerical modelling of fracture in rock: With special emphasis on the potash mines of Saskatachewan*. PhD thesis, Civil Engineering Department, University of Manitoba, Winnipeg, Manitoba, Canada, 1992.

[23] B. J. Carter. Size and stress gradients effects on fracture around cavities. *Rock Mechanics and Rock Engineering*, 25(3):167–186, 1992.

[24] B. J. Carter, E. J. S. Duncan, and E. Z. Lajtai. Fitting strength criteria to intact rock. *Geological and Geotechnical Engineering*, 9:73–81, 1991.

[25] B. J. Carter, E. Z. Lajtai, and E. Z. Petukhov. Primary and remote fractures around underground cavities. *International Journal for Numerical Methods in Geomechanics*, 15:21–40, 1991.

[26] N. A. Chandler. *An energy approach to sleeve fracture stress measurements.* PhD thesis, Civil Engineering Department, University of Manitoba, Winnipeg, Manitoba, Canada, 1989.

[27] Ph. A. Charlez. *Rock Mechanics volume 1 Technical Fundamentals.* Éditions Technip, Paris, first edition, 1991.

[28] Rui Chen. *In situ and laboratory study of potash deformation with reference to Saskatchewan potash.* PhD thesis, Civil Engineering Department, University of Manitoba, Winnipeg, Manitoba, Canada, 1993.

[29] P. J. Chernis. Comparison of the pore-microstructure of shallow and deep samples of the Lac du Bonnet granite. Technical Record 223, Atomic Energy of Canada Limited, 1984.

[30] P. S. B. Colback and B. L. Wiid. The influence of moisture content on the compressive strength of rock. In *Proc.3rd Canadian Rock Mechanics Symposium*, pages 65–83, Toronto, 1965.

[31] D. S. Collins and R. P. Young. Monitoring and source location of microseismicity induced by excavation of the Mine-by Test Tunnel: Preliminary analysis. Atomic Energy of Canada Ltd. RP013AECL, Engineering Seismology Laboratory, Queen's University, Kingston, Canada, 1992.

[32] N. G. W. Cook. The failure of rock. *Int. J. Rock Mech. Min. Sci. & Geomech. Abstr.*, 2:389–403, 1965.

[33] N. G. W. Cook. An experiment proving that dilatancy is a pervasive volumetric property of brittle rocks loaded to failure. *Rock Mechanics and Rock Engineering*, 2:181–188, 1970.

[34] N. G. W. Cook. Origin of rockbursts. In *Proc. of Symposium on Rockbursts: prediction and control, London*, pages 1–9. The Institution of Mining and Metallurgy, London, 1983.

[35] N. G. W. Cook, E. Hoek, J. P. G. Pretorius, W. D. Ortlepp, and M. D. G. Salamon. Rock mechanics applied to the study of rockbursts: a synthesis of the results of rockburst research in South Africa up to 1965. *J. South African Institute of Mining and Metallurgy*, pages 436–528, May 1966.

[36] J. H. Curran and B. T. Corkum. *Examine^{3D}–A 3D boundary element program for calculating stresses around underground excavations in rock, Version 1.5.* Data Visualization Laboratory, University of Toronto, Toronto, Canada, 1993.

[37] C. C. Davison. Hydrogeological characterization at the site of Canada's Underground Research Laboratory. In *Proc. IAH Int. Symp. Groundwater Resource Utilization and Contaminant Hydrogeology*, pages 310–335, Montreal, 1984.

[38] D. U. Deere. Geological considerations. In K. G. Stagg and O. C. Zienkiewicz, editors, *Rock Mechanics in Engineering Practice*, pages 1–20. John Wiley & Sons, London, 1980.

[39] P. Desayi and C. S. Vishwanath. True ultimate strength of plain concrete. *RILEM Bulletin*, 36:163–173, 1967.

[40] R. K. Dhir and C. M. Sangha. A study of the relationship between time, strength, deformation and fracture of concrete. *Magzine of Concrete Research*, 24:197–208, 1967.

[41] Y. Du and A. Aydin. Interaction of multiple cracks and formation of echelon crack arrays. *Int. J. for Numerical and Analytical Methods in Geomechanics*, 15:205–218, 1991.

[42] M. B. Dusseault and N. R. Morgenstern. Locked sands. *Quarterly J. Engineering Geology*, 12:117–131, 1979.

[43] C. G. Dyke. Core discing: Its potential as an indicator of principal in situ stress directions. In V. Maury and D. Fourmaintraux, editors, *Proc. ISRM–SPE International Symposium Rock at Great Depth, Pau*, volume II, pages 1057–1064. A.A. Balkema, Rotterdam, 1989.

[44] E. J. Dzik, E. Z. Lajtai, and C. D. Martin. Numerical modelling of discrete fracture in granite. In H.J. Siriwardane, editor, *Proc. 8th Int. Conf. on Computer Methods and Advances in Geomechanics (IACMAG94), Morgantown, West Virginia*. A.A. Balkema, Rotterdam, in prep.

[45] L. A. Endersbee. Brittle fracture in concrete and rocks. *Transactions Institute of Engineers, Australia, Civil Engineering*, CE9:217–233, 1967.

[46] R. A. Everitt, A. Brown, C. C. Davison, M. Gascoyne, and C. D. Martin. Regional and local setting of the Underground Research Laboratory. In R. S. Sinha, editor, *Proc. Int. Symp. on Unique Underground Structures, Denver*, volume 2, pages 64:1–23. CSM Press, Denver, 1990.

[47] R. T. Ewy and N. G. W. Cook. Deformation and fracture around cylindrical openings in rock, parts i and ii. *Int. J. Rock Mech. Min. Sci. & Geomech. Abstr.*, 27:387–427, 1990.

[48] R. T. Ewy, J. M. Kemeny, Z. Zheng, and N. G. W. Cook. Generation and analysis of stable excavation shapes under high rock stresses. In S. Herget, G. & Vongpaisal, editor, *Proc. 6th International Congress on Rock Mechanics, Montreal*, volume 2, pages 875–881. A.A. Balkema, Rotterdam, 1987.

[49] C. Fairhurst. Fundamental considerations relating to the strength of rock. Technical Report Colloquium on Rock Fracture, Ruhr Universitat, Bochum, Germany, 1972.

[50] S. D. Falls and R. P. Young. Uniaxial compression testing of large samples of Lac du Bonnet granite at low strain rates. Atomic Energy of Canada Ltd. RP014AECL, Engineering Seismology Laboratory, Queen's University, Kingston, Canada, 1992.

[51] B. Feignier and R. P. Young. Moment tensor inversion of induced microseismic events: Evidence of non-shear failures in the $-4 < m < -2$ moment magnitude range. *Geophysical Research Letters*, 19(14):1503–1506, July 24 1992.

[52] G. M. Fonseka, S. A. F. Murrell, and P. Barnes. Scanning electron microscope and acoustic emission studies of crack development in rocks. *Int. J. Rock Mech. Min. Sci. & Geomech. Abstr.*, 22:273–289, 1985.

[53] Y. C. Fung. *Foundations of solid mechanics*. Prentice-Hall, Inc., Englewood Cliffs, New Jersey, 1965.

[54] N. C. Gay. Fracture growth around openings in thick-walled cylinders of rock subjected to hydrostatic compression. *Int. J. Rock Mech. Min. Sci. & Geomech. Abstr.*, 10:209–233, 1973.

[55] N. C. Gay. Fracture growth around openings in large blocks of rock subjected to uniaxial and biaxial compression. *Int. J. Rock Mech. Min. Sci. & Geomech. Abstr.*, 13:231–243, 1976.

[56] N. G. A. Gerogiannopoulos. *A critical state approach to rock mechanics*. PhD thesis, University of London, 1979.

[57] J. Glucklich and L. J. Cohen. Size as a factor in the brittle-ductile transition and the strength of some materials. *Int. J. Fract. Mech.*, 3:278–289, 1967.

[58] J. Glucklich and L. J. Cohen. Strain energy and size effects in a brittle material. *Materials Research & Standards*, 8(10):17–22, 1968.

[59] A. A. Griffith. The phenomena of rupture and flow in solids. *Phil. Trans. Royal Soc. London*, 221A:163–198, 1921.

[60] A. A. Griffith. Theory of rupture. In *First International Congress Allpied Mechanics, Delft*, pages 55–63, 1924.

[61] M. Gyenge, R. Jackson, and B. Gorski. Residual strength envelopes using the confined shear test method. In J.-C. Roegiers, editor, *Proc. 32th U.S.Symposium on Rock Mechanics, Norman*, pages 629–635. A.A. Balkema, Rotterdam, 1991.

[62] B. C. Haimson. Mechanical behaviour of rock under cyclic loading. In *Proc. 3rd Congress Int. Soc. Rock Mech., Denver*, volume II, pages 373–379. National Academy of Sciences, Washington, D.C., 1974.

[63] B. C. Haimson and C. G. Herrick. Borehole breakouts and in situ stress. In *Proc. 12th Annual Energy-Sources Technology Cof. & Exhibition, Drilling Symp.*, pages 17–22. American Society Mechanical Engineers, New York, 1989.

[64] B. C. Haimson and C. M. Kim. Mechanical behaviour of rock under cyclic fatigue. In E. J. Cording, editor, *Proc. 13th U.S. Symp. on Rock Mechanics, University of Illinois*, pages 373–378. American Society of Civil Engineers, New York, 1972.

[65] B. C. Haimson and Z. Zhao. Laboratory hydraulic fracturing tests in Lac du Bonnet granite from the Underground Research Laboratory. Contract report, Atomic Energy of Canada Limited, 1991.

[66] D. K. Hallbauer, H. Wagner, and N. G. W. Cook. Some observations concerning the microscopic and mechanical behaviour of quartzite specimens in stiff, triaxial compression tests. *Int. J. Rock Mech. Min. Sci & Geomech. Abstr.*, 10:713–726, 1973.

[67] A. Hefny and K. Y. Lo. The interpretation of horizontal and mixed-mode fractures in hydraulic fracturing tests in rocks. *Canadian Geotechnical Jornal*, 29(6):902–917, 1992.

[68] G. Herget. Regional stresses in the Canadian Shield. In *Proc. of 13th Canadian Rock Mechanics Symposium (The H.R. Rice Memorial Symposium)*, volume CIM 22, pages 9–16. Can. Inst. Min. and Metall., 1980.

[69] G. Herget. *Stresses in rock*. A.A.Balkema, Rotterdam, 1988.

[70] G. Herget and B. Arjang. Update on ground stresses in the Canadian Shield. In G. Herget, editor, *Proc. Stresses in Underground Structures, Ottawa*, pages 33–47, 1990.

[71] K. Hodgson and N. G. W. Cook. The effect of size and stress gradient on the strength of rock. In *Proc. 2nd Congress Int. Soc. Rock Mech., Belgrade*, volume 2, pages 32–34, 1970.

[72] E. Hoek. Rock fracture under static stress conditions. CSIR Report MEG 383, National Mechanical Engineering Research Institute, Council for Scientific and Industrial Research, Pretoria, South Africa, 1965.

[73] E. Hoek. Strength of jointed rock masses. *Geotechnique*, 33(3):187–223, 1983.

[74] E. Hoek and Z. T. Bieniawski. Brittle fracture propagation in rock under compression. *Journal of Fracture Mechanics*, 1(3):137–155, 1965.

[75] E. Hoek and E. T. Brown. *Underground excavations in rock*. The Institution of Mining and Metallurgy, London, 1980.

[76] C. T. Holland. The strength of coal in mine pillars. In *Proc. 6th Symp. Rock Mech. Univ. of Missouri (Rolla)*, pages 41–49, 1964.

[77] H. Horii and S. Nemat-Nasser. Brittle failure in compression: splitting, faulting, and brittle ductile transition. *Phil. Trans. Royal Society London, Math Phys. Sci.*, 319:337–374, 1986.

[78] J. A. Hudson, E. T Brown, and C. Fairhurst. Shape of the complete stress-strain curve for rock. In E.J. Cording, editor, *Proc. 13th U.S. Symp. on Rock Mechanics, Urbana*, pages 773–795. American Society of Civil Engineers, New York, 1972.

[79] C. E. Inglis. Stresses in a plate due to the presence of cracks and sharp corners. *Trans. Instn. Nav. Archit., London*, 55:219–241, 1913.

[80] Itasca Consulting Group, Inc. *UDEC–Universal Distinct Element Code, Version 1.8*. Minneapolis, Minnesota, 1992.

[81] R. Jackson. The effect of loading rate on the uniaxial mechanical properties of Lac du Bonnet granite. Divisional Report MRL 90-058(TR), CANMET, Energy Mines and Resources, Canada, 1991.

[82] R. Jackson and J. S. O. Lau. The effect of specimen size on the mechanical properties of Lac du Bonnet grey granite. In A. Pinto da Cunha, editor, *Proc. 1st. Int. Workshop on Scale Effects in Rock Masses, Loen, Norway*, pages 165–174. A.A.Balkema, Rotterdam, 1990.

[83] R. Jackson, J. S. O. Lau, and A. Annor. Mechanical, thermo-mechanical and joint properties of rock samples from the site of AECL's Underground Research Laboratory, Lac du Bonnet, Manitoba. In *Proc. 42nd Canadian Geotechnical Conference, Winnipeg*, pages 41–49, 1989.

[84] J. C. Jaeger and N. G. W. Cook. *Fundamentals of rock mechanics*. Chapman and Hall, London, third edition, 1979.

[85] N. C. Joughin and A. J. Jager. Fracture of rock at stope faces in South African gold mines. In *Proc. Rockbursts: Prediction and Control, London*, pages 53–67. The Institution of Mining and Metallurgy, London, 1983.

[86] T. J. Katsube. Pore structure and pore parameters that control the radionuclide transport in crystalline rocks. In *Proc. Tech. Prog., Int. Powder and Bulk Solids Handling and Processing, Rosemont, Ill.*, pages 394–409, 1981.

[87] J. M. Kemeny and N. G. W. Cook. Crack models for the failure of rock under compression. In C. S. Desai, E. Krempl, P. D. Kiousis, and T. Kundu, editors, *Proc. 2nd Int. Conference Constitutive Laws for Engineering Materials, Theory and Applications*, volume 1, pages 879–887, Tucson, Arizona, 1987. Elsevier Science Publishing Co.

[88] J. M. Kemeny and N. G. W. Cook. Determination of rock fracture parameters from crack models for failure in compression. In C. S. Desai, E. Krempl, P. D. Kiousis, and T. Kundu, editors, *Proc.28th U.S. Symp. on Rock Mechanics, Tuscon*, pages 367–375. A.A. Balkema, Rotterdam, 1987.

[89] J. M. Kemeny and N. G. W. Cook. Micromechanics of deformation in rocks. In S. P. Shaw, editor, *Toughening Mechanics in Quasi-Brittle Materials*, volume 2, pages 155–188. Klewer Academic, The Netherlands, 1991.

[90] R. L. Kranz. Crack-crack and crack-pore interactions in stressed granite. *Int. J. Rock Mech. Min. Sci. & Geomech. Abstr.*, 16:37–47, 1979.

[91] R. L. Kranz. Microcracks in rocks: A review. *Tectonophysics*, 100:449–480, 1983.

[92] E. Krempl. Models of viscoplasticity–some comments on equilibrium (back) stress and drag stress. *Acta Mechanica*, 69:25–42, 1987.

[93] J. F. Labuz and D. J. Berger. Moisture effects and the mechanical response of granite beams. In W.A. Hustrulid and G.A. Johnson, editors, *Proc. 31st U.S. Symp. on Rock Mech.*, pages 605–611, Denver, Colorado, 1990. Elsevier Science Publishing Co.

[94] J. F. Labuz, S. P. Shah, and C. H. Dowding. The fracture process zone in granite: Evidence and effect. *Int. J. Rock Mech. Min. Sci. & Geomech. Abstr.*, 24(4):235–246, 1987.

[95] E. Z. Lajtai. The fracture of Lac du Bonnet granite. Contract report, Atomic Energy of Canada Limited, 1982. pages 126.

[96] E. Z. Lajtai, B. J. Carter, and M. L. Ayari. Criteria for brittle fracture in compression. *Engineering Fracture Mechanics*, 37(1):25–49, 1990.

[97] E. Z. Lajtai, B. J. Carter, and E. J. S. Duncan. Mapping the state of fracture around cavities. *Engineering Geology*, 31:277–289, 1991.

[98] E. Z. Lajtai and A. M. Gadi. Friction on a granite to granite interface. *Rock Mechanics and Rock Engineering*, 22:25–49, 1989.

[99] E. Z. Lajtai and V. N. Lajtai. The collapse of cavities. *Int. J. Rock Mech. Min. Sci. & Geomech. Abstr.*, 12:81–86, 1975.

[100] J. S. O. Lau and B. Gorski. The post failure behaviour of Lac du Bonnet grey granite. Divisional Report MRL 91-079(TR), CANMET, Energy Mines and Resources, Canada, 1991.

[101] K. S. Li. A simple procedure for calculating vertical soil stress due to an arbitrarily shaped foundation. *Geotechnique*, 41(3):467–469, 1991.

[102] R. K. Livesley. *Mathematical methods for engineers*. Ellis Horwood Limited, Chichester, first edition, 1989.

[103] C. Ljunggren and B. Amadei. Estimation of virgin rock stresses from horizontal hydrofractures. *Int. J. Rock Mech. Min. Sci & Geomech. Abstr.*, 26(1):69–78, 1989.

[104] D. A. Lockner, J. D. Byerlee, V. Kuksenko, A. Ponomarev, and A. Sidorin. Quasi-static fault growth and shear fracture energy in granite. *Nature*, 350(6313):39–42, 1991.

[105] C. D. Martin. Failure observations and in situ stress domains at the Underground Research Laboratory. In V. Maury and D. Fourmaintraux, editors, *Proc. Conf. on Rock Mech. and Rock Physics at Great Depth, Pau, France*, volume 2, pages 719–726. A.A. Balkema, Rotterdam, 1989.

[106] C. D. Martin. Characterizing in situ stress domains at the AECL Underground Research Laboratory. *Can. Geotech. J.*, 27:631–646, 1990.

[107] C. D. Martin and R. Christiansson. Overcoring in highly stressed granite – The influence of microcracking. *Int. J. Rock Mech. Min. Sci. & Geomech. Abstr.*, 28(1):53–70, 1991.

[108] C. D. Martin, C. C. Davison, and E. T. Kozak. Characterizing normal stiffness and hydraulic conductivity of a major shear zone in granite. In N. Barton and O. Stephansson, editors, *Proc. Int. Symp. on Rock Joints, Loen, Norway*, pages 549–556. A.A. Balkema, Rotterdam, 1990.

[109] C. D. Martin, R. S. Read, and N. A. Chandler. Does scale influence in situ stress measurements?– Some findings at the Underground Research Laboratory. In A. Pinto da Cunha, editor, *Proc. First Int. Workshop on Scale Effects in Rock Masses, Loen, Norway*, pages 307–316. A.A. Balkema, Rotterdam, 1990.

[110] C. D. Martin, M. H. Spinney, J. B. Martino, and F. W. Stanchell. Excavation response recoded by Trivec and Distometer instruments during shaft sinking at the Underground Research Laboratory. In J .H. Curran, editor, *Proc. 15th Canadian Rock Mechanics Symposium, Toronto*, pages 1–10. Department of Civil Engineering, University of Toronto, Toronto, 1988.

[111] C. D. Martin and R. P. Young. The effect of excavation-induced seismicity on the strength of Lac du Bonnet granite. In R. P. Young, editor, *Proc. 3rd Int. Symp. on Rockbursts and Seismicity in Mines*, Kingston, Ontario, in prep. A.A. Balkema, Rotterdam.

[112] L. Mastin. The development of borehole breakouts in sandstone. Master's thesis, Stanford University, Berkley, Calfornia, 1984.

[113] D.J. Millard, P.C. Newman, and J.W. Phillips. The apparent strength of extensively cracked materials. *Proc. Phys. Soc., London*, B68:723–728, 1989.

[114] K. Mogi. Study of the elastic shocks caused by the fracture of heterogeneous materials and its relation to the earthquake phenomena. *Bulletin Earthquake Res. Inst.*, 46:1103–1112, 1962.

[115] N. R. Morgenstern. Progressive failure in theory and practice: 28th Terzaghi Lecture. *A.S.C.E. J. Geotech. and Environ. Engin.*, in prep.

[116] J. G. L. Munday and R. K. Dhir. Long-term strength of concrete under sustained load. In *Proc. 2nd Australian Conference on Engineering Materials, Sydney, Australia*, pages 109–120. University of NSW, Australia, 1981.

[117] A. M. Myrvang. Estimation of in situ compressive strength of rocks from in situ stress measurements in highly stressed rock structures. In W. Wittke, editor, *Proc. 7th ISRM Congress on Rock mechanics, Aachen*, pages 573–575. A.A. Balkema, Rotterdam, 1991.

[118] S. Nemat-Nasser and H. Hori. Compression-induced nonplanar crack extension with application to splitting, exfoliation and rockburst. *Journal of Geophysical Research*, 87(B8):6805–6821, 1982.

[119] V. Nesetova and E. Z. Lajtai. Fracture from compressive stress concentrations around elastic flaws. *Int. J. Rock Mech. Min. Sci. & Geomech. Abstr.*, 10:265–284, 1973.

[120] Nowakowski. The size effect on the tensile strength of Lac du Bonnet granite using the Brazilian test. B.sc. report, Dept. of Geological Engineering, University of Manitoba, 1984.

[121] L. Obert and D. E. Stephenson. Stress conditions under which core discing occurs. *Transactions of the Society of Mining Engineers of AIME*, pages 227–235, September 1965.

[122] D. P. Onagi, S. G. Keith, and G. W. Kuzyk. Non-explosive excavation technique developed for the excavtion of AECL's Mine-by Experiment Test Tunnel at the Underground Research Laboratory. In *Proc. 10th TAC Annual Canadian Tunnelling Conference, Banff*, pages 1–11. Bi-Tech publishers, Vancouver, 1992.

[123] W. D. Ortlepp, R. C. O'Ferral, and J. W. Wilson. Support methods in tunnels. *Assoc. Mine Managers of South Africa. Papers and Discussion*, pages 167–195, 1972.

[124] F. Ouchterlony. Suggested methods for determining the fracture toughness of rock. *Int. J. Rock Mech. Min. Sci & Geomech. Abstr.*, 25(2):71–96, 1988.

[125] F. Pelli, P. K. Kaiser, and N. R. Morgenstern. An interpretation of ground movements recorded during construction of the Donkin-Morien tunnel. *Can. Geotech. J.*, 28(2):239–254, 1991.

[126] S. S. Peng and A. M. Johnson. Crack growth and faulting in cylindrical specimens of Chelmsford granite. *Int. J. Rock Mech. Min. Sci & Geomech. Abstr.*, 9:37–86, 1972.

[127] D. D. Pollard and A. Aydin. Progress in understanding jointing over the past century. *Geological Society of America Bulletin*, 100:1118–1204, August 1988.

[128] Stacey T. R. A simple extension strain criterion for fracture of brittle rock. *Int. J. Rock Mech. Min. Sci. & Geomech Abst.*, 18:469–474, 1981.

[129] R. S. Read and C. D. Martin. Monitoring the excavation-induced response of granite. In J.A. Tillerson and W.R. Wawersik, editors, *Proc. 33rd U.S. Symp. on Rock Mechanics, Santa Fe*, pages 201–210. A.A. Balkema, Rotterdam, 1992.

[130] J. R. Rice. The mechanics of earthquake rupture. In A. M. Dziewonski and E. Boschi, editors, *Proc. Int. School of Physics, Course LXXVIII, Physics of the Earth's Interior*, pages 555–649. North-Holland Publishing Company, Amsterdam, 1980.

[131] F. E. Richart, A. Brandtzaeg, and R. L. Brown. A study of the failure of concrete under combined compressive stresses. Bulletin 128, University of Illinois Engineering Experiment Station, 1928.

[132] K. J. Rosengren and J. C. Jaeger. The mechanical properties of a low-porosity interlocked aggregate. *Geotechnique*, 18(3):317–326, 1968.

[133] H. Rusch. Physical problems in the testing of concrete. *Zement-Kalk-Gips (Cement and Concrete Association Library Translation No.86, 1960)*, pages 1–9, 1959.

[134] H. Rusch. Research towards a general flexural theory for structural concrete. *Proc. Am. Concrete Inst.*, 57:1–28, 1960.

[135] C. Saint-Leu and P. Sirieys. La fatigue des roches. In *Proc. Int. Symp. on Rock Mechanics, Nancy*, volume 1, pages II–18, 1971.

[136] M. D. G. Salamon and A. H. Munro. A study of the strength of coal pillars. *J. South Afr. Inst. Min. Metall.*, 68:55–67, 1967.

[137] C. G. Sammis and M. F. Ashby. The failure of brittle porous solids under compressive stress states. *Acta metall.*, 34:511–526, 1986.

[138] C. M. Sangha and R. K. Dhir. Influence of time on the strength deformation and fracture properties of a lower Devonian sandstone. *Int. J. Rock Mech. Min. Sci. & Geomech. Abstr.*, 9:343–354, 1972.

[139] F. J. Santarelli and E. T. Brown. Performance of deep wellbores in rock with a confining pressure-dependent elastic modulus. In G. Herget and S. Vongpaisal, editors, *Proc. 6th Int. Soc. Rock Mech. Congress, Montreal*, volume 2, pages 1217–1222. A.A. Balkema, Rotterdam, 1987.

[140] R. H. Schmidtke and E.Z. Lajtai. The long-term strength of Lac du Bonnet granite. *Int. J. Rock Mech. Min. Sci. & Geomech. Abstr.*, 22(6):461–465, 1985.

[141] C. H. Scholz. Experimental study of the fracturing process in brittle rocks. *Journal of Geophysical Research*, 73(4):1447–1453, 1968.

[142] C. H. Scholz. The role of microcracking in rock deformation. In *Proc. 2nd Congress of Int. Soc. Rock Mech., Belgrade*, volume 1, pages 1–8, 1970.

[143] C. H. Scholz and R. Kranz. Notes on dilatancy recovery. *J. of Geophy. Res.*, 79(9):2132–2135, 1974.

[144] E. M. Shulson. The brittle compressive fracture of ice. *Acta. metall. mater.*, 38(10):1963–1976, 1990.

[145] E. M. Shulson, G. A. Kuehn, D. A. Jones, and D. A. Fifolt. The growth of wing cracks and the brittle compressive failure of ice. *Acta. metall. mater.*, 39(11):2651–2655, 1991.

[146] G. R. Simmons. Operating phase experiments planned for Atomic Energy of Canada Limited's Underground Research Laboratory. In R. S. Sinha, editor, *Proc. Int. Symp. on Unique Underground Structures, Denver*, volume 2, pages 67:1–19. CSM Press, Denver, 1990.

[147] A. T. Starr. Slip in a crystal and rupture in a solid due to shear. *Proc. Cambridge Philosophical Society*, 24:489–500, 1928.

[148] M. Svab and E. Z. Lajtai. Microstructural control of crack growth in Lac du Bonnet granite. In L.A. Simpson, editor, *Proc. 5th Canadian Fracture Conference, Winnipeg*, pages 219–228. Pergamon Press., 1981.

[149] S. Talebi and R. P. Young. Microseismic monitoring in highly stressed granite: Relation between shaft-wall cracking and in situ stress. *Int. J. Rock Mech. Min. Sci. & Geomech Abst.*, 29(1):25–34, 1992.

[150] P. Tapponnier and W. F. Brace. Development of stress-induced microcracks in Westerly granite. *Int. J. Rock Mech. Min. Sci. & Geomech Abst.*, 13:103–112, 1976.

[151] H. Wagner. Design and support of underground excavations in highly stressed rock. In G. Herget & S. Vongpaisal, editor, *Proc. 6th ISRM Int. Congress on Rock Mechanics, Montreal*, volume 3, pages 1443–1457. A.A. Balkema, Netherlands, 1987.

[152] W. R. Wawersik and W. F. Brace. Post failure behaviour of a granite and diabase. *Rock Mech. and Rock Engin.*, 3:61–85, 1971.

[153] W. R. Wawersik and C. Fairhurst. A study of brittle rock fracture in laboratory compression experiments. *Int. J. Rock Mech. Min. Sci. & Geomech. Abst*, 7:561–575, 1970.

[154] B. L. Wiid. The influence of moisture on the pre-rupture fracturing of two rock types. In *Proc. 2nd Congress Int. Soc. Rock Mech. Belgrade*, volume 2, pages 239–245, 1970.

[155] B.L. Wiid. The time-dependent behaviour of rock: Considerations with regard to a research program. CSIR Report MEG 514, Rock Mechanics Division, National Mechanical Engineering Research Institute, Pretoria, South Africa, 1966.

[156] G. Wijk, G. Rehbinder, and G. Lögdström. The relation between the uniaxial tensile strength and the sample size for Bohus granite. *Rock Mechanics and Rock Engineering*, 10:201–219, 1978.

[157] T. Wiles. *MAP3D–A Mining Analysis Program in 3-Dimensions, Version 1.26*. Mine Modelling Limited, Copper Cliff, Canada, 1993.

[158] B. J. S. Wilkins, A. R. Reich, and W. R. Wallace. Slow cracking in plutonic rocks. Technical Record TR-264, Atomic Energy of Canada Limited, 1984.

[159] T. Wiseman. Size/tensile strength relationship of Pinawa pink granite tested by Brazilian method. Divisional Report MRL 91-021 (INT), CANMET, Energy Mines and Resources, Canada,, 1991.

[160] S. Wolfram. *Mathematica: A system for doing mathematics by computer*. Addison-Wesley Publishing Co., Redwood City, California, second edition, 1991.

[161] H. Wu and D. D. Pollard. Possible secondary fracture patterns due to a change in the direction of loading. In *Preprints Conf. on Fractured and Jointed Rock Masses, Lake Tahoe*, volume 2, pages 505–512. US Dept of Energy, 1992.

[162] Z. Zheng, J. Kemmeny, and N. G. W. Cook. Analysis of borehole breakouts. *Journal of Geophysical Research*, 94(B6):7171–7182, 1989.

[163] D. Zou and P. K. Kaiser. Determination of in situ stresses from excavation induced stress change. *Rock Mechanics and Rock Engineering*, 23(3):167–184, 1990.

Appendix A

In Situ Stress From Convergence Measurements

Consider an infinite plate of thickness t with a circular hole of radius a located at the origin as illustrated in Figure A.1. Let the applied stress in the x direction be σ_x and in the y direction be σ_y.

In an xy coordinate system a counterclockwise rotation of angle θ will result in the following stress transformation.

$$
\begin{aligned}
\sigma_{x'} &= \sigma_x \cos^2 \theta + \sigma_y \sin^2 \theta + 2\tau_{xy} \sin \theta \cos \theta \\
\sigma_{y'} &= \sigma_x \sin^2 \theta + \sigma_y \cos^2 \theta - 2\tau_{xy} \sin \theta \cos \theta \\
\tau_{x'y'} &= \tfrac{\sigma_y - \sigma_x}{2} \sin 2\theta + \tau_{xy}(\cos^2 \theta - \sin^2 \theta)
\end{aligned}
\tag{A.1}
$$

Thus in polar coordinates and at $r = \infty$ equations A.1 become

$$
\begin{aligned}
(\sigma_r)_{r=\infty} &= \sigma_x \cos^2 \theta + \sigma_y \sin^2 \theta + 2\tau_{xy} \sin \theta \cos \theta \\
(\sigma_\theta)_{r=\infty} &= \sigma_x \sin^2 \theta + \sigma_y \cos^2 \theta - 2\tau_{xy} \sin \theta \cos \theta \\
(\tau_{r\theta})_{r=\infty} &= \tfrac{\sigma_y - \sigma_x}{2} \sin 2\theta + \tau_{xy}(\cos^2 \theta - \sin^2 \theta)
\end{aligned}
\tag{A.2}
$$

A.1 Solution

Using the approach of Fung [53], the plane strain ($\epsilon_z = 0$) problem shown in Figure A.1 can be solved by assuming a stress function of the form

$$
\begin{aligned}
\Phi =\ & Ar^2 + B \log r + C_1 \cos 2\theta + C_2 \sin 2\theta + D_1 r^2 \cos 2\theta + D_2 r^2 \sin 2\theta + \\
& \tfrac{E_1 \cos 2\theta}{r^2} + \tfrac{E_2 \sin 2\theta}{r^2}
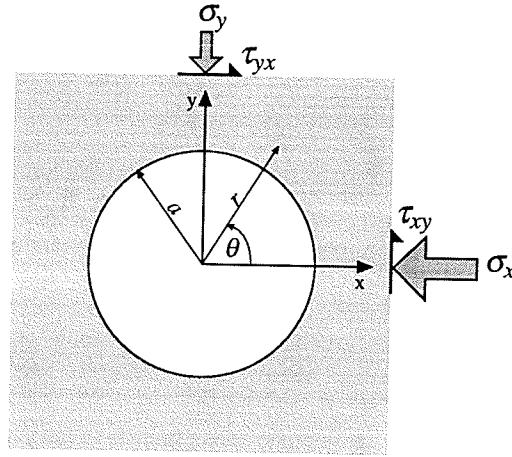\end{aligned}
\tag{A.3}
$$

Figure A.1: Circular hole in a an infinite plate with far-field stress conditions.

where the stresses in terms of the stress function Φ are given by

$$
\begin{aligned}
\sigma_{\theta\theta} &= \frac{\partial^2 \Phi}{\partial r^2} \\
\sigma_{rr} &= \frac{1}{r}\frac{\partial \Phi}{\partial r} + \frac{1}{r^2}\frac{\partial \Phi}{\partial \theta^2} \\
\sigma_{r\theta} &= -\frac{\partial}{\partial r}\left(\frac{1}{r}\frac{\partial \Phi}{\partial \theta}\right)
\end{aligned}
\tag{A.4}
$$

The above satisfies the equilibrium equations and satisfies the biharmonic equation such that

$$\nabla^4 \Phi = 0$$

The tangential stress (σ_θ), radial stress(σ_r) and the shear stress ($\tau_{r\theta}$) for equation A.3, in polar coordinates, is given by

$$
\begin{aligned}
\sigma_{\theta\theta} &= 2A - \frac{B}{r^2} + 2D_1 \cos 2\theta + 2D_2 \sin 2\theta + \frac{6E_1 \cos 2\theta}{r^4} + \frac{6E_2 \sin 2\theta}{r^4} \\
\sigma_{rr} &= 2A + \frac{B}{r^2} - \frac{4C_1 \cos 2\theta}{r^2} - \frac{4C_2 \sin 2\theta}{r^2} - 2D_1 \cos 2\theta - 2D_2 \sin 2\theta - \\
&\quad \frac{6E_1 \cos 2\theta}{r^4} - \frac{6E_2 \sin 2\theta}{r^4} \\
\tau_{r\theta} &= -\frac{2C_1}{r^2}\sin 2\theta + \frac{2C_2}{r^2}\cos 2\theta + 2D_1 \sin 2\theta - 2D_2 \cos 2\theta - \frac{6E_1 \sin 2\theta}{r^4} + \frac{6E_2 \cos 2\theta}{r^4}
\end{aligned}
\tag{A.5}
$$

Boundary Conditions ($r = \infty$)

Using the trigonometric identities

$$\sin^2 \theta = \frac{1 - \cos 2\theta}{2}$$

$$\cos^2 \theta \;=\; \frac{1 + \cos 2\theta}{2}$$

$$\sin \theta \cos \theta \;=\; \frac{\sin 2\theta}{2}$$

equations A.2 give

$$
\begin{aligned}
(\sigma_\theta)_{r=\infty} &= \tfrac{\sigma_x+\sigma_y}{2} + \tfrac{\sigma_y-\sigma_x}{2}\cos 2\theta - \tau_{xy}\sin 2\theta \\
(\sigma_r)_{r=\infty} &= \tfrac{\sigma_x+\sigma_y}{2} + \tfrac{\sigma_x-\sigma_y}{2}\cos 2\theta + \tau_{xy}\sin 2\theta \\
(\tau_{r\theta})_{r=\infty} &= \tfrac{\sigma_y-\sigma_x}{2}\sin 2\theta + \tau_{xy}\cos 2\theta
\end{aligned}
\tag{A.6}
$$

Solving equations A.5 for $r = \infty$ and equating the results with equations A.6 gives

$$
\begin{aligned}
A &= \tfrac{\sigma_x+\sigma_y}{4} \\
D_1 &= -\tfrac{\sigma_x-\sigma_y}{4} \\
D_2 &= -\tfrac{\tau_{xy}}{2}
\end{aligned}
\tag{A.7}
$$

Boundary Conditions ($r = a$)

The boundary conditions at $r = a$ are

$$(\sigma_r)_{r=a} = (\tau_{r\theta})_{r=a} = 0$$

Solving equations A.5 for $r = a$ and equating the results with equations A.6 gives

$$
\begin{aligned}
B &= -a^2\left(\tfrac{\sigma_x+\sigma_y}{2}\right) \\
C_1 &= a^2\left(\tfrac{\sigma_x-\sigma_y}{2}\right) \\
C_2 &= a^2\tau_{xy} \\
E_1 &= -a^4\left(\tfrac{\sigma_x-\sigma_y}{4}\right) \\
E_2 &= -\tfrac{a^4\tau_{xy}}{2}
\end{aligned}
\tag{A.8}
$$

Substituting equations A.7 and A.8 into equation A.5 gives

$$
\begin{aligned}
\sigma_r &= \tfrac{\sigma_x+\sigma_y}{2} - \tfrac{a^2(\sigma_x+\sigma_y)}{2r^2} + \tfrac{(\sigma_x-\sigma_y)(3a^4-4a^2r^2+r^4)}{2r^4}\cos 2\theta + \\
& \quad \tfrac{(3a^4-4a^2r^2+r^4)\tau_{xy}}{2r^4}\sin 2\theta \\
\sigma_\theta &= \tfrac{\sigma_x+\sigma_y}{2} + \tfrac{a^2(\sigma_x+\sigma_y)}{2r^2} + \tfrac{(-\sigma_x+\sigma_y)(3a^4+r^4)}{2r^4}\cos 2\theta + \\
& \quad -\left(1 + \tfrac{3a^4}{r^4}\right)\tau_{xy}\sin 2\theta \\
\tau_{r\theta} &= \tfrac{(-3a^4+2a^2r^2+r^4)(2\tau_{xy}\cos 2\theta - \sigma_x\sin 2\theta + \sigma_y\sin 2\theta)}{2r^2}
\end{aligned}
\tag{A.9}
$$

From elastic theory

$$\frac{\partial u}{\partial r} = \epsilon_r = \frac{1}{E}\left[\sigma_r - \nu(\sigma_\theta + \sigma_z)\right]$$

and

$$\sigma_z = \nu(\sigma_r + \sigma_\theta)$$

which gives

$$\epsilon_r = \frac{1}{E}\left[(1 - \nu^2)\sigma_r - \nu(1 + \nu)\sigma_\theta\right] \tag{A.10}$$

This gives the total radial displacements due to the far-field stresses plus the radial displacements due to the hole.

The radial displacements u_r as a function of θ will be the difference between u_r due to the hole and u_r with the hole absent and can be found by substituting equations A.9 into equation A.10 and carrying out the integration from $r = a$ to ∞

$$u_r(\theta) = \frac{1+\nu}{E}\left\{\int_{r=a}^{r=\infty}((1-\nu)\sigma_r - \nu\sigma_\theta)\,dr - \int_{r=a}^{r=\infty}((1-\nu)\sigma_{rr=\infty} - \nu\sigma_{\theta r=\infty})\,dr\right\} \tag{A.11}$$

which gives the convergence (U) as

$$U = \frac{a}{2G}\left\{(1 + (3 - 4\nu)\cos 2\theta)\sigma_x + (1 - (3 - 4\nu)\cos 2\theta)\sigma_y + 2(3 - 4\nu)\sin 2\theta\tau_{xy}\right\} \tag{A.12}$$

where $G =$ the shear modulus and $\nu =$ Poisson's ratio.

Equation A.12 is of the general form

$$U = C_1\sigma_x + C_2\sigma_y + C_3\tau_{xy} \tag{A.13}$$

Hence equation A.12 can be solved provided at least three convergence measurements are taken.

A.2   Example Calculation

Changes in the shaft diameter using four diametrical lines was monitored during the construction of the 2.3-m diameter circular shaft from the 240 Level to the 420 Level (Figure A.2). Using the orientation of each diameter in Figure A.2 it is possible to determine the values of σ_x, σ_y and τ_{xy} for equation A.13.
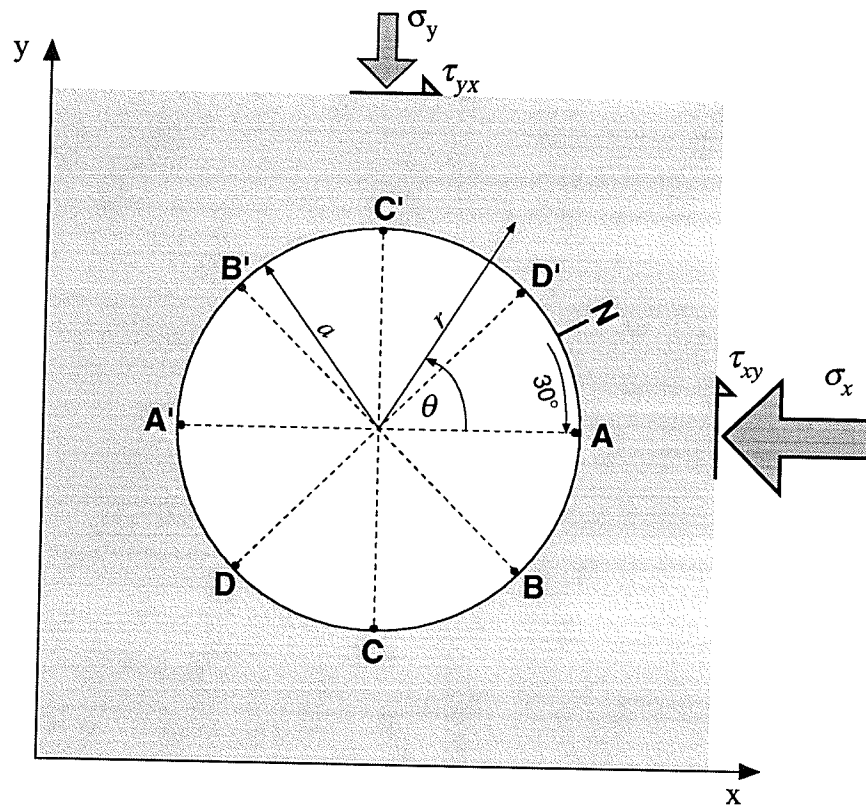
Figure A.2: Convergence measurements used for the construction of URL Shaft from 240 Level to the 420 Level.

Example: Set up the matrix for the coefficients (C) for the orientation of each diameter

$$\begin{bmatrix} C_{A1} & C_{A2} & C_{A3} \\ C_{B1} & C_{B2} & C_{B3} \\ C_{C1} & C_{C2} & C_{C3} \\ C_{D1} & C_{D2} & C_{D3} \end{bmatrix} \begin{Bmatrix} \sigma_x \\ \sigma_y \\ \tau_{xy} \end{Bmatrix} = \begin{bmatrix} U_A \\ U_B \\ U_C \\ U_D \end{bmatrix} \tag{A.14}$$

where

$$\begin{aligned} C_1 &= \tfrac{a}{4G}\left\{(1 + (3 - 4\nu)\cos 2\theta)\right\} \\ C_2 &= \tfrac{a}{4G}\left\{(1 - (3 - 4\nu)\cos 2\theta)\right\} \\ C_3 &= \tfrac{a}{4G}\left\{2(3 - 4\nu)\sin 2\theta\right\} \end{aligned} \tag{A.15}$$

$C_{1\cdots3}$ in equation A.15 refers to the coefficients, θ is the orientation of the convergence line and the subscripts $A \cdots D$ refer to the diameters in Figure A.2. The in situ stresses $(\sigma_x, \sigma_y, \tau_{xy})$ responsible for the convergences can be found from equation A.14 using a least squares matrix solution (see the next section for the details of the solution) given the values of the elastic constants (G, ν).

A.2.1 Least Squares Matrix Operations

For m equations and n unknowns the following is the least squares matrix solution for n values of the unknown parameter X

$$[C]_{m \times n} \{X\}_{n \times 1} = [U]_{m \times 1}$$

$$\begin{bmatrix} C_{11} & + & C_{12} & + & \cdots & C_{1n} \\ C_{21} & + & C_{22} & + & \cdots & C_{2n} \\ \vdots & + & \vdots & + & \vdots & \vdots \\ C_{m1} & + & C_{m2} & + & \cdots & C_{mn} \end{bmatrix} \begin{Bmatrix} X_1 \\ X_2 \\ \vdots \\ X_n \end{Bmatrix} = \begin{bmatrix} U_1 \\ U_2 \\ \vdots \\ U_m \end{bmatrix}$$

The solution to the above equation is given by:

$$\{X\}_{n \times 1} = \left([C]_{n \times m}^t \, [C]_{m \times n}\right)^{-1} [C]_{n \times m}^t \, [U]_{m \times 1} \tag{A.16}$$

The $X_{1\cdots n}$ obtained by solving equation A.16 correspond to a least squares approximation in which the errors e_i are given equal weight [102].

Appendix B

Griffith Locus

B.1 Elastic Strain Energy

Energy is defined as the capacity to do work and work is the product of a force by the distance in the direction the force moves. For a body loaded in uniaxial compression (see Figure B.1) the elastic strain energy ($S.E.$) stored in the body is

$$S.E. = \frac{1}{2}P\delta$$

where

$$\delta = \frac{Pl}{bE}$$

and P is the applied force, l is the length, b is the width and E is the Young's modulus of elasticity.

Substituting for δ gives

$$S.E. = \frac{1}{2}\frac{P^2 l}{bE}.$$

and since $\sigma = \frac{P}{bl}$ then $S.E.$ becomes

$$S.E. = \frac{1}{2}\frac{\sigma^2 l b}{E}.$$

The shear modulus (G) is given by

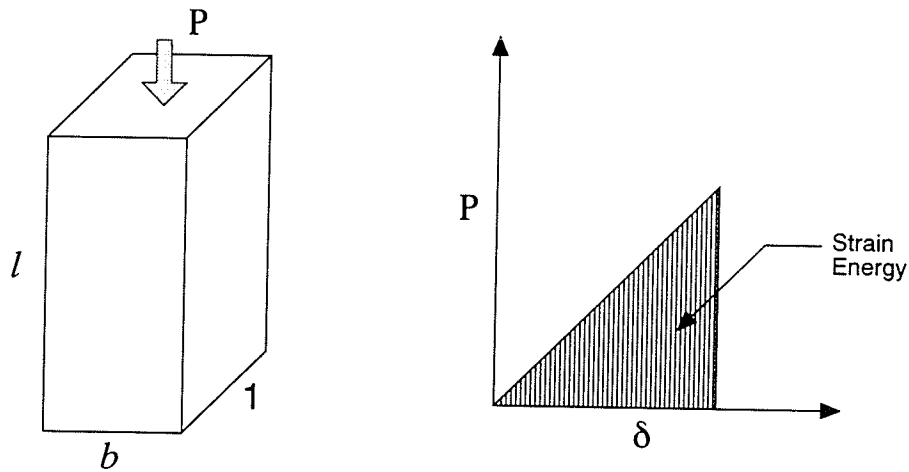$$G = \frac{E}{2(1+\nu)} \tag{B.1}$$

Figure B.1: Strain energy for a body of length (l), width (b) and unit thickness loaded in uniaxial compression.

and S.E. can be expressed as

$$S.E. = \frac{1}{2}\frac{\sigma^2\, l\, b}{2(1+\nu)G} = \frac{\sigma^2 lb}{4(1+\nu)G}.$$ (B.2)

B.2 Strain Energy Release Rate

Griffith [59] used energy methods to develop a criteria for crack extension. The elastic modulus of a plate with a crack is given as E_c and with a crack that has extended by $c + dc$, as E_{c+dc} in Figure B.2. In Griffith's original formulation the system was rigidly fixed, hence the load had to drop as the crack extended and the stiffness had to decrease to E_{c+dc}. The energy of the plate with crack c is given by OAC and when the crack extends to $c + dc$ the energy is given by OBC. Thus the energy released as the modulus softens from E_c to E_{c+dc} is equal to the area OAB and must be equal to or greater than the fracture surface energy i.e. the energy required to create a unit surface area of new fracture. Based on this approach Griffith stated that the condition for crack extension occurred when
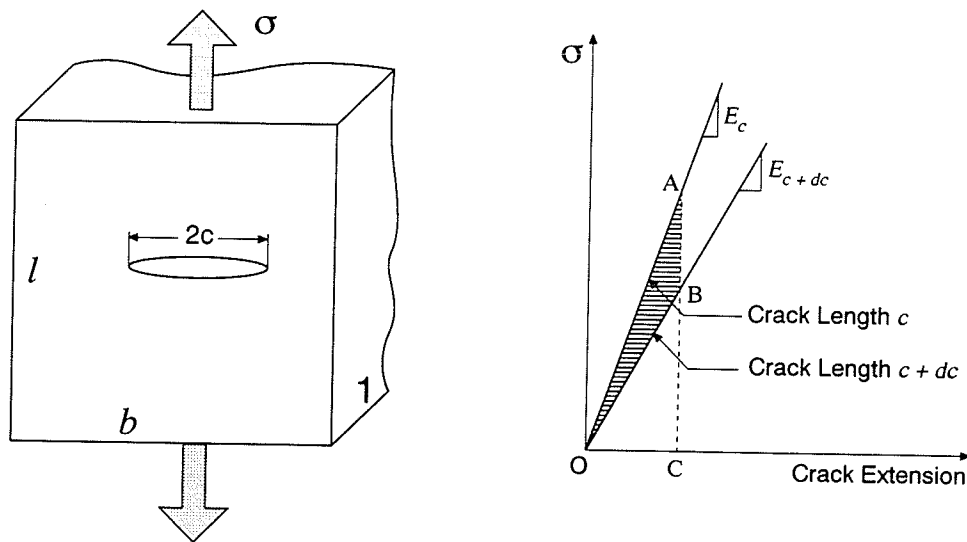
$$\frac{dU}{dc} = \frac{dW}{dc}$$

Figure B.2: The Griffith conditions for crack extension in uniaxial tension for a fixed grip system.

where U is the elastic energy and W is the energy for crack growth. Griffith found that the crack growth occurs when

$$\sigma_t = \sqrt{\frac{E\mathcal{G}}{\pi c}}$$

where $\mathcal{G}$ is the strain energy release rate per crack tip. For plain strain conditions $\mathcal{G}$ is given by

$$\mathcal{G} = \frac{K_I^2}{E}(1 - \nu^2) = \frac{\sigma^2 \pi c}{2(1 + \nu)G}(1 - \nu^2) = \frac{\sigma^2 \pi c}{2G}(1 - \nu) \tag{B.3}$$

where K_I is the stress intensity factor which describes the stress at the tip of the crack in Figure B.2. For the conditions in Figure B.2 the stress intensity factor is given as

$$K_I = \sigma\sqrt{\pi c}.$$

B.3 Griffith Locus in Tension

Following along the original work of Griffith, Berry [6, 7] developed the Griffith locus of failure for the "growing crack" when the load was in tension. Cook [32] extended Berry's

work to the case of uniaxial compression. This section is a review of that work before extending the Griffith locus to triaxial compression.

Assume a single crack subjected to a constant tensile stress as in Figure B.2. If the crack is closed and then slowly released the released energy (W_s) is stored around the crack. For crack extension at both crack tips

$$2\mathcal{G} = \frac{dW_s}{dc}.$$

Hence the stored energy

$$W_s = \frac{2}{2}\frac{\sigma^2 \pi c^2}{2G}(1-\nu) = \frac{\sigma^2 \pi c^2}{2G}(1-\nu) \tag{B.4}$$

If ϵ is the strain associated with the external load σ in the presence of the crack then the total work done (WD) by the application of σ is

$$WD = \frac{1}{2}\sigma\epsilon(bl) \tag{B.5}$$

The total work done (WD) as the specimen containing the crack is subjected to a load σ is equal to the work stored in the specimen without the crack (S.E.) plus the work stored around the crack as the crack opens (W_s).

$$WD = S.E. + W_s \tag{B.6}$$

Substituting eq B.2 and eq B.4 into eq B.6 gives

$$\frac{1}{2}\sigma\epsilon(bl) = \frac{\sigma^2 lb}{4(1+\nu)G} + \frac{\sigma^2 \pi c^2}{2G}(1-\nu)$$

from which

$$\epsilon = \frac{\sigma}{G}\left[\frac{1}{2(1+\nu)} + \pi c^2(1-\nu)n\right]. \tag{B.7}$$

where n = the number of cracks per unit volume and bl = volume per crack,i.e. $n = \frac{1}{bl}$.

Since a crack extending in its own plane, will extend in 2 opposite directions $\frac{dW}{dc} = 2\mathcal{G}$ and since 2 crack surfaces are created with the extension of one crack tip $2\mathcal{G} \geq 4\gamma$ where γ is the fracture surface energy for tension and $\mathcal{G}$ is the strain energy release rate.

Thus from eq B.3

$$2\mathcal{G} = \frac{\sigma^2 \pi c}{G}(1 - \nu) \geq 4\gamma$$

and the critical crack length required for extension becomes

$$c \geq \frac{4\gamma G}{\sigma^2 \pi (1 - \nu)}. \tag{B.8}$$

Substituting eq B.8 into eq B.7 gives the critical strain (ϵ_{cr}) required for crack extension, i.e., failure.

$$\epsilon_{cr} = \frac{\sigma}{G}\left[\frac{1}{2(1 + \nu)} + \frac{16\gamma^2 G^2}{\sigma^4 \pi (1 - \nu)^2}(1 - \nu)n\right]$$

which reduces to

$$\epsilon_{cr} = \frac{\sigma}{2G(1 + \nu)} + \frac{16\gamma^2 Gn}{\sigma^3 \pi (1 - \nu)} \tag{B.9}$$

Equation B.9 is the plane strain equivalent of Berry's [6] Griffith locus developed by Cook [32]. Equation B.7 defines the linear stress-strain paths for different crack sizes and densities prior to failure and equation B.9 defines the region of the stress-strain curve over which equation B.7 is valid.

B.4 Griffith Locus in Compression

Starr [147] showed that the strain energy, for plane strain, in a plate due to a crack undergoing shear displacement was given by

$$U = \frac{\pi \tau^2 c^2}{2G}(1 - \nu) \tag{B.10}$$

where τ is the shear stress parallel to the frictionless crack, c is the crack half-length and E is the Young's modulus. Cook [32] modified equation B.10 to take in to account the friction along the crack due to the compressive shearing. Equation B.10 then becomes

$$U = \frac{\pi (\tau - \mu \sigma_n)^2 c^2}{2G}(1 - \nu)$$

where μ is the coefficient of friction and σ_n is the compressive normal stress across the crack. In this case the crack is inclined at an angle θ to the maximum applied load (Figure B.3)
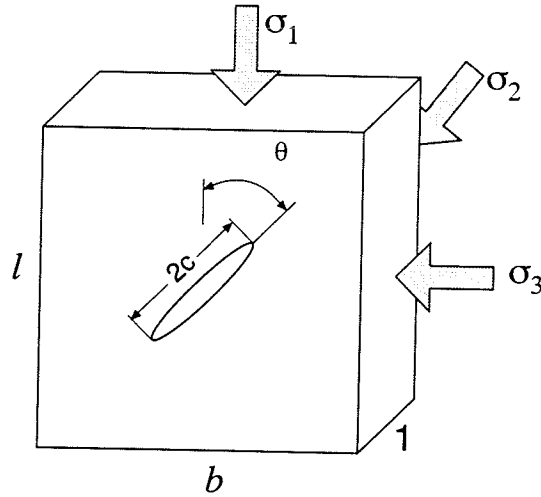
Figure B.3: The Griffith conditions for crack extension in triaxial compression.

and hence the crack is subjected to a normal stress (σ_n) and shear stress (τ) where

$$\sigma_n = \sigma_1 \sin^2 \theta + \sigma_3 \cos^2 \theta$$

$$\tau = (\sigma_1 - \sigma_3) \cos \theta \sin \theta$$

Since

$$\sin^2 \theta = \frac{1}{2}(1 - \cos 2\theta)$$

$$\cos^2 \theta = \frac{1}{2}(1 + \cos 2\theta)$$

$$\cos \theta \sin \theta = \frac{\sin 2\theta}{2}$$

then

$$\sigma_n = \frac{\sigma_1 + \sigma_3}{2} - \frac{\sigma_1 - \sigma_3}{2} \cos 2\theta \qquad (B.11)$$

$$\tau = \frac{\sigma_1 - \sigma_3}{2} \sin 2\theta \qquad (B.12)$$

In this case because the crack is closed, a frictional force $\mu\sigma_n$ will arise across the crack surface and sliding of the crack surface will occur when

$$\tau > \mu\sigma_n$$

As the closed crack crack is released the work done and hence the additional strain energy can be found using Figure B.4. In Figure B.4 it is assumed that τ decreases while σ_n remains constant, and that slip stops when $\tau \leq \mu \sigma_n$.

Refering to Figure B.4, the work done is

$$W_s = \frac{1}{2} 2c\tau\delta\tau = \delta c\tau^2 \text{ when } \mu\sigma_n = 0$$

and when $\mu\sigma_n > 0$

$$
\begin{aligned}
W_s &= W_e + W_f \\
W_s &= \delta c(\tau^2 - \mu^2\sigma_n^2)
\end{aligned}
\tag{B.13}
$$

As σ is increased from zero, in the presence of the crack, the surfaces displace linearly from 0 to $\delta(\tau - \mu\sigma_n)$ and the work done against the friction forces is $W_f/2$ (see Figure B.4).

In Figure B.4 when $\mu = 0$ than

$$W = \delta c\tau^2 \tag{B.14}$$

According to Starr [147] the work done against a frictionless crack $\mu = 0$ is given by

$$W = \frac{\pi}{4}(1 - 2\nu)\tau^2\frac{c^2}{G} \tag{B.15}$$

Therefore the crack displacement δ can be found by equating equations B.14 and B.15 which gives

$$\delta = \frac{\pi}{4G}(1 - \nu)c \tag{B.16}$$

In this process the total work done (WD) as the specimen containing the crack is subjected to a load σ, is equal to the work stored in the specimen without the crack (S.E.) plus the work stored around the crack as the crack opens (W_s) plus the frictional work associated with crack slip (W_f), thus

$$WD = S.E. + \left(W_s + \frac{W_f}{2}\right) \tag{B.17}$$

Since the total work done on the specimen with the crack by the deviatoric stress $\sigma_1 - \sigma_3$ is

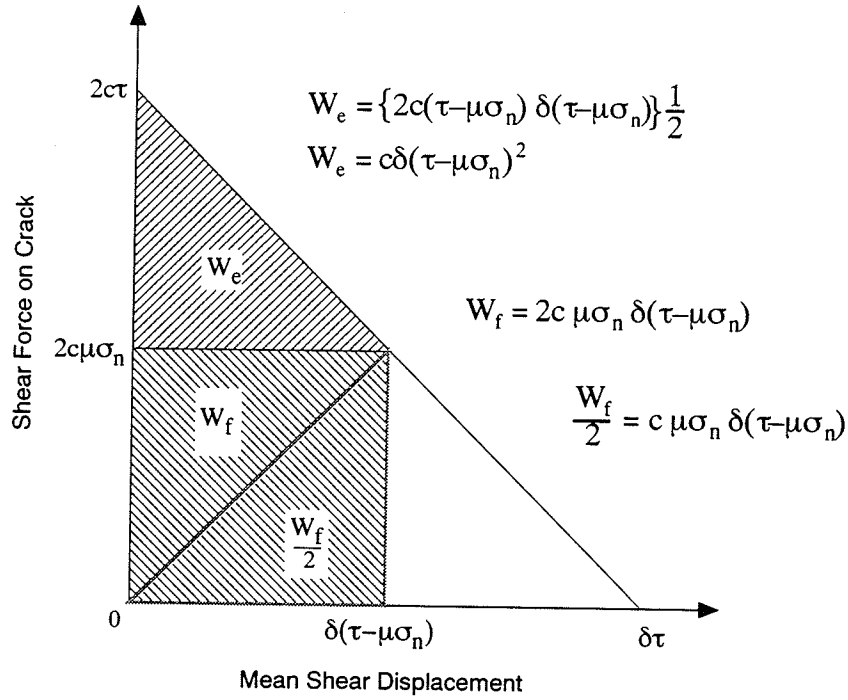$$WD = \left(\frac{\sigma_1 - \sigma_3}{2}\right)\epsilon bl \tag{B.18}$$

Figure B.4: Shear force and displacement (δ) of a crack surface.

then WD in equation B.17 can be solved for axial strain ϵ as in the tension case.

The elastic strain in a specimen under triaxial compression is given by

$$\begin{aligned}
\epsilon_1 &= \tfrac{1}{E}\left[\sigma_1 - \nu(\sigma_2 + \sigma_3)\right] \\
\epsilon_2 &= \tfrac{1}{E}\left[\sigma_2 - \nu(\sigma_1 + \sigma_3)\right] \\
\epsilon_3 &= \tfrac{1}{E}\left[\sigma_3 - \nu(\sigma_1 + \sigma_2)\right]
\end{aligned} \tag{B.19}$$

Since in a triaxial compression test $\sigma_2 = \sigma_3$ therefore the elastic strain energy is

$$\begin{aligned}
S.E. &= (\epsilon_1\sigma_1 + \epsilon_2\sigma_2 + \epsilon_3\sigma_3)\tfrac{bl}{2} = (\sigma_1^2 - 4\nu\sigma_1\sigma_3 + 2\sigma_3^2 - 2\nu\sigma_3^2)\tfrac{bl}{2E} \\
S.E. &= \left(\tfrac{\sigma_1 - \sigma_3}{2}\right)\tfrac{\sigma_1 - 2\mu\sigma_3}{E}bl
\end{aligned} \tag{B.20}$$

Now the total work done becomes

$$\left(\frac{\sigma_1 - \sigma_3}{2}\right)\epsilon bl = \left(\frac{\sigma_1 - \sigma_3}{2}\right)\frac{\sigma_1 - 2\mu\sigma_3}{E}bl + \left(W_s + \frac{W_f}{2}\right) \tag{B.21}$$

When $\mu\sigma_n > 0$ the work associated with W_s and W_f is given, according to Cook [32], as

$$\begin{aligned}
W_s &= \tfrac{\pi}{4}(1 - \nu)\frac{(\tau^2 - \mu^2\sigma_n^2)}{G}c^2 \\
W_f &= \tfrac{\pi}{4}(1 - \nu)\mu\sigma_n\frac{(\tau - \mu\sigma_n)}{G}c^2
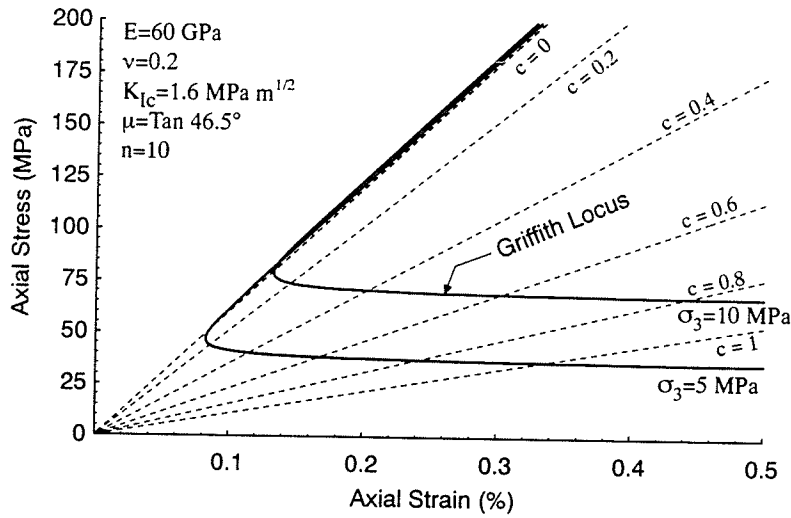\end{aligned} \tag{B.22}$$

Figure B.5: The Griffith locus in triaxial compression.

Equation B.21 can now be solved for strain (ϵ)

$$\epsilon = \frac{\sigma_1 - \nu\sigma_3}{2G(1+\nu)} + \frac{2}{\sigma_1 - \sigma_3}\left\{\frac{\pi}{4}(1-\nu)\frac{(\tau^2 - \mu^2\sigma_n^2)}{G}c^2 + \frac{\pi}{2}(1-\nu)\mu\sigma_n\frac{(\tau - \mu\sigma_n)}{G}c^2\right\}n \quad \text{(B.23)}$$

Equation B.23 defines the linear stress-strain paths for different crack sizes which is essentially a map of how the modulus changes as the crack grows Figure B.5.

As before the criterion for crack extension is

$$\frac{dW_s}{dc} \geq 4\alpha$$

where $\alpha =$ the fracture surface energy.

From Cook [32]

$$
\begin{aligned}
W_e &= \frac{\pi}{4}(1-\nu)\frac{(\tau-\mu\sigma_n)^2}{G}c^2 \\
\frac{dW_e}{dc} &= \frac{\pi}{2}(1-\nu)\frac{(\tau-\mu\sigma_n)^2}{G}c
\end{aligned}
\quad \text{(B.24)}
$$

Thus the critical crack length at failure is

$$\frac{dW_e}{dc} = \frac{\pi}{2}(1-\nu)\frac{(\tau - \mu\sigma_n)^2}{G}c = 4\alpha$$

which may be rewritten as

$$c = \frac{8\alpha G}{\pi(1-\nu)(\tau - \mu\sigma_n)^2}.$$ (B.25)

Substituting the critical crack length at failure from equation B.25 into equation B.23 gives the critical strain at failure and is referred to as the Griffith locus. The locus is shown in Figure B.5 as the two solid lines. As expected the locus is sensitive to confining pressure.

B.4.1 Sensitivity of Griffith Locus to Input Parameters

The Griffith locus was shown in Figure B.5. It can be seen from Figure B.5 that the locus can be divided into two parts: part one consists of the positive slope and reflects the stiffness of the material when the cracks are very small, and part two consists of the negative slope or threshold and defines the strength of the material as a function of crack length.

The Griffith locus contains five unknowns, G = the shear modulus, ν = Poisson's ratio, μ = coefficient of friction, θ = critical crack angle, α = fracture surface energy and n = number of cracks. The locus is also dependent on σ_3 = the confining stress. Only n is difficult to quantify. All the other parameters are available from standard laboratory testing methods. However, it is difficult to determine which of these parameters the Griffith locus might be highly sensitive to. Thus a parametric study was carried out to investigate the sensitivity of the locus to input parameters. The input parameters for the study were taken from standard laboratory test results for Lac du Bonnet granite.

Modulus

The shear modulus (G) in equation B.23 can be related to the modulus (E) by equation B.1. Figure B.6 shows the change in Griffith locus as E varies from 20 to 70 GPa. The modulus determines the position of the positive slope of the Griffith locus and has essentially no effect on the negative slope position, i.e., the threshold value of the locus.
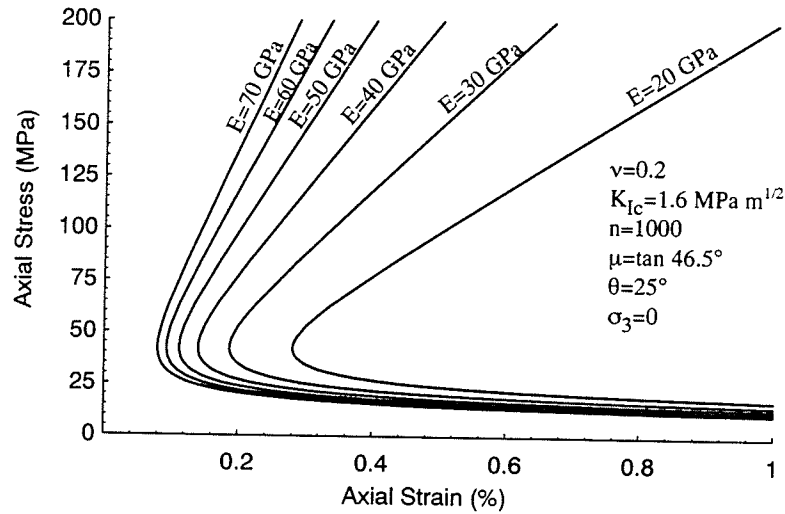
Figure B.6: The Griffith locus as a function of modulus (E).

Poisson's ratio

Figure B.7 shows the change in Griffith locus as Poisson's ratio (ν) varies from 0.15 to 0.3. The Poisson's ratio for Lac du Bonnet granite is typically around 0.22. As indicated in Figure B.7 ν has no effect on the Griffith locus.

Fracture Surface Energy

The fracture surface energy (α) in compression is seldom measured. However, α in tension is found through equation B.3 and K_{Ic} can be obtained through simple laboratory tests. Figure B.8 shows the change in Griffith locus as K_{Ic} varies from 1 to 2 MPa$\sqrt{\text{m}}$. The fracture surface energy has essentially no effect on the positive slope position (stiffness) of the locus and only minor effects on the threshold value of the locus.

Number of Cracks

Figure B.9 shows the change in Griffith locus as the number of cracks goes from 0 to 10,000. Notice that when $n = 0$ there is no sliding and the result is a straight line corresponding to the modulus of the material. Hence it is the number of cracks which determines when the
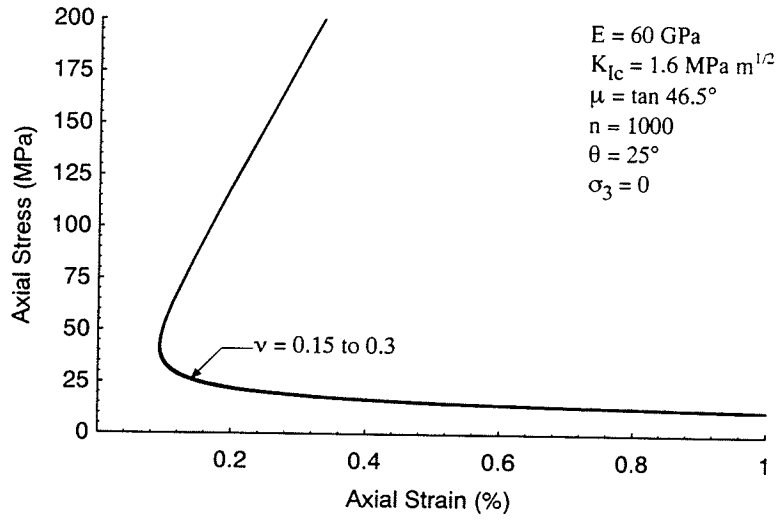
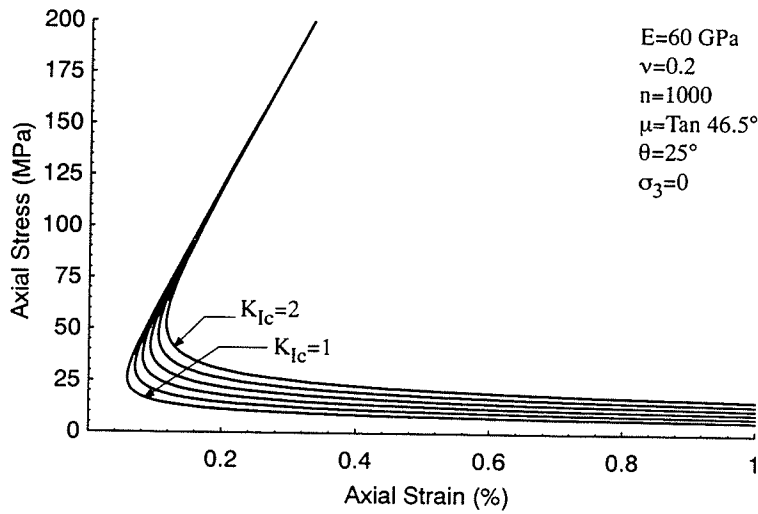Figure B.7: The Griffith locus as a function of Poisson's ratio (ν).

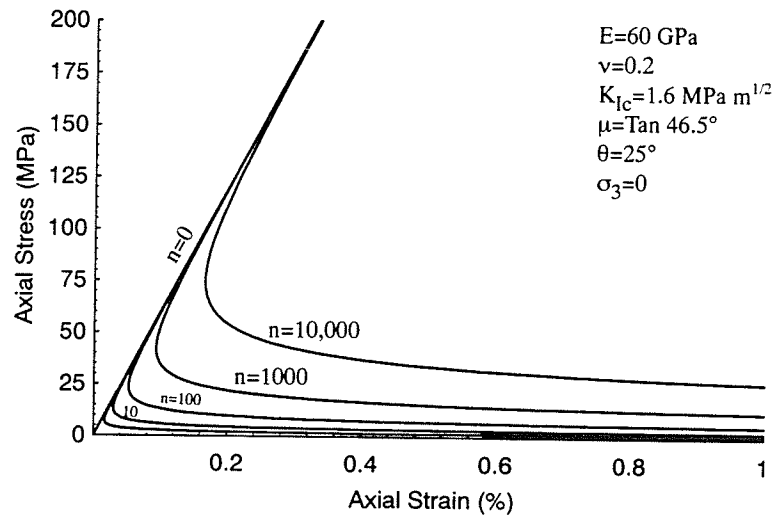Figure B.8: The Griffith locus as a function of fracture toughness (K_{Ic}).

Figure B.9: The Griffith locus as a function of the number of cracks (n).

slope of the locus changes from positive to negative. Also note that when $1000 < n < 10,000$ there are only minor changes in the position of the locus.

Coefficient of Friction

Figure B.10 shows the change in Griffith locus as μ varies from 30 to 60°. Friction has only minor effects on the locus threshold and no effect on the positive slope.

Critical Crack Angle

Figure B.11 shows the change in Griffith locus as θ varies from 20 to 60°. The locus is fairly insensitive to θ in the range 20 to 30° but the threshold rises quickly as the θ increase above 30°. This is not surprising since rotating the crack away from the applied load is similar to applying a confining stress which has a significant effect on the threshold position.

Confining Stress

Figure B.5 shows the change in Griffith locus as the confining stress(σ_3) increases from 5 to 10 MPa. This shows that the threshold of the Griffith locus, for any given crack
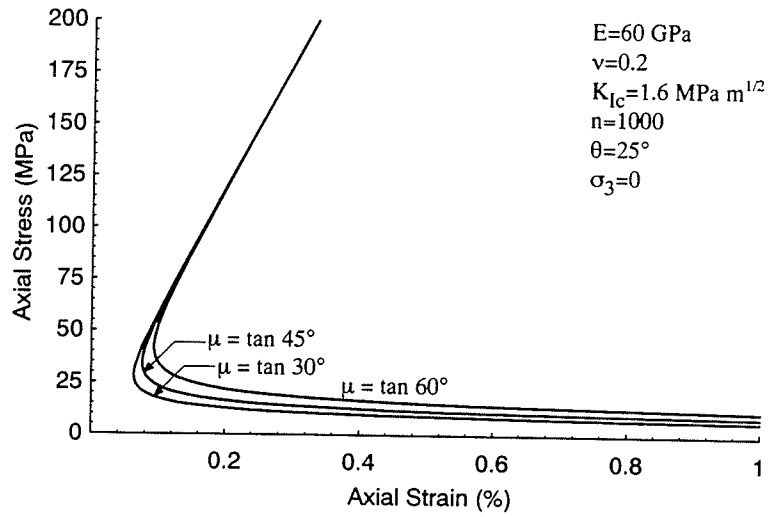
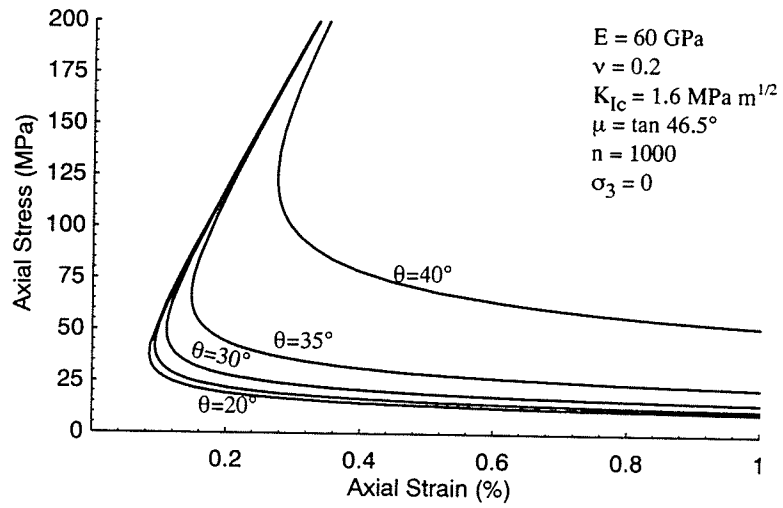Figure B.10: The Griffith locus as a function of the coefficient of friction (μ).

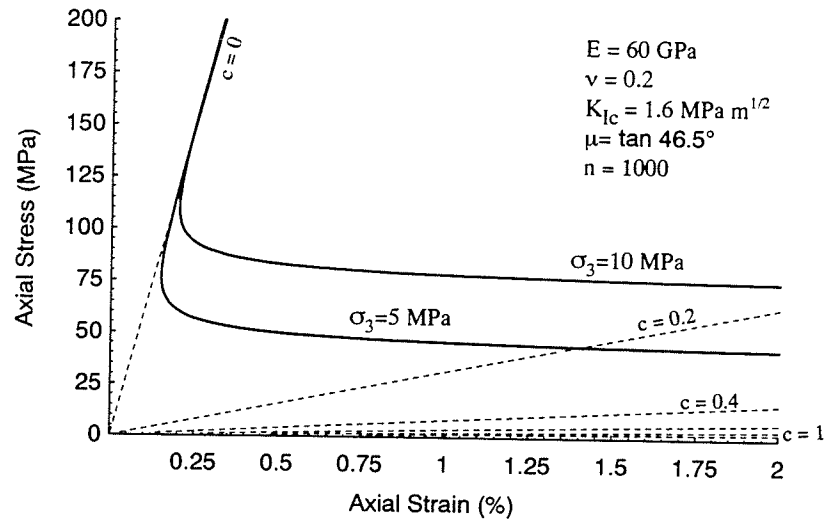Figure B.11: The Griffith locus as a function of the critical crack angle (θ).

Figure B.12: The Griffith locus as a function of confining stress (σ_3).

length is increased by an increase in the confining stress. The impact of confining stress is illustrated in Figure B.12 which shows that much larger strains are required for failure when the confining stress is increased. This is very similar to the notion that as confining stress increases a material becomes less brittle. Thus the confining stress has a significant effect on the Griffith locus.

B.5   Failure Envelope

Equation B.25 may be written as

$$\tau - \mu\sigma_n \geq \sqrt{\frac{8\alpha G}{\pi(1-\nu)c}} \qquad (B.26)$$

which gives the shear strength of the material in terms of crack length (c) and fracture surface energy (α).

Using

$$\sigma_n = \sigma_1 \sin^2\theta + \sigma_3 \cos^2\theta$$

$$\tau = (\sigma_1 - \sigma_3)\cos\theta\sin\theta$$

in equation B.26 gives

$$(\sigma_1 - \sigma_3)\cos\theta\sin\theta \ - \mu(\sigma_1\sin^2\theta + \sigma_3\cos^2\theta) \geq \sqrt{\frac{8\alpha G}{\pi(1-\nu)c}}$$

Dividing by $\sin\theta\cos\theta$ gives

$$(\sigma_1 - \sigma_3) - \mu\sigma_1\tan\theta - \frac{\mu\sigma_3}{\tan\theta} \geq \frac{\sqrt{\frac{8\alpha G}{\pi(1-\nu)c}}}{\sin\theta\cos\theta}$$

which reduces to

$$\sigma_1(1 - \mu\tan\theta) - \sigma_3\left(1 + \frac{\mu}{\tan\theta}\right) \geq \frac{\sqrt{\frac{8\alpha G}{\pi(1-\nu)c}}}{\sin\theta\cos\theta}$$

and solving for σ_1 gives

$$\sigma_1 = \frac{\sqrt{\frac{8\alpha G}{\pi(1-\nu)c}}}{\sin\theta\cos\theta(1 - \mu\tan\theta)} + \sigma_3\frac{\left(1 + \frac{\mu}{\tan\theta}\right)}{1 - \mu\tan\theta} \qquad (B.27)$$

Note that in equation B.27 the critical angle (θ_{cr}) will be related to μ in order that σ_1 in equation B.27 is a minimum.

Let

$$X = \frac{\left(1 + \frac{\mu}{\tan\theta}\right)}{1 - \mu\tan\theta}$$

Thus

$$\frac{dX}{d\theta} = \frac{\mu\csc^2\theta}{(\mu\sin\theta - \cos\theta)^2}(\mu\sin 2\theta - \cos 2\theta)$$
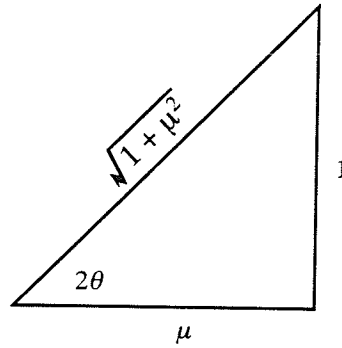
Hence

$$\frac{dX}{d\theta} = 0 \text{ when } \mu\sin 2\theta - \cos 2\theta = 0$$

Simplifying gives the relationship in Figure B.13

$$\mu\tan 2\theta - 1 = 0 \ \text{ or } \ \tan 2\theta = \frac{1}{\mu}$$

Using the following relations based on Figure B.13

$$\sin 2\theta \ = \ \frac{1}{\sqrt{1+\mu^2}}$$
$$\cos 2\theta \ = \ \frac{\mu}{\sqrt{1+\mu^2}}$$

Figure B.13: Relationship between angle θ and μ.

$$
\begin{aligned}
\sin 2\theta &= 2\sin\theta\cos\theta = \frac{1}{\sqrt{1+\mu^2}} \\
\cos 2\theta &= 1 - 2\sin^2\theta = \frac{\mu}{\sqrt{1+\mu^2}} \\
2\sin^2\theta &= \frac{\sqrt{1+\mu^2}-\mu}{\sqrt{1+\mu^2}}
\end{aligned}
$$

Then

$$
\tan\theta = \frac{2\sin^2\theta}{2\sin\theta\cos\theta} = \sqrt{1+\mu^2}-\mu
$$

Thus

$$
\frac{dX}{d\theta} = 0 \text{ when } \theta_{cr} = \tan^{-1}(\sqrt{1+\mu^2}-\mu)
$$

Now equation B.27 can be written as

$$
\sigma_1 = \frac{2\sqrt{\frac{8\alpha G}{\pi(1-\nu)c}}}{\sqrt{1+\mu^2}-\mu} + \left[\frac{\sigma_3}{\left(\sqrt{1+\mu^2}-\mu\right)^2} \right]
$$

or

$$
\sigma_1 = \frac{2\sqrt{\frac{8\alpha G}{\pi(1-\nu)c}}}{\sqrt{1+\mu^2}-\mu} + \sigma_3 \left[\frac{\sqrt{1+\mu^2}+\mu}{\sqrt{1+\mu^2}-\mu} \right] \tag{B.28}
$$

since

$$
\frac{1}{\left(\sqrt{1+\mu^2}-\mu\right)^2} = \frac{\sqrt{1+\mu^2}+\mu}{\sqrt{1+\mu^2}-\mu}
$$

Note that equation B.28 give a linear failure envelope similar to the general Mohr-Coulomb form. The cohesion part of equation B.28 can be reduced using

$$2\alpha = \mathcal{G} = \frac{K_{Ic}^2}{E}(1 - \nu^2)$$

and

$$G = \frac{E}{2(1 + \nu)}$$

Therefore

$$
\begin{aligned}
2\sqrt{\frac{8\alpha G}{\pi(1-\nu)c}} &= 2\sqrt{\frac{8}{c\pi(1-\nu)}\frac{K_{Ic}^2(1-\nu^2)}{2E}\frac{E}{2(1+\nu)}} \\
&= 2\sqrt{2}\frac{K_{Ic}}{\sqrt{\pi c}}
\end{aligned}
$$

Hence equation B.28 becomes

$$\sigma_1 \geq \frac{2\sqrt{2}\frac{K_{Ic}}{\sqrt{\pi c}}}{\sqrt{1+\mu^2}-\mu} + \sigma_3\left[\frac{\sqrt{1+\mu^2}+\mu}{\sqrt{1+\mu^2}-\mu}\right] \qquad (B.29)$$

Ashby and Sammis [2] derived a similar expression for crack initiation

$$\sigma_1 \geq \frac{\sqrt{3}\frac{K_{Ic}}{\sqrt{c\pi}}}{\sqrt{1+\mu^2}-\mu} + \sigma_3\left[\frac{\sqrt{1+\mu^2}+\mu}{\sqrt{1+\mu^2}-\mu}\right] \qquad (B.30)$$

The only difference between the two equations is $2\sqrt{2}$ in equation B.29 and $\sqrt{3}$ in equation B.30. It should be noted that

$$\frac{K_{Ic}}{\sqrt{c\pi}}$$

is considered equal to the tensile strength when K_{Ic} is the Mode I fracture toughness. Thus it is preferable to use equation B.28 as the fracture surface energy (α) is a material property and not dependent on the mode of fracture.

According to equation B.26 failure initiates when the shear driving stresses are greater resisting stresses in terms of fracture surface energy, and it has been shown that the form of this failure envelope is linear.

Since $\mu = \tan\phi$ then

$$\sigma_1 = \frac{2\sqrt{\frac{8\alpha G}{\pi(1-\nu)c}}}{\sqrt{1+\tan^2\phi}-\tan\phi} + \sigma_3\left[\frac{\sqrt{1+\tan^2\phi}+\tan\phi}{\sqrt{1+\tan^2\phi}-\tan\phi}\right]$$

Using

$$1+\tan^2\phi = \frac{1}{cos^2\phi} \text{ and } \tan\phi = \frac{\sin\phi}{\cos\phi}$$

this becomes

$$\sigma_1 = \frac{2\sqrt{\frac{8\alpha G}{\pi(1-\nu)c}}}{\sqrt{\frac{1}{cos^2\phi}}-\frac{\sin\phi}{\cos\phi}} + \sigma_3\left[\frac{\frac{1}{\cos\phi}+\frac{\sin\phi}{\cos\phi}}{\frac{1}{\cos\phi}-\frac{\sin\phi}{\cos\phi}}\right]$$

which reduces to

$$\sigma_1 = 2\sqrt{\frac{8\alpha G}{\pi(1-\nu)c}}\frac{\cos\phi}{1-\sin\phi} + \sigma_3\left(\frac{1+\sin\phi}{1-\sin\phi}\right)$$

But

$$\cos^2\phi = 1 - \sin^2\phi$$

which gives

$$\frac{\cos\phi}{1-\sin\phi} = \frac{\sqrt{1-\sin^2\phi}}{1-\sin\phi} = \frac{\sqrt{(1-\sin\phi)(1+\sin\phi)}}{\sqrt{(1-\sin\phi)(1-\sin\phi)}}$$

or

$$\frac{\cos\phi}{1-\sin\phi} = \sqrt{\frac{1+\sin\phi}{1-\sin\phi}}$$

Which gives

$$\sigma_1 = 2\sqrt{\frac{8\alpha G}{\pi(1-\nu)c}}\sqrt{\frac{1+\sin\phi}{1-\sin\phi}} + \sigma_3\left(\frac{1+\sin\phi}{1-\sin\phi}\right)$$

Since

$$\frac{1+\sin\phi}{1-\sin\phi} = \tan^2\left(45+\frac{\phi}{2}\right)$$

equation B.26 can be expressed in the general Mohr-Coulomb failure form of

$$\sigma_1 = 2S_o\tan\left(45+\frac{\phi}{2}\right) + \sigma_3\tan^2\left(45+\frac{\phi}{2}\right)$$

Thus the cohesion S_o in Mohr-Coulomb can be stated in terms of fracture surface energy as

$$S_o = \sqrt{\frac{8\alpha G}{\pi(1-\nu)c}}$$

B.5.1 Sensitivity of Failure Envelope to Input Parameters

As stated previously equation B.28 is a linear failure envelope with two components, cohesion and friction. The cohesion part of equation B.28

$$\frac{2\sqrt{\frac{8\alpha G}{\pi(1-\nu)c}}}{\sqrt{1-\mu^2}-\mu}$$

is dominated by the fracture surface energy (α) and the crack length (c) and the friction part of equation B.28 is dependent entirely on μ. In the following sections a parametric study is carried to determine which of the input parameters has the most significant impact on the failure envelope.

Crack Length

Figure B.14 shows the change in strength as c ranges from 1 to 9 mm. The grain size of the Lac du Bonnet granite is about 5 mm. As shown in Figure B.14 cohesion is significantly affected by crack length with cohesion decreasing as crack length increases. Note that the cohesion drops about 100 MPa as the crack grows from 1 to 3 mm but only 50 MPa as the crack grows from 3 to 9 mm.

Fracture Surface energy

As shown previously the parameter K_{Ic} is related to the fracture surface energy (α). Figure B.15 shows the change in strength as K_{Ic} ranges from 1 to 2 MPa$\sqrt{\text{m}}$. The K_{Ic} of the Lac du Bonnet granite is about 1.6 MPa$\sqrt{\text{m}}$. As shown in Figure B.15 cohesion increases from 60 to 120 MPa as K_{Ic} increases from 1 to 2 MPa$\sqrt{\text{m}}$.

Coefficient of Friction

Figure B.16 shows the change in strength as the angle of friction ranges from 30 to 60°. As shown in Figure B.16 there is a small increase in cohesion as μ increases but the slope of the failure envelope is significantly affected by the change in μ.
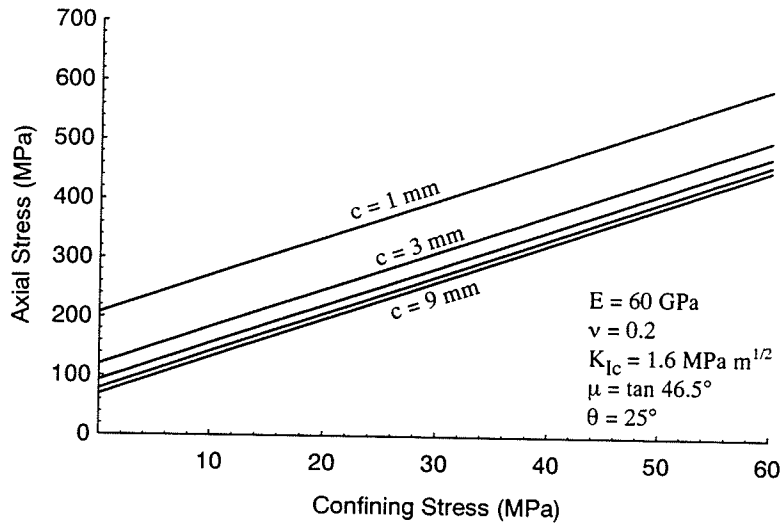
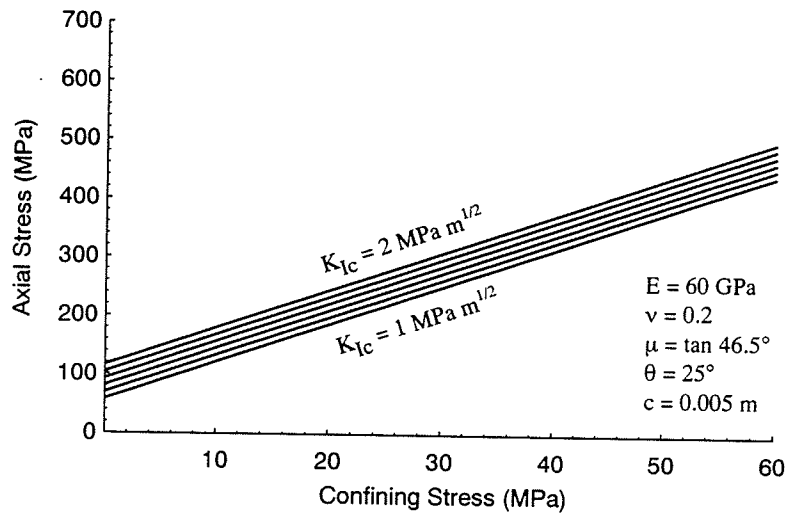Figure B.14: The failure envelope as a function of crack length (c).

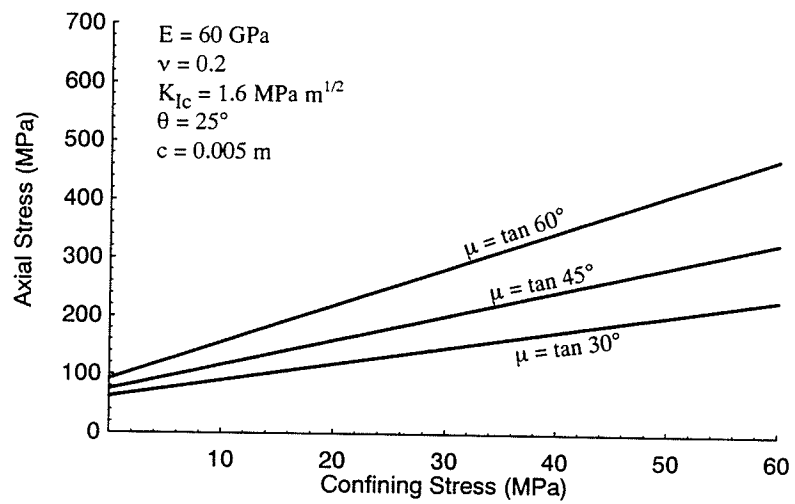Figure B.15: The failure envelope as a function of fracture toughness (K_{Ic}).

Figure B.16: The failure envelope as a function of friction (μ).

Appendix C

Fracture Surface Energy

According to Starr [147] and Cook [32] failure occurs when the fracture surface energy is exceeded. Therefore, the fracture surface energy becomes a key parameter in estimating the failure strength. It is instructive to examine the various means available to measure the fracture surface energy.

In fracture mechanics three modes of fracture are considered possible (Figure C.1). With mode I the loading is perpendicular to the plane of the crack and is generally referred to as "opening mode". Mode II requires in-plane shear and is called the "sliding mode". Mode III is caused by out-of-plane shear. The superposition of the three modes describes the general case of loading, although mode I is considered the most important mode in fracture mechanics. Mode II or the "sliding crack" is the model used in the development of the Griffith locus.

According to Brock [16], the elastic stress field surrounding the tip of the crack in mode I loading in the coordinate system of Figure C.2 is given by

$$\sigma_{ij} = \frac{K_I}{\sqrt{2\pi r}} f_{ij}(\theta) \tag{C.1}$$

The stresses σ_{ij} will be known once the stress intensity factor K_I is defined for the loading conditions. According to Brock [16], for the mode I problem in Figure C.2, K_I is given by

$$K_I = \sigma\sqrt{\pi c} \tag{C.2}$$

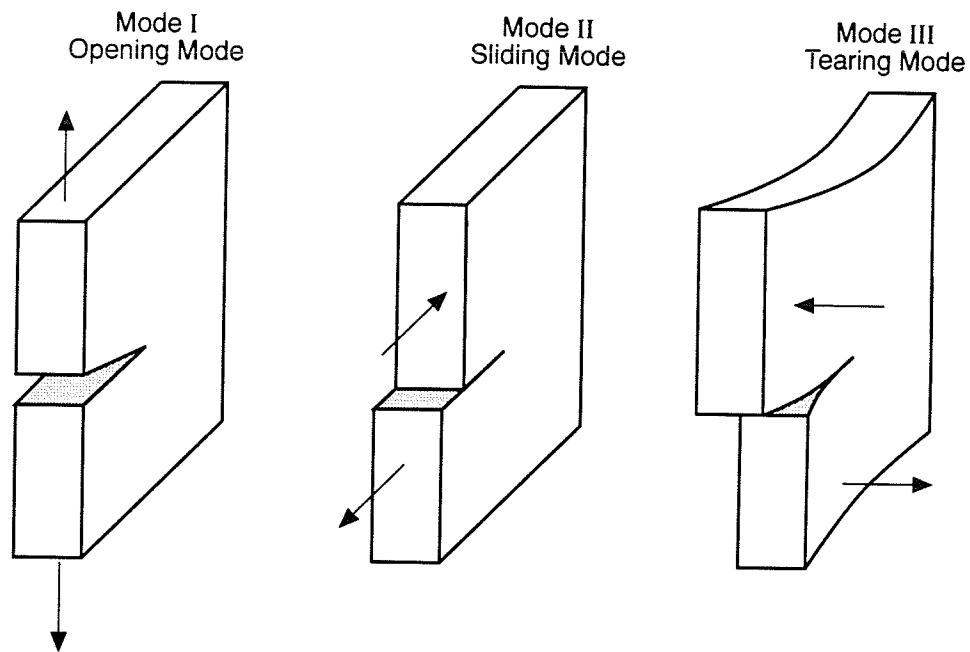The distribution of elastic stress σ_y, along OA, is illustrated in Figure C.3. However,

Figure C.1: The three modes of fracturing.

from equation C.1 it is evident that near the crack tip, i.e., $r = 0$, the stress at the tip is infinite. Since the stress at the tip cannot be infinite a plastic or process zone is considered to exist at the tip which limits the stress concentration to a maximum value (σ_{ys} in Figure C.3). Thus it becomes clear that the stress intensity factor, although essential for calculating the distribution of stress around the crack, may be a difficult parameter to quantify, especially, since rocks contain numerous flaws or cracks and the stress intensity formulation is based on a single crack.

C.1 The Griffith Criterion in Tension

Griffith [59] developed a criterion for fracture in mode I loading based on energy principles. Griffith's condition for crack growth is

$$\mathcal{G} = \frac{\pi c \sigma^2}{E} \qquad (C.3)$$

where $\mathcal{G}$ is the strain energy release rate per crack tip and has dimensions of energy per
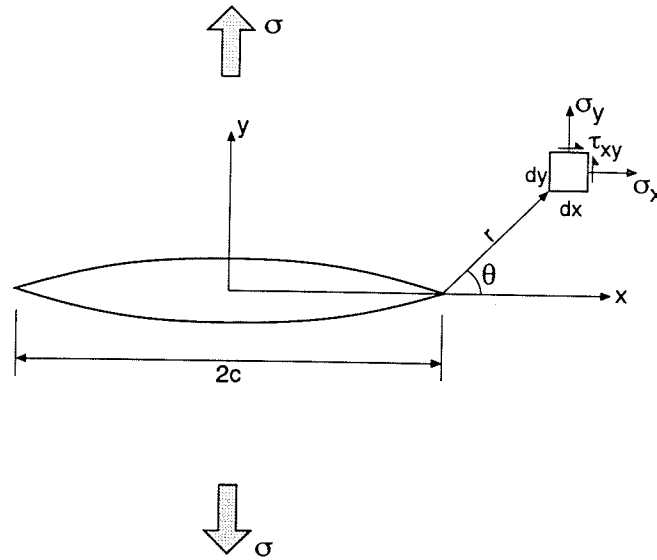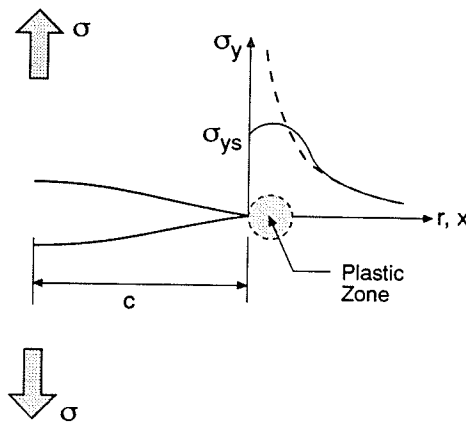
Figure C.2: Mode I fracture problem.

Figure C.3: Stress distribution with and without a plastic zone at the crack tip.

unit thickness. The strain energy release rate can be equated to the fracture surface energy (γ), which has the same dimensions, for the whole crack by

$$2\mathcal{G} = 4\gamma \tag{C.4}$$

Thus, equation C.3 can solved for the stress (σ_t) required to cause mode I failure in terms of γ by substituting, for $\mathcal{G}$ from equation C.4 into equation C.3

$$\sigma_t = \sqrt{\frac{2\gamma E}{\pi c}} \tag{C.5}$$

where σ_t is the tensile strength of the rock. The fracture surface energy γ can be expressed in terms of the stress intensity factor K_I, using equations C.2 and C.5 for plane stress giving:

$$\gamma = \frac{K_{Ic}^2}{2E} \tag{C.6}$$

and for plane strain

$$\gamma = \frac{K_{Ic}^2}{2E}(1 - \nu^2) \tag{C.7}$$

C.2 Direct Tensile Tests

The formulation of the fracture surface energy, γ in terms of K_{Ic} in equation C.6 provides an opportunity to compare the laboratory determined K_{Ic} with the fracture surface energy γ assuming that the critical crack is equivalent to the grain size. This is not an unrealistic assumption since it was demonstrated earlier that cleavage planes in feldspar were the first minerals to register cracking.

A series of direct tension tests were carried out on ten samples of Lac du Bonnet granite from the URL using the test specimen setup shown in Figure C.4. The test dimensions and results are given in Table C.1. The mean tensile strength for the ten tests was 6.93 and the mean Young's modulus, in tension, for the samples was 40.4 GPa. The ratio of Young's modulus in tension to the Young's modulus in compression is about 0.62. A similar ratio for
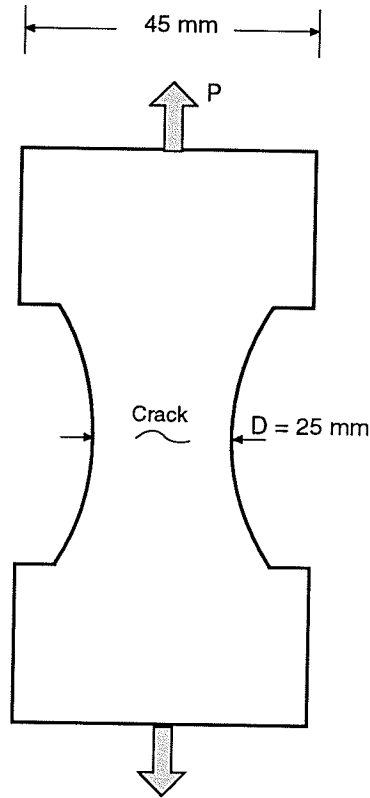
Figure C.4: Direct tension specimen and loading.

Lac du Bonnet granite has also been found by Rui [28] using a unique compression/tension testing configuration.

In Chapter 3 the mode I fracture toughness K_{Ic} for Lac du Bonnet granite ranged from 1.5 to 2.5 MPa$\sqrt{\text{m}}$. At the Underground Research Laboratory K_{Ic} is about 1.8 MPa$\sqrt{\text{m}}$. Using this value for K_{Ic}, $\sigma_t = 6.93$ MPa and the following equation for the crack length (obtained from equations C.5 and C.6)

$$c_t = \frac{2K_{Ic}^2}{\pi \sigma_t^2} \tag{C.8}$$

the estimated critical crack length at failure is 42 mm long. Clearly, since the diameter of the samples is about 45 mm (see Table C.1) this crack length is not realistic. If we now assume that the crack length $2c$ is about 4 mm (the average grain size of Lac du Bonnet granite), we find that the fracture surface energy is considerably smaller than that given by

Table C.1: Summary of the tensile strength obtained from the direct tension test.

Sample Number	Diameter (mm)	Thickness (mm)	Young's modulus (GPa)	σ_t (MPa)
34.134A	44.97	27.38	43.01	8.56
34.449A	44.98	27.37	47.48	7.83
34.763A	44.97	29.27	46.69	6.81
34.133A	44.98	28.76	29.29	6.52
35.533A	44.98	29.64	N/A	7.81
35.860A	44.98	28.74	N/A	7.57
38.030A	44.98	29.43	30.42	5.46
38.517A	44.99	29.34	42.87	5.63
41.043A	44.91	28.55	41.73	6.72
41.362A	44.92	28.85	41.56	6.38
mean			40.38	6.93

equation C.6. Figure C.5 shows the ratio of γ calculated with the 4 mm crack length, to γ_{theory} calculated using the measured laboratory value of K_{Ic} versus the tensile strength. These results suggest that the mode I stress intensity factor or fracture toughness is not a good representation of the stresses around the crack tip and hence the fracture surface energy should be best determined by equation C.5 and assuming $c =$ half the grain diameter.

C.3 Fracture Surface Energy in Compression and Tension

In Chapter 4 it was shown that the fracture surface energy only applies to the cohesion component of strength in both compression and tension. It was also shown in Chapter 4 that in compression testing the cohesive strength of the sample is given by the crack damage stress. In both the compression test and the tensile test the fracture is growing in its own plane. However in compression the mode of crack growth is mode II whereas in tension it is mode I.
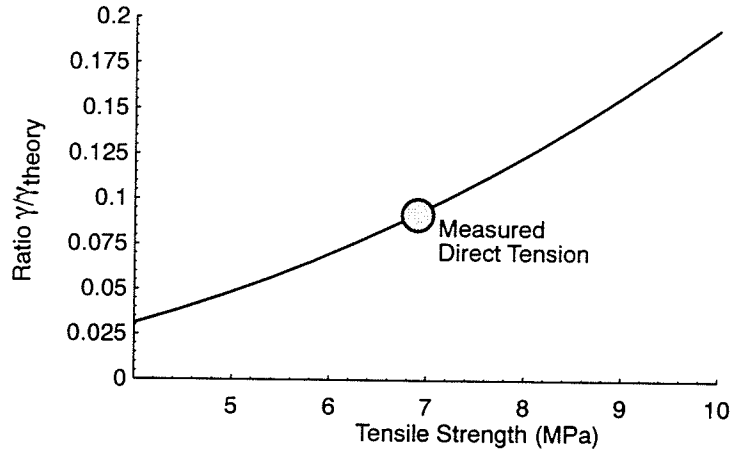
Figure C.5: The fracture surface energy required for failure compared to the fracture surface energy determined from the laboratory determined mode I K_{Ic}.

According to Cook [32] the condition for mode II fracture in compression occurs when

$$\tau - \mu\sigma_n = \sqrt{\frac{8\alpha E_c}{\pi(1 - \nu^2)c}} \qquad (C.9)$$

where E_c is the Young's modulus in compression. For the unconfined compression test equation C.9 reduces to

$$S_o = \sqrt{\frac{8\alpha E_c}{\pi(1 - \nu^2)c}} \qquad (C.10)$$

where S_o is the cohesion in $\tau - \sigma_n$ space. Equation C.10 can be solved for crack length and S_o replaced by $\sigma_{cd}/2$ to give

$$c = \frac{4\alpha E_c}{\sigma_{cd}^2(1 - \nu^2)\pi} \qquad (C.11)$$

If the crack length is considered equal to the grain size in both the tension and compression testing methods, the fracture surface energy in compression α can be determined in terms of the fracture surface energy in tension γ by equating equations C.11 and C.8

$$\frac{4\alpha E_c}{\sigma_{cd}^2(1 - \nu^2)\pi} = \frac{2E_t\gamma}{\pi\sigma_t^2} \qquad (C.12)$$

Substituting the appropriate values into equation C.12 gives
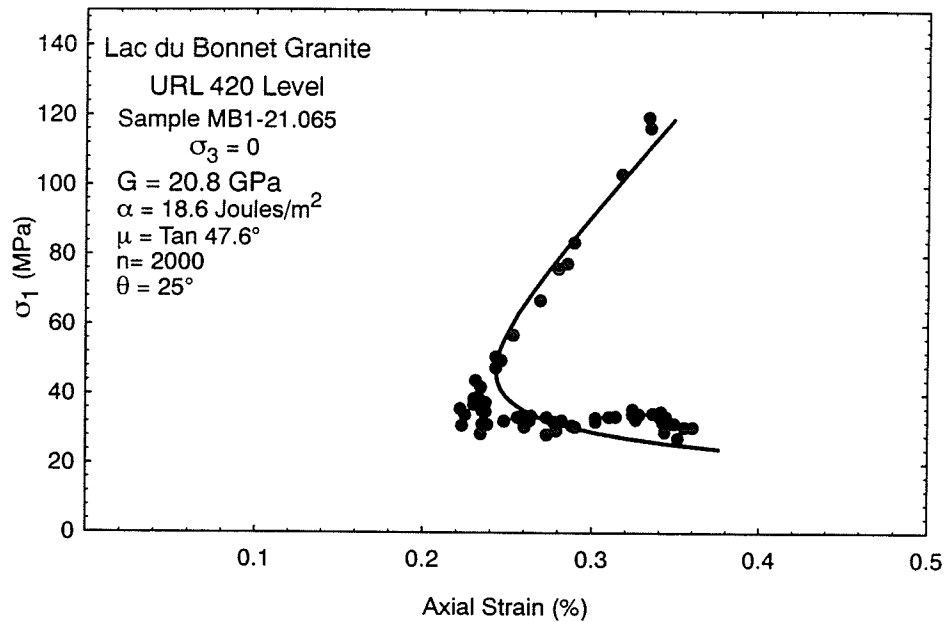
$$\alpha = 4.83\gamma \qquad (C.13)$$

Figure C.6: Comparison of the Griffith locus, using the calculated fracture surface energy from direct tension tests, with the measured crack damage locus. The new fracture surface energy increases the number of cracks (n).

The analysis above provides an alternate approach to measuring the fracture surface energy and avoids the limitations of the stress intensity factor approach of linear elastic fracture mechanics. The Griffith locus was recalculated for the unconfined case using the relationship in equation C.13 and the fracture surface energy determined from the direct tension tests, and re-compared with the crack damage locus. Now in order to get the same fit as before the number of cracks/unit volume had to increase from $n = 1200$ to $n = 2000$ (Figure C.6).